

Department of

Dipartimento di Scienze dell'Ambiente e della Terra

PhD program: Science Cycle: XXIX

Curriculum: Chemistry

Investigation of Sodium-ion Battery Materials

Surname: Longoni Name: Gianluca

Registration number: 787814

Tutor: Prof. Riccardo Ruffo

Coordinator: Prof. Maria Luce Frezzotti

ACADEMIC YEAR: 2016 / 2017

Declaration

I, Gianluca Longoni, declare that this is an original work which was conducted by the undersigned using the laboratory facilities at following institutes (listed as they were involved in the work): Materials Science Department, University of Milan-Bicocca, in Milan, Italy, Materials Science and Engineering Department, Faculty of Engineering, Stanford university, Stanford, California, U.S and Materials Science and Engineering Department, Faculty of Engineering, Korean Advanced Institute for Science and Technology (KAIST), Daejeon, Republic of Korea. and I referenced and acknowledged it. In addition I declare that this document has never been submitted as it is to other institution for qualifications.

Gianluca Longoni

9 January, 2017

Aknowledgements

This work has been done with keeping in mind.....-to be edited-

Contents

Declaration	ii
Aknowledgements.....	iii
Abstract	ix
List of Abbreviations	xiii
List of Symbols.....	xv
List of Figures	xvii
List of Tables	xxiii
CHAPTER I: Introductory elements	1
1. Objectives of the research	1
2. Thesis structure	1
CHAPTER II: General background	5
1. Introduction	5
2. Global energy landscape	6
3. The not-so-short history of rechargeable battery	9
4. Modern applications of rechargeable batteries: Li-ion for automotive and stationary storage	13
5. Concerns in lithium abundance	14
6. Sodium ion batteries.....	15
7. Bibliography.....	18
CHAPTER III: Technical part	21
1. Introduction	21
2. General thermodynamics.....	22
2.1. Nernst Equation.....	25
3. Kinetics of electrode reactions	29

4.	Figures of merit for batteries	30
4.1.	Specific energy, Specific power and specific capacity	30
4.2.	Open circuit Voltage (OCV) and Operational Potential (Working Voltage)..	33
4.3.	C-Rate.....	35
4.4.	Agreement on battery nomenclature	35
5.	Aqueous electrochemical cell.....	36
6.	Non-aqueous electrochemical cell	37
6.1.	Solid Electrolyte Interphase (SEI).....	38
7.	Active materials for aprotic alkaline secondary batteries	40
7.1.	Simple oxidation reaction from (alkali metal) bulk elemental species	40
7.2.	Insertion reaction.....	42
7.3.	Conversion reaction.....	46
7.4.	Pseudocapacitive mechanisms as source of capacity	49
8.	Bibliography.....	52
CHAPTER IV: SIBs anode materials review		55
1.	Introduction	55
2.	Carbon-based Materials.....	56
3.	Conversion Oxide Materials.....	62
4.	Binary Na-Me compounds	68
4.1.	Alloying materials	68
4.2.	Phosphorous-based materials	72
5.	Insertion anode materials	74
5.1.	TiO ₂ based insertion compounds.....	74
5.2.	MXenes	75
6.	Bibliography.....	76

CHAPTER V: SIBs cathode materials review	82
1. Introduction	82
2. Layered transition metal oxide (TMO)	83
2.1. P2-type TMOs	83
2.2. O3-type TMOs	87
3. Polyanionic compounds	89
3.1. Single-electron compounds	89
3.2. Multi-electron compounds	93
4. Bibliography	97
CHAPTER VI: Co ₃ O ₄ negative electrode material for SIBs: investigation of conversion reaction mechanism and morphology-performances correlation	103
1. Introduction	103
2. Background	103
3. Experimental	106
3.1. Material synthesis	106
3.2. Samples characterization	107
3.3. Electrochemical measurements	107
3.4. Electrode sodiation	108
4. Result and discussion	108
5. Conclusions	122
6. Bibliography	124
CHAPTER VII: The Na ₂ FeP ₂ O ₇ -carbon nanotubes composite as high rate cathode material	129
1. Introduction	129
2. Background	129
3. Experimental	131

3.1. Material synthesis.....	131
3.2. Sample characterization	132
3.3. Electrochemical characterization	132
4. Result and discussion	133
4.1. Chemical-physical characterization	133
4.2. General electrochemical characterization	138
4.3. EIS measurements	141
5. Conclusions	146
6. Bibliography.....	148
CHAPTER VIII: Morphology/properties correlation in nano-structured TiO ₂ as	
negative electrode in SIBs	151
1. Introduction	151
2. Background	151
3. Experimental	154
3.1. Synthesis.....	154
3.2. Sample characterization	157
3.3. Electrochemical characterization	157
4. Result and discussion	158
4.1. Chemical-physical characterization	158
4.2. Crystal dimensions and facets extension determination	160
4.3. Surface and pore distribution analysis (BET and BJH)	167
4.4. Electrochemical characterization results.....	169
5. Investigation of energy storage mechanism in TiO ₂	174
6. Conclusion.....	177
7. Bibliography.....	179

CHAPTER IX: Conclusions and Outlook.....	185
CHAPTER X: Appendix	187
1. GITT (Galvanostatic Intermittent Titration Technique)	187
2. BET (Brunauer-Emmet-Teller Surface Area Analysis)	189
3. PEIS (Potentiondynamic Electrochemical Impedance Spectroscopy).....	193
3.1. Response functions of simple circuits.....	194
3.2. Response of a parallel RC circuit.....	195
3.3. Warburg impedance element.....	196
4. XRPD	197
5. Bibliography.....	201

Abstract

Na-ion battery technology has recently aroused great interest among all the scientific community, as a valid and more environmentally friendly alternative to Li-ion batteries. The PhD research activity has been mostly devoted to the investigation of reliable active materials for sodium ion battery technology. It has been indeed stressed the importance of pursuing sodium-based battery research as a more cost efficient and sustainable solution compared to lithium and other more exotic battery chemistries recently proposed (Mg^{2+} and Al^{3+}). All the investigated materials, either anode or cathode, have been investigated trying to highlight the major limits and difficulties connected to sodium intercalation and conversion reactions. Among these, some are: i) assessment of Na diffusion in an intercalating host structure, ii) products and reversibility of transition metal oxides conversion reactions, iii) effects of materials crystalline properties on electrochemical performances and iv) features influencing the overall stability of a functional material. In order to keep the most broad-based overview of the problem, it has been chosen to systematically start, for each species electrochemically investigated, from its synthesis and thorough chemical-physical characterization. Rather than a pure electrochemical analysis, a continuous parallelism between morphological features, structural characteristics and performances was encouraged, eventually obtaining a detailed overlook of different classes of active materials for sodium batteries. What has been screened all along the three year-long research period has been a comprehensive investigation of new generation electrochemically active materials for energy storage applications. This implied an inter-disciplinary work in which advanced electro-analytical techniques have been widely used to characterize inorganic compounds or *ad-hoc* synthesized composites keeping in mind precise structure-performance correlations. Among the investigated classes, a role of relevance has been reserved to intercalating cathode species and conversion anode materials. The former, typically layered transition metal oxides, phosphates and pyrophosphates, are capable of sodium cations insertion, with fast kinetics, between layers or inside channels generated from peculiar atoms arrangement. Conversion anode materials on the other hand, carries out the sodium storage via spontaneous chemical reactions with oxide-based material, such as Co_3O_4 or Fe_2O_3 ,

a chalcogenide or a halide. Compared to intercalation materials, conversion ones are more challenging to deal with, due to the following difficulties: i) their not negligible volume change during conversion reaction and the correlated induced mechanical stresses leading to electrode fracturing and pulverization, ii) occurrence of irreversible and parasitic reactions and iii) material operating potentials is often too high (around 1.0 V vs. Na/Na⁺) and thus not suitable for being used as anode materials inside a sodium cell. A positive feature that makes these material worthy to be studied is the high sodium uptake they are able to bear, bestowing them high theoretical specific capacities (>800 mAh·g⁻¹). All these aspects have been tackled in designing a conversion anode that might constitute a valid solution toward a sodium secondary battery whole-cell assembly.

The results achieved will be in this abstract briefly presented starting from the preparation and characterization of a low-cost and highly efficient cathode material for sodium-ion batteries. The exploratory study of pyrophosphate-MWCNT (multiple walled carbon nanotubes) composite intercalation material led to interesting results referred to fast kinetics and material reliability throughout the cycles. Among the notable characteristics of the prepared composite, worthy to be quoted are the trivial synthetic procedure, based on a co-precipitation mechanism, and the high electrochemical stability that allowed to achieve 90 mAh g⁻¹ for more than 60 cycle with a coulombic efficiency close to 99.8 %. For the above mentioned composite, in-depth studies have been conducted also in order to quantify the sodium diffusion inside pyrophosphate lattice. To do so, an extensive analysis using Electrochemical Impedance Spectroscopy (EIS) technique has been performed. Results confirmed the high sodium diffusion inside 3D lattice channels giving a diffusion coefficient D_{Na} of $8.45 \times 10^{-13} \text{ cm}^2 \cdot \text{s}^{-1}$, one order of magnitude higher than sodium diffusion coefficients of layered oxides previously investigated in literature. Positive practical aspects of the composite is the flat potential plateau, peculiar of intercalation materials and a desirable feature assuring a more stable overall potential if coupled with an anode material in a whole cell.

To oxide-based anode materials study, has been dedicated the majority of the research work. A pure conversion material, spinel Co₃O₄, has been investigated first. In a hydrothermal synthesis environment a large number of reaction parameters (temperature, time, mineralizing agent, reagents concentration and fill factor) have been modulated. The final goal was to obtain a highly crystalline product, with high porosity and peculiar morphological arrangement

differences that would have evidenced how secondary structures might have an influence over conversion reaction. High porosity and hierarchical structures led to positive effects on materials electrochemical performances, especially better accommodating volume expansion and mechanical stress build-ups. Nevertheless 3D dimensionality of primary particles agglomerates impedes capacity retain. Slab-like and flake-like agglomerates are also less active towards a chemical sodiation pre-treatment, aimed at reducing the irreversible capacity experienced by conversion materials during the first sodiation/desodiation cycle. This pre-treatment is surpassingly useful in the case of 2D-like agglomerates in which primary particles are arranged in a linear fashion. The irreversible capacity related to the first cycle is sensibly reduced and during the following cycles an overall higher specific capacity is retained. Compared to recent analogue studies on similar compounds, the novelty of this work resides in having proposed a systematic study of a conversion material without a conductive substrate. This allowed to evaluate exclusively the contribution of the electrochemically active material alone, and justifies the slight fading capacity throughout the tests. Added to this, chemical sodiation of a conversion material has been here proposed for the first time on record. In-depth study of the occurring conversion event has been carried out using specific *ex-situ* XRD analysis on cycled electrodes. Interesting results have emerged concerning a non-complete restoration of spinel Co_3O_4 after each de-sodiation step (discharge). X-ray diffraction from cycled electrodes has evidenced the presence of crystalline CoO instead, revealing how CoO rather than fully oxidized form is more stable in a strong reducing environment. This aspect partially justifies the reduction in capacity, being the theoretical capacity of CoO, 25 % lower than theoretical value for Co_3O_4 .

Object of the research in the last part of the PhD activity has been the investigation of anode transition metal oxide materials (TiO_2) in which energy storage mechanism has been demonstrated to be based on an intercalation pseudocapacitance mechanism, at least for slow scan rates. Anatase- TiO_2 represents a valid candidate as anode material for sodium batteries, and has been recently demonstrated that carbon-coated TiO_2 crystals conveniently engineered, can give capacity as high as $150 \text{ mAh}\cdot\text{g}^{-1}$ at the astonishingly high scan rate of 5 C. Since it is widely accepted that TiO_2 interaction with sodium does not proceed exclusively *via* a conversion mechanism, the aim was to investigate how this process occurs and which might be the dependence between an intercalation mechanism and the exposed crystalline facets of

tailored TiO₂ crystals. A tailored solvothermal synthesis using different surfactants has been employed. Different capping agents were used in relation to their ability in adsorbing on specific crystalline faces. Changing their relative ratio, allowed to selectively direct the crystal growth obtaining in the end, different crystalline surfaces with different percent exposures (in m²·g⁻¹). Different crystalline facets have demonstrated to have a heavy influence on sodium uptake. In particular, intermediate-energetic facets (100) guarantee notable specific capacity and higher stability over cycles. Further analysis showed that anatase phase integrity is not compromised during cycling, as *ex-situ* XRD measurements revealed.

Cyclic voltammetry allowed analyzing the electrochemical mechanism nature that guarantees the majority of the stored capacity. The concurring mechanisms would be i) a pure capacitive one deriving from a double-layer instauration, ii) a Faradaic diffusion-limited process connected to sodium intercalation or surface red-ox reaction or Na⁺ intercalation. The observed behavior in the case of nano-crystalline TiO₂, has to be considered as a linear combination of the two contributes previously introduced. At each potential value scanned a specific ratio between contributes is achieved. For scan rates below 0.5 mV·s⁻¹ and at currents collected at peak potential, there is no diffusion limitation of active species and the occurring process must be assimilated to an intercalation mechanism with capacitive behavior. These and other tests have been performed in order to prove the importance in investigating the effect of crystalline exposed facets on alkaline cation intercalation. In this way a more systematic and less serendipity-dependent approach can be exploited in classifying materials suitable for application as sodium-ion battery anodes. In conclusion, nanostructures TiO₂, as already highlighted in literature in the case of Li⁺, does not interact with sodium through a conversion process, but a more sophisticate intercalation mechanism has to be considered. The latter, in particular, has a strong dependence with the exposed crystalline facets being sodium cations intercalation more sensitive to titanium and oxygen atoms density at the interface and, consequently, the surface energy densities of facets. Intercalation pseudocapacitance has been also found to be a relevant mechanism in TiO₂-reduced graphene oxide composite, confirming results presented in literature.

List of Abbreviations

Abbreviation	Full name
ASA	Active Surface Area
BET	Brunauer Emmet Teller
BMS	Battery management system
CB	Carbon black
CE	Coulombic Efficiency
CUBICON	Cubic ionic conductor
DEC	Diethylene carbonate
DMC	Dimethyl carbonate
EC	Ethylene carbonate
EDLC	Electric double layer capacitor
EV	Electric vehicle
FEC	Fluoroethylene carbonate
GHG	Green house gases
GIC	Graphite intercalation compound
GITT	Galvanostatic intermittent titration technique
GNS	Graphene nano-sheet
HC	Hard Carbon
HEMM	High energy milling machine
HEV	Hybrid electric vehicle
HOMO	Higher occupied molecular orbital
IPE	Ideally polarizable electrode
LIB	lithium ion battery
LUMO	Lowest unoccupied molecular orbital
Mtoe	Megaton of oil equivalent
MTSC	Maximum theoretic specific charge
MTSE	Maximum theoretical specific energy
MWCNT	Multiple walled carbon nanotubes
NASICON	Sodium (Na ⁺) Superionic Conductors
NHE	Normal hydrogen electrode
NIB	sodium ion battery

OCV	Open circuit potential
OECD	Organization for economic co-operation and development
PAA	Plyacrylyc acid
PAN	Polyacrylonitrile
PC	Propylene carbonate
PDDA	Poly(diallyldimethylammonium chloride)
PEIS	Potentiostatic electrochemical impedance spectroscopy
PEO	Polyethylene oxide
PSA	Poly(sodium 4-styrenesulfonate)
PWRD	Powder X-Rays diffraction
SAED	Selected Area Electron Diffraction
SAXS	Small angle X-Rays scattering
SEI	Solid electrolyte interface
SES	Stationary electric storare
SIB	Sodium ion battery
SLI	Start-Lighting-Ignition
SOC	State of charge
TGA	Thermal Gravimetric Analysis
TMO	Transition metal oxide
TPES	Total primary energy supply (or total gross inland energy consumption)
UPS	Uninterruptible power supply
XRD	X-Ray diffraction

List of Symbols

Symbol	Name	Unit
E_a	Activation energy	$\text{kJ}\cdot\text{mol}^{-1}$
2θ	Detection angle in XRD	Degree
C-Rate	Charge/discharge current	$\text{mA}\cdot\text{g}^{-1}$
F	Farady constant = 96485	C
f	Frequency in EIS measurement	Hz
I	Current density	$\text{A}\cdot\text{cm}^{-2}$
i_0	Exchange current	A
L	Crystalline size	nm
m	Active material weight	g
W_t	Molar weighth	$\text{g}\cdot\text{mol}^{-1}$
P	Relative pressure	Pa
P_0	Saturation pressure	Pa
x	Stoichiometric composition of a phase	-
λ	X-Ray wavelength	nm
Z_w or W	Warburg impedance	Ω
Z_{re}	Real part of impedance	Ω
Z_{im}	Imaginary part of impedance	Ω
T	Temperature	$^{\circ}\text{C}$
t	Time	h or s
R	Gas constant = 8.319	$\text{J}\cdot\text{K}^{-1}\cdot\text{mol}^{-1}$
R_{ct}	Charge transfer resistance	Ω
e	Electrons equivalents	$\text{eq}\cdot\text{mol}^{-1}$
Q	Specific capacity	$\text{mAh}\cdot\text{g}^{-1}$
Φ	Work function	eV
E_g	Energy gap	eV
μ	Fermi level	eV
E°	Standard redox potential	V vs. ref
E	Formal redox potential	V vs. ref
D	Diffusion coefficient	$\text{Cm}^2\cdot\text{S}^{-1}$

List of Figures

FIGURE II-1: TYPICAL SPECIFIC ENERGY DENSITY FOR LEAD-, NICKEL- AND LITHIUM-BASED RECHARGEABLE BATTERIES.	13
FIGURE II-2: MANUFACTURING COSTS FOR SIBS AND LIBS HIGHLIGHTING SINGLE CONTRIBUTION TO THE OVERALL COST.	17
FIGURE III-1: SIMPLE SCHEMATIC MODEL OF THE CHEMICAL REACTION OF A AND B TO FORM C, INDICATING HOW THE MICROSTRUCTURE OF THE SYSTEM VARIES WITH TIME.	23
FIGURE III-2: SIMPLE SCHEMATIC MODEL OF THE TIME EVOLUTION OF THE MICROSTRUCTURE DURING THE ELECTROCHEMICAL REACTION OF A AND B TO FORM C, A MIXED CONDUCTOR. IT IS ASSUMED THAT B^+ IONS ARE THE PREDOMINANT IONIC SPECIES IN THE ELECTROLYTE. THE SIMPLE EXTERNAL CIRCUIT IS REPRESENTED ONLY AS THE PATH GUARANTEEING ELECTRONIC CONTINUITY BETWEEN A AND B.	23
FIGURE III-3: PROPOSED MODEL OF THE DOUBLE-LAYER REGION UNDER CONDITIONS WHERE NO SPECIFIC ADSORPTION OF CHARGED SPECIES HAPPENS.	28
FIGURE III-4: EQUIVALENT CIRCUIT OF A GALVANOSTATIC CELL WITH DIFFERENT PHYSICAL PROPERTIES MODELED WITH EQUIVALENT CIRCUIT ELEMENTS; N_b ELEMENT REPRESENTS THE OPERATIONAL CELL POTENTIAL, SEE TEXT FOR FURTHER DETAILS.	29
FIGURE III-5: RAGONE PLOT, PLOTTING SPECIFIC POWER VS. SPECIFIC ENERGY, FOR VARIOUS BATTERY CHEMISTRIES. ON THE RIGHT Y-AXIS THE DRAIN CURRENT BORN BY BATTERY SYSTEMS ARE ALSO REPORTED.	32
FIGURE III-6: GRAPHICAL DESCRIPTION OF A SODIUM RECHARGEABLE BATTERIES; ANODE AND CATHODE MATERIAL CHOICE IS PURELY DESCRIPTIVE AND HAS NO MEANING OF COMPLETENESS.	35
FIGURE III-7: SCHEMATIC OPEN CIRCUIT ENERGY DIAGRAM OF AN ELECTROLYTE; Φ_C AND Φ_A ARE CATHODE AND ANODE WORK FUNCTIONS RESPECTIVELY, E_G IS THE THERMODYNAMIC STABILITY WINDOW OF THE ELECTROLYTE. $M_A > LUMO$ AND $MC <$ $HOMO$ REQUIRE A KINETIC ACHIEVED WITH THE FORMATION OF A SEI LAYER.	38
TABLE III-1: PHYSICAL AND CHEMICAL RELEVANT PROPERTIES FOR LI AND NA METALS, USEFUL TO CONTEXTUALIZE THEIR PERFORMANCES IF USED AS ANODE MATERIALS IN SECONDARY LIBS AND SIBS.	41
FIGURE III-8: COULOMETRIC TITRATION OF NA INSERTION IN HOST MATERIAL. TWO SOLID-STATE SOLUTION TYPE OF INSERTION ARE FOLLOWED BY A RECONSTITUTION REACTION OFR POTENTIAL VALUES BELOW 1.5 V vs. Na/Na^+	44
FIGURE III-9: SHEETS OF EDGE-SHARING MeO_6 OCTAHEDRAL ACCOMMODATE IN THE SPACE IN BETWEEN SODIUM IONS AND DEPENDING ON THE GEOMETRY OF SODIUM ATOM ENVIRONMENT, O AND P STRUCTURES CAN BE DISTINGUISHED.	45
FIGURE III-10: CALCULATED DIFFERENCES IN CELL POTENTIAL BETWEEN CONVERSION COMPOUNDS M_aX_b WITH SODIUM AND LITHIUM. POSITIVE VALUES MEAN THAT REPLACING LITHIUM WITH SODIUM WILL RESULT IN LOWERING THE CELL POTENTIAL BY THE REPORTED AMOUNT, AND VICE VERSA FOR NEGATIVE VALUES.	48
FIGURE IV-1: A) CARTOONS DEPICTING DIFFERENT TYPES OF CARBONACEOUS MATERIAL ACCORDING TO THEIR MICROSTRUCTURE; HARD CARBON NON-GRAPHITIZABLE CARBONS, IN THE "FALLING CARDS" MODEL POSSESSES A HIERARCHICAL STRUCTURE IN WHICH INSERTION DOMAIN AND ADSORPTION MICRO- AND MESO-POROUS SITES ARE BOTH PRESENT; B) THE TWO MECHANISM OF	

SODIUM STORAGE OCCURRING IN A HARD-CARBON STRUCTURE; D) EVOLUTION OF RAMAN (LEFT) AND XRD (RIGHT) SIGNALS FOR A HARD-CARBON OBTAINED FROM PAN PYROLIZED AT DIFFERENT TEMPERATURES.	60
TABLE IV-1: CARBON-BASED MATERIAL MORPHOLOGIES SO FAR INVESTIGATED AS ANODES FOR SIBS; FOR EACH SAMPLE THE MAIN ELECTROCHEMICAL AND PHYSICAL FEATURES ARE REPORTED.....	61
FIGURE IV-2: A) SYNTHETIC APPROACH PROPOSED BY YANG AND CO-WORKERS BASED ON A TEMPLATE OR NANOCASTING METHOD FOR THE PREPARATION OF A POROUS 3D-STRUCTURED Co_3O_4 ; B) TEM IMAGE OF THE NANOCASTED STRUCTURE IN WHICH THE ORDERED PATTERNING MADE BY VOIDS IS VISIBLE; C) <i>EX-SITU</i> XRD STUDIES CONDUCTED ON M Co_3O_4 SAMPLE IN ORDER TO MONITOR PHASES EVOLUTION DURING CHARGE AND DISCHARGE OF THE MATERIAL; D) GALVANOSTATIC PERFORMANCES OF THE PREPARED MATERIALS.	64
FIGURE IV-3: A) GALVANOSTATIC ANALYSIS RESULT FOR SnO , SnO_2 AND SnO_2/C FROM THE WORK BY LU AND CO-WORKERS; B) SODIATION/DE-SODIATION CURVES FOR THE ABOVE INTRODUCED SAMPLES USING DIFFERENT SODIATION CUT-OFF POTENTIAL VALUES; C) XRD PATTERN EVOLUTION THROUGH CYCLING FOR SnO AND SnO_2/C ; D) TEM AND SAED PATTERNS FOR SnO_2/C PARTICLES BEFORE (A-C-E) AND AFTER (B-D-F) SODIATION.	66
TABLE IV-2: NA-ALLOYING ELEMENTS BELONGING TO P-GROUP OF PERIODIC TABLE WITH THEIR ELECTROCHEMICAL PROPERTIES	69
FIGURE IV-4: A) SODIATION/SE-SODIATION CURVES SUPERIMPOSED TO NA-SN PHASE DIAGRAM; B) EXPERIMENTAL SODIATION/DE-SODIATION CURVES SUPERIMPOSED TO DFT CALCULATION FOR TIN SODIATION AND MEASURES TAKEN AT HIGH TEMPERATURES....	70
FIGURE IV-5: A) CYCLIC PERFORMANCE AND COULOMBIC EFFICIENCY OF RED P/NITROGEN DOPED GRAPHENE OXIDE COMPOSITE AT 200 AND 800 $\text{mA}\cdot\text{g}^{-1}$; B) GALVANOSTATIC CHARGE/DISCHARGE PROFILES OF ELECTRODE AT 200 $\text{mA}\cdot\text{g}^{-1}$ AND C) RATE TEST ON THE SAME PHOSPHORUS/GRAPHENE COMPOSITE.....	73
FIGURE V-1: TEMPERATURE/COMPOSITION PHASE DIAGRAM OF LAYERED CoO_2 COMPOUND IN WHICH SINGLE PHASE STABILITY ZONES AND EQUILIBRIUM LINES OF DIFFERENT STRUCTURES ARE INDICATED.	84
FIGURE V-2: A) INTERCALATION/DE-INTERCALATION POTENTIAL VS. CAPACITY PROFILE OF LAYERED CoO_2 WITH LITHIUM (BLUE CURVE) AND SODIUM (RED CURVE); B) LATTICE PARAMETERS EVOLUTION OF $\text{P2-Na}_{0.7}\text{Fe}_{0.4}\text{Mn}_{0.4}\text{Co}_{0.2}\text{O}_2$ ELECTRODE FROM <i>IN SITU</i> SYNCHROTRON ANALYSIS, POTENTIAL PROFILE OF CAPILLARY CELL IS ALSO REPORTED AT THE TOP OF THE IMAGE; C) SCHEMATIC ILLUSTRATION USED IN A CAPILLARY CELL USED IN SYNCHROTRON ANALYSIS AND <i>IN SITU</i> XRD PATTERNS $\text{P2-Na}_{0.7}\text{Fe}_{0.4}\text{Mn}_{0.4}\text{Co}_{0.2}\text{O}_2$ EVOLUTION AS THE $\text{Na}/\text{P2-Na}_{0.7}\text{Fe}_{0.4}\text{Mn}_{0.4}\text{Co}_{0.2}\text{O}_2$ WAS CYCLED INSIDE THE CAPILLARY CELL.	85
FIGURE V-3: A) MATERIAL DESIGN OF RADIALLY ALIGNED SPHERICAL PARTICLES WITH A GRADIENT COMPOSITION AND B) CHARGE/DISCHARGE PROFILE (LEFT) AND GCPL ELECTROCHEMICAL CHARACTERIZATION AT DIFFERENT TEMPERATURE (RIGHT) OF RADIALLY ALIGNED PARTICLE AND A CONTROL BULK SAMPLE.	88
FIGURE V-4: A) MECHANISM OF LI-NA SUBSTITUTION IN OLIVINE LiFePO_4 STRUCTURE, IN ORDER TO MAINTAIN AN ELECTROCHEMICALLY ACTIVE PHASE TO SODIUM INSERTION; B) ELECTROCHEMICAL PERFORMANCES OF NaFePO_4 AT DIFFERENT CHARGE/DISCHARGE RATES, C(I) IS RELATED TO OLIVINE LiFePO_4 , C(II) MARICITE NaFePO_4 IN 101 PLANE, C(III) REFERS TO LAYERED STRUCTURE OF $\text{Na}_2\text{FePO}_4\text{F}$ STRUCTURED (FeO_6 OCTAHEDRAL SHOWN IN GREY, PO_4 TETRAHEDRAL IN PURPLE, AND SODIUM ION ARE DEPICTED AS BLACK SPHERES), C(IV) IS CRYSTAL STRUCTURE OF $\text{Na}_{1.5}\text{VPO}_{4.8}\text{F}_{0.7}$ WITH $\text{VO}_5\text{F}/\text{VO}_4\text{F}_2$ OCTAHEDRAL SHOWN IN CYAN AND YELLOW SPHERES REPRESENTING THE Na^+ IONS, D) CHARGE/DISCHARGE PROFILE OF LAYERED $\text{Na}_2\text{CoPO}_4\text{F}$ STRUCTURE.....	90

FIGURE V-5: CRYSTAL STRUCTURE OF $\text{Na}_{1.5}\text{VPO}_{4.8}\text{F}_{0.7}$, WITH THE TWO DIFFERENT ENVIRONMENT BUILT AROUND V^{4+} AND V^{3+} CENTERS (I.E., VO_5F AND VO_4F_2 OCTAHEDRA RESPECTIVELY). NA, V, P, O AND F ARE DEPICTED AS YELLOW, CYAN, PURPLE, RED AND GREEN SPHERES, RESPECTIVELY.....	95
FIGURE V-6: A) CHARGE/DISCHARGE PROFILE OF $\text{Na}_{1.5}\text{VPO}_{4.8}\text{F}_{0.7}$ IN THE ONE-ELECTRON WINDOW, INSET OF THE FIGURE REPORTS THE DIFFERENTIAL CAPACITY GRAPH; B) POTENTIAL VS. SPECIFIC CAPACITY PLOT OF WIDELY INVESTIGATED CATHODE FOR LIBS AMONG WHICH $\text{Na}_{1.5}\text{VPO}_{4.8}\text{F}_{0.7}$ IS INSERTED AS ELEMENT OF COMPARISON, (BPOE = POLYETHYLENE OXIDE BASED BATTERY); C) VOLUME EXPANSION FOR RECENTLY INVESTIGATED CATHODES FOR SIBS AND CORRESPONDENT STOICHIOMETRIC SODIUM COMPOSITION, IN THE BOTTOM RIGHT CORNER CYCLING STABILITY AT ROOM TEMPERATURE AND AT 60 °C IS REPORTED.....	96
TABLE VI-1: HYDROTHERMAL STEP PARAMETERS EMPLOYED FOR THE CO INTERMEDIATED SYNTHESIS.....	107
FIGURE VI-1: XRD PATTERN OF Co_3O_4 SAMPLES.....	109
FIGURE VI-2: SEM AND TEM MICROGRAPHS OF (A,D) NR7, (B,E) NR16 AND (C,F) NR21; INSETS OF IMAGES D9, E9, F9 SHOW MAGNIFICATION OF Co_3O_4 CRYSTALLITES IN WHICH LATTICE FRINGES ARE VISIBLE.	110
FIGURE VI-3: HIGH MAGNIFICATION TEM IMAGES OF A) NR7, B) NR16 AND C) NR21 SAMPLES. EACH COMPOSITION INCLUDES A LOWER MAGNIFICATION IMAGE IN WHICH SOME PORES ARE QUANTIFIED IN WIDTH; MAGNIFICATIONS ARE DIFFERENT IN ORDER TO APPRECIATE THE FINE POROUS STRUCTURE OF EACH SAMPLE. IN THE LOWER LEFT CORNER OF THE COMPOSITION IS REPORTED A HRTEM IMAGE IN WHICH THE AREA FROM WHICH ELECTRON DIFFRACTION PATTERN HAS BEEN OBTAINED IS HIGHLIGHTED; THE CORRESPONDENT SAEDs FFT ARE REPORTED ON THE LOWER RIGHT CORNERS.	111
FIGURE VI-4: A) ELECTROCHEMICAL CHARACTERIZATION OF Co_3O_4 POWDERS USING GALVANOSTATIC CYCLING WITH POTENTIAL LIMITATION (GCPL); B) DISCHARGE/CHARGE PROFILES ARE REPORTED FOR NR16 SAMPLE, ALL THE ELECTRODES HAVE BEEN DISCHARGED/CHARGED AT 0.1 C ($89 \text{ mA}\cdot\text{g}^{-1}$).....	112
FIGURE VI-5: SODIATION/DE-SODIATION PROFILES RELATED TO FIRST AND SECOND CYCLE FOR A) NR7, B) NR16 AND C) NR21 RESPECTIVELY.	113
FIGURE VI-6: A) XRD DIFFRACTOGRAMS OF PRISTINE NR16 ELECTRODE (BLACK) AND CYCLED ONE (RED); WITH ASTERISKS ARE INDICATED DIFFRACTION PEAKS COMING FROM COPPER CURRENT COLLECTOR; B) EDX TAKEN ON PRISTINE ELECTRODE AND B) ON CYCLED ONE AFTER THE 4 TH DE-SODIATION STEP.....	115
FIGURE VI-7: SEM MICROGRAPHS OF CO_N ELECTRODE AT DIFFERENT TIMES DURING GCPL TESTS; A) REFERS TO THE PRISTINE ELECTRODE AS PREPARED AFTER BLADE CASTING OF THE ACTIVE MATERIAL ON THE CURRENT COLLECTOR; B) AND C) THE OTHER TWO PICTURES WERE TAKEN DISASSEMBLING THE COIN CELLS AFTER 1 ST AND 4 TH CYCLES RESPECTIVELY (FOLLOWING THE DESODIATION STEP OF Co_3O_4 ELECTRODES) INSIDE THE ARGON-FILLED GLOVE BOX AND WASHING THE WORKING ELECTRODE WITH PURE ACETONITRILE IN ORDER TO REMOVE SEI LAYER AS MUCH AS POSSIBLE.....	116
FIGURE VI-8: A) RATE TEST ON CO_N . FOR EACH CURRENT DENSITY, SIX CYCLES HAVE BEEN PERFORMED, PROGRESSIVELY GOING FROM 0.1C ($89 \text{ mA}\cdot\text{g}^{-1}$), 0.5C ($445 \text{ mA}\cdot\text{g}^{-1}$), 1C ($890 \text{ mA}\cdot\text{g}^{-1}$), 2C ($1780 \text{ mA}\cdot\text{g}^{-1}$) AND AS HIGH AS 5C ($4450 \text{ mA}\cdot\text{g}^{-1}$); B) CHARGE/DISCHARGE PROFILES OBTAINED DERIVED FROM RATE TEST PERFORMED ON CO_N SAMPLE, LAST CYCLE PERFORMED AT LOW RATE (0.1 C) IS REPORTED WITH THE BLACK DASHED LINE.....	117

FIGURE VI-9: A) SODIATION/DESODIATION PROFILES OF PRE-TREATED (RED) AND PRISTINE (BLACK) CO_N ELECTRODE, SOLID AND DASHED LINES REFER TO FIRST AND SECOND CYCLE RESPECTIVELY; B) CYCLING STABILITY AND COULOMBIC EFFICIENCY OF THE TWO ELECTRODES, NAMELY CO_N PRISTINE (BLACK) AND CO_N PRE-SODIATED (RED). TESTS TAKEN AT 0.1 C ($89 \text{ mA}\cdot\text{g}^{-1}$).....	119
TABLE VI-2: SODIUM UPTAKE EVALUATED USING AAS CORRELATED TO SODIATION TIMES.....	119
FIGURE VI-10: GCPL TESTS ON PRISTINE (LEFT) AND PRE-SODIATED (RIGHT) CO_3O_4 FLAKES (NR21).	121
FIGURE VI-11: GCPL TESTS ON PRISTINE (LEFT) AND PRE-SODIATED (RIGHT) CO_3O_4 SLABS (NR7).	122
FIGURE VII-1: SEM MICROGRAPHS OF AS SYNTHESIZED A) NFPY AND B) NFPY/MWCNT. TEM IMAGES AT INCREASING MAGNIFICATION OF B), C) NFPY AND E), F) NFPY/MWCNT COMPOSITE.	135
TABLE VII-1: ELEMENTAL ANALYSIS OF NFPY AND NFPY/MWCNT.	135
FIGURE VII-2: STEM IMAGES AND EDS ELEMENTAL MAPPING OF (A) AS-SYNTHESIZED NFPY AND (B) NFPY/MWCNT PARTICLES.	137
FIGURE VII-3: DIFFRACTION PATTERN OF NFPY (BLACK LINE) AND NFPY/MWCNT COMPOSITE (BLUE LINE).....	138
FIGURE VII-4: CAPACITY RETENTION TESTS FOR A) NFPY AND NFPY/MWCNT AT 1 C (THE FIRST 10 CYCLES FOR NFPY/MWCNT COMPOSITE HAVE BEEN RECORDED AT C/10 THE REST AT 1 C); B) NFPY/MWCNT ELECTRODES FABRICATED WITH AND WITHOUT CARBON BLACK; C) CHARGE AND DISCHARGE PROFILES OF NFPY/MWCNT COMPOSITE RECORDED CYCLING THE ELECTRODE AT 2 C ($97 \text{ mA}\cdot\text{g}^{-1}$); D) CYCLIC VOLTAMMOGRAMS OF NFPY/MWCNT ELECTRODE OBTAINED AT DIFFERENT SCAN RATES, INSETS OF FIGURE CONTAINS THE MAGNIFICATION OF MIDDLE SECTION OF LOWER SCAN RATES CURVES.	139
FIGURE VII-5: RATE CAPABILITY TESTS: A) NFPY/MWCNT ELECTRODE FABRICATED WITHOUT CARBON BLACK; B) NFPY/MWCNT ELECTRODE FABRICATED WITH CARBON BLACK; C) RATE TEST OF A SECOND COIN CELL OF NFPY/MWCNT ELECTRODE PREPARED WITH CARBON BLACK ADDITION; D) CHARGE DISCHARGE PROFILES OF NFPY/MWCNT ELECTRODE FABRICATED WITH CARBON BLACK.	141
FIGURE VII-6: EIS TESTS SET COMPOSED BY (A) NYQUIST PLOT OF NFPY/MWCNT AND NFPY ELECTRODES. IN BLACK LINES ARE REPORTED THE EQUIVALENT CIRCUITS FITTING CURVES AND IN THE INSET ARE REPORTED SCHEMATICALLY THE RELATED EQUIVALENT CIRCUITS.....	143
TABLE VII-2: RESULTS OF IMPEDANCE SPECTROSCOPY ANALYSIS.....	144
FIGURE VII-7: A) NYQUIST PLOT OF NFPY/MWCNT EIS ANALYSIS, HAVING THE FREQUENCIES WINDOW EXTENDED TO 0.5 MHz, IN ORDER TO HIGHLIGHT THE DEVIATION FROM THE PURE WARBURG BEHAVIOR AT MID-LOW FREQUENCIES; B) EIS SPECTRA CONDUCTED AT DIFFERENT TEMPERATURE (SOC 0.5); INSET REFERS TO MID-HIGH FREQUENCY RANGE.	145
FIGURE VII-8: ARRHENIUS PLOT FOR A) RESISTANCE VALUES RELATED TO INTERFACE RESISTANCE AND CHARGE TRANSFER RESISTANCE, AND B) EXCHANGE CURRENT i_0	146
TABLE VII-3: TEMPERATURE DEPENDENCE OF ELECTRODE RESISTANCES.....	146
FIGURE VIII-1: A) LEFT PART, SCHEMATIC REPRESENTATION OF THE SHAPE-CONTROLLED GROWTH MECHANISM AND SYNTHESIS CONDITION OF TiO_2 CRYSTALLITES THANKS TO THE SELECTIVE CAPPING EFFECT OF OLEIC ACID (OA) AND OLEYLAMINE (OM); A) RIGHT PART, 3D-SKETCHING OF THE INVESTIGATED MORPHOLOGIES WITH THE CORRESPONDING TEM MAGNIFICATION ON SINGLE PARTICLES AND THE RELATIVE AMOUNT OF THE THREE REACTANTS EMPLOYED IN THE SYNTHETIC ROUTES; B) X-RAY DIFFRACTOGRAMS OF ANATASE- TiO_2 NANOCRYSTALS (RE BLACK, R RED, NB BLUE AND SP PURPLE LINES) AND PDF CARD 00-	

021-1272 PEAKS OF TETRAGONAL ANATASE (VERTICAL BLACK LINES); C) OVERALL APPEARANCE OF TiO ₂ POWDERS DURING PROCESSING	156
FIGURE VIII-2: TEM IMAGES OF THE AS SYNTHESIZED TiO ₂ NANO-CRYSTALS MORPHOLOGIES IMMEDIATELY AFTER THE DE-CAPPING PROCESS. IN EACH IMAGE IS REPORTED AN INSET WITH A SINGLE MAGNIFIED PARTICLE.	159
FIGURE VIII-3: TGA ANALYSIS OF THE AS PREPARED TiO ₂ SAMPLES FROM THE SOLVOTHERMAL STEP (SOLID LINES), AND AFTER THE CLEANING PROCEDURE USING NYTROSIL TETRAFLUOROBORATE (DASHED LINES). BLACK LINES REFER TO RE, WHILE RED AND BLUE LINES REFER TO R AND NB SAMPLES RESPECTIVELY.....	160
TABLE VIII-1: CRYSTALS DIMENSION CALCULATED FROM SCHERRER'S EQUATION ALONG THREE DIFFERENT DIRECTION: [101], [004] AND [200]. TOGETHER WITH PARTICLES LENGTHS AND WIDTHS, 2THETA ANGLES AND FULL WIDTH AT HALF MAXIMUM OF CORRESPONDING PEAKS ARE REPORTED.	161
TABLE VIII-2: MEASURED DIMENSIONS OF TiO ₂ CRYSTALS. THESE VALUES HAS UTILIZED USED TO CALCULATE THE RELATIVE PERCENTAGE EXPOSURE OF CRYSTALLINE FACETS USING THE EQUATIONS REPORTED ELSEWHERE.....	161
TABLE VIII-3: CRYSTALS DIMENSION MEASURED MANUALLY FROM TEM IMAGES ALONG TWO CRYSTALLINE DIRECTION CORRESPONDING TO LENGTH AND WIDTH OF EACH GEOMETRY.....	162
FIGURE VIII-4: GRAPHIC EXAMPLE OF THE PARTICLE SIZE EVALUATION FROM TEM PICTURES FOR (A) TOTAL LENGTH ALONG [001] DIRECTION, (D) WIDTH AND (G) (001) FACE EDGES LENGTH OF RE PARTICLES; (B) LENGTH, (E) MAJOR EDGE AND (H) MINOR EDGE OF R SAMPLE PARTICLES AND (C) LENGTH AND (F) WIDTH OF NB PARTICLES	163
FIGURE VIII-5: HRTEM IMAGES OF (A,D) RE, (B,E) R AND (C,F) NB. FROM LATTICE FRINGES IN MAGNIFIED IMAGES (D-F), THROUGH IMAGES PROCESSING, THE CHARACTERISTIC LATTICE PLANE SPACINGS AND ANGLES HAVE BEEN IDENTIFIED (RED DASHED LINES AND ARROWS) AND NUMERIC VALUES ARE REPORTED ON THE IMAGES USING WHITE LETTERING AND NUMBERING; (G) HISTOGRAM COLLECTING THE PERCENTAGE OF CRYSTAL FACETS EXPOSURE FOR EACH MORPHOLOGY, THE COLOR CODE REPRESENTS THE ENERGY DENSITY OF EACH CRYSTALLINE FACE; (H,I) TEM IMAGES OF TiO ₂ NANOCRYSTALS GRAFTED ON REDUCED GRAPHENE OXIDE, RED ARROWS POINTING AT THE GRAPHENE OXIDE SHEETS.	165
FIGURE VIII-6: ADSORPTION ISOTHERMS FOR RE, R, NB AND SP SAMPLES; EACH IMAGE INCLUDES THE GRAPHS PLOTTING THE LINEAR RELATION BETWEEN RELATIVE PRESSURE BELOW 0.4 AND ADSORBED MONOLAYER VOLUME. FROM THE INTERCEPT THE VALUE OF THE SURFACE AREA (SSA _{BET}) HAS BEEN CALCULATED.	168
TABLE VIII-4: CHARACTERISTIC PARAMETERS FOR RE,R,NB AND SP MORPHOLOGIES, SSA _{BET} ASSOCIATED TO EACH EXPOSED FACETS FOR RE, R AND NB SAMPLES.....	168
FIGURE VIII-7: A) CHARGE/DISCHARGE PROFILES FOR RE,R AND NB, TAKEN CYCLING THE HALF CELL AT 50 mA·G ⁻¹ ; FIRST CYCLES (WHOSE CAPACITY CAN BE PRESUMED FROM RATE TESTS) HAVE BEEN VOLUNTARILY OMITTED IN ORDER TO BETTER APPRECIATE THE CURVE PROFILE EVOLUTION THROUGH CYCLING; B) GCPL RESULT FOR RE (BLACK LINE), R (RED LINE) AND NB (BLUE LINE) RGO WRAPPED SAMPLES AT PROGRESSIVELY INCREASING CURRENTS; C) RATE TEST PERFORMED ON ALL THE FOUR SAMPLES, INCLUDING SP RGO WRAPPED ONE (PURPLE LINE).	169
FIGURE VIII-8: REDUCED GRAPHENE OXIDE WRAPPED TiO ₂ R SAMPLE: PARTICLES AGGLOMERATES ARE EVIDENCED IN THE TEM IMAGE; RED ARROWS POINT AT GRAPHENE OXIDE SHEETS.....	171

FIGURE VIII-10: A) GCPL TESTS TAKEN AT DIFFERENT C-RATE (0.1, 0.2 AND 1 C), OF PRISTINE RE, R AND NB SAMPLES, WITH THE SPECIFIC CAPACITY NORMALIZED OVER THE SPECIFIC SURFACE AREA (FROM BET ANALYSIS, 67.53 AND 103.64 $\text{m}^2\cdot\text{g}^{-1}$ AND 122.27 FOR RE, R AND NB RESPECTIVELY); B) GCPL TESTS, CONDUCTED AT 1, 0.2 AND 0.1 C, OF REDUCED GRAPHENE OXIDE RE, R AND NB COMPOSITES, WITH SPECIFIC CAPACITY NORMALIZED OVER THE SPECIFIC SURFACE AREA OF THE SAMPLE172

FIGURE VIII-10: STABILITY TEST PERFORMED ON RE ELECTRODE ALONE, OVER 600 CYCLES. IN ALL THE ELECTROCHEMICAL TESTS CUT-OFF POTENTIALS OF 0.1 AND 2.0 V VS. Na/Na^+ WERE USED DURING THE SODIATION AND DE-SODIATION STEP RESPECTIVELY.173

FIGURE VIII-11: A) XRD DIFFRACTOGRAMS OF THE RE, R AND NB ELECTRODES (BLACK, RED AND BLUE LINE RESPECTIVELY), ASTERISKS MARK THE PEAKS COMING FROM CU CURRENT COLLECTOR; B) XRD DIFFRACTOGRAMS TAKEN ON A FRESH RE ELECTRODE (BLACK LINE) AND ON A CYCLED ONE (RED LINE), AFTER THE 10TH CYCLE OF A GCPL ANALYSIS, WHERE THE LAST CURRENT STEP WAS A DE-SODIATION ONE; ASTERISKS REFER TO DIFFRACTION PEAKS OF THE CU CURRENT COLLECTOR.175

FIGURE VIII-12: A) RE, (B) R AND C) NB CYCLIC VOLTAMMETRY CURVES OF PURE SAMPLES (NO RGO WRAPPING) REGISTERED AT DIFFERENT SCAN RATES; D) $\log(i)$ - $\log(\gamma)$ PLOT FOR THE INVESTIGATED MORPHOLOGIES WHERE THE VERTICAL DASHED LINE SEPARATES THE LINEAR REGIME (B-VALUE = 1) FROM THE NON-LINEAR ONE (B-VALUE<1) OF $\log(i)$176

FIGURE X-1: A) APPLIED CURRENT PULSE VS VOLTAGE PROFILE FOR A SINGLE TITRATION DURING A CHARGING STEP WITH SCHEMATIC REPRESENTATION OF DIFFERENT PARAMETERS; B) VARIATION OF CELL VOLTAGE FOR THE ABOVE TITRATION PLOTTED AGAINST $t^{1/2}$ TO SHOW THE LINEAR FIT.188

FIGURE X-2: ADSORPTION ISOTHERMS, SEE TEXT FOR FURTHER DESCRIPTION.190

FIGURE X-3: NYQUIST PLOT OF A PARALLEL RC CIRCUIT, WITH IN SERIES ANOTHER RESISTIVE CONTRIBUTION (PROBABLY EXPRESSED BY THE ELECTROLYTE RESISTIVITY).196

FIGURE X-4: A) PICTURE OF A VACUUM TUBE FOR X-RAYS PRODUCTION; B) SET-UP OF A DIFFRACTOMETER IN THE BRAGG-BRENTANO CONFIGURATION.198

List of Tables

TABLE III-1: PHYSICAL AND CHEMICAL RELEVANT PROPERTIES FOR LI AND NA METALS, USEFUL TO CONTEXTUALIZE THEIR PERFORMANCES IF USED AS ANODE MATERIALS IN SECONDARY LIBS AND SIBS.....	41
TABLE IV-1: CARBON-BASED MATERIAL MORPHOLOGIES SO FAR INVESTIGATED AS ANODES FOR SIBS; FOR EACH SAMPLE THE MAIN ELECTROCHEMICAL AND PHYSICAL FEATURES ARE REPORTED.....	61
TABLE IV-2: NA-ALLOYING ELEMENTS BELONGING TO P-GROUP OF PERIODIC TABLE WITH THEIR ELECTROCHEMICAL PROPERTIES	69
TABLE VI-1: HYDROTHERMAL STEP PARAMETERS EMPLOYED FOR THE CO INTERMEDIATED SYNTHESIS.....	107
TABLE VI-2: SODIUM UPTAKE EVALUATED USING AAS CORRELATED TO SODIATION TIMES.....	119
TABLE VII-1: ELEMENTAL ANALYSIS OF NFPY AND NFPY/MWCNT.....	135
TABLE VII-2: RESULTS OF IMPEDANCE SPECTROSCOPY ANALYSIS.....	144
TABLE VII-3: TEMPERATURE DEPENDENCE OF ELECTRODE RESISTANCES.....	146
TABLE VIII-1: CRYSTALS DIMENSION CALCULATED FROM SCHERRER'S EQUATION ALONG THREE DIFFERENT DIRECTION: [101], [004] AND [200]. TOGETHER WITH PARTICLES LENGTHS AND WIDTHS, 2THETA ANGLES AND FULL WIDTH AT HALF MAXIMUM OF CORRESPONDING PEAKS ARE REPORTED.	161
TABLE VIII-2: MEASURED DIMENSIONS OF TiO2 CRYSTALS. THESE VALUES HAS UTILIZED USED TO CALCULATE THE RELATIVE PERCENTAGE EXPOSURE OF CRYSTALLINE FACETS USING THE EQUATIONS REPORTED ELSEWHERE.....	161
TABLE VIII-3: CRYSTALS DIMENSION MEASURED MANUALLY FROM TEM IMAGES ALONG TWO CRYSTALLINE DIRECTION CORRESPONDING TO LENGTH AND WIDTH OF EACH GEOMETRY.....	162
TABLE VIII-4: CHARACTERISTIC PARAMETERS FOR RE,R,NB AND SP MORPHOLOGIES, SSA_{BET} ASSOCIATED TO EACH EXPOSED FACETS FOR RE, R AND NB SAMPLES.....	168

CHAPTER I: Introductory elements

1. Objectives of the research

Differentiation in energy production, utilization and storage will be an essential asset in the future, and will certainly drive the forthcoming development of society, economy and most of all, environment. Energy storage systems and high efficiency rechargeable batteries in particular will play a pivotal role in this landscape and, as demonstrated by recent trends in markets and research, will represent the key stone in many fields such as automotive, power back-up industry, stationary storage couple to renewable energy sources and so on. With the present contribute the research on new generation anode and cathode materials for sodium-ion batteries, a more forward-looking alternative to lithium-ion batteries, is fostered. The solid experimental work undertaken to synthesize and characterize functional inorganic materials during the doctorate, will be thoroughly presented after an exhaustive contextualization of proposed compounds in the most recent literature advancements both in anodes and cathodes design. Attention will be addressed not only to a trial-and-error driven research but also to a systematic study of chemical-physical properties/electrochemical characteristic correlations, fundamental in directing further development of entire classes of material. The very latter approach has been applied firstly to an oxide-based conversion anode material, investigated in its hierarchical structure/electrochemical performances correlations and its response to pre-sodiation treatment, using *ex situ* XRD and SEM analysis. Concerning the cathode side an iron pyrophosphate/carbon nanotubes composite will be than described, emphasizing the simplicity of preparation route, extraordinary kinetic properties and sodium diffusion capabilities investigated through electrochemical impedance spectroscopy (EIS). Lastly a low-cost nano-structured anatase TiO₂ will be presented; in this case the surface crystalline properties influences on sodium uptake will be stressed, and the electrochemical mechanism originating the extraordinarily stable capacity retention investigated.

2. Thesis structure

In order to pursue a thorough and detailed description of the work of research, the report of the doctoral activity has been structured providing intentionally an in-depth description of the

most important materials science challenges commonly encountered in energy storage material development and design. Said that the thesis will disclose as follow.

In Chapter II an introductory description of the development of electrochemical energy storage throughout the decades will be provided. Starting from lithium-ion batteries and ultimately getting to sodium-ion the most important scientific players will be briefly described and the motivation behind switching to sodium analyzed.

In Chapter III technical notions mandatory to the full comprehension of subsequent chapters will be listed. Sodium-ion batteries will be analyzed under a theoretical point of view and the working principles, in their chemical and physical meanings, of the novel electrochemically active materials collected.

Chapter IV and Chapter V are dedicated to an in-depth literature review of respectively anode and cathode materials for sodium-ion batteries. These two chapters are to be intended as preparatory material to following chapters in which innovative materials are proposed in light of previous research conducted by others.

Chapters VI, VII and VIII, core of the thesis and build on solid experimental work, contain the description of synthesis, characterization, mechanistic studies of active materials considered worth to be valid candidate for new generation sodium-ion batteries. Particularly in Chapter VI nano-structured porous Co_3O_4 anode material synthesis will be taken into account. *Ex situ* XRD characterization will be presented trying to trace the evolution of material structure and phase composition upon sodiation/de-sodiation. Chapter VII is dedicated to pyrophosphate/carbon nanotubes-based composite proposed as a sodium intercalating cathode. It will be investigated in its general electrochemical capabilities, namely cycling and rate performance, and sodium diffusion properties inside its lattice structure will be evaluated by means of impedance analysis and galvanostatic titration techniques. Lastly Chapter VIII will be entirely dedicated to anatase TiO_2 nano-crystals electrochemical properties investigation. TiO_2 arising as a promising and low-cost anode material for sodium secondary batteries, is lacking of a deep understanding of sodium uptake mechanism. In this chapter this still unclear aspect is tried to be unveiled and interesting surfaces crystalline structure/electrochemical properties correlations are collected.

Chapter IX eventually summarizes the doctoral work and provides the outlook for further research work.

In the Chapter X, the appendix section, some experimental and instrumental analytical techniques, whose understanding might not appear trivial to the most, will be described in their general features and mathematical justification. Precisely Galvanostatic Intermittent Tritration Techniques (GITT) will be described as well as BET surface analysis, X-Ray diffraction from powder and a compendium about Potentiostatic Electrochemical Impedance Spectroscopy (PEIS).

CHAPTER II: General background

1. Introduction

In the introductory part of this work a due description of the world energetic landscape is provided. More specifically, some of the fundamental questions such as “why do we need to store energy nowadays?” and “which instruments do we have to achieve an efficient way to do it?” will be tried to be answered. Added to this, a closer look will be addressed to current available technologies capable of storing energy and the room for their potential further improvement thoroughly discussed. As it will be illustrated, in a reality in which enormous amount of energies, tens of TWh (terawatts hour) annually, are moved, most of the time unevenly, to fulfill everyone needs, every piece of technology or scientific advancement involved in energy production, diffusion and storage should be carefully evaluated. Humanity is learning “the hard way”, and is becoming clearer as the time passes, what might be the cost of neglecting a mass diffusion of a scientific advancement of human intellect addressed to gaining energetic sustenance. Further technical solution to energetic supply issues will have to be thoroughly assessed, in order not to create resources accessibility unbalances as well as supply and demand mismatch.

In this chapter the attention will be primarily directed to the description of the global energetic problem the scientific community is facing nowadays. Since the discussion above energy storage devices will be the core of the dissertation, an in-depth analysis of the path that led to nowadays successful technologies, lithium-ion batteries for example, will be provided. It will appear immediately clear how storing effectively power in more or less portable devices is going to represent a strategic commodity in the near future, forecasting a capillary diffusion of small/medium renewable energy sources production plant. So the major actors in this scenario, namely scientist and companies, that revolutionized society by means of their inventions and products, are worth to be mentioned as a proper recognition to their vital contribution. Together with the outstanding advancement that these complex assembly ensure in many fields, will be also presented the major limitation that still today remain un-answered.

2. Global energy landscape

Anthropogenic green house gases (GHGs) emissions have progressively increased over 1970 to 2010 with larger absolute values. Global economic crisis that stroke in 2007/2008 only temporarily contributed in curbing emissions, and in 2010 GHGs emission rate shot back to 1.0 GtCO₂eq (2.2 %) per year. CO₂ emissions accounted for 49 Gt in 2010, with the highest share directly coming from energy production (47 %) and industry (30 %). This scenario has already produced measurable consequences on energetic balance of our planet: an increasing amount of energy irradiated by the sun is trapped by CO₂-richer earth atmosphere and transformed in thermal agitation producing quantifiable local temperature anomalies. Radiative forcing is a practical quantity, measured at the tropopause in W over square meter of earth surface, balancing positive forcing effects of GHGs and solar irradiance, with negative forcing effect of soil and cloud albedo. The output is a quantification of the temperature growth driving force. Climate change effects have acquired a primary importance in evaluating the discrepancy between actual climate evolution and documented “warm periods” of earth history. In making this comparison, hazard of climate events, vulnerability of economies and populations and exposure have taken on themselves the role of indicators of the overall risk of a climate twisting set on a human time-scale. In front of this scenario, two reasonable reactions ought to be adopted: The mitigation of CO₂ concentration build up in the atmosphere and adaptation to climate change impacts which has already become a reality. If adapting to extreme climatic conditions is somewhat a passive attitude, most of all concerning social, cultural and economic aspects of everyday life, mitigating further deleterious effects of GHGs accumulation implies a proactive behavior, in which technological advancement assumes a key role.

Massive renewable energy exploitation is emerging as an essential tile in an energetic sustainable future. Solar, wind, geothermal, hydro together with improved efficiency in energy production and utilization, will have to satisfy the ravenous energy appetite a population of more than seven billion will feel. There are several indicators that more or less exhaustively describe world energy landscape evolution and thus allow to precisely quantifying the renewable energy sources share. One of them is the total primary energy supply (TPES). It quantifies the gross inland energy production from primary sources and imports net of export and storage. Promisingly, total primary energy supply coming from renewable sources (including hydro biofuels and wastes) has risen steeply in the last decades and hit nearly 14 %

of world energy production in 2014. Nevertheless, despite the exponential increase in renewable energy sources exploitation (moving from 5.96 Mtoe of TPES in 1973 to 185.55 Mtoe in 2014)¹, coal and crude oil extraction steadily grew. Intense fossil fuels utilization has made the lightning-quick economic growth of developing countries like China and India possible, and partially undid the CO₂-emission curbing effect of renewable energy harvesting sites spread. Strict energy policies, imposed on an international scale during latest summits facing climate change, did sound unfair to developing nations that could not take advantage of the industrial boom that crossed western countries in the past two centuries. Intense utilization of fossil fuels, thus contributed in projecting CO₂ emission levels to 32381 Mt CO₂ in 2014, doubling the levels measured in 1973 (15458 Mt CO₂). If OECD nations hardly contributed to this trend, Asia and China in particular, are playing a major role and just recently showed concerns in limiting fossil fuels (coal in particular) exploitation for energy purpose. European (EU-28) energy scenario is one of the most heterogeneous among the developed and developing countries. The European gross inland energy consumption accounts for 1605,931 Mtoe (2014)², which 12,5 % comes from renewable energy sources. Sources contributing to the renewable energy basket, vary with each European country, and strongly relates to inland and offshore availability of renewable energy primary sources. Northern territories rely more on wind and tidal cycles while central and southern countries on hydropower and solar photovoltaic. Some nations arise as excellences in exploiting a renewable source in particular; worth to be mentioned are central Europe countries Slovakia, Croatia, and Austria where energy from hydro hovers around 30 % of total energy production from renewable sources. Italy holds the record as the nation with the highest share of renewable energy derived from geothermal (22 %). Renewable energy statistics often includes energy shares obtained from biomass and waste thermal disposal, although it is an efficient way to add value to secondary raw materials, processing them for energetic purposes generates a considerable amount of CO₂. As a matter of comparison, lifecycle emissions of biomass and waste utilization is considerably higher (820 gCO₂ per kWh hour produced) than solar or wind technologies (41 and 11 gCO₂ per kWh respectively)³. Lately, another parameter has become a valid indicator that not only gives an insight into energy production rates, but also gives a description efficiency of energy utilization inside a country. It is the per-capita energy consumption, and it is, as the name suggests, the normalization of the gross inland energy production over the population of the territory.

It is certain that the cut back in CO₂ emission must necessarily pass through a rather quick transition from solid and liquid fossil fuels exploitation to renewable energies, together with an improvement in utilization efficiency and wastes control. Nonetheless, a future limit to an additional penetration of renewable energies in energy production might be the irregular operation of energy plants due to intermittence of primary sources (solar irradiation, winds, tidal waves and river flows). This, in particular cases, might be incompatible with everyday energy demand. For example, photovoltaic plants typically produce an excess of energy when the need is lower, namely during the day, while during evenings, depending on the latitude, and nights, energy produced may not be enough to fulfill the momentary increased demand. This energy production/consumption unbalance may concern time periods ranging from minutes, considering dips and spikes due to instant energy production failure (cloudy weather or lull) to months (in the case of photovoltaic this effect has a particular bearing at higher latitudes due to heavy seasonal discrepancies in solar irradiation). In order to progressively increase renewable energy penetration in the market, these and other drawbacks have to be taken seriously into account, so that “clean” energy could become competitive with non-renewable energy sources. Eminent scientists affirm that, considering all the other “externalities” involved in fossil fuels exploitation, namely depletion of primary resources, pollution and general higher carbon footprint, renewable energies are already well above classical energy production methods for what concern competitiveness and environmental friendliness, also including ancillary technologies⁴. Among the latter, to ensure continuity and stability in energy distribution in energy production off-peak moments, has been proposed the utilization of energy carriers such as hydrogen. It would be produced from water electrolysis and stored during energetic bonanza, in order to be used later on powering fuel cells or for methane production (another energy carrier). Other viable technologies are: compressed air energy storage, flexible and scalable, and pumping hydro for vaster application. This last possibility has required infrastructure as a clear limitation in its application. Electrochemical energy storage in rechargeable batteries still is considered an impracticable choice for many reasons. Primarily, choosing which battery chemistry would be more suitable for a stationary energy storage application is not a trivial matter. Efficiency, reliability, scalability, costs and safety are the major factors manufacturers should take into consideration. To be competitive on the market, secondary batteries for large scale energy storage should go below 300 \$ per kWh of stored energy, and the actual value

seems not to be far from that. Nevertheless, together with substantial obstacles, there are multiple advantages in employing batteries, especially connected to the matchless benefit of having electric energy “out of the box” without any other energy transduction, essential in devices previously listed. Domestic energy storage, for example, could represent a beneficial short-circuit between energy production and consumption. Complete grid autonomy might be achieved coupling domestic exploitation of renewable energy sources to in-place battery storage, in order to face production off-peak periods. Around 40 % of U.S. 2015 energy consumption has been consumed in residential and commercial buildings. This is a large share whose energetic self-sustainment should be a primary concern, since it requires smaller infrastructures and thus lower investments. As a future-brightening aspect of the capillary penetration of secondary batteries in everyday life is the building up the so called “smart energy networks”, inside which energy packages can be shared among devices (cars, houses and other portable electronics with comparable energy capacity) in order to limit wastes and increase energy utilization efficiency. Many distinguished scientific reports involved in energy policies monitoring and evaluation, stress the importance of a proactive approach based on distribution of energy generation. This involves infrastructures deployment, increasing investments, robust policies and strong leadership to advance the energy transition to a more decentralized energy production system⁵. In order to get a better grasp on how rechargeable batteries ended up to be such an essential technological asset in modern society, an instructive description of their birth and development is provided in this chapter.

3. The not-so-short history of rechargeable battery

Scientific discoveries and technological advancements made possible by the “*organe electrique artificiel*”, as in 1800 Alessandro Volta described the first battery to the Royal Society, are countless. Thanks to their portable electrons flow released at will, batteries helped the English chemist Humphry Davy to break apart several minerals to ultimately isolate sodium, potassium, strontium, magnesium, calcium and barium. Water composition was unveiled by electrochemically separating hydrogen and oxygen using an electric source and fundamental Maxwell equations describing magnetism-electricity relation could be derived by Hans Christian Oersted observations of how the magnetic field induced by electric flow coming from a battery affected a compass⁶. In order to store electric energy reversibly inside a galvanic

cell, 59 years from Volta's copper and zinc disks stacking had to pass by, allowing the French physicist Gaston Planté (Orthez, France, 1834) to develop the first lead-acid rechargeable battery, whose overall chemistry is of primary importance still today in cars starting-lightning-ignition (SLI) batteries. In the early development of automotive industry during the first years of 20th century, an electric-powered car was the obvious competitor of the still inefficient and clumsy combustion engine automobiles, for this reason, whole electric cars made their appearance in those years with a discrete success. Thomas Edison, challenging the lead acid battery market-leading Electric Battery System (EBS) Company of Philadelphia, proposed an alternative to 50 year-old EBS technology by developing an alkaline based nickel-iron battery with double the stored energy and a longer lifespan than competitors technologies. The hype for what we might consider the first electric vehicle of history did not last longer, turned off by the mounting excitement for gasoline engines getting more and more performing each passing day. Affordable Ford and powerful Roll-Royce cars in which, thanks to an automatic ignition motor powered by a lead-acid battery, invented by Charles Kettering, the unsafe starting crank was no more needed, started to fill the market, confining Edison batteries to mining lamps and warfare power backups for communication.

Oil crisis, in early '70s, revived the thrill for electric propulsion and battery storage. Smog plague and air pollution were the burden modern society inherited from more than 70 years of combustion engine refinement. Compared to latest propulsion engines, batteries appeared as cumbersome and anemic devices, capable of barely powering a small size vehicle for few miles. Battery technology research, neglected for decades, gained a renovated attention from the scientific community thanks also to the pioneering work of Robert Huggins at Stanford University (California, USA) and Max Planck Institute (Germany), concerning ionic diffusion of alkaline metals into host structures. In order to revolutionize rechargeable batteries, stuck on lead-acid technology, a strong paradigm shift was necessary. Lead based devices appear to be extremely inefficient due to the relevant molecular weight of lead as well as the electro active mechanism limited to only exposed surfaces to liquid acidic media. Specific energy is thus as low as 40 Wh per kg. What Huggins, and Micheal Stanley Whittinigham and Micheal Armand later on started was a systematic screening of inorganic compounds able to accommodate sufficiently small ions, alkaline metals ions typically, in gaps and paths in their very crystalline structure. First material to be proposed for energy storage purpose was TiS_2 , as

a direct consequence of energetic studies on superconductivity of the similar TaS_2 . TiS_2 is a layered crystalline material in which potassium and lithium ions could safely be accommodated⁷. If paired with an appropriate negative material, this could lead to a promising specific energy as high as 400 Wh per kg, higher enough to be theoretically competitive with a combustion engine. A major advancement of this set-up was the room operating temperature, unlike the sodium-sulfur batteries developed for Ford Motors by Kummer and Webber in 1967, utilizing molten sulfur and sodium at 350 °C separated by a β -alumina solid electrolyte. These scientific findings, immediately met the interest of the automotive industry and incentives started to flow also from oil companies (Exxon, Sohio), eager to diversify in order to face the oil production peak forecasted for the end of the millennium. At the beginning of the '70s General Motors and Argonne National Labs were both working on lithium-based chemistry for rechargeable batteries. Safety issues of TiS_2 coupled with metallic lithium and '80s US discontinuous energetic government policies put a hiatus in the alternative energy interest. Battery research was not producing fast and appreciable advancements in transport compared to what has been in the past with gasoline-based industry. Elton Cairns (Lawrence Berkeley National Laboratories) defiantly stated that the key for feasibility of advanced batteries of all types is the price and supply of oil. Almost contemporarily in Europe, studies aimed at studying hydrogen storage in alloys, led to the discovery of the first nickel-metal hydride rechargeable battery exploiting metals hydride anodes and nickel oxyhydroxide cathodes. Compared to the previous nickel-cadmium sealed cell, nickel-metal hydride battery (Ni-MH) showed the advantage of a rapid charge capabilities, longer cycle life in any state of charge and absence of toxic elements (cadmium). Practical specific energies, hovering around 75 Wh per kg⁸, though, were not as outstanding as the automotive market would have required.

With the battery hype stagnating due to the gradual recovering from '70s oil crisis, only a ground-shaking innovation in energy storage chemistry could have revived the technology. This breakthrough arrived from John Goodenough research group, solid-state chemist at the University of Texas, Austin. The leap was represented by an outstanding 4 Volts as the operational voltage compared to 2.4 volts of Whittingham battery. This result was made possible thanks to transition metal oxide-based cathode materials (generic formula Li_xMO_2 , with M being Ni, Co or Mn), stable at high voltage and delivering significant specific capacities. In particular layered Lithium cobalt oxide (Li_xCoO_2 , $0 < x \leq 1$), unveiled for the first

time in 1980⁹, was the most performing and the first to be commercialized by Sony coupled with a carbon anode in late '90s. An aspect often neglected of this new class of material, emphasized in 1980 Goodenough's paper, is the peculiar synthesis of the lithium cobalt oxide active material in its discharged state (lithium-rich state), so that both cathode and anode materials could be safely handled in ambient atmosphere. While Sony was paving the way for the mass diffusion of the first generation of lithium-ion battery for portable electronics, Goodenough never received a credit from the Japanese company for the exploitation of his unprotected intellectual effort. During the following years material scientists and chemists from all over the world went through all the periodic table string to find safer, cheaper and new battery material with an extra boost in term of stored capacity and operational potential. A small revolution happened with the development of a iron phosphate based cathode material by John Goodenough team, cheaper, with a discrete capacity. What it also came what Michel Armand, eminent professor active in the lithium-metal battery configuration, defined as the "Biggest scandal in lithium batteries". A controversy between Yet-Ming Chiang, co-founder of A123 battery manufacturing company, and Michel Armand himself, burst out when the former published in 2002 a paper in which he claimed to have solved the poor electric conductivity of lithium iron phosphate by doping it with supervalent cations¹⁰. Armand replied that by no means solving this problem could have passed through an impurity-level doping of bulk material, and that the improved electronically performances must have been due to a thin outer carbonaceous coating unwittingly derived from carbon-containing synthetic precursors, as he had previously observed in other experiments. This objections merged in a letter to the editor in 2003 issue of *Nature Materials*¹¹ and the debate between the two scientists went on also involving other personalities of the battery universe such as Linda Nazara, professor at the University of Waterloo. The litigation crossed the academic boundaries when in 2005, Hydro-Quebec licensed for lithium iron phosphate manufacturing, which Michel Armand was a consultant of and backed up by University of Texas, sent a warning to A123, Chiang's company that started producing batteries for Black&Decker power tools. Litigation, patent dispute and overpromising and get-rich-quick hype have stained the battery business since the very beginning.

4. Modern applications of rechargeable batteries: Li-ion for automotive and stationary storage

With a market penetration accounting for 95 %, lithium-ion technology, in its different forms (lithium-ion, lithium-polymer and different cathode materials) is the most sensible choice for a vast number of applications. Its versatility which emerges also from multiple cathode (LiFePO_4 , $\text{LiCr}_{1/3}\text{Ni}_{1/3}\text{Mn}_{1/3}\text{O}_2$, LiCoO_2 , LiMn_2O_4 , LiNiCoAlO_2) and anode (graphite, Si-additivated graphite, $\text{Li}_4\text{Ti}_5\text{O}_{12}$) chemistries currently available and is above any other energy storage device being it mechanical, physical or chemical. Some recent application of lithium technologies includes the most advanced pieces of cutting-edge technologies (laptops, tablets, smart-phones and smart-watch above all) and any other technological gizmos requiring a compact and at the same time powerful power source. Recently, LIBs made their entrance in the automotive field, and previously stated, most of the time replacing less efficient rechargeable battery chemistries such as Ni-Metal hydride batteries. LIBs made reliability of full electric vehicle stronger and mileage sensibly higher thanks to their impressive energy densities (Figure II-1).

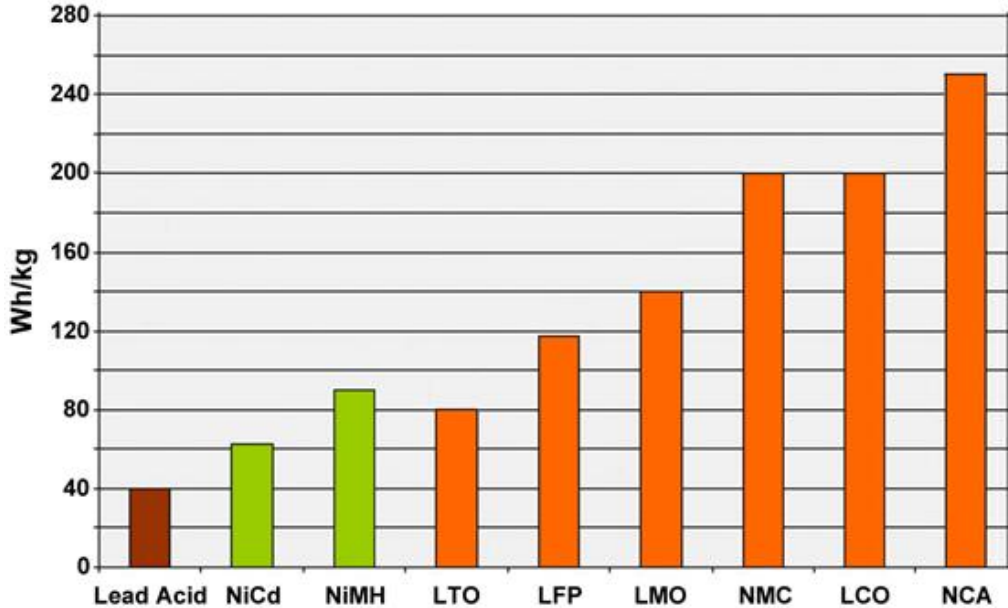


Figure II-1: Typical specific energy density for lead-, nickel- and lithium-based rechargeable batteries.

Tesla, firstly, made performing lithium batteries the core technology of high-end full electric vehicles and, as if it was not a sufficient and courageous technological advancement,

recently incorporated LIBs also in stationary storage devices for medium-small scales and especially for the domestic use. Economy of scale and detours some companies (including Tesla) are actuating on lithium extraction and refinement chain are contributing in numbing the increasing prizes of the raw matter. This is powering the batteries manufacturing making it available for uses that, if coupled with local and even domestic renewable energy sources, can completely bypass common energy network in which electric energy is inserted thanks to traditional production strategies, including fossil fuels-based technologies. This possibility discloses a serene future for what concern energy independence of individuals, isolated communities, being less dependent by market prices and occurring black outs. Nevertheless this silver lining of a energy greedy future might have a severe cost if its exploitation won't be properly and wisely addressed.

5. Concerns in lithium abundance

Lithium-ion batteries are not all peaches and dandelion especially when it comes to cost and safety. Other disadvantages are related to a strong temperature dependence of battery performances and low tolerance of deep discharge process. Added to these aspects an increasing concern is shedding its shadows over an oil economy-free future: will lithium, with the exponential increase in the raw material demand, become the new gold? With the full electric and hybrid cars industry growing fast (talking of an electric vehicle boom is still too soon) several scientist started questioning the future sustainability of a lithium economy¹². Reports on global lithium available reserves talk about 13.5 million tons of lithium carbonate equivalent, 38 thousands of which coming from Nevada brines on U.S. territories only. This reasonable amount would ensure, at the current global production rate (34,577 tons in 2014, slightly increasing 2013 rate of 33,940), supply for 365 years. A comforting forecast. This, however, owing the electric vehicle and stationary storage market not shooting up the lithium demands in the next decades. An exponential growth in electric car distribution is a scenario not far to be realized if sales trend of electric vehicles like Nissan Leaf and Tesla Model S are considered: in three years (2011-2014) the number of EVs on the road hit the vertiginous number of 150,000 units (+700 %) in the first case and 50,000 units for the Californian company. Total amount of whole-electric vehicles at the end of 2014 has been evaluated to be around 740,000 units and it is expected to reach the million in the next years. In an act of wild

speculation, let's consider that the electric vehicle will hit vigorously the mass market in the next decades, and that the lithium-ion technology will also be the preferred choice for stationary storage, the world would need about 800,000 million metric tons of lithium by 2040 only for battery manufacturing. Battery production only, requires one third of the lithium carbonate dig out from brines and minerals, while ceramics, greases and lubricant, glasses and drugs cover the other two thirds. According to this, with the known lithium resources, an automotive and stationary storage scale up would be hardly bearable, guaranteeing approximately just 50-year of supply, and this is a lot less comforting scenario. How the lithium price will increase in the future will depend on how well global production of lithium will keep up with demand. This is the reason why, in the recent years we didn't witness to a steady growth in battery grade lithium cost together with the increase in EVs diffusion. Together with this exponential growth in electric cars diffusion, goes a steady drop in lithium-ion battery price with a rate of 14 % per year since 2007¹³, this aspect is mostly due to process refinement of battery-grade lithium carbonate production and economy of scale. Practically speaking, accessible lithium reserves are not uniformly distributed on the planet. As what might resemble the uneven distribution of liquid fossil fuels, lithium-rich brines are concentrated in south-American countries often characterized by political and economical instabilities like Chile, Argentina and Bolivia, the latter among the poorest countries in the continent. Salar de Uyuni, (Bolivia) Salar de Atacama (Chile) and Salar del Hombre Muerto (Argentina), known as the "lithium triangle" collect a huge stash of lithium as soluble lithium salts, and a first low grade purification can be operated immediately on the field via selective crystallization of brines. After these consideration, what might have imagined as a bright and environmentally friendly energetic future, acquires a gloomy shade. As the case of fossil fuels, differentiation might come in help. As previously illustrated, lithium based batteries represented a huge technological leap in energy storage if compared to lead acid, Ni-Cd and Ni-MH batteries. In between there are chemistries that, despite a lower energetic content if compared to lithium, are based on more abundant and evenly spread raw materials.

6. Sodium ion batteries

Sodium-based rechargeable batteries have recently drawn the attention as a cheap and sustainable alternative to lithium chemistry. At the dawn of lithium intercalation studies in

oxides, other alkaline metals, including sodium, were taken into consideration, and publications describing sodium shuttling in inorganic material lattice can be dated back to the late 70s. Nevertheless only in recent years, after exhaustive investigation of high-temperature systems such as solid electrolyte based sodium-sulfur batteries¹⁴, research on room-temperature sodium-ion batteries boomed incredibly. Before the lately hype in this topic, room-temperature sodium ion batteries have been investigated bashfully due to overwhelming scientific success of lithium batteries, technologically more interesting. The so-called layered inorganic materials such as TiS_2 , firstly discovered as effective host structures for lithium ions insertion, have been investigated also in sodium environment¹⁵. The early history of sodium insertion materials was reviewed in the literature published in 1982. Nevertheless studies on sodium insertion materials for energy almost disappeared¹⁶. Curiously, a net divide between a poor academic activity around sodium batteries and a tremendously productive period appeared to be the 2010 Jean Marie Tarascon's article titled "Is lithium the new gold?"¹², that for the first time raised the concern of a possible unsustainable diffusion of lithium technology. Illustrative is the number of scientific articles "Sodium-ion battery"-related published between 2004 and 2010 period, only 17, compared to 2010-2016 timespan instead, during which 1577 works have been produced^a. Motivation behind room temperature sodium-ion battery research is however truly clear from being just an academic exercise, and a tangible proof of that is the vast amount of patents filed in the last five years period, claiming active materials structures and cells architectures for SIBs. In the light lithium reserves esteem previously considered sodium ion batteries and other energy storage technologies based on other chemistries such as magnesium, metal-air, and metal-sulfur are being considered as alternative to replace lithium. According to utilization, availability of investments, volume, weight and cost restrictions energy and power density demand, some chemistries might be more appropriate than lithium, whose costs are still too demanding hovering around $350 \text{ \$}\cdot\text{kWh}^{-1}$. Recently, thanks to economy of scale and green chemistries sagacity, Tesla company, world leader in full electric high-end automobiles, claimed to be able to break the $100 \text{ \$}\cdot\text{kWh}^{-1}$ barrier in few years¹⁷. But practically evaluate the saving in adopting sodium chemistries is everything but an easy task. If on one hand cheaper material precursors may curb manufacturing costs, this perk might be nullified by lower energy densities leading to a higher cost of energy ($\text{\$}\cdot\text{Wh}^{-1}$) connected to energy density limitation

^a SciFinder data, <https://scifinder.cas.org/scifinder/view/scifinder/scifinderExplore.jsf>

offset due to the use of Na. Switching from lithium to sodium chemistries, due to thermodynamics aspect that will be clear in a while, automatically reduces the harvestable energy from the system by 10.8 %. At the same time, looking at manufacturing cost of every single part of the cell (Figure II-2), it is clear how a considerable cost reduction of about 10 % might be achieved from cathodes cost effective precursors and substitution of copper current collector with the cheaper aluminum, thanks to Na not alloying with Al. The net cost balance, close to zero, might appear unseemly and it gets even worse. Under a closer look, infact, the cathode material cost reduction might be misleading. It could be achieved only if expensive precursors such as Co, Ni and Mn, are replaced with cheaper, more abundant, safer and reusable ones. Precursor for alkali metals lithium and sodium, only account for 10 % of the total cost for the cathode material, and thus, substituting lithium with sodium would result in a modest cost curtailment. Nevertheless, there are other aspects that might turn into cost reduction sources, such as substitution of Li salts with Na salts in the electrolyte solution.

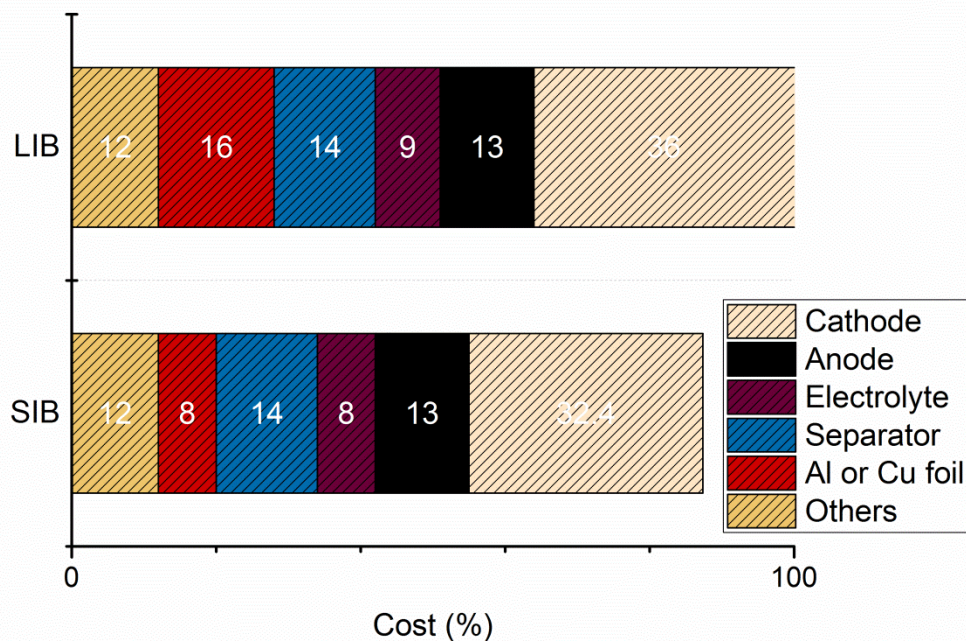


Figure II-2: manufacturing costs for SIBs and LIBs highlighting single contribution to the overall cost.

7. Bibliography

- (1) International Energy Agency. Energy Statistics. *Statistics (Ber)*. **2016**.
- (2) Eurostat. *Energy Balance Sheets.*; 2016; Vol. 33.
- (3) Schlomer, S.; Bruckner, T.; Fulton, L.; Hertwich, E.; McKinnon, A.; Perczyk, D.; Roy, J.; Schaeffer, R.; Sims, R.; Smith, P.; Wisner, R. Annex III: Technology-Specific Cost and Performance Parameters. *Clim. Chang. 2014 Mitig. Clim. Chang. Contrib. Work. Gr. III to Fifth Assess. Rep. Intergov. Panel Clim. Chang.* **2014**, 1329–1356.
- (4) Armaroli, N.; Balzani, V. *Energia per L'astronave Terra*; Zanichelli, 2011.
- (5) Keiningham, T. L.; Cooil, B. Renewables 2016, Global Status Report-Key Findings. **2015**, 1–23.
- (6) Fletcher, S. *Bottle Lightning. Superbatteries, Electric Cars, and the New Lithium Economy.*; 2011.
- (7) Whittingham, M. S. Electrical Energy Storage and Intercalation Chemistry. *Science (80-.)*. **1976**, *192*, 1126–1127.
- (8) Linden, D.; Reddy, T. B. *HANDBOOK OF BATTERIES*.
- (9) Mizushima, K.; Jones, P. C.; Wiseman, P. J.; Goodenough, J. B. Li_xCoO_2 ($0 < x < 1$): A New Cathode Material for Batteries of High Energy Density. **1981**, *4*, 171–174.
- (10) Chung, S.-Y.; Bloking, J. T.; Chiang, Y.-M. Electronically Conductive Phospho-Olivines as Lithium Storage Electrodes. *Nat. Mater.* **2002**, *1* (October), 123–128.
- (11) Orld, F. W.; Atch, W. From Our Readers: On the Electronic Conductivity of Phospho-Olivines as Lithium Storage Electrodes. *Group* **2005**, *2* (November), 724–724.
- (12) Tarascon, J.-M. Is Lithium the New Gold? *Nat. Chem.* **2010**, *2* (6), 510.
- (13) Hunt, T. Is there enough lithium to maintain the growth of lithium-ion battery market? <https://www.greentechmedia.com/articles/read/Is-There-Enough-Lithium-to-Maintain-the-Growth-of-the-Lithium-Ion-Battery-M>.
- (14) Oshima, T.; Kajita, M.; Okuno, A. Development of Sodium-Sulfur Batteries. *Int. J. Appl. Ceram. Technol.* **2005**, *1* (3), 269–276.
- (15) Newmann, G. H.; Klemann, L. P. Ambient Temperature Cycling of an Na - TiS_2 Cell. *J. Electrochem. Soc.* **1980**, *127* (10), 2097–2099.
- (16) Abraham, K. M. Intercalation Positive Electrodes for Rechargeable Sodium Cells. *Solid State Ionics* **1982**, *7* (3), 199–212.

(17) Wesoff, E. How Soon Can Tesla Get Battery Cell Costs Below \$100 per Kilowatt-Hour? <https://www.greentechmedia.com/articles/read/How-Soon-Can-Tesla-Get-Battery-Cell-Cost-Below-100-per-Kilowatt-Hour>.

CHAPTER III: Technical part

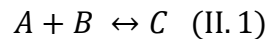
1. Introduction

Secondary batteries or rechargeable batteries as they are often referred, is a sufficiently complex matter that requires an interdisciplinary approach to be fully understood. Their operating principles can be discussed under a pure electrochemical point of view, and it will be addressed shortly, but this would result in a short-sighted approach neglecting fundamental materials science aspects. In recent years, apart from pure electroanalytical methods, many other disciplines gave their contribution to the field, spanning from materials science, engineering, theoretical calculation and mathematical modeling of whole battery systems¹ symptom of a deep interest bestowed in reversible devices for energy storage. Rechargeable cells have become a keystone for important and even delicate tasks, such as providing an electric continuity to automotive, aircraft systems, emergency no-fail and standby (UPS) power sources, hybrid electric vehicles (HEV) and stationary storage (SES). In all these application, batteries are supposed to be recharged “on-the-go” by an electrical connection from a primary energy source². The final user should not be required to have any specific technical capability to operate the cell recharge process. All the reliability should be demanded to robust and reversible battery chemistry, materials resilience to any kind of improper use and efficient battery management circuitry (BMS).

In this chapter fundamental electrochemical and materials science notions will be provided to the reader so that he or she will be able to go easily through the following chapter counting on a solid theoretical background. After a brief skim of thermodynamics and kinetics of electrochemical processes, fundamental energy storage mechanisms, involved in modern battery chemistries, will be discussed in details. In Chapter III:Chapter III:4 a commented list of quantities helpful in defining battery performances will be provided. These concepts will be cited often in the following chapter and a deep grasp on their meaning will avoid misunderstandings.

2. General thermodynamics

Oversimplifying the processes happening inside a battery cell, one may say that a transduction of chemical energy into electrical one is taking place, and that all the variables that play a relevant role in defining whether a material is working properly or not, can be narrowed down to two general practical parameters: output potential (measured in Volt) and capacity (measured in mAh or coulomb). In order to get a grasp onto where these two properties come from, a theoretic approach is due and has to be presented. In a general chemical reaction A and B are converted into the product C:



The driving force ruling this equilibrium is held by the standard Gibbs free energy of the reaction namely the difference between the standard Gibbs free energy of formation of the products and the standard Gibbs free energy of formation of the reactants as illustrated in the following equation.

$$\Delta G_r^\circ = \sum \Delta G_f^\circ (\text{products}) - \sum \Delta G_f^\circ (\text{reactants}) \quad (\text{II.2})$$

If reactants of the sample reaction are both solids, in order for the reaction to take place, a physical contact has to be assumed and so has the realization of an interface between A and B. As the reaction take place, the new compound C nucleation and growth, as in all pure solid-state reactions, will take place at the very interface and progressively will substitute reactants in a symmetric/asymmetric fashion depending on the stoichiometry of the reaction and diffusivity of A and B in C, in order to reach the nearest two-phase boundary, as illustrated Figure III-1. When a direct contact between A and B is not achieved, the process II.1 can still take place provided some sort of continuity between the reactants other than a direct physical contact. The whole process can be depicted as an electrochemical reaction and can happen only if other requirements are fulfilled. As depicted in Figure III-2, A and B are separated by an electrolyte solution that typically has ionic-conduction properties and is electronically insulating. Externally to the cell, an electronic circuit including loads, guarantees the electronic continuity between A and B, owing the A and B to be electronically conductive. Depending on the thermodynamically driven galvanic chain that builds up in the cell, a net flux of charged species, for example A^+ , through the electrolyte, and a negative charged species, namely e^- , through the external circuit, will start to flow.

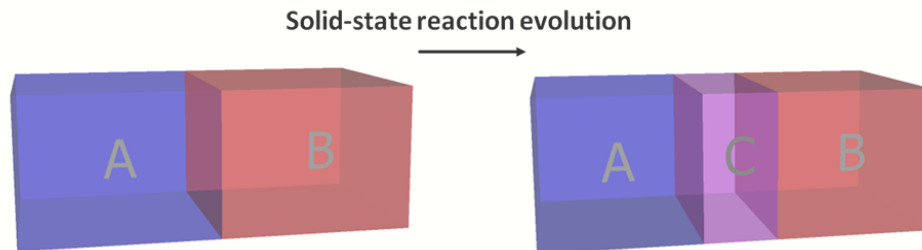


Figure III-1: Simple schematic model of the chemical reaction of A and B to form C, indicating how the microstructure of the system varies with time.

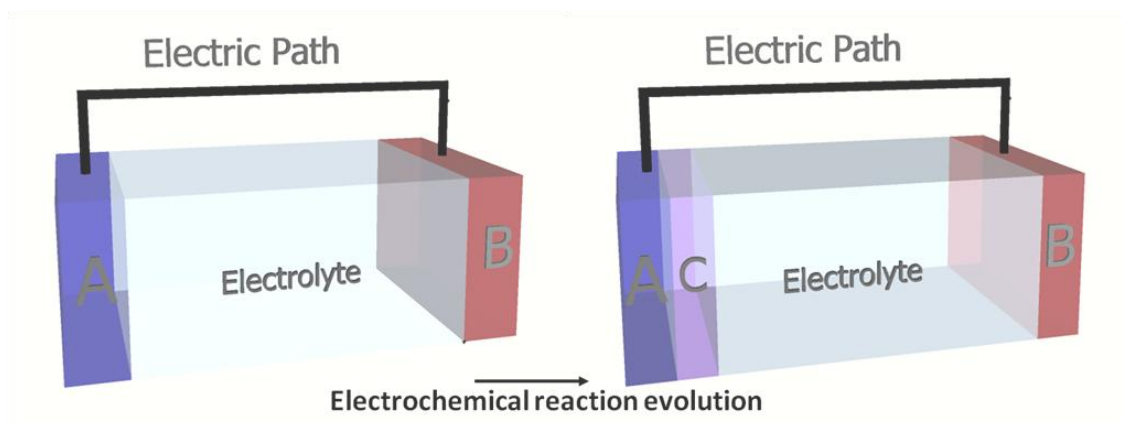
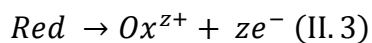
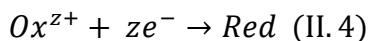


Figure III-2: Simple schematic model of the time evolution of the microstructure during the electrochemical reaction of A and B to form C, a mixed conductor. It is assumed that B^+ ions are the predominant ionic species in the electrolyte. The simple external circuit is represented only as the path guaranteeing electronic continuity between A and B.

If electrons are allowed to flow in the external circuit, the reaction will happen until one of these condition is satisfied: i) ionic conduction inside the electrolyte is impeded, ii) electric current in the external circuit is interrupted, namely the circuit is opened and iii) the reaction itself come to an halt due to reagent depletion or because the chemical equilibrium is met. While the electrons are flowing through the external circuit the electric charge motion is counterbalanced by the chemical driving force related to the reaction standard Gibbs free energy. This value is the summation of standard Gibbs free energy contributions derived from half reaction included in the galvanic chain. The overall reaction can thus be split into two half electrochemical reactions, or red-ox reactions, involving charged species, such as:





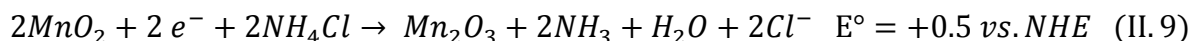
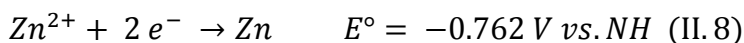
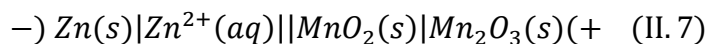
Equation II.3 represents the oxidation reaction, and II.4 is instead the reduction reaction, while $z e^{-}$ is the number of electrons exchanged for mole of reduced or oxidized species, as well as the charge of the ionic species Ox^{z+} . It is possible to calculate the electrostatic energy E_e , or in other words the amount of electric work done by the system and related to electrons flowing, through equation II.5:

$$E_e = -zFE \quad (II. 5)$$

where F is the Faraday constant and stands for the charge, measured in Coulomb, carried by one equivalent of electrons and is 96485 C/eq, and E is the electrochemical potential measured between the two electrodes. Can be demonstrated that ΔG_r° , coincides with the amount of non expansion-work done by a system in standard condition of temperature and pressure, and thus it can be written:

$$\Delta G_r^\circ = -zFE^\circ \quad (II. 6)$$

E° is called the standard electromotive force (*emf*) or standard potential of the cell. Conventionally half reactions are always reported as reduction reaction (II.4), and the electrochemical potential acquires a positive or negative sign according to the spontaneity of the process. Each Red/Ox couple involved in the electrode reaction, contributes to the theoretical potential of the cell with its standard electrochemical potential, correlated with the Gibbs free energy of the half-reaction through equation II.6. Theoretical values of standard potential of a galvanic chain as the one for the widely known zinc-carbon battery reported below, can be calculated from tabulated standard potential values³, formally expressed as standard reduction potentials.



and the whole cell potential being the difference between standard reduction potentials of cathode (+) and anode(-):

$$E^\circ(+)-E^\circ(-) = +0.5 V - (-0.762 V) = +1.262 V \text{ vs. } NHE \quad (II. 10)$$

All the voltage values expressed so far are reported in reference to the normal hydrogen electrode (NHE). From the equation II.6 other important thermodynamic relations involving E° can be derived, such as the definition of the entropy variation of an electrochemical process:

$$\Delta S = nF \left(\frac{\delta E}{\delta T} \right) \quad (\text{II. 11})$$

2.1. Nernst Equation

So far it has been referred to potential as to a standard quantity. Deviation from standard conditions are expressed by the *Nernst equation* in which formal value of electrochemical potential incorporates deviation coming from temperature changes and phases composition in electrochemical active species. This deviation can be experimentally quantified by measuring the electrode potential with respect to a reference electrode (an electrode whose potential remains constant) and can be correlated to electrolyte solution activity of the electrochemically active species using the formula

$$E = E^\circ + \frac{RT}{nF} \ln \left(\frac{a_{ox}}{a_{red}} \right) \quad (\text{II. 12})$$

where a_{ox} and a_{red} are the activities of oxidized and reduced species respectively. The as reported equation specifies equilibrium potential at known species activities. Considering a single active species whose activity a_i is different in each one of the two electrodes of the cell, the difference in chemical potential, namely molar free Gibbs energy of the species i in phase j , of the two electrodes can be written as

$$\mu_i(+)-\mu_i(-) = RT \ln a_i [a_i(+)/a_i(-)] \quad (\text{II. 13})$$

If equation II.6 is recalled to balance the chemical potential discrepancy by the electrostatic energy

$$E = - \left(\frac{RT}{z_i F} \right) \ln \left[\frac{a_i(+)}{a_i(-)} \right] \quad (\text{II. 14})$$

The last equation, the *Nernst equation* for the whole galvanic chain, sets a correlation between the measurable potential, experimentally quantified with respect to a reference electrode, and the difference in chemical composition across the cell, or in other words it allows to operate a transduction between the chemical and electrical driving forces. The electrode potential can be thus altered by altering the ratio of the activities of oxidized and reduced states. An alteration of this ration by a factor of ten, leads to a change of $0.059/n$ volt in E . As will become clear later, Nernst relation describes not only the electrode potential evolution of an inert metal electrode immersed in an electrolyte solution containing a redox couple, but it also can be applied to some classes of battery materials for which the electrode bulk phase changes

its composition in the electrochemically active species, as it happens in solid state solution type cathode materials hosting lithium or sodium ions. In practical cells, the electromotive force is never exactly equal to the electrodes potential difference. Obstacles to free-flow of ions and electrons always exist and determine impedance to increase to some extent depending on which process is being considered. Overpotential values, namely the extent in curbing formal potential expressed by Nernst relation, can originate from mainly four processes that concur in defining the operational output voltage of the cell:

- Ion mobility inside the electrolyte (Ohmic drop η_{IR});
- ions and electrons mobility inside electrode material (η_{el});
- charge transfer at the electrode/electrolyte interface (η_{ct});
- electron leakage through the electrolyte.

Impedance rather resistance would be a more appropriate term to address phenomena curbing conductivity, since inside an electrochemical cell this contributes are not constant and typically their effect evolves with a time-varying current. Thus impedance (Z_e) assumes the meaning of the instantaneous changes of operational potential, referred also as voltage, and the flowing current.

$$Z_e = \frac{\delta E}{\delta I_e} \text{ (II. 15)}$$

Z_e changes with time-dependent processes involving active materials at the electrodes and electrolyte solution. In order to bring some order in these sometimes confusing mechanisms, it is useful to rationalize impedance components as follows. Charge transport of ionic species in electrolyte solution conductivity depends on diffusion (under a concentration gradient) and migration (under an electrostatic potential gradient) of charged species and viscosity of the media. Transport numbers are commonly utilized in defining the contribute to electrolyte solution conductivity of a charged solvated species, especially if there are more than one. Transference number of a ionic species i is defined as

$$t_i = \frac{I_i}{(I_i + I_j)} \text{ (II. 16)}$$

where I_i and I_j are partial currents upon the application of an external voltage across the system. The sum of all the transference numbers for all the ions in solution equals unity. Inside a solid, even transference number related to electrons mobility acquire a relevance, and it could become

a limiting factor inside an occurring electrochemical process. Diffusion of charged species or atomic species in the bulk of electrode phase might have a different relevance depending on mechanisms involved in electrode reactions, as discussed in detail in Chapter III:7. At the electrode/electrolyte charge (electron), instead, transfer is related to energetic landscape at phases boundaries.

In some extent, resistive behavior is always occurring when electro-active ions or atomic species are transferred across the cell. They may derive from electrolyte resistance to ionic transport or charge transfer difficulties at electrode/electrolyte interfaces. Despite practical battery electrodes are far from being even remotely similar to ideally polarizable electrodes (IPEs), they can express some typical characters of polarizable electrodes, such as the instauration of a capacitive double layer equipped with a certain capacity value C_{dl} (measured in F, farad, not to be misled with the capacity measured in mAh, expression of the stored charge) function of electrode potential. Physically, the capacitive behavior can be depicted as the instauration of a double-layer region of ions, counterbalancing electrode surface electric potential excess. Several models, each one with a progressively increasing level of accuracy, have been proposed throughout the decades to supply a physical description to this phenomenon. In Figure III-3 is depicted a model in which the stored capacity can be visualized by the building up of a solvated cations layer within a certain distance from electrode material surface. Within the outer Helmholtz plane, a significantly dense solvated cations layer can be formed and a linear decrease in electrode potential, achieved. In the bulk of electrolyte solution, beyond the OHP, an exponential decrease of residual potential occur instead, until a negligible value is reached. This physical process can gain relevance as a storing energy mechanism if some conditions are met. The case of highly porous active electrode materials represents one of those, and is a welcomed material peculiarity when supercapacitors are being studied, provided also a fast charge/discharge kinetic of the above mentioned double layer.

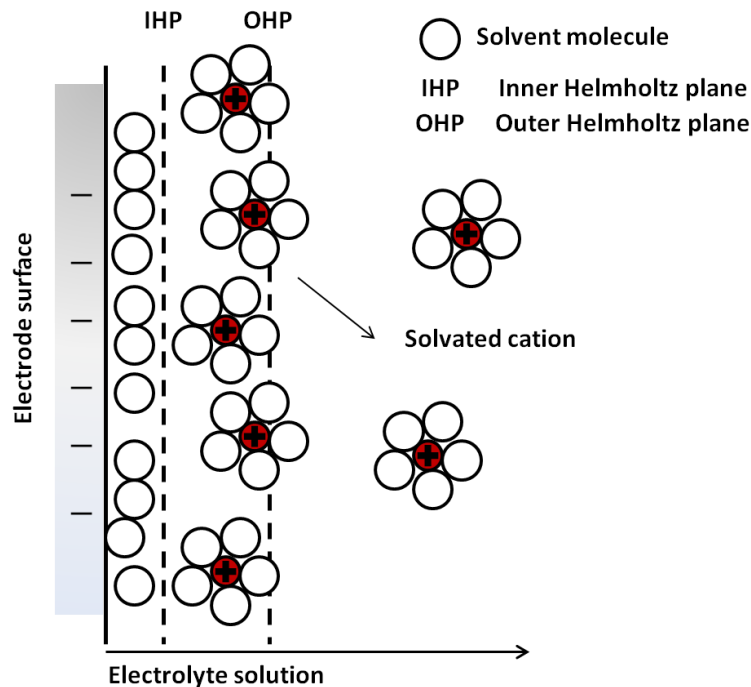


Figure III-3: proposed model of the double-layer region under conditions where no specific adsorption of charged species happens.

In order to better elucidate each listed resistive and capacitive contribution, an equivalent electronic circuit might be of help if each electrochemical event is modeled by simplified circuitual element such as resistors and capacitors. Circuits reported in Figure III-4 simplifies the mechanisms previously introduced, and in particular includes circuitual elements modeling the galvanic chain (v_{OC}) whose formal potential may be connected to its state of charge (SOC), resistance contribute due to electrolyte solution (R_s), charge transfer resistance (R_t) and double layer capacitance (C_t). Worth noting is that R_s and C_t element may also include resistive and capacitive contribute due to ions transport inside the SEI (see further), SEI capacitance, ion and electrons transport inside electrode material. There are electrochemical techniques, such as the electrochemical impedance spectroscopy (EIS) that, analyzing the different system response to a frequency dependent stimulus, can distinguish between the listed processes, both resistive and capacitive. R_d element has been included in the circuit in order to account for a possible *self-discharge* mechanism due to an electrons-leaking electrolyte solution.

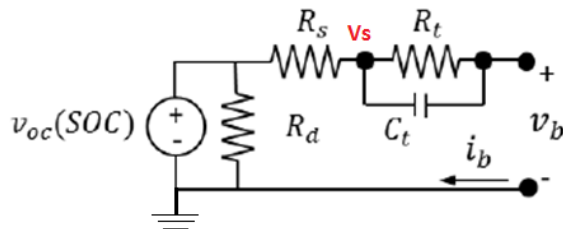


Figure III-4: Equivalent circuit of a galvanostatic cell with different physical properties modeled with equivalent circuit elements; v_b element represents the operational cell potential, see text for further details.

3. Kinetics of electrode reactions

It is an experimental fact that most of the rate constant k of solution-phase reactions vary with temperature T in a common fashion: nearly always, $\ln k$ is linear with $1/T$. This behavior has been firstly recognized by Arrhenius who proposed the correlated mathematical expression, as an empirical generalization of reality, fitting many distinct cases

$$k = A e^{-E_a/RT} \quad (\text{II. 17})$$

where E_a , the *activation energy*, has unit of energy and refers to the height maximum of the energy barrier that has to be overcome in order to start the reaction. Many events occurring inside a cell can follow an Arrhenius-type mechanism. Charge transfer, previously introduced, if properly isolated from other processes via specific analysis techniques (EIS), can manifest linearity with $1/T$ values. From an opportunely modified relation, where k and the *frequency factor* A are substituted with resistance correlated parameters, is thus possible to obtain activation energy parameter related to electron transfer taking place at electrode material surface. There are several important electroanalytical methods capable of probing kinetic of redox processes: GITT and PITT are some examples and their brief description and mathematical interpretation of experimental data can be found in Chapter X. Low rates GITT allows to investigate redox processes in quasi-equilibrium conditions, excluding the blurring effect of high rates over redox mechanism distinction⁴. A more general approach for one-step, one-electron process is expressed by the *Butler-Volmer* equation

$$i = F A k^0 \left[C_o(0, t) e^{-\alpha f(E-E^{o'})} - C_R(0, t) e^{(1-\alpha)f(E-E^{o'})} \right] \quad (\text{II. 18})$$

It is used for almost every problem treating heterogeneous kinetics and correlates current, expression of the rate at which the electron transfer is taking place, to overpotential coming from discrepancies between equilibrium potential and applied one, in a potentiostatic

experiment. The importance of this relation resides in the power of correlating experimentally quantifiable quantities (i and E) with parameters closely referred to the energetic evolution of charge transfer reaction (kinetic constant k^0 , and transfer coefficient α).

4. Figures of merit for batteries

When considering the use of electrochemical energy storage system in various applications, it is important to be aware of properties that might be relevant, for they are not always the same in every case. According to utilization, some rechargeable battery rather than other types are desirable and useful instruments involved in cell choice include specific energy, specific power and specific capacity, operating voltage and so on. These physical characteristics will be often referred to throughout the entire dissertation and a tight grasp on their meaning is mandatory. This section has been thought to as a handy and easily consultable list to quick recall the definition of rechargeable battery characters.

4.1. Specific energy, Specific power and specific capacity

There are several important practical parameters that contribute in making a secondary battery efficient and reliable. The most easily understood among them is certainly the *specific capacity* (measured in $\text{mAh}\cdot\text{g}^{-1}$), or in other words, the total stored capacity normalized over the mass of electrochemically active material. This is a quantity specifically utilized in defining the sodium uptake theoretically or practically achievable by an anode or cathode material. More comprehensive parameters often mentioned in classifying batteries according to utilization are *specific energy* ($\text{Wh}\cdot\text{kg}^{-1}$) and *specific power* ($\text{W}\cdot\text{kg}^{-1}$). The first one, calculated as follow:

$$\text{Specific Energy} = \frac{\int E dq}{m} \quad (\text{II. 19})$$

It embodies a quality factor of the battery. As well as the temperature of the hot source defines the energy quality of a combustion engine, cell potential, and energy that is tied to it calculated by the product $E \times Q$ ($Q =$ stored charge), sets the position of the cell in a quality energy ranking made up of three places:

- 3.5 - 5.5 V High quality energy
- 1.5 - 3.5 V Medium quality energy
- 0.5 -1.5 Low quality energy

High quality energy cells, and thus high potentials, are required for several applications, such as powering hybrid or fully electric vehicle motors or as SLI systems in normal combustion engine cars. In this application high voltages are required (200 volts in the EV), so the higher is the energy quality of battery chemistry employed, fewer cells are needed to achieve required voltages values. Intermediate energy qualities are instead preferred when modest energy densities are preferred, as it is in powering high-end electronics. Specific power, moreover, sets an important parameter to look at when specific amount of energies have to be dispensed in a short period of time. Utilizations for which an instant supply of energy is required, should be powered by system whose chemistry can withstand fast drain of capacity, without suffering irreversible material disruption. A handy representation of the influence of the discharge load on the energy that can be delivered is provided by the Ragone plot (Figure III-5), named after D.V. Ragone, chairman of a governmental committee, who for the first time proposed the specific power vs. specific energy as a representation of the properties of different rechargeable batteries. Worth to be mentioned is that E , as it appears in equation (II.19), may vary depending on the material SOC as well as on kinetic parameters. Alternative quantities to specific energy and power can be utilized in order to highlight peculiar characteristics of the cell and to express they suitability for some uses. Energy and power densities, expressed in $\text{Wh}\cdot\text{dm}^{-3}$ and $\text{W}\cdot\text{dm}^{-3}$, are particularly useful when volume is a limiting factor in practical utilization. For example energy density, strongly dependent on cell geometry and casing volume, is a delicate feature when miniaturization is a mandatory aspect, such as in portable electronics.

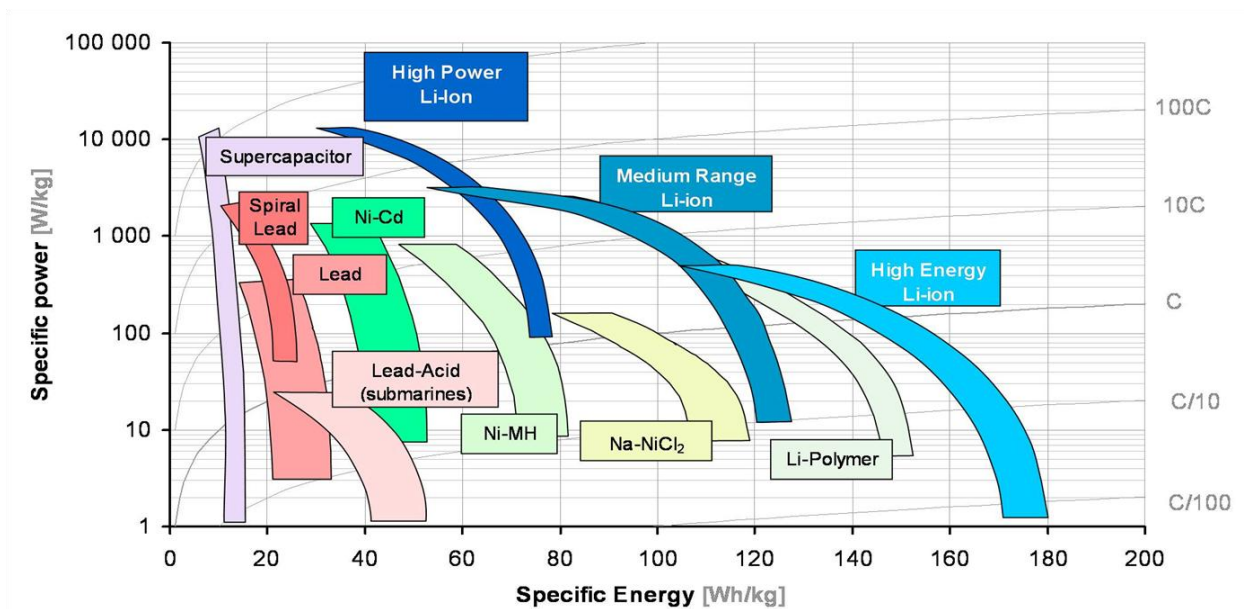
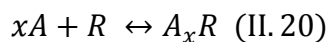


Figure III-5: Ragone plot, plotting specific power vs. specific energy, for various battery chemistries. On the right y-axis the drain current born by battery systems are also reported.

Is often useful quantified the values theoretically achievable for specific energy as well as for specific capacity. In the former case, the quantity is referred as the maximum theoretical specific energy (MTSE), and has to be evaluated according to the type of reaction, stoichiometry and compound molar weight referred to the electrode process. For a generic reaction,



where x is the mols of A reacting as well as, in this case, the elemental electronic charge if E is the average voltage at which the reaction occurs, and W_t the sum of the molar weights of the reactants, the maximum theoretical specific energy, measured in $\text{KJ}\cdot\text{kg}^{-1}$ is:

$$MTSE = \left(\frac{x \times E}{W_t} \right) \times F \quad (\text{II. 21})$$

Since the product between a charge (namely the Faraday constant, equal to 96485 C per equivalent of electrons) and a voltage, result to be equal to an energy. Value of MTSE can be also expressed in $\text{Wh}\cdot\text{kg}^{-1}$ (multiplying by 0.000278) and may also be modified in order to give energy maximum theoretical energy density value for the system (in $\text{Wh}\cdot\text{dm}^{-3}$), normalizing its value by the mean density of the compounds engaged in the reaction. Theoretical specific capacity (MTSC) is often reported in order to identify the storage capacity of a compound.

Commonly expressed in $\text{mAh}\cdot\text{g}^{-1}$, it is calculated starting, likewise MTSE, from the cell half reaction:

$$MTSC = \frac{e \times F \times 0.000278}{W} \quad (\text{II. 22})$$

being e the electron equivalents exchanged for mole of electrochemically active compound and W the molar weight of the above mentioned compound as the reactant of the reaction. This theoretical value represents the quantity in respect to what the practical specific capacity can be compared in order to quantify the process efficiency. Practically speaking, depending on the reversibility of the electrode mechanism, a certain amount of the specific capacity can be lost with every charge/discharge cycle. Independently from whether anode or cathode material in a half-cell systems or a whole-cell are being investigated, a useful parameter in order to evaluate the electrode process reversibility is the so called Coulombic efficiency (CE), calculated as:

$$CE = \frac{Q(\text{discharge})}{Q(\text{charge})} \times 100 \quad (\text{II. 23})$$

with $Q(\text{charge})$ has to be considered the amount charge, erroneously called capacity, provided to the system as it is being recharged, while $Q(\text{discharge})$ is the amount of practical capacity extracted from the system during capacity draining due to utilization of the battery. Each quantity Q is calculated by integrating currents over time, $\int i dt$. Capacity that is not recovered after each cycle is addressed as the irreversible capacity and depends on parasitic reactions and surface mechanisms as further illustrated. Irreversible capacities are practically quantified through the discrepancies between capacities extracted from two consecutive charge or discharge curves whose percent quantity is the Coulombic efficiency.

4.2. Open circuit Voltage (OCV) and Operational Potential (Working Voltage)

Open circuit voltage (OCV) is the measured voltage when no net charge flows through the external circuit. It mathematically coincides with the difference between formal potential of cathode and formal potential of anode, or in other words, the difference between Fermi level energies of cathode and anode normalized over the electronic charge ($\text{OCV} = (\mu_C - \mu_A)/e$). The formal potential is the thermodynamic quantity resulting from Nernst equation after the insertion of the actual activity of electrochemically active species as previously reported. The OCV does not coincide with the operational potential since ohmic drop (IR) occurs inside the electrolyte solution. When the electrolyte impedance is not negligible, or other charge-transfer

limiting factors will come into play, a considerable discrepancy between operational potential and OCV will be realized. In some cases, even in OCV condition, a self-discharge process might be triggered. This effect might be caused by electronic charge leakage inside the electrolyte solution that progressively leads to a drop in the SOC and OCV as well, if output potential has a strong dependence with SOC. This tendency of losing a percentage of stored charge, over a period of time, even if no load is applied is referred as *self-discharge*, and for a lithium-ion commercial cell is esteemed to be around 1-2 % per month at room temperature (20-30 °C). Temperature and condition of storage and utilization, might have a heavy effect on self-discharge evolution. Theoretically opposite to the OCV concept stands the short-circuit one. A short-circuit is realized when current can freely travel across an unintended path where no (or very low) electrical impedance is met. It can be either realized internally to a cell, either externally. When it happens internally to the galvanic cell, a fast electron-conducting channel realizes across the anode and cathode and through the electrolyte solution. This of course leads to the triggering of fast discharge process with a fast and localized build up of the temperature (Joule heating) that might eventually end up with a potentially catastrophic thermal runaway, if flammable materials (solvent) are used. Metallic particle impurities enclosed in battery assembly during manufacturing, or growing alkaline metal dendrites poking through the electrolyte layer, are commonly the causes for internal short-circuit failures of sodium-ion, lithium-ion cell, sodium-metal and lithium-metal cells. As the cell discharge, a progressive drop in the operational voltage is often observed. This, as mentioned, is a symptom of a strong dependence between state of charge and output voltage of the cell and can be clearly visualized in the so called *charge/discharge curves* where potential is plotted as a function of SOC or absolute charge. The relationship can vary greatly upon the rate at which capacity is added, or extracted, from the cell. At equilibrium or near-equilibrium conditions, potential vs. charge curves assume a very important role in distinguishing different sequential steps involving even phase changes. Technique called *Coulometric Titration*, performed at near-equilibrium condition, provide useful thermodynamic information regarding phases transition and stoichiometry. Weppner and Huggins investigating poly-phase alloy systems were able to determine phase diagrams by the use of these techniques⁵.

4.3. C-Rate

The C-rate is a term, alternative to current or current density, expressing the speed at which a material is being charged or discharged respect to its theoretic specific capacity. A charge/discharge nC -rate signifies a charge or discharge rate corresponding to a current high enough to charge/discharge the whole mass of material in n hours. For example, owing a 100 % Coulombic efficiency, for a 1 Ah battery, a rate of C would correspond to 1 A and 1 hour charge/discharge process. A Charge rate of 0.2 C, would be instead equal to 0.5 A and would require double the time, two hours, to end, while a charge rate of 2 C, namely 2 A, would need 30 minutes.

4.4. Agreement on battery nomenclature

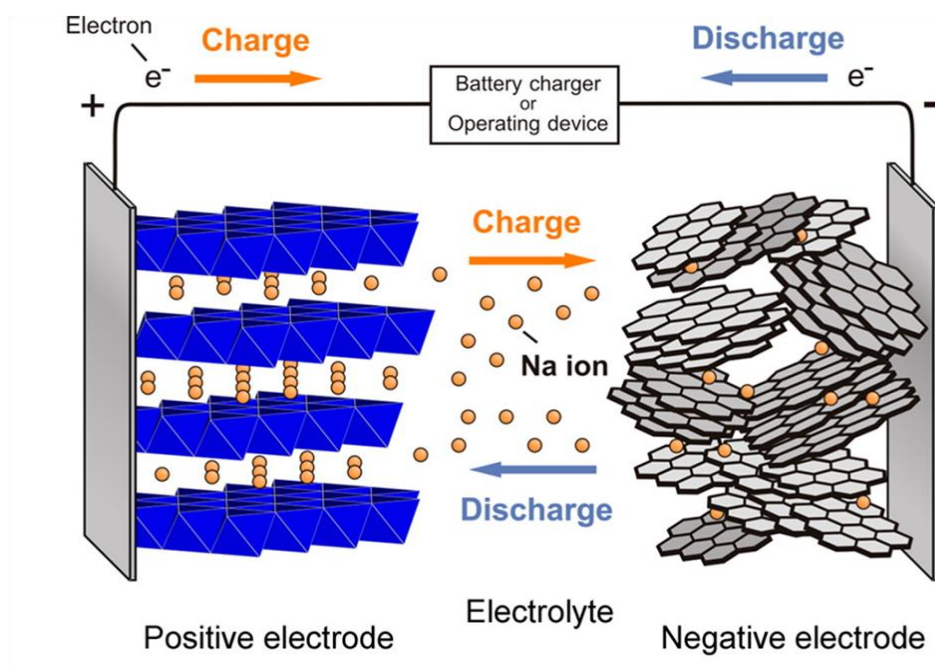


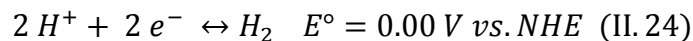
Figure III-6: Graphical description of a sodium rechargeable batteries; anode and cathode material choice is purely descriptive and has no meaning of completeness.

Talking about electrochemical processes evolving inside a galvanic cell, often a lot of confusion arises due to a lack of agreement on technical terms. For sodium-ion rechargeable cells, focus of this research, has been adopted the term “charge” referring to sodium ion migration from cathode (positive electrode) to anode (negative electrode), while “discharge” to addressing the opposite process, as depicted in Figure III-6. Alternatively, the attention will

directed to the investigation of anode and cathode material separately, commonly studied in half-cells coupled with metallic sodium acting both as a reference electrode (RE) and counter electrode (RE) in two-electrode experiment, or simply as a counter electrode in a three-electrode configurations. In these set-ups, when an anode material is investigated, sodium uptake step will be thus defined as the charging phase, and will be associated to a negative current in the typical galvanostatic analysis technique (at constant current). The charging phase will coincide with the depletion of sodium, and will be coupled to a positive current, if a cathode material will be the object of the analysis.

5. Aqueous electrochemical cell

Amongst the low- and medium-quality energy storage systems, aqueous cells are the cheapest and most abundantly utilized so far. As the name itself suggests, they relies on water-based electrolyte solutions ether basic or acidic. For this reason an intrinsic limitation to obtainable theoretical output voltage is imposed by water splitting oxygen and hydrogen evolution reactions:



Standard potentials of the above mentioned reactions are pH-sensitive, and thus depending on the electrolyte solution formulation, a different potential window become available. Theoretically no more than 1.3 V would be obtainable from an aqueous based rechargeable battery, under a practical point of view this value can be altered by increasing the concentration of additive and supporting electrolytes. Amongst the countless aqueous chemistry proposed throughout the centuries, worth to be mentioned are Lead-acid batteries, Nickel-Cadmium and the most recent Nickel-metal hydride ones. Sodium-based aqueous, as well as lithium-based ones, rechargeable batteries have been known a scarce fortune due to the high incompatibility between metallic sodium, or a Na-containing material with a high Na activity and water. Nevertheless, recently some materials investigated for non-aqueous rechargeable batteries have been discovered to be suitable also for the utilization in an aqueous environment⁶, disclosing new possibility for low-cost and low-potential sodium ion batteries.

6. Non-aqueous electrochemical cell

Most of the nowadays efforts in investigating room-temperature sodium cells is being addressed to aprotic non-aqueous sodium-ion batteries. The foremost purpose in employing organic solvent-based electrolytes is primarily aimed at exploiting the theoretical electro-positive potential of sodium, in the same fashion as with lithium, to harvest the highest energy density possibly achievable. Organic solvents commonly used in electrolyte formulation for both sodium and lithium-ion batteries, are carbonates, ethers and recently also room-temperature ionic liquids have been investigated. For what concern solvated sodium salts NaTFSI (sodium trifluoromethanesulfonimide), NaClO_4 and NaPF_6 are commonly employed. Generally the above mentioned solvents, with high dielectric constants, and salts can guarantee a wider potential window of operation thanks to their electrochemical stability (wide HOMO-LUMO gap, Figure III-7). Nevertheless they are not devoid of critical aspects. As a matter of facts solvents like propylene carbonate (PC), ethylene carbonate (EC), dimethyl carbonate (DMC), diethyl carbonate (DEC), dimethoxyethane (DME), tetrahydrofuran (THF), triethylene glycol dimethyl ether (Triglyme) are flammable (PC), with flash points even at low temperatures (17 °C for DMC and 25 °C for DEC) or hazardous for health (DME and THF). Concerning sodium salts, NaPF_6 can potentially deliver NaF, corrosive for metal casings and other materials. Another major issue vexing the proper operation of a rechargeable cell is the contamination of sodium salt. Studies have highlighted how reagent grade, instead of battery (high purity) grade sodium salts, negatively affect the cycling performances, incrementing the irreversible capacity per cycle, if tested in a half cell against a hard carbon anode material⁷. As a rule of thumb, a proper balance between conductivity and viscosity has to be fulfilled together with a good electrochemical stability over a wide potential window. A part for TFSI-anions inducing aluminum corrosion, all the limitation to electrolyte stability are induced by the solvent alone. Owing that, decomposition effect catalyzed by specific active electrode materials cannot be excluded⁸.

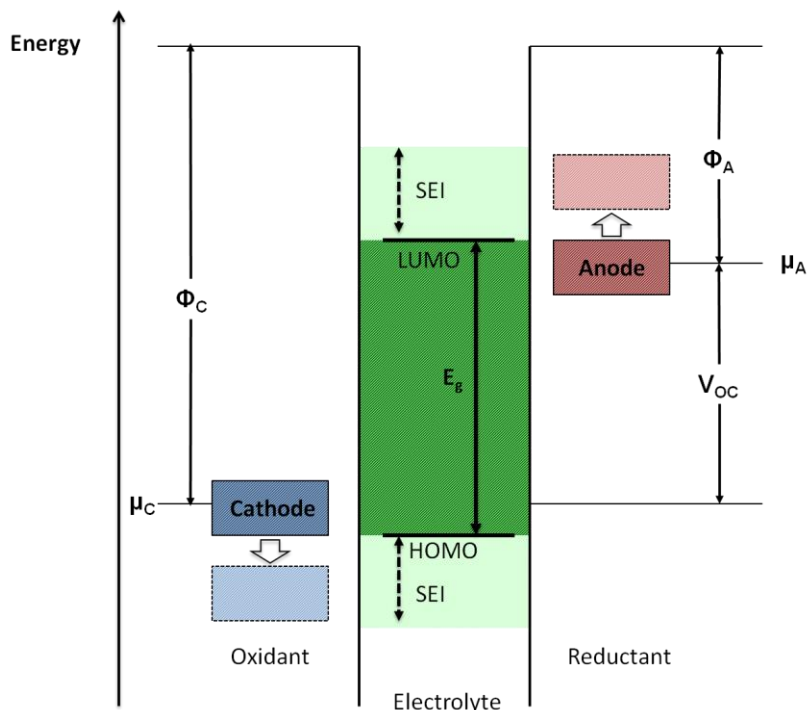


Figure III-7: Schematic open circuit energy diagram of an electrolyte; Φ_C and Φ_A are cathode and anode work functions respectively, E_g is the thermodynamic stability window of the electrolyte. A $\mu_A > \text{LUMO}$ and $\mu_C < \text{HOMO}$ require a kinetic achieved with the formation of a SEI layer.

6.1. Solid Electrolyte Interphase (SEI)

Solvent, electrolyte salts, additives and binders heavily affect electrochemical performances of anode materials (hard carbon and other potential negative compounds), and the difference originates from the decomposition of organic/inorganic molecules forming a solid film on the electrode surface, and ideally leading to its passivation⁹. Generally aprotic solvents, as the ones mentioned above, are poorly thermodynamically stable in proximity of 0.0 V vs. Na/Na⁺. The solid electrolyte interphase (SEI) as firstly named by Peled¹⁰ has thus an essential role in guaranteeing cycle stability and good electrochemical performances. Among the most notable effect enabled by the presence of a stable SEI layer there is, first of all, the suppression of further decomposition of the electrolyte. Added to this, the solid interphase should meet the following requirements: i) a surface as thin as possible but sufficiently thick thus to impede the direct contact between high energy surface and fresh electrolyte, ii) electronic insulation and iii) good ionic conductivity. This last feature is of extreme importance since a poor ionic conductivity could slow down electrode processes increasing the impedance of the system.

Although the SEI composition for lithium systems has been widely studied and consistent results have been obtained, SIBs deep understanding of electrolyte decomposition still lacks of completeness. Techniques aimed at classifying SEI composition and physical properties would be of foremost importance in formulating reliable commercial electrolyte solutions. So far TEM, SEM, X-ray photoelectron spectroscopy (XPS, time-of-flight secondary ion mass spectroscopy (TOF-SIMS) and NMR have been used to comparatively examine SEI in Na cells on different anode substrates. Rough, non-uniform deposits mainly composed by inorganic species (Na_2CO_3 , NaF and NaOH) were observed on carbonaceous anode material (Hard-carbon)¹¹. On a different type of SEI has been observed forming on a different class of anode material, that is the sodium titanate $\text{Na}_3\text{Ti}_2\text{O}_7$. In this case a degradation of the electrolyte solution is achieved not only during the very first sodiation phase, during which it is abundant and leads to a modest irreversible capacity, but it is observed also during the following cycles, after a partial dissolution of the originally formed SEI layer. Among the compounds building up the interphase layer have been here detected inorganic compounds (NaF and NaCl, coming from sodium salt decomposition), organic species (PEO and alkylcarbonates as the soluble species) and adsorbed oxygen¹². Depending on the anode material, related organic/inorganic compounds SEI content varies sensibly, and so does its stability. Type of anode material also plays an important role. Alloying or conversion materials (see Chapter III:7.3 for further details) for which large volume hysteresis is involved between sodiation and de-sodiation contribute in building up unbearable mechanical stresses on the SEI layer, generating local fracturing and thus exposition of fresh material surface to the electrolyte solution. This ultimately and repeatedly brings the formation of new SEI matter with every passing cycle. Electrolyte salts, binders, solvents, additives and anode materials influence the quality of the solid electrolyte layer and although SIBs might be compared, under many points on view, to LIBs all the understanding on SEI composition collected until now for lithium anode material, poorly adapt to sodium system.

The binder, namely the polymer included in electrode formulation to convey mechanical robustness, has a major effect, even though indirect, on the SEI formation and stability. According to electrode reaction taking place a more or less pronounced elasticity of binder molecules is required. Binder such as polyacrylic acid (PAA) and carboxymethyl cellulose (CMC) could largely endure the repeated volume variation during charge and discharge,

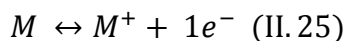
therefore keeping the integrity of the electrode and avoiding continuous material fragmentation and exposition of new SEI-free surface to the electrolyte. PVDF instead, has been recognized to be not suited as a binder for conversion oxide-based materials, due to its higher rigidity¹³. This brief introduction to SEI chemistry does not pretend to be exhaustive and a further detailed study is behind the purpose of this work.

7. Active materials for aprotic alkaline secondary batteries

In this section are reported the most important classes of active materials for SIBs. They will be here analyzed in their theoretical principles and mechanisms while an exhaustive list of compounds and elements belonging to these classes will be provided in the following chapters (III and IV) when the state-of-the-art regarding SIBs anode and cathode materials will be outlined.

7.1. Simple oxidation reaction from (alkali metal) bulk elemental species

Using elemental alkaline metals as anode material in lithium and sodium ion batteries has been a trend since the early stage of secondary batteries research. Obviously the occurring electrode reaction is the oxidation reaction of the metallic alkaline element during discharge and plating during charge



The considerable advantages deriving from that include the extremely negative standard reduction potential (-2.71 for sodium and -3.04 V vs. NHE for lithium) theoretically achievable thanks to the unit activity of sodium and lithium, absence of dead weight carried by alloying or non electrochemically active materials and outstanding energy densities achieved thanks to the modest molar weight. In Table III-1 these and other important parameters are collected in order to provide a fast and effective comparison between sodium and lithium as anode material for batteries.

Table III-1: Physical and chemical relevant properties for Li and Na metals, useful to contextualize their performances if used as anode materials in secondary LIBs and SIBs.

	Lithium	Sodium
E°red (V vs. NHE)	-3.04	-2.71
Atomic weight (g·mol⁻¹)	6.94	22.99
Density (g·cm³)	0.534	0.968
Energy density (Wh·kg⁻¹)	11732	3542
Cost (\$·ton CE^b-1)¹⁴	5000	150

In an electrochemical cell in which an elemental metal serves as anode, the most puzzling process is the recharging one, since many unwanted and potentially hazardous phenomena may occur. The ideal process guaranteeing a high Coulombic efficiency and effective recharge ability would be a plating process maintaining unchanged the starting electrode geometry and structure at the microscopic scale. Unfortunately this is not easily achievable due to occurring shape changes thermodynamically active or kinetically activated by poorly controlled charge currents. Electroplating of alkaline metal at unwanted locations, such as current collector or cell casing, is one of these. An event that created many troubles in metallic anode cells during the advent of first rechargeable lithium batteries has been the dendrite and filament growth during the charge step. This process has to do with the intrinsic instability of a flat surface on a microscopic scale during electroplating, emerging from local solute depletion. This fact creates a positive gradient of the element's chemical potential in the electrolyte solution immediately adjacent to the depletion region, making the growth of any even small protuberance on metallic lithium surface to grow faster. Eventually this will lead to the development of inhomogeneous plating, and in the worst cases, dendrites formation and branching. Protrusion of these formations into the electrolyte and contacting the cathode is a worst-case scenario in a cell failure and systematically end up with the internal short-circuiting of the cell with a potential development of violent runaway reactions. This deleterious process has been recognized to be a major issue both for sodium and lithium systems, and a fundamental role seem to be played by solvents employed in electrolyte solution preparation. In fact electrolyte not containing carbonate-based solvents (propylene carbonate, ethylene

^b CE stands for (SCE for sodium and LCE lithium) carbonate equivalent, that is the compound to which cost and other quantities, as alkaline content in a whole battery, are often expressed.

carbonate, diethylene carbonate) seem to favor a more homogeneous and flaws-free sodium plating less prone to build a SEI layer with uneven impedance characteristics¹⁵.

7.2. Insertion reaction

Since few years ago, insertion mechanism didn't even appear in publications related to batteries. The possibility that electrochemical reactions might occur not only on the surface of the material but also could interest the bulk phase of the active material was considered not of critical importance. B-alumina phase has been one of the first compound in which ions mobility inside lattice has been demonstrated to occur under a potential gradient. Its use as a solid electrolyte, even if at high temperature, allowed to develop the very first sodium-ion battery based on a melted sodium anode and a sulfur cathode. *Insertion or intercalation* mechanism happens when a host crystalline species can accept inside its structure a guest without perturbing its general character. Guest species can be positively or negatively charged ion as well as neutral molecules, and currently plenty exempla of all the above mentioned cases are present in literature. Their insertion in the host crystalline lattice may induce little to no changes in crystalline parameters, such as interatomic distance, crystalline planar spacing, cell volume and crystalline phase. Guest species uptake and concentration inside host structure is controlled by thermodynamic equilibriums establishing at the electrode material/electrolyte interface.

Insertion reactions, nevertheless are not simple processes to realize, and specific conditions have to be fulfilled in order to get a reversible mechanism. First of all only neutral guest species suffice an electrostatic interaction with the host structure in order to penetrate into its lattice, for charged ions instead, and this is the case for the totality of modern battery systems, a net negative electron addition is required to balance the charge unbalance carried by the insertion of a charged entity. This electrons accumulation (during guest insertion) and depletion (during guest extraction) is usually supported by an electrochemically active atom inside the host compound structure, that reversibly undergoes a redox reaction. Owing the reduction and oxidation of the host species, a moderate electronic conductivity has to be met by the host system, and added to this a sufficiently open structure is needed in order to facilitate the accommodation and fast diffusion of ions. From this last mandatory feature for an insertion compounds, derives the *topotacticity* of several insertion processes, namely the selectivity for inserting ions to occupy specific positions in the lattice structure such as void interstitial sites that create a two or three dimensional network.

7.2.1. Types of insertion reactions

There are several types of insertion reaction, seeking clarity a schematic representation of the most important insertion mechanisms encountered in sodium-ion systems is reported. A first simple mechanism concerns the random occupation of available sites realizing the solid-solution type of behavior with a measured electrode potential changing over time, depending on the activity of the guest species inside the host. The host structure is not modified and ions are accommodated accordingly to elongation of atom-atom bonds without a structural change in the host material. If this is the case, a two phase process has to be considered and a phase front can be recognized. In the latter case either guest species can accommodate randomly in the forming phase either they can occupy specific sites. When the two phase process is occurring, according to the Gibbs phase rule (1.12), given temperature and pressure both constant, no degree of freedom (F) are left when two phases (P) are present at the same time in a binary system ($C = 2$). For this reason electrochemical potential doesn't change while electrode gets richer in the new phase.

$$F = C - P + 2 \quad (\text{II.26})$$

This two-phase mechanism, rather than a pure insertion reaction, is often referred as a constant-potential *reconstitution* reaction, since a net structural modification is happening in the host material. For certain types of material, different insertion mechanisms can be sequential as depicted in the explanatory Figure III-8: random occupation of two different sites is followed by a reconstitution reaction occurring at higher content of sodium in the structure. Usually sequential reactions happen when tangled 3D tunnel network is available inside the host structure for ion insertion. Multiple insertion sites are thus available at different insertion energies according to their accessibility.

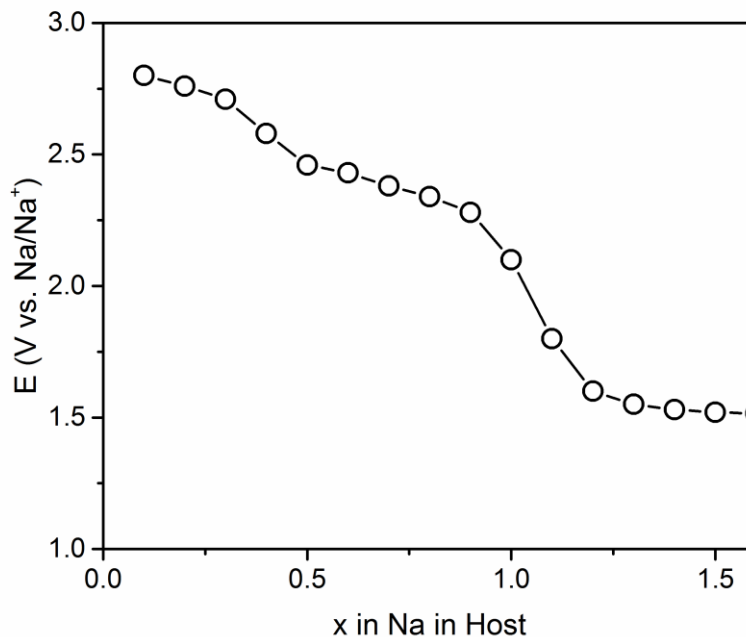


Figure III-8: Coulometric titration of Na insertion in host material. Two solid-state solution type of insertion are followed by a reconstitution reaction of potential values below 1.5 V vs. Na/Na⁺.

Another important insertion mechanism involves occupation of interstitial gap between slabs, made of covalently bonded atoms, in a layered crystal structure. It is usually accepted referring to this process as to *intercalation* and *de-intercalation* in place of insertion and extraction. The intercalation process exclusively involves a two-dimensional diffusion mechanism and that is often referred as *staging*. The order of staging sets the criterion toward which the galleries, namely the spaces between consecutive slabs, are occupied. A second-order staging, for examples, assumes an alternating occupation of the galleries whilst a third-order staging is verified if only one gallery every three is subjected to insertion. While graphite is widely known to be an efficient first-order staged layered material employed in commercial lithium batteries, it undergoes disruption, if not properly expanded¹⁶, when utilized in sodium environment. Belong to this class also transition metal chalcogenides such as TiS₂, originally explored as a viable material for lithium insertion. A peculiar class of layered materials known to be of great importance in sodium rechargeable batteries research, is the one including O2-, O3-, P2-, P3- layered transition metal oxides. Hereafter is reported their theoretical presentation while in the following chapters plenty of examples will be provided. In this class of layered

material, similar to chalcogenide compounds like TiS_2 , edge-sharing MeO_6 octahedra are the constituent unit of the horizontally aligned sheets. Along the vertical c -axis, instead, the recursive stacking of the sheets determines the order of the layered structure (2 or 3), according to the classification proposed by Delmas¹⁷. O and P letters refer instead to how sodium is being accommodated between layers, occupying central positions of octahedrons (O) or prisms (P) (Figure III-9).

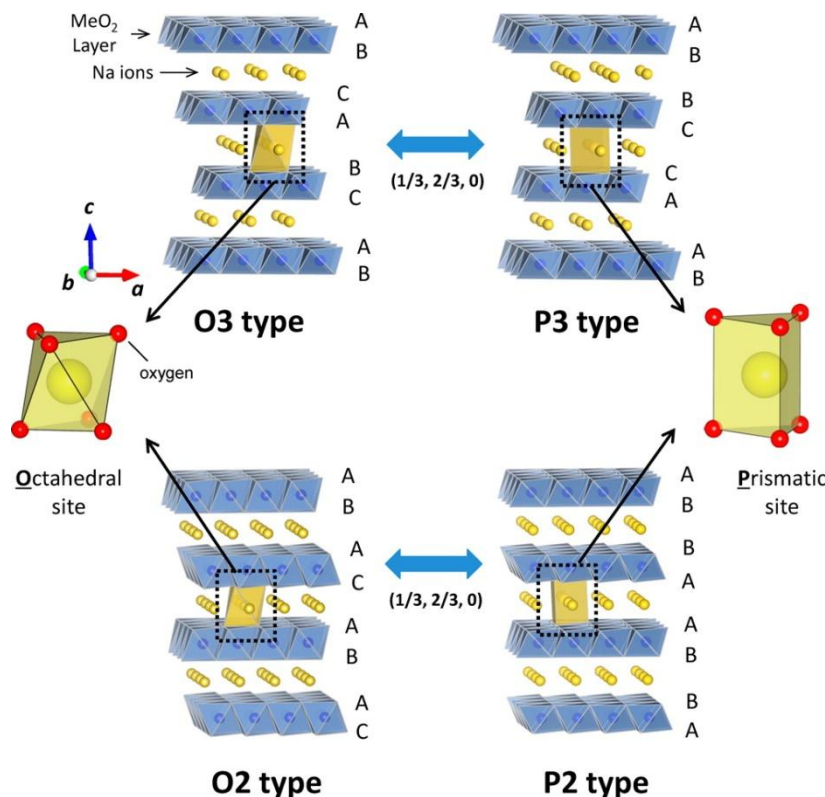


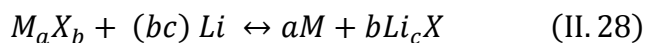
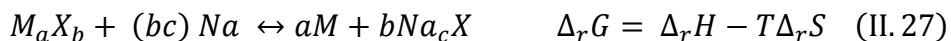
Figure III-9: Sheets of edge-sharing MeO_6 octahedral accommodate in the space in between sodium ions and depending on the geometry of sodium atom environment, O and P structures can be distinguished.

A peculiar characteristic of these type of structures, is the possible interconversion among different layered geometries depending on the stoichiometry of the compound. Sodium extraction, for example, generally induces a phase transition for O3- and P2-type structures into the correspondent P and O counterparts. This is achieved thanks to weaker forces keeping together slabs compared to covalent bonds within them, that allows a certain extent of gliding of Me_2O slabs, leading to the modification of sodium coordination sites from/to prismatic to/from octahedral. Worth to be mentioned is that transition from P3/O3- to P2-type via sodium insertion/extraction is thermodynamically impeded since Me-O bond breaking would be

required and higher energies would be involved¹⁸. It has also been verified via *in-situ* and *ex-situ* XRD analysis how a symmetry reduction connected to a monoclinic distortion is achievable upon deep desodiation due to a sodium vacancies ordering¹⁹. These distorted morphologies, valid for both P3 and O3 configuration, are termed as P'3 and O'3. Layered transition metal oxides just discussed might show potential vs. composition curves that can be erroneously assimilated to reconstitution reactions since layered ions insertion can occur in a stepped fashion at fixed potential values. This happens not only because a two-phase transition occurs due to O-P geometries interconversion, but also because a multiple patterning of a single phase, namely a different planar occupation of available sites, is possible. These materials are often referred to as pseudobinary materials and a clear example in sodium environment is P2-Na_{0.71}CoO₂²⁰. Some other layered oxides are free from any phase rearrangement and pseudo transition process, and can accommodate ions, counterbalancing through a redox couple included in the structure, via a moving-interface insertion reaction showing just one potential plateau in the potential vs. composition curves.

7.3. Conversion reaction

Limits in exploitable capacity of insertion and intercalation materials resides in compounds stoichiometry and material stability in accommodating an excessively high or low amount of ions, crystalline layered structures can in fact collapse after an excessive depletion of inserted ions or disrupt due to the accumulation. Practically, specific capacities higher than 200 mAh·g⁻¹, are hardly achievable especially for anode materials. In recent years investigation of conversion compounds as anode material for sodium in batteries has been knowing a renaissance. Conversion reactions mechanism, studied for the first time in 70s and 80s dealt with high temperature conversion compound such as Fe₂O₃ and FeS₂, but only recently the attention has been directed to room temperature conversion mechanism. Conversion reactions are in general summarized, respectively for sodium and lithium, by the formulas:

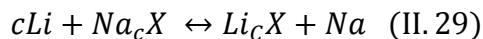


where M_aX_b is usually a chalcogenide, halide or hydride of an electropositive atom, typically a transition metal, and Na_cX and Li_cX is the correspondent chalcogenide, halide or hydride of sodium and lithium, forming as a product of the conversion mechanism. Thanks to the transfer of a considerable amount of electronic charge per mole of reactant, conversion reactions are

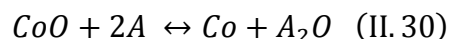
generous for what concern theoretic specific capacities. Co_3O_4 , for example, theoretically would supplies $890 \text{ mAh}\cdot\text{g}(\text{Co}_3\text{O}_4)^{-1}$ if the reaction with sodium leading to completion, namely to Na_2O , is considered. Since this class embraces a large number of inorganic compounds a systematic approach can be used in studying them. Progressive substitution of M and X can be useful to understand effect on single atom on conversions reaction. As a matter of facts, it has been demonstrated that a correlation exists between the ionicity of M-X bond and measured operational potential. Fluorides exhibit the highest potential (3 V vs. Li/Li^+) while oxides, sulfide and phosphides hover around intermediate values (1-2 V vs. Li/Li^+)²¹. Also the transition metal M plays a role in defining the electrochemistry of the whole material. Increasing the atomic number of M, cell voltage tends to grow. Nevertheless conversion materials suffer from non negligible drawbacks such as irreversible capacities, large polarization effects that determines sloping potential vs. composition curves. To this latter characteristic, several intermediate steps also contribute. They occur before the final products are obtained. Irreversible capacity causes, quantifiable in coulombic efficiencies lower than 80 %, have to be researched in progressive fragmentation of the active material due to mechanical stresses build up during the process. These stresses emerge from considerable molar volume discrepancies between reagents and products, and induce cracks and faults in material particles that continuously expose virgin surface to electrolyte solution, determining the formation of new SEI layers. Heterogeneity of final material, made of electronically conductive (metallic particles), and insulating (lithium and sodium chalcogenide or halide) entities, strongly affects stability upon cycling and endangers reversibility of conversion reaction. Has been observed that only if a composite structure consisting of nanometric metallic particles embedded in a likewise Li_cX matrix is formed during the first lithiation cycle, reversibility can be met thanks to the fulfillment of small diffusion distances.

Despite the straightforward thermodynamic treatment of conversion reaction compared to intercalation or insertion processes, theoretic potential values rarely agree with practical ones. If products and reactants Gibbs free energies of formation are usually known, it is not the case for intermediates, amorphous phases and parasitic products not easily detectable. Still, as stated before, they strongly affect electrochemical properties, deviating from normal thermodynamic properties. Nonetheless, calculating thermodynamic data connected to a complete conversion reaction can be useful to get a general idea of the energies and general

properties involved in the process. If thermodynamic data of lithium and sodium conversion reactions are compared, a guideline on which compounds can be classified as positive or negative material can be provided. If eq (1.13) is subtracted from equation (1.14), the net equation is obtained



This means that, interestingly, differences between sodium and lithium in a conversion mechanism, solely depend on X, the nonmetal. If we take CoO as starting material, for example, the related conversion reaction will be



Being A either Na or Li. From standard Gibbs energies, the standard potential is easily obtained according to equation (II.6), and the difference in cell potential between sodium and lithium based conversion reaction can be thus calculated as $\Delta E^\circ_{(\text{Li-Na})} = E^\circ_{(\text{Li})} - E^\circ_{(\text{Na})} = 1.80 - 0.84 = 0.96 \text{ V}$. In Figure III-10 are reported differences in cell potential for other conversion mechanism based on different nonmetal atoms included in the formula. It appears clear how, in the perspective of having anodes material with half cell operational potential as low as possible, some conversion material might be better than other in sodium environment.

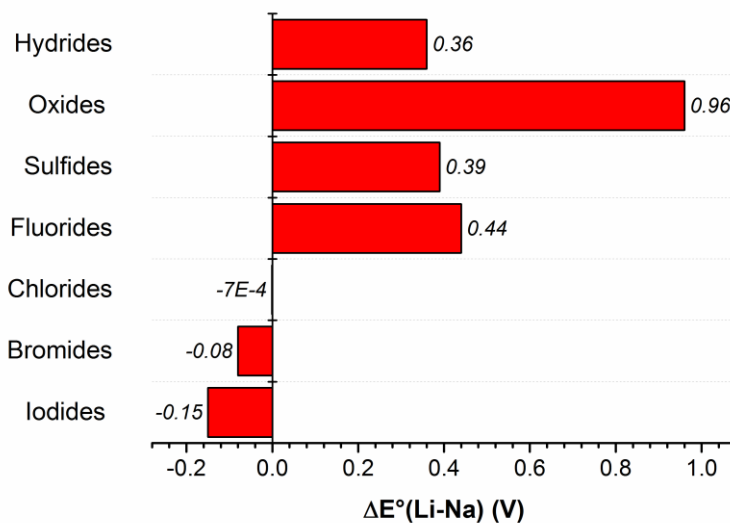


Figure III-10: Calculated differences in cell potential between conversion compounds M_aX_b with sodium and lithium. Positive values mean that replacing lithium with sodium will result in lowering the cell potential by the reported amount, and vice versa for negative values.

Particles volume expansion is a major issue that must be dealt with when conversion reactions are considered. If compared to insertion reaction process, for which volume variation are negligible and seldom higher than 5 %, conversion reactions involve huge dimension variation, since formation of compounds and composite with different molar volumes happens. This leads to 150 % to 250 % volume variation for conversion reaction in sodium environment for oxide-based materials and 400 % for phosphorus-base compounds. In light of this consideration, it appears straightforward how oxides would be theoretically the best choice, as anode conversion material for sodium batteries. This general principle guided us in specifically investigating transition metal oxides in sodium environment thanks to their surpassingly favorable thermodynamic properties compared to other conversion compounds.

7.4. Pseudocapacitive mechanisms as source of capacity

Beyond the just mentioned energy storing mechanisms a relatively simple and handy way of accumulating charge, is by exploiting the capacitive double-layer forming following the adsorption of ions on electronically polarized surfaces in aqueous or non-aqueous environment. Electric double layers capacitors (EDLCs) are being known since the 50s, and thanks to the recent improvements in carbonaceous materials with optimum pores size and high specific surface area, capacities as high as $150 \text{ F}\cdot\text{g}^{-1}$ can be achieved. Commercial EDLCs can store energies from 3 to $6 \text{ Wh}\cdot\text{kg}^{-1}$. Due to the absence of an actual Faradaic process and thus a charge transfer, double layer instauration/depletion is not diffusion limited, leading to a very fast responsivity to high current densities. In 1971 a new type of capacitive behavior was discovered in RuO_2 thin film electrodes²². This process, termed as pseudocapacitance, despite the Faradaic nature of the hydrogen adsorption on the electrode showed cyclic voltammogram typical for a capacitor, *i.e.* rectangular in shape. There are few mechanisms able to originate such an interesting feature, desirable in energy storage devices due to interesting kinetic properties involved: i) under-potential deposition, ii) redox pseudocapacitance and iii) intercalation pseudocapacitance. In the latter case, interesting for the purposes of the present investigation, mandatory features for a pseudo-capacitive behavior to manifest are i) the presence of an active redox species in the electrode material, ii) a good electronic conductivity of the electrode material, iii) a relatively large outer surface area enabling fast diffusion paths and iv) sufficiently large interlayer spacing or channels diameter to accommodate intercalating ions without registering the compound phase change or appreciable volume expansion. As

expected for a pure capacitor, a constant change in potential is registered for pseudocapacitive materials, following the Nernstian relation

$$E \sim E^\circ - \frac{RT}{nF} \ln \left(\frac{X}{1-X} \right) \quad (\text{II. 31})$$

where X embodies the occupancy fraction of intercalation sites in the inner structure. The main utility of these materials for energy storage does not lie in the thermodynamic properties expressed by relation II.31, common to insertion reactions, but mostly in their kinetic properties. Reaction that are limited by the surface, as intercalation on suitable crystalline facets, are not diffusion-limited and thus exhibit high rate capability. The most striking electrochemical difference between a faradic and a capacitive behavior, stems in the evolution of current response at different scan rates (v , $\text{mV}\cdot\text{s}^{-1}$) in cyclic voltammetry analysis. If for a redox reaction currents varies with $v^{1/2}$, for a capacitive process it scales with v only. Thus at every potential along the potential scan, the current appear as linear combination made of two components:

$$i(V) = k_1 v^{1/2} + k_2 v \quad (\text{II. 32})$$

Equation II.32 only states a general dependence and does not pretend to be mathematically exhaustive. To confirm the pseudocapacitive nature of an intercalation process, multiple characterizations and comparison are due in order to dispel any doubt. A first empirical esteem of the capacity contribution carried by a pseudocapacitive process can be derived by extrapolating Q value at infinite diffusion condition in a Q vs. $(1/v^{1/2})$ graph, according to the linear relation

$$Q = Q_{v=\infty} + \text{constant} (v^{1/2}) \quad (\text{II. 33})$$

Other features diagnostic of a pseudocapacitive intercalation are the small hysteresis between cathodic and anodic processes experimented both in CV and galvanostatic cycling. In the former analysis characteristic mirrored broad peaks would appear, and little to no drift will occur at high scan rates, while in the latter, the hysteresis between the charge and discharge profile would be limited to few mV. Since no phase transformation is involved, potential profile will be almost linear, obeying equation II.31 while occasional pseudo-plateaus might appear in presence of patterning or specific sites occupation during intercalation. Since the capacity related to double-layer establishment is in the range $20\text{-}50 \mu\text{F}\cdot\text{cm}^{-2}$, while values between 500

and $1000 \mu\text{F}\cdot\text{cm}^{-2}$ have been registered for faradaic pseudocapacitive processes²³, it is clear how a growing interest towards materials manifesting this kind of behavior has arisen in recent years.

8. Bibliography

- (1) Rahn, C.; Wang, C. *Battery Systems Engineering*; 2012.
- (2) Linden, D.; Reddy, T. B. *HANDBOOK OF BATTERIES*.
- (3) Caroli, S.; Sharma, V. K.; Parsons, R.; Jordan, J.; Dekker, M. ELECTROCHEMICAL SERIES Petr Vany TABLE 1 Alphabetical Listing ELECTROCHEMICAL SERIES (Continued) TABLE 1 Alphabetical Listing (Continued). **2000**.
- (4) Lu, Y.-C.; Shao-Horn, Y. Probing the Reaction Kinetics of the Charge Reactions of Nonaqueous Li-O₂ Batteries. *J. Phys. Chem. Lett.* **2012**, *4*, 93–99.
- (5) Weppner, W.; Huggins, R. A. Thermodynamic Properties of the Intermetallic Systems Lithium- Antimony and Lithium- Bismuth. *J. Electrochem. Soc.* **1978**, *125* (1), 7–14.
- (6) Jung, Y. H.; Lim, C. H.; Kim, J.-H.; Kim, D. K. Na₂FeP₂O₇ as a Positive Electrode Material for Rechargeable Aqueous Sodium-Ion Batteries. *RSC Adv.* **2014**, *4* (19), 9799.
- (7) Kubota, K.; Komaba, S. Review—Practical Issues and Future Perspective for Na-Ion Batteries. *J. Electrochem. Soc.* **2015**, *162* (14), A2538–A2550.
- (8) Ponrouch, A.; Marchante, E.; Courty, M.; Tarascon, J.-M.; Palacín, M. R. In Search of an Optimized Electrolyte for Na-Ion Batteries. *Energy Environ. Sci.* **2012**, *5* (9), 8572.
- (9) Dahbi, M.; Yabuuchi, N.; Kubota, K.; Tokiwa, K.; Komaba, S. Negative Electrodes for Na-Ion Batteries. *Phys. Chem. Chem. Phys.* **2014**.
- (10) Peled, E. The Electrochemical Behavior of Alkali and Alkaline Earth Metals in Nonaqueous Battery Systems—The Solid Electrolyte Interphase Model. *J. Electrochem. Soc.* **1979**, *126* (12), 2047.
- (11) Komaba, S.; Murata, W.; Ishikawa, T.; Yabuuchi, N.; Ozeki, T.; Nakayama, T.; Ogata, A.; Gotoh, K.; Fujiwara, K. Electrochemical Na Insertion and Solid Electrolyte Interphase for Hard-Carbon Electrodes and Application to Na-Ion Batteries. *Adv. Funct. Mater.* **2011**, *21* (20), 3859–3867.
- (12) Munoz-Marquez, M. A.; Zarrabeitia, M.; Castillo-Martínez, E.; Eguía-Barrio, A.; Rojo, T.; Casas-Cabanas, M. Composition and Evolution of the Solid-Electrolyte Interphase in Na₂Ti₃O₇ Electrodes for Na-Ion Batteries: XPS and Auger Parameter Analysis. *ACS Appl. Mater. Interfaces* **2015**, *7* (14), 7801–7808.
- (13) Ming, J.; Ming, H.; Kwak, W.-J.; Shin, C.; Zheng, J.; Sun, Y.-K. The Binder Effect on an Oxide-Based Anode in Lithium and Sodium-Ion Battery Applications: The Fastest Way

- to Ultrahigh Performance. *Chem. Commun. (Camb)*. **2014**, 50 (87), 13307–13310.
- (14) Slater, M. D.; Kim, D.; Lee, E.; Johnson, C. S. Sodium-Ion Batteries. *Adv. Funct. Mater.* **2013**, 23 (8), 947–958.
- (15) Seh, Z. W.; Sun, J.; Sun, Y.; Cui, Y. A Highly Reversible Room-Temperature Sodium Metal Anode. *ACS Cent. Sci.* **2015**, 1 (8), 449–455.
- (16) Wen, Y.; He, K.; Zhu, Y.; Han, F.; Xu, Y.; Matsuda, I.; Ishii, Y.; Cumings, J.; Wang, C. Expanded Graphite as Superior Anode for Sodium-Ion Batteries. *Nat. Commun.* **2014**, 5 (May), 4033.
- (17) Delmas, C.; Fouassier, C.; Hagemuller, P. Structural Classification and Properties of the Layered Oxides. *Phys. B+C* **1980**, 99 (1–4), 81–85.
- (18) Yabuuchi, N.; Kubota, K.; Dahbi, M.; Komaba, S. Research Development on Sodium-Ion Batteries. *Chaical Rev.* **2014**.
- (19) Delmas, C.; Braconnier, J.-J.; Fouassier, C.; HAGENMULLER, P. Electrochemical Intercalation of Sodium in Na_xCoO_2 Bronzes. *Solid State Ionics* **1981**, 3/4, 165–169.
- (20) D’Arienzo, M.; Ruffo, R.; Scotti, R.; Morazzoni, F.; Mari, C. M.; Polizzi, S. Layered $\text{Na}(0.71)\text{CoO}(2)$: A Powerful Candidate for Viable and High Performance Na-Batteries. *Phys. Chem. Chem. Phys.* **2012**, 14 (17), 5945–5952.
- (21) Klein, F.; Jache, B.; Bhide, A.; Adelhelm, P. Conversion Reactions for Sodium-Ion Batteries. *Phys. Chem. Chem. Phys.* **2013**, 15 (38), 15876–15887.
- (22) Trasatti, S.; Buzzanca, G. Ruthenium Dioxide: A New Interesting Electrode Material. Solid State Structure and Electrochemical Behaviour. *J. Electroanal. Chem. Interfacial Electrochem.* **1971**, 29 (2), A1–A5.
- (23) Conway, B. E. E.; Birss, V.; Wojtowicz, J. The Role and Utilization of Pseudocapacitance for Energy Storage by Supercapacitors. *J. Power Sources* **1997**, 66 (1–2), 1–14.

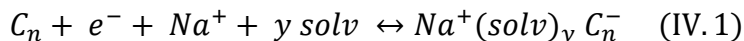
CHAPTER IV: SIBs anode materials review

1. Introduction

Research about anode material of a sodium-ion cell has recently drawn the attention of the scientific community. Despite this, a net numerical discrepancy between published works on cathode material and anode ones has been registered in favor of the former. Among the difficulties experienced by people approaching the negative side topic worth to be mentioned are the operational potential of the material in a sodium environment, often too high to guarantee an appreciable energy density, overall stability and frequent disruption of the material throughout cycling and low Coulombic efficiencies. A worldwide accepted criterion in investigating this type of species has been so far, mimicking the modern research trend in Lithium-ion battery research, the proposal of negative material with exceptionally high gravimetric capacities, well above the average values of modern commercial LIBs ($\sim 300 \text{ mAh} \cdot \text{g}^{-1}$). This approach, albeit source of extraordinary results often limited to first cycles, is short-sighted towards a possible coupling with a cathode material, in a full cell assembly. It must be in fact considered that nowadays research on cathode materials for SIBs, and it will become clear in following chapters, is limited to insertion compounds with gravimetric capacities limited to only few hundreds of $\text{mAh} \cdot \text{g}^{-1}$. Managing materials quantity balance inside the cell and thicknesses of active depositions will then become a critical aspect when a commercial SIB commercial prototype will be put under study. Investigation about the latter topic is behind the scope of the present dissertation. Throughout the years many materials belonging to different classes and based on as much chemistries have been proposed; seeking completeness and clarity, in this chapter the most recent advancements in research around negative materials for sodium batteries will be discussed. The overwhelming number of compounds proposed will be, to facilitate navigation, organized in four categories, namely i) carbonaceous materials, ii) oxides based on conversion reaction, iii) p-block elements (metals, alloys and phosphorous) showing reversible sodiation/de-sodiation reaction and iv) oxides as Na-insertion topotactic materials.

2. Carbon-based Materials

Carbonaceous materials were the most immediate and trivial answers to the need of an anode material for sodium ion batteries. Many aspects can be listed among motivations beyond this, such as lithium-ion batteries heritage connected to graphite, low costs, environmental friendliness and electrochemical stability. Most likely, studies of graphite-based anode material intercalating sodium started together with those about lithium and potassium, which confirmed their reversibly intercalation forming LiC_6 and KC_8 graphite intercalation compound (GIC) respectively. Despite Na having a ionic radius ($\sim 1.05 \text{ \AA}$) situated in the middle between that of Li ($\sim 0.76 \text{ \AA}$) and K ($\sim 1.5 \text{ \AA}$), and thus a higher chance to trigger staging into layered material, (see Chapter III7.2 for staging process description) only $12 \text{ mAh}\cdot\text{g}^{-1}$ are delivered by its insertion. Stage 1 Na-GIC formation has been demonstrated to be thermodynamically unfavorable, due to excessively high sodium redox potential differently from LiC_6 and KC_8 that make the sodium plating upon graphite, rather than its intercalation into it, more likely¹. Other factors that might underlie the failing stage 1 insertion are the large elongation of C-C bond length and the scarce binding energy between carbon and sodium atoms. Recently has been demonstrated how expanding along c axis the single layers stacking of graphite, is possible to achieve reversible capacities hovering around $284 \text{ mAh}\cdot\text{g}^{-1}$ at $20 \text{ mA}\cdot\text{g}^{-1}$, with the superior capacity retention of 73 % after 2000 cycles if cycled at $100 \text{ mA}\cdot\text{g}^{-1}$. In Wen's work, indeed, the importance of maintaining a long-range vertical ordering is stressed, and moreover, concentration of oxidized carbon sites, namely surface oxygen concentration, is considered a fundamental aspect². Jache et al. claimed that also the electrolyte solution plays a relevant role in allowing sodium intercalation, and they have been able to obtain a reversible insertion of sodium ions using an diglyme-based electrolyte solution³. In their work the co-intercalation of solvent molecules chelating sodium ions, according to the reported equation, is emphasized.



Low potential intercalation occurs, in this case, with a modest overpotential and extending for circa $100 \text{ mAh}\cdot\text{g}^{-1}$. Structural XRD analysis confirm graphite layers expansion along c axis, leading to a total volume expansion of 15 %. Theoretical study hypothesized a ether co-intercalation of 1-2 molecules of diglyme considering that alkaline atoms a preferentially coordinated by six oxygen atoms⁴.

As the utilization of pure graphite has been discouraged, other carbonaceous material, like hard-carbon, soft-carbon and amorphous carbon started being extensively investigated as alternatives. In this section a brief introduction to major advancement brought to carbon-based anode material is provided. A large number of non-graphitic carbons has demonstrated to reversibly interact with sodium with mechanisms other than pure intercalation. This class of material includes partially crystalline hard carbons and soft carbons. These two materials differ not only for the synthetic methods and precursors involved but also upon crystalline structure and stability to thermal treatments. If Hard carbons are defined as nongraphitic non-graphitizable carbons and are obtained from solid-phase pyrolysis of phenol-formaldehyde resins, cellulose, charcoal, coconut and sugar⁵, Soft carbons, termed as nongraphitic graphitizable, are obtained from liquid or gas-phase pyrolysis. In contrast with the apparently beneficial thermal end chemical stability of hard carbons, there is the inter-layer spacing tunability, upon appropriate heat treatment, of soft carbons. As thoroughly reported by Lou, increasing heat treatment temperature for soft carbon, induces a denser stacking of graphitic layers, as confirmed by shift towards higher angles of (002) XRD diffraction peak⁶. Nevertheless, compared to reversible capacity extracted from hard carbons, soft carbons deliver lower capacities ($\sim 120 \text{ mAh}\cdot\text{g}^{-1}$ at $20 \text{ mA}\cdot\text{g}^{-1}$) at slightly higher potential (0.6 V vs Na/Na⁺). As previously quoted, for nongraphitic carbon and hard carbon in particular, multiple processes contribute to sodium storage and they are inevitably connected to carbon microstructure. Hard carbons show the higher heterogeneity in structure, namely micrometric-size graphitic domains (image b) in Figure IV-1) whose long-range continuity is interrupted by randomly arranged single and few-layer graphene sheets as well as amorphous areas. This casual arrangement, intuitively simplified by depicting it as a “falling cards model”, confers a porous structure whose degree depends on pyrolysis conditions such as temperature and gas fluxes. As an explicative case, using sugar as carbon precursor, a step decrease in micropore surface has been observed if pyrolysis temperature is raised from 900 to 1000 °C, while a smoother decrease occurs above 1200 °C. The surface area changes accordingly from hundreds to $<10 \text{ m}^2\cdot\text{g}^{-1}$ if pyrolysis takes place above 1000 °C due to micropores closure⁷. Worth to be noted is that porosity and surface area extension can be also tuned by precursor pre-treatments as well as by post-pyrolysis heat treatment in particular flowing atmospheres⁸. Analyzing in more details the involved mechanisms in sodium uptake, two main processes are found to be responsible for the

majority of the stored capacity. They can be easily spotted by looking at a potential vs. capacity curves of a galvanostatic cyclation, and consist in a sloping potential region extending to ca 0.2 V and a low potential plateau that gently glides towards 0.0 V vs. Na/Na⁺ (Figure IV-1). The former of the two is widely recognized to be due to alkaline ion insertion between layers in pseudo-graphitic domains. These process is not limited and does not coincides with a single potential plateau, as in the case of lithium insertion into graphite, since the pseudo-graphitic domains disorder produces sites with different chemical environments and thus different insertion energies. The process occurring at lower potentials is instead related to ions adsorption in micropores as well depicted by recent DFT calculation⁹. These two processes, also active for lithium, can be practically monitored by *ex situ* XRD and SAXS analysis. During the first step an expansion of the interlayer distance between graphene sheets from 3.8 Å to ca. 4.15 Å can be detected, while in connection with the second step, a reduction of the scattering intensity around 0.03-0.07 Å⁻¹ in the SAXS spectra well agrees with the filling of micropores via adsorption mechanism¹⁰. A common drawback shared, in different extents, by nearly all hard carbons investigated as anode for sodium batteries, is the non negligible irreversible capacity correlated with the first sodiation. This is mostly due to SEI formation and only partially to irreversible sodium trapping inside carbon structure. In general massive capacity losses related to first cycle, are deleterious and highly energetically problematic since they creates a mismatch between anode and cathode in relation to available sodium cyclation inside the whole cell. An excess of the positive material would not effectively overcome this problem since the exact amount of irreversibly reacted sodium is can't be precisely predicted and an excess of negative material would be as well required in order to avoid sodium plating and thus dangerous consequences upon overcharge or low temperature operation. Irreversible capacity is unfortunately a common feature for anode materials, and the highest coulombic efficiency upon the first cycle reported to date is 85 % for hard carbon samples with low surface BET area (<10 m²·g⁻¹). A detailed review of carbon materials, so far the most cost effective and easy to synthesize candidates, as suitable anode for SIBs has been recently provided by Muhammad-Sadeeq¹¹. Since, as stated in Chapter III, details referred to electrolyte formulation, additives and solvents are not the focus of this research, the attention will be directed prevalently to structural and morphological parameter influencing electrochemical performances. Together with concentration of surface functional groups, surface area extension has been demonstrated

to be a crucial parameter in defining the SEI layer formation and thus irreversible capacity build up, and a direct linear relation between BET specific surface and irreversible capacity is often observed. Some studies conducted with lithium suggested that more than the surface BET accessible to electrolyte, a more indicative parameter of the surface reactivity with alkaline atoms and salts would be the active surface area (ASA), determined via oxygen chemisorptions to form oxygenated complexes that can be further quantified by mass spectroscopy during outgassing¹². Direct truthfulness of this aspect for SIBs has still to be confirmed. Anyway, as a general rule of thumb, low surface specific area hard carbons have to be preferred to higher area ones in consuming less material during SEI formation. Since SEI layer composition strongly depends on sodium salt and solvent employed in electrolyte formulation, many efforts have been addressed to find an optimum composition. Komaba and co-workers successfully achieved a stable capacity of $230 \text{ mAh}\cdot\text{g}^{-1}$ for more than 100 cycles with 1 M NaClO_4 in PC or EC:DEC based electrolytes¹⁰. Many aspects acquire significance when the quality of the SEI layer has to be evaluated. Among them the most relevant are its composition either organic or inorganic, its stability and permeability to ions. It is widely recognized, for example, that EC is beneficial to the formation of a stable SEI as well as DMC contributes in lowering viscosity and thus ionic conductivity still keeping electrode polarization low allowing to access to the full capacity at low potential plateau. Under a structural point of view, a progressive reduction in reversible capacity connected to Na^+ insertion in HC graphene layers is observed if the layers spacing is reduced upon increased pyrolysis temperature¹³. In other words, by increasing heat treatment temperature, an ordering process is induced and eventually a more graphitic structure is obtained as showed by I_D/I_G bands intensity Raman spectra (image c) in Figure IV-1).

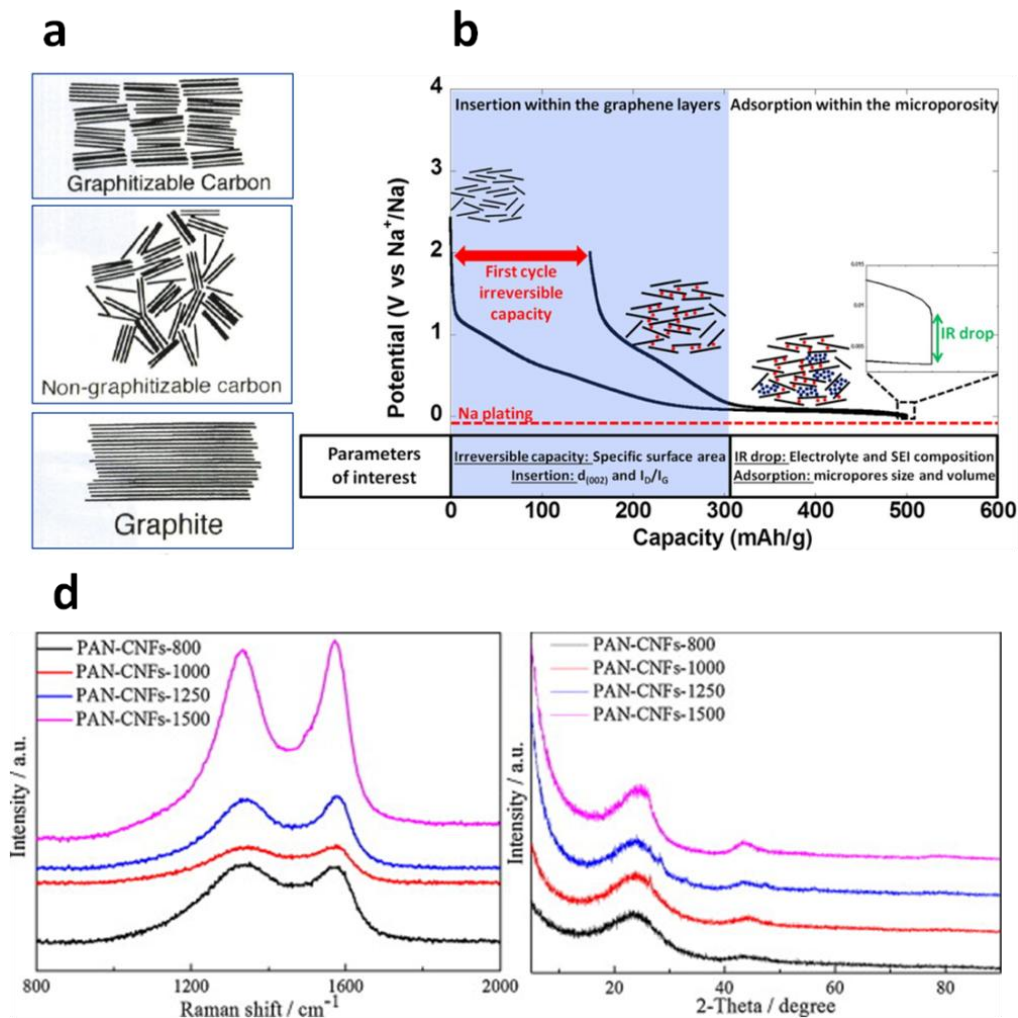
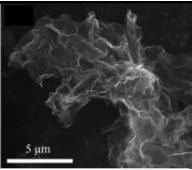
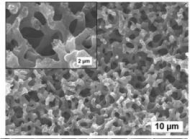
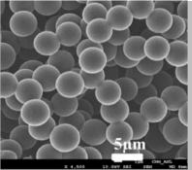
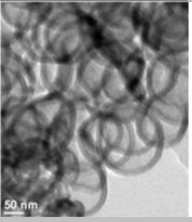
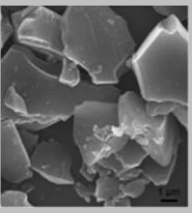
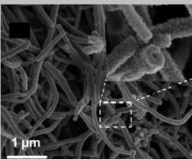
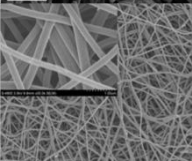


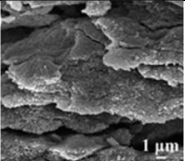
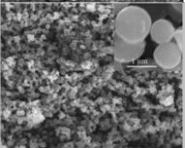
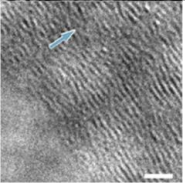
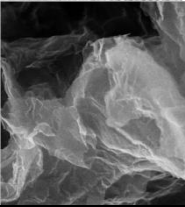
Figure IV-1: a) Cartoons depicting different types of carbonaceous material according to their microstructure; hard carbon non-graphitizable carbons, in the “falling cards” model possesses a hierarchical structure in which insertion domain and adsorption micro- and meso-porous sites are both present; b) the two mechanism of sodium storage occurring in a hard-carbon structure; d) evolution of Raman (left) and XRD (right) signals for a hard-carbon obtained from PAN pyrolyzed at different temperatures.

This latter has been recognized as a further diagnostic parameter of the ordering level of carbon structure, being D-band and G-band in Raman spectra a defect-induced and E_{2g} graphitic induced modes respectively. Typical I_D/I_G values range from 1.05 to 0.94 as the heat treatment temperature is increased from 800 to 1500 °C. On the other hand, reversible capacity associated to low potential plateau, and thus to sodium adsorption in micropores was found to increase with temperature. This means that, even if micropores close as the temperature is raised, they are still accessible for Na^+ adsorption and the only parameter controlling low potential capacity

if the average pore size. Thanks to the comprehensive work by Muhammad-Sadeeq as well as characterization of carbon samples in our laboratory, a direct correlation between carbon particles morphology and structure and electrochemical performances has been highlighted and the most relevant findings are collected in the table below.

Table IV-1: Carbon-based material morphologies so far investigated as anodes for SIBs; for each sample the main electrochemical and physical features are reported.

Electrode	Precursor and Synthesis	Morphology	Pyrolysis conditions	I_D/I_G or type of carbon	SSA_{BET}	CE (1 st cycle)	Reversible Capacity
N-doped carbon sheet	Dopamine		800 °C, 2 h	0.93	76 m ² ·g ⁻¹ , mesoporous	26.4 %	165 mAh·g ⁻¹ at 200 mA·g ⁻¹
Template carbon¹⁴	Mesophase-pitch infiltrated silica monoliths		700 °C	Mostly non-graphitic	346 m ² ·g ⁻¹ meso- and macroporous	~ 17 %	110 mAh·g ⁻¹ at 372 mA·g ⁻¹ decreasing
Nanospheres¹⁵	Controlled thermal decomposition of mesitylene		700 °C, 5 min	1.1	4 m ² ·g ⁻¹ mesoporous	~ 60 %	92 mAh·g ⁻¹ at 150 mA·g ⁻¹ stable
Hollow Nanospheres¹⁶	Glucose carbonization on latex templating spheres		1000 °C	Weakly ordered turbostratic carbon structuring	410 m ² ·g ⁻¹ microporous	41.53 %	150 mAh·g ⁻¹ at 100 mA·g ⁻¹ stable
Highly disordered carbon¹⁷	Self-assembling of polyelectrolytes (PDDA and PSA) in water		800 °C, 2h	< 1.0	2.5 m ² ·g ⁻¹ macroporous	57.61 %	225 mAh·g ⁻¹ at 100 mA·g ⁻¹ after 180 cycles
Hollow Nanowires¹⁸	Pyrolysis of hollow polyaniline		1150 °C, 6h	Disordered graphite nanocrustallites		50.5 %	206 mAh·g ⁻¹ at 50 mA·g ⁻¹ after 400 cycles
Electrospun Nanofiber^{13,19}	Electrospun PAN fiber		1250 °C N ₂ 30 min	0.97	14.6 m ² ·g ⁻¹ mesoporous	72.0 %	271 mAh·g ⁻¹ at 100 mA·g ⁻¹ stable after 100 cycles

H₃PO₄-activated porous carbon²⁰	Pyrolysis of H ₃ PO ₄ treated pomelo peels		700 °C, 2h N ₂ flow	>1.0	1272 m ² ·g ⁻¹ mesoporous	27 %	181 mAh·g ⁻¹ at 50 mA·g ⁻¹ after 200 cycles
Microspheres²¹	Sucrose microwave-assisted reaction		500 °C, 2h	Disordered carbon material	393.1 m ² ·g ⁻¹ microporous	~ 40 %	183 mAh·g ⁻¹ at 30 mA·g ⁻¹ after 50 cycles
Expanded graphite²	Modified Hummer's method		600 °C 1h Ar	Graphitic		49.5 %	280 mAh·g ⁻¹ at 100 mA·g ⁻¹ after 2000 cycles
Reduced graphene oxide^c	Modified Hummer's method ²²		1000 °C 4h Ar	>1.0	509.3 m ² ·g ⁻¹ macroporous	~ 11 %	110 mAh·g ⁻¹ at 50 mA·g ⁻¹ after 50 cycles

3. Conversion Oxide Materials

As thoroughly discussed in Chapter III:7.3, conversion transition metal oxides are materials worth of interest as anode for SIBs due to their high theoretical specific capacity (~900 mAh·g⁻¹). They are also thermodynamically favored among other transition metal halides and chalcogenides thanks to the surpassingly advantageous potential gain in sodium environment if compared with lithium. Considering a full conversion reaction leading to metallic transition metal and sodium oxide, the theoretical specific capacity increases with the starting oxidation state of the transition metal (715 mAh·g⁻¹ for CoO where Co^{II} and 891 mAh·g⁻¹ for Co₃O₄ where Co^{III}) and decreases with its atomic number. One of the major challenge that conversion oxides material bare with themselves is the important volume expansion occurring during conversion mechanism. It accounts for a 150-250 % volume change for oxides and is second only to transition metal phosphide for which it can reach the extraordinary value of 400 %. The induced structural strain connected to expansion and contraction is thus considerable especially at the interface between metal and Na₂O, due to lattice mismatch. Using material engineering, many solutions have been proposed in order to minimize this drawback and endless efforts have been addressed to investigating mechanism in

^c Electrochemically characterized in our laboratories and structurally characterized by University of Cosenza, Italy.

order to provide a more detailed analysis of the tricky conversion process. A list of the most emblematic conversion oxides investigated as anode for SIBs is provided below, together with an in-depth discussion of their mechanisms and chemistries.

Iron oxide, in its multiple crystalline phases, represents a well investigated conversion material for both lithium and sodium batteries. Hematite Fe_2O_3 as well as Magnetite Fe_3O_4 have been taken into consideration and their conversion reactivity has been widely characterized. Hariharan and co-workers²³ proposed a material design approach in trying to curb material active disruption induced by mechanical stresses upon cycling. In A one-pot hydrothermal synthesis they have been able to synthesize nanometric Fe_3O_4 particles embedded in a carbon matrix, the latter expected to take upon itself the sluggish electronic conduction of magnetite and provide a mechanical reinforcement capable of withstanding volume expansion stresses. Despite the promising first sodiation specific capacity of $643 \text{ mAh}\cdot\text{g}^{-1}$, a fast decay within the following ten cycle, symptom of progressive material degeneration, is observed. SAED patterns of de-sodiated (charged) electrodes were selectively used to study the reaction path. Traces of metallic Fe and crystalline Na_2O have been observed as a clear footprint of an incomplete oxidation to Fe_3O_4 during Na removal. Magnetite Fe_3O_4 phase diffraction rings are however present, and no intermediate iron oxide phases have been spotted. Even though a thorough description of the dynamic evolution of phases upon sodiation and de-sodiation is still lacking, the general conversion mechanism is widely accepted as the main occurring process for iron oxide. Recently a $\text{Fe}_2\text{O}_3@\text{GNS}$ (graphene nano-sheets) composite has been proposed²⁴ as a viable solution to two of the major issues pestering iron oxides, namely the i) sluggish kinetic properties due to low electronic conductivity and ii) limits to sodium intercalation due to a 55 % excess of sodium ionic radius if compared to lithium. The gravimetric GNS content achieved via simple nanocasting technology was considerable and quantified, by TGA, to be around 37.4 % and thus no supporting carbon matrix has been added in electrode preparation. Despite the conspicuous irreversible capacity registered during the first cycle ($\sim 50 \%$), possibly connected to the high content of a carbonaceous matrix, electrochemical performances are quite impressive and result in a stable specific capacity of nearly $400 \text{ mAh}\cdot\text{g}^{-1}$ obtained at $100 \text{ mA}\cdot\text{g}^{-1}$ and maintained for more than 200 cycles. The operational potential is 0.75 V vs. Na/Na^+ , an interesting value for an anode material able to guarantee a satisfactorily energy density. Graphene oxide is often suggested as a submissive element to improve both capacity and

kinetic properties of conversion transition metal oxides, and frequently in modest gravimetric amount²⁵. Among its exploited positive features can be enumerated the excellent electronic properties, interesting mechanical properties in accommodating volume changes and providing a uniform substrate for an evenly distribution of electrochemically active particles. Worth to be noted is the necessity of nanocasting or hydrothermal methods are required in order to achieve an intimate connection between graphene oxide sheets and particles and that a simple mechanical mixing won't suffice. Nevertheless this approach does not allow to accurately distinguish the capacity directly deriving from conversion mechanisms from that related to carbon based additive which can be notable, as previously illustrated. A significantly different material design has been proposed by Yang in investigating spinel Co_3O_4 conversion material²⁶. A highly ordered 3D porous structure has been obtained by a nanocasting synthesis using nanoporous silica (KIT-6) as a templating agent. A detailed XRD *ex-situ* analysis is provided (Figure IV-2) in order to monitor phase transformation during sodiation and de-sodiation.

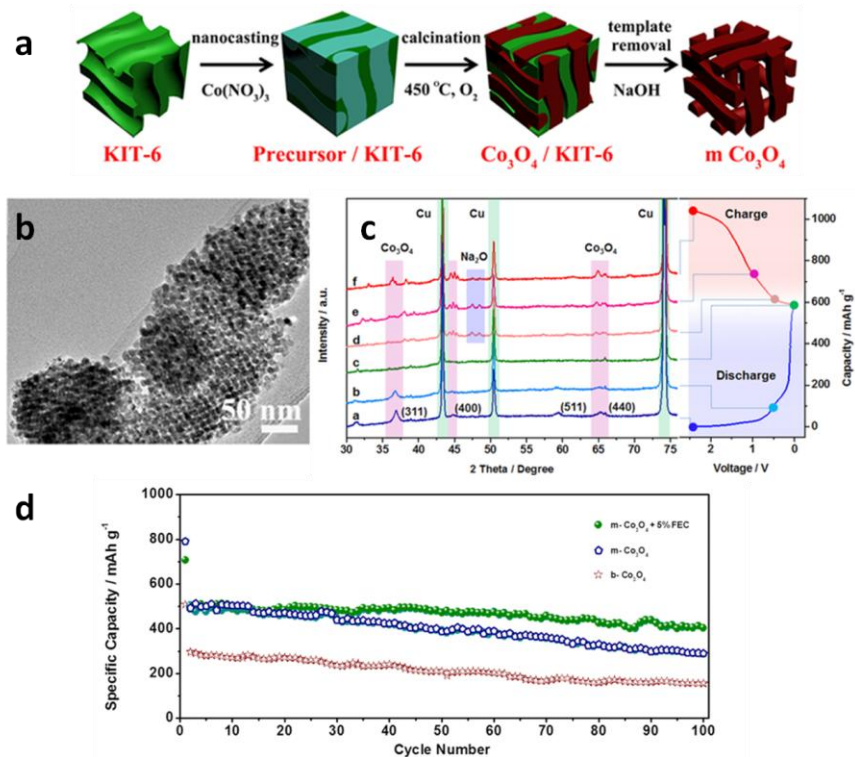


Figure IV-2: a) synthetic approach proposed by Yang and co-workers based on a template or nanocasting method for the preparation of a porous 3D-structured Co_3O_4 ; b) TEM image of the nanocasted structure in which the ordered patterning made by voids is visible; c) *ex-situ* XRD studies conducted on $m\text{-Co}_3\text{O}_4$ sample in order to monitor phases evolution during charge and discharge of the material; d) galvanostatic performances of the prepared materials.

All the diffraction peaks indexed to Co_3O_4 spinel phase progressively disappear as potential reaches the first sodiation low potential values pseudo plateau. Only when a further downward bending of potential curve occurs, close to 0.0 vs Na/Na^+ , Na_2O peaks appear in the diffractogram. Co_3O_4 is partially recovered upon de-sodiation. Impurities formation or other Co_xO_y phases evolution cannot be excluded since weaker diffraction peak can be clearly distinguished at the end of the first cycle. Added to this the extension of the mechanism as just described to the following cycle, would be a too strong abstraction since a distinct modification of charge/discharge profile occurs after the very first cycle. Under the electrochemical performances point of view, nanoporous Co_3O_4 shows upon long cycling a surpassing specific capacity of nearly $500 \text{ mAh}\cdot\text{g}^{-1}$, if compared to bulk Co_3O_4 particles. Practical specific capacity is considerably lower than the theoretical value ($891 \text{ mAh}\cdot\text{g}^{-1}$) but still an interesting value if compared to carbonaceous anode materials. The almost halving of the theoretical value has to be attributed to high irreversible capacity involved in first cycle as well as to the large size and thus poor mobility of Na^+ inside the oxide lattice. In comparison Li, giving a pure conversion mechanism with Co_3O_4 , is a lot more performing giving capacity closer or higher to $800 \text{ mAh}\cdot\text{g}^{-1}$ at $1 \text{ C}^{27,28}$. Other solution have been proposed to accommodate electrode expansion such as homogeneous dispersion of cobalt oxide particles on graphene oxides sheets using a wet method²⁹ as well as on a carbon nanotubes network via pulsed plasma technique³⁰. In the latter case *ex-situ* SAED analysis taken after the tenth charge to 0.01 V vs Na/Na^+ revealed how only Na_2O and metallic Co are present, symptom of a complete conversion reaction. On the other hand, after each discharge back to 3.0 V only one components is identified, whose SAED pattern well matches with crystallographic parameters of Co_3O_4 . These results seem to be backed up by TEM and *ex situ* XRD analysis of cycled electrodes. As will be plentifully discussed in the following chapter, throughout the experimental activity of the present study, nanostructured spinel Co_3O_4 will be taken as a case study in trying to better define the occurring mechanism taking place during the very first sodiation process and following cycles.

Same way as iron oxide, tin oxides, SnO and SnO_2 , have been also proposed as safer anodes for SIBs instead of cobalt-based compounds. Flower-like SnO particles and nanometric sized SnO_2 (carbon coated) particles have been hydrothermally synthesized by Lu and co-

workers, and their electrochemical properties in sodium environment thoroughly tested in the potential window with different sodiation cut-off values³¹.

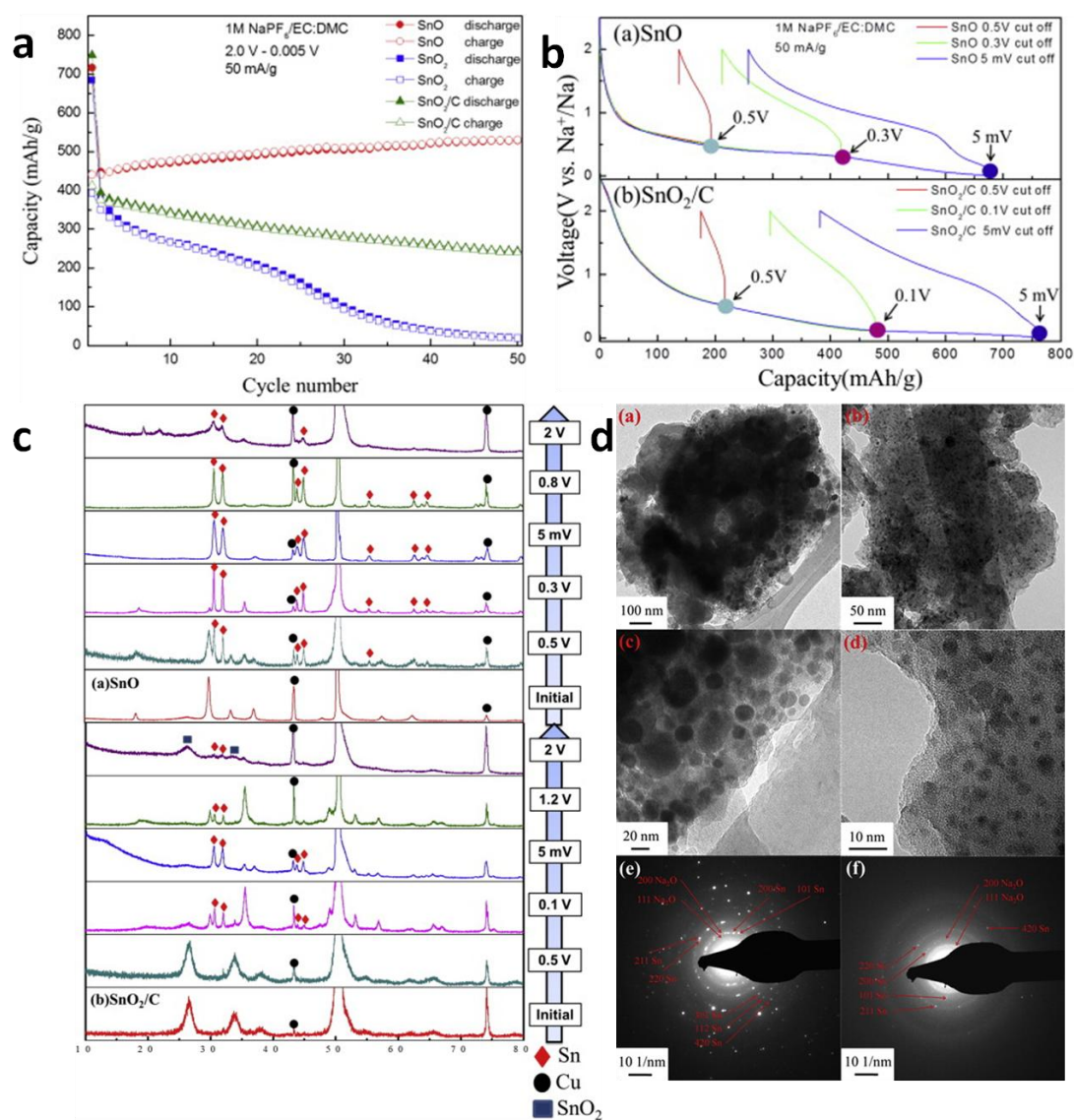
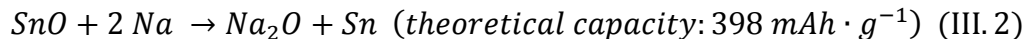


Figure IV-3: a) galvanostatic analysis result for SnO, SnO₂ and SnO₂/C from the work by Lu and co-workers; b) sodiation/de-sodiation curves for the above introduced samples using different sodiation cut-off potential values; c) XRD pattern evolution through cycling for SnO and SnO₂/C; d) TEM and SAED patterns for SnO₂/C particles before (a-c-e) and after (b-d-f) sodiation.

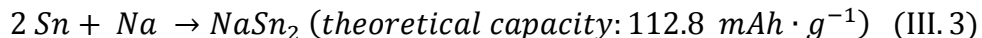
Surprisingly SnO particles show, at a first galvanostatic screening analysis, the best electrochemical behavior, guaranteeing a stable specific capacity of 530 mAh·g⁻¹ after 50 cycles. On the other hand a decreasing trend is obtained from carbon coated SnO₂, with a capacity retention of 58 % after 50 cycles. From galvanostatic cycling tests adopting different

sodiation cut-off potentials (0.3 and 0.05 V vs Na/Na⁺) progressively increasing Coulombic efficiencies, 49.4 % to 61.7 % for SnO and 38.5 to 52.5 % for SnO₂/C, are recorded (image b) in Figure IV-3). The even lower Coulombic efficiencies recorder for a higher cut-off (0.5 V) has to be than related to irreversible SEI formation mechanisms taking place at relatively higher potentials during the first sodiation, as observed for other oxide materials. By following reaction mechanism using *ex-situ* XRD analysis (image c) in Figure IV-3), metallic Sn phase starts being detected from 0.5 V for SnO and is not fully re-oxidized when electrode potential jumps back to 2.0 V. It is worth noting that by looking at SAED patterns, SnO₂ rather SnO is spotted when the electrode is desodiated, this is presumably due to the higher thermodynamic stability of SnO₂ phase compared to SnO. If this would be completely true, relative performances of the two materials, in term of charge/discharge profiles and specific capacities, should tend to uniform upon cycling resulting in an overlap. The discrepancies in material morphologies, which are remarkable, must thus have a role. In the case of SnO, theoretical specific capacity of 2 Na·mol⁻¹ conversion reaction of SnO is 398 mAh·g⁻¹, nearly half of the capacity extracted during first sodiation (720 mAh·g⁻¹). Authors claimed that this is a demonstration of the reaction mechanism occurring for 55 % via conversion reaction and for 45 % through the alloying reaction of sodium in metallic Sn. Added to this a lower reversibility in the reaction region is also called since Coulombic efficiencies are low for high cut-off potentials. The theoretical conversion capacity for SnO₂ is instead considerably higher (711 mAh·g⁻¹) and therefore in compliance with the practical capacity value extracted from first sodiation. The conversion/alloying balance for SnO₂ has been thus calculated to be 95/5. Having the conversion mechanism, affected by a large irreversibility, a major role in contributing to capacity harvesting, SnO₂ performances progressively degrade. The authors then concluded that the outstanding SnO energy storage capabilities must be attributed to various degree of alloying reactions in the sodiation. Partial re-oxidation of metallic Sn finds also a countercheck in the work by Su³², where tetragonal metallic Sn is detected when the electrode is discharged to 3.0 V. Contrary to what Lu and co-workers reported, here SnO is not entirely converted to SnO₂ upon following oxidations, on the other hand, SnO is restored with a change in its crystallographic phase that passes from a tetragonal symmetry to an orthorhombic one. Despite the widespread disagreements still present in literature concerning the reversible mechanism involved in SnO energy storage, two main processes can be undoubtedly cited: the

complete conversion reaction leading to metallic Sn, possibly (but not completely excluded) bypassing a potential sodium intercalation in SnO structure according to the equation



and sodium alloying in Sn at low potentials leading to NaSn₂, as elucidated by more accurate XRD analysis



The total amount of theoretical specific charge would thus amount to 511 mAh·g⁻¹, that well agrees with experimental reversible capacity values (403 mAh·g⁻¹ at 20 mA·g⁻¹). Formation of a Na_xSn phase has been also recently confirmed by theoretical calculation by Wang et al³³. Sodium alloying in pure element will be extensively described in following paragraphs.

4. Binary Na-Me compounds

4.1. Alloying materials

Vast computational efforts have been recently dedicated to predicting electrode potentials and stoichiometries for binary Na-Me intermetallic compounds formed with Group 14 (Si, Ge, Sn and Pb) and Group 15 (P, As, Sb and Bi) metallic and non-metallic elements. Differently from intercalation compounds, for which sodium uptake is limited by constraint induced by rigid frameworks, usually metals and metalloids can withstand multiple sodium atoms per single atom, resulting in capacities ranging from 300 to 2000 mAh·g⁻¹ with operational voltages sufficiently low (below 1.0 V vs. Na/Na⁺) to be appealing for usage on SIBs anode side. Table IV-2 summarized the experimentally or theoretically investigated intermetallic or intermetalloids compounds with sodium. As already highlighted for conversion material, the uptake of more than a sodium atom has dramatic consequences on structural stability of the host material. If this aspect is mild for lithium compounds, it is overwhelmingly severe for sodium, due to the larger ionic radius, and leads to irreparable consequences if not properly addressed.

Table IV-2: Na-alloying elements belonging to p-group of periodic table with their electrochemical properties

	Sodiation product	Theoretical capacity (mAh·g⁻¹)	Volume expansion (Na_xX/X) (%)	Average voltage (vs Na/Na⁺) (V)
Si	Na _{0.76} Si	725	11434	~0.234
Ge	NaGe	369	20534	~0.536
	Na _{1.56} Ge ₃₅	552	300	
Sn	Na _{3.75} Sn	847	42037	~0.238
Pb	Na _{3.75} Pb	482	~40039	~0.340
P	Na ₃ P	2596	408 (red)	~0.4
			~500 (black)	
Sb	Na ₃ Sb	660	393	~0.641
Bi				

Contrarily to lithium, for which silicon is representing a true game changer for what concern achievable energy densities⁴²⁻⁴⁴, sodium does not form intermetallic compounds being the formation of the amorphous compound Na_xSi energetically unlikely starting from crystalline silicon^{34,45}. Nevertheless recent theoretical atomic-level assessment³⁴ revealed how pure amorphous silicon would allow the uptake of 0.76 Na per Si atom guaranteeing capacity of 725 mAh·g⁻¹ comparable with other Group 14 elements. Such interesting property is supposed to derive from the relatively strong ionic bond between Si and Na atoms, connected to a modest decrease in Na charge state with x increase, before clustering of Na in Si bulk phase leading to neutral Na atoms. A very recent work aimed at finding an experimental confirmation failed at obtaining the forecasted theoretical capacities, and only a stable capacity of almost 150 mAh·g⁻¹ has been achieved at 0.05 C, after a poor first cycle Coulombic efficiency of 17 %⁴⁶.

Baggetto and co-workers took a basic but thorough electrochemical analysis of sodium alloying in a germanium thin film sputtered on roughened copper foil³⁶. Throughout GITT (Galvanostatic Intermittent Titration Technique) measurement at low current (C/60), calculated thermodynamic potential values could be closely approached during sodiation. A larger gap is instead observed when the desodiation is ongoing due to a high polarization connected to

sodium removal. Capacity retention, despite promising values extracted during first cycles ($\sim 300 \text{ mAh}\cdot\text{g}^{-1}$) quickly drops, within 15 cycles, to few tens of $\text{mAh}\cdot\text{g}^{-1}$.

Recent *in situ* TEM analysis of amorphous germanium nanowires revealed fast sodiation/de-sodiation kinetics associated to sodium richer stoichiometries with $x = 1.56$ ³⁵. Experimental studies conducted on metallic tin have showed a general inconsistency with DFT calculation aimed at finding the stable intermediate phases in Na-Sn system. Despite calculation would predict a sodiation proceeding through the steps NaSn_5 , NaSn , Na_9Sn_4 and $\text{Na}_{15}\text{Sn}_4$ ³⁸, *ex situ* characterization attempted by Ellis et al. on an experimentally sodiated tin electrode identified four alloying steps with different composition and phases, namely amorphous NaSn_3 , $\alpha\text{-NaSn}$, Na_9Sn_4 and crystalline $\text{Na}_{15}\text{Sn}_4$. Conclusion of the authors has been that, the correspondence between experimental and calculated plateaus, as evidenced in Figure IV-4 is only apparent and conceals the intrinsic thermodynamic limits in achieving complex crystalline intermetallic phases, even though stable, at room temperature.

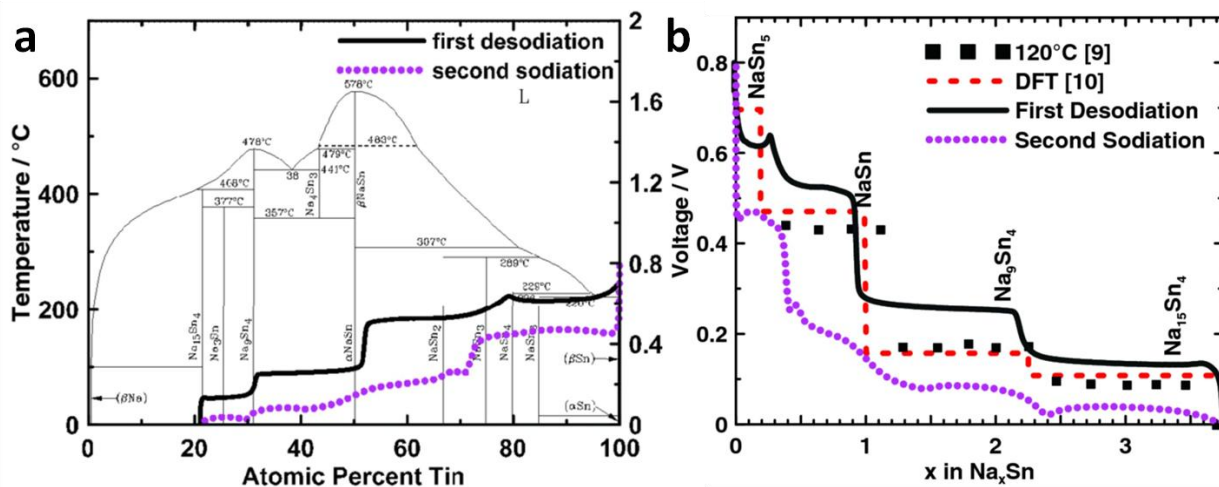


Figure IV-4: a) Sodiation/se-sodiation curves superimposed to Na-Sn phase diagram; b) experimental sodiation/de-sodiation curves superimposed to DFT calculation for tin sodiation and measures taken at high temperatures.

The formation of amorphous phases³⁷, not predicted by DFT calculation, can be thus motivated by low mobility of sodium and tin particle morphological specific features that deviate the system from calculate equilibrium crystalline states. Volume expansion evaluations derived from *in situ* TEM analysis suggested how drastic measures were due to guarantee the

electrode survival to cycling and overcome rupture. Fine dispersion of tin particles on carbonaceous matrix, achieved by high energy milling method (HEMM) has been then proposed to avoid mechanical stress build up with discrete results in terms of Coulombic efficiency and rate capabilities⁴⁷. More exotic approaches, using cellulose fiber as a mechanical buffer has been recently proposed⁴⁸. According to Sb phase diagram, two intermetallic phases are suitable for sodium storage: NaSb and Na₃Sb. Quian et al. firstly demonstrated a Sb-carbon nanocomposite with the initial capacity of 610 mAh·g⁻¹. Both rate capabilities and cyclability were astonishingly impressive since 300 mAh·g⁻¹ could be achieved at the surprisingly high current of 2000 mA·g⁻¹ and capacity fade was limited to few percent within the first 100 cycles. Nonetheless, the latter feature was achieved only if FEC was employed as electrolyte additive and SEI-forming agent. This aspect strongly bonds the reversibility of sodium alloying mechanism to the stability and mechanical robustness of solid electrolyte interface, and can be reasonably extended to other intermetallic compounds. As for other metals also for antimony information on charge storage mechanism is nowadays limited. XRD patterns of the ongoing alloying process are rather featureless, symptom of intermediate amorphous phases between Sb and Na₃Sb⁴⁹. Added to this sensible differences between first cycle potential profile and following ones are registered, and appreciable discrepancies in mechanisms are also collected if Sb particles with different morphologies and dimension are investigated. As an insight derived from in situ synchrotron XRD measurements taken on Sb/C composite (7:3), Ramireddy and co-workers brought the failed recovery of crystallinity of Sb after first de-sodiation.

While binary systems involving Sn-Sb⁵⁰, Sn-Cu⁵¹ and Al-Sb⁵² have been studied as potential SIBs anode, a recent trend is to inspect ternary Sn-Sb-Ge phases. Addition of a third element to a binary system further complicate phases stability and equilibria, marking the appearance of amorphous phases or modified lattice parameters due to substitutional solid solubility of Sn into Ge, for example. Many ternary phases have been investigated, and among them Sn₈₀Ge₁₀Sb₁₀, Sn₆₀Ge₂₀Sb₂₀, Sn₅₀Ge₂₅Sb₂₅ and Sn₃₃Ge₃₃Sb₃₃ demonstrated to be valid candidates as anode material for SIBs with reversible capacities of 728, 829, 833 and 669 mAh·g⁻¹ respectively. The highest stability is achieved by Sn₅₀Ge₂₅Sb₂₅ composition, which guarantees 662 mAh·g⁻¹ after 50 cycles. Interestingly all the experimental values, except for Sn₈₀Ge₁₀Sb₁₀, are well above the weighted average combination of the theoretical capacities of a single element, 800, 743, 714 and 664 mAh·g⁻¹. A possible explanation for this

advantageous behavior has been put fourth thanks to TEM and HRTEM microstructural analysis and concerns the optimum system constituted by 10-15 nm Sn and Ge(Sn) crystals nano-particles dispersed in an amorphous matrix. The enhanced capacity would be a consequence of a unique ability of Ge nanocrystallites that are heavily alloyed with Sn to sodiated beyond 1:1 Ge:Na ($369 \text{ mAh}\cdot\text{g}^{-1}$) ratio⁵³.

An hybrid conversion-alloying mechanism has been recently proposed to explain SnSe/rGO composite electrochemical behavior⁵⁴. Overlapping potential profiles and CV scans have been obtained in this case, symptom of highly reversible processes. Sorting all the ongoing process out is however a tough task that requires further investigation.

4.2. Phosphorous-based materials

Phosphorous, belonging to the 15th group of the periodic table has three widely known allotropes commonly named red, black and white phosphorus. The latter, whose fundamental forming unit is the P₄ tetrahedron is highly reactive and toxic. Red phosphorus electrochemical reactivity with sodium has been investigated before but its poor electronic properties make it only a modest and not reliable anode material for SIBs⁵⁵. Black phosphorus, with its unique crystalline structure, is the element currently addressed as the “holy Grail” in many field, including the energy storage one. It is a layered material resembling graphite with an unusual puckered structure made of covalently bonded P atoms. It has an interestingly high electronic conductivity ($\sim 300 \text{ S}\cdot\text{m}^{-1}$). Its cycling performances are known to be promising with lithium⁵⁶, but sluggish with sodium. Cui et al. overcame the limitation imposed by the conversion mechanism by preparing a sandwiched graphene-black phosphorus hybrid material with impressive capacity retention and rate capabilities⁵⁷. As claimed by the authors the graphene sheets provide an elastic buffer accommodating the expansion of exfoliated black phosphorous (phosphorene) layers along *y* and *z* axis during alloying to Na₃P. This guarantees capacities abundantly above $2000 \text{ mAh}\cdot\text{g}^{-1}$, stable over 100 cycles, at 0.02 C. The sandwiched structure has been obtained by a relatively simple self-assembly approach, that is mixing N-methyl-2-pyrrolydone based suspensions of exfoliated black phosphorous and graphene, and letting the solvent evaporate in an Ar atmosphere. Recently Komaba et al. tried to investigate the mechanism taking place during the three-electron reduction of P to Na₃P, and a complete conversion from orthorhombic black P to hexagonal red P was found⁵⁸. Crystalline black P is not obtained upon re-oxidation and this has been addressed to the metastable nature of the

allotrope. In the same research the electrolyte solutions and additives have been recognized to have a fundamental role in stabilizing conversion reaction. Amorphous phosphorous has been recognized to be favorable under the volume change point of view and in recent studies this route is encouraged rather than the crystalline phosphorus one. Amorphous red P/carbon composites in which the P-C bonds formation is intentionally sought to firmly anchor P to graphene layers, are nowadays able to ensure ultrastable efficiencies (0.002 % decay per cycle within 400 cycles) and excellent rate capabilities ($809 \text{ mAh}\cdot\text{g}^{-1}$ at $1500 \text{ mA}\cdot\text{g}^{-1}$) as can be seen in Figure IV-5⁵⁹.

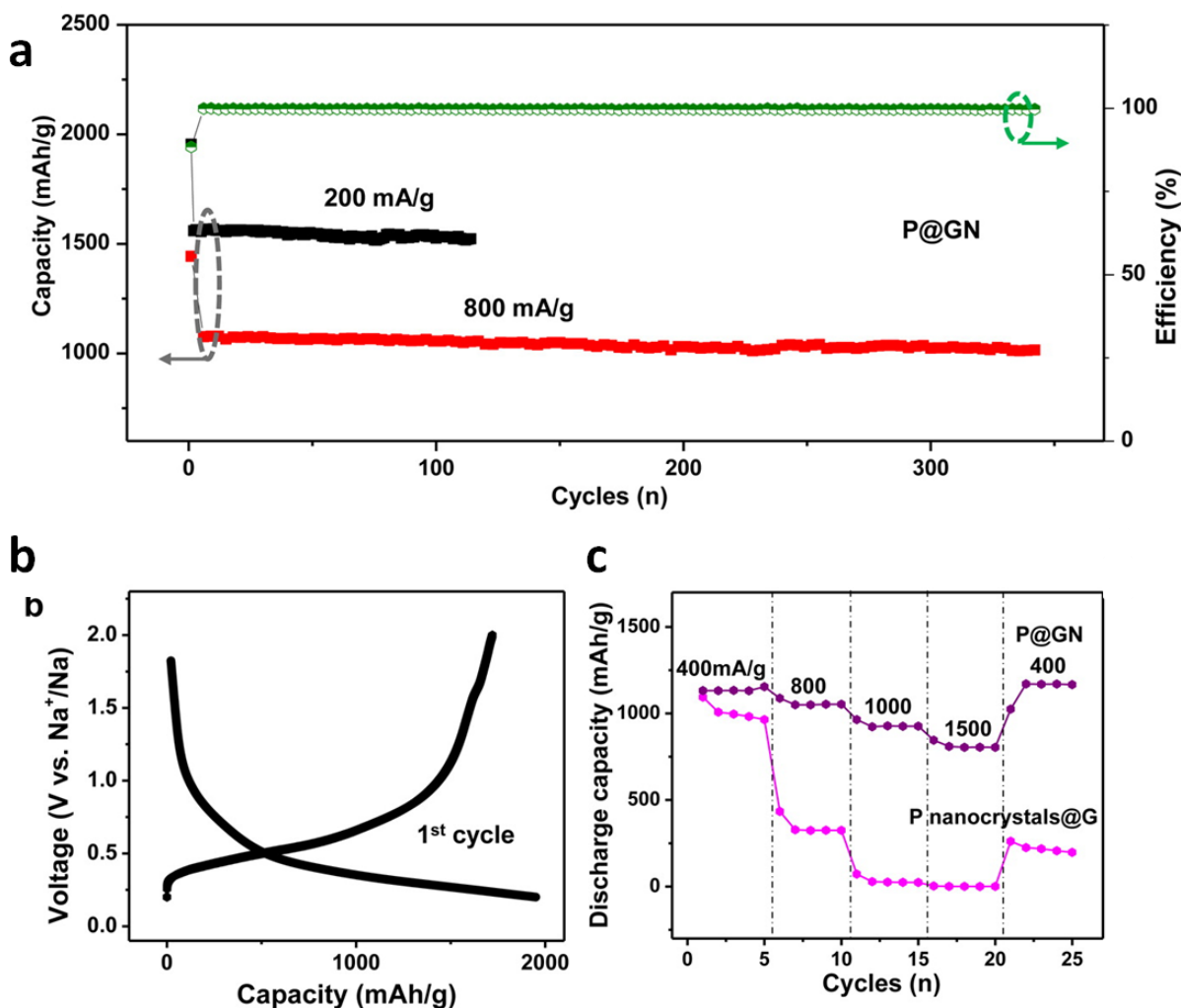


Figure IV-5: a) Cyclic performance and Coulombic efficiency of red P/nitrogen doped graphene oxide composite at 200 and $800 \text{ mA}\cdot\text{g}^{-1}$; b) galvanostatic charge/discharge profiles of electrode at $200 \text{ mA}\cdot\text{g}^{-1}$ and c) rate test on the same phosphorus/graphene composite.

5. Insertion anode materials

Some inorganic compounds are known to be active towards sodium ions intercalation at low potentials. This feature makes them attractive to be used as anodes in SIBs. The study of such compounds have been focusing in the recent years on TiO₂-based materials, layered transition metal carbides or as generally called MXenes layered compounds.

5.1. TiO₂ based insertion compounds

Titanium oxide in all its polymorphs (anatase, rutile, brookite and TiO₂-B⁶⁰) has repeatedly fascinated the scientific community thanks to its interesting physical properties that worth it the honor to be studied in many different technological fields such as photocatalysis applied to pollutant degradation and water splitting, sensors technology, medicine and ultimately energy storage facilities. Added to this a further drive to its fortune has been the natural abundance, environmental friendliness, tunable synthesis and non-toxicity for human beings. Ti³⁺/Ti⁴⁺ couple exhibit the relatively high redox potential around 1.5 V if cycled against lithium as widely demonstrated in literature⁶¹. This aspect makes him unsuitable to be used both as high energy anode and cathode for LIBs. In a sodium environment, Ti-based compounds show an electrochemical activity centered at lower potential values, from 0.5 to 1.0 V vs. Na/Na⁺, also interesting for a possible development of anodes not shadowed by sodium plating danger. Both amorphous and crystalline TiO₂ has been tested against sodium. The former, shaped in nanotubes directly grown on a Ti substrate, manifests a slow and undesirable activation process that progressively sets the capacity up to approximately 100 mAh·g⁻¹. In this case the energy storage mechanism seems to occur almost exclusively via double layer capacitance instauration⁶². Mechanism involved in sodium interaction with crystalline TiO₂ is controversial still today. Some studies revealed that the crystalline structures of nano-sized anatase TiO₂ is well retained upon sodiation, conversely, other research groups claim that a conversion-like process which in the end leads to metallic Ti is involved, when commercial anatase is investigated⁶³. A carbon coating sensibly increase electrochemical performances of anatase nanocrystals⁶⁴.

Sodium titanate with the unit formula Na₂Ti₃O₇, prepared using a ball milling procedure, has been recently investigated⁶⁵. It has been found it to be active toward insertion of 2 sodium ions per unit formula (Na₄Ti₃O₇) at an incredibly low potentials (< 0.5 V vs Na/Na⁺)

through a two-phase process to which correspond stable plateaus with low charge/discharge hysteresis. Structural analysis of intercalated structured disclosed interesting properties of crystalline lattice in varying Na site through variation of joint angles between Ti-O block, demonstrating an overall structural flexibility never observed in TMOs. Nevertheless few days storage of the sodiated compounds in an inert environment gradually makes it reverting back to the Na-poor phase, unveiling a self-discharge mechanism potentially bottlenecking the use of this material as an anode in a full-cell assembly.

5.2. MXenes

MXenes are a class of 2D transition metal carbides and carbonitrides firstly proposed by Barsoum's research group⁶⁶. They are obtained by chemical etching (HF based) the A layers from $M_{n+1}AX_n$ ($n = 1,2,3$), being M a early transition metal, A a 13 or 14 group element and X carbon or nitrogen. Since when they were for the first time proposed as anode materials for LIBs the debate focused on the type of mechanism involved in the energy storage process, possibly capacitive/pseudocapacitive involving material surface⁶⁷ or more based on a pure intercalation of desolvated Na ions⁶⁸. In both cases, in which the investigation of Ti_2CT_x was perpetrated (T_x are selected surface terminations), high energy performances resembling supercapacitor ones could be achieved. Wang et al. shed light onto the surface and intercalation processes using DFT and scanning transmission electron microscopy (STEM) and they emphasized the topotactic localization of functional groups (*e.g.*, OH^- , F^- , O^{2-}) and intercalated Na atoms on the top site of the central-Ti atoms and C atoms on the $Ti_3C_2T_x$ monolayer⁶⁹.

6. Bibliography

- (1) Okamoto, Y. Density Functional Theory Calculations of Alkali Metal (Li, Na, and K) Graphite Intercalation Compounds. *J. Phys. Chem. C* **2014**, *118*(1), 16–19.
- (2) Wen, Y.; He, K.; Zhu, Y.; Han, F.; Xu, Y.; Matsuda, I.; Ishii, Y.; Cumings, J.; Wang, C. Expanded Graphite as Superior Anode for Sodium-Ion Batteries. *Nat. Commun.* **2014**, *5* (May), 4033.
- (3) Jache, B.; Adelhelm, P. Use of Graphite as a Highly Reversible Electrode with Superior Cycle Life for Sodium-Ion Batteries by Making Use of Co-Intercalation Phenomena. *Angew. Chemie - Int. Ed.* **2014**, *53* (38), 10169–10173.
- (4) Henderson, W. A. Glyme–Lithium Salt Phase Behavior. **2006**.
- (5) Irisarri, E.; Ponrouch, A.; Palacin, M. R. Review—Hard Carbon Negative Electrode Materials for Sodium-Ion Batteries. *J. Electrochem. Soc.* **2015**, *162* (14), A2476–A2482.
- (6) Luo, W.; Jian, Z.; Xing, Z.; Wang, W.; Bommier, C.; Lerner, M. M.; Ji, X. Electrochemically Expandable Soft Carbon as Anodes for Na-Ion Batteries. *ACS Cent. Sci.* **2015**, *1*, 516–522.
- (7) Buiel, E. R.; George, A. E.; Dahn, J. R. Model of Micropore Closure in Hard Carbon Prepared from Sucrose. *Carbon N. Y.* **1999**, *37*, 1399–1407.
- (8) Xing, W.; Xue, J. S.; Dahn, J. R. Optimizing Pyrolysis of Sugar Carbons for Use as Anode Materials in Lithium-Ion Batteries. *J. Electrochem. Soc.* **1996**, *143* (10), 3046.
- (9) Tsai, P.-C.; Chung, S.-C.; Lin, S.-K.; Yamada, A. Ab Initio Study of Sodium Intercalation into Disordered Carbon. *J. Mater. Chem. A* **2015**, *3*, 9763–9768.
- (10) Komaba, S.; Murata, W.; Ishikawa, T.; Yabuuchi, N.; Ozeki, T.; Nakayama, T.; Ogata, A.; Gotoh, K.; Fujiwara, K. Electrochemical Na Insertion and Solid Electrolyte Interphase for Hard-Carbon Electrodes and Application to Na-Ion Batteries. *Adv. Funct. Mater.* **2011**, *21* (20), 3859–3867.
- (11) Balogun, M. S.; Luo, Y.; Qiu, W.; Liu, P.; Tong, Y. A Review of Carbon Materials and Their Composites with Alloy Metals for Sodium Ion Battery Anodes. *Carbon N. Y.* **2016**, *98*, 162–178.
- (12) Béguin, F.; Chevallier, F.; Vix-Guterl, C.; Saadallah, S.; Bertagna, V.; Rouzaud, J. N.; Frackowiak, E. Correlation of the Irreversible Lithium Capacity with the Active Surface Area of Modified Carbons. *Carbon N. Y.* **2005**, *43*, 2160–2167.

- (13) Jin, J.; Shi, Z.-Q.; Wang, C.-Y. Electrochemical Performance of Electrospun Carbon Nanofibers as Free-Standing and Binder-Free Anodes for Sodium-Ion and Lithium-Ion Batteries. *Electrochim. Acta* **2014**, *141*, 302–310.
- (14) Wenzel, S.; Hara, T.; Janek, U.; Adelhelm, P. Room-Temperature Sodium-Ion Batteries: Improving the Rate Capability of Carbon Anode Materials by Templating Strategies. *Energy Environ. Sci.* **2011**, *4*, 3342–3345.
- (15) Pol, V. G.; Lee, E.; Zhou, D.; Dogan, F.; Calderon-Moreno, J. M.; Johnson, C. S. Spherical Carbon as a New High-Rate Anode for Sodium-Ion Batteries. *Electrochim. Acta* **2014**, *127*, 61–67.
- (16) Tang, K.; Fu, L.; White, R. J.; Yu, L.; Titirici, M.-M.; Antonietti, M.; Maier, J. Hollow Carbon Nanospheres with Superior Rate Capability for Sodium-Based Batteries. *Adv. Energy Mater.* **2012**, *2* (7), 873–877.
- (17) Zhou, X.; Guo, Y.-G. Highly Disordered Carbon as a Superior Anode Material for Room-Temperature Sodium-Ion Batteries. *ChemElectroChem* **2014**, *1* (1), 83–86.
- (18) Cao, Y.; Xiao, L.; Sushko, M. L.; Wang, W.; Schwenzler, B.; Xiao, J.; Nie, Z.; Saraf, L. V.; Yang, Z.; Liu, J. Sodium Ion Insertion in Hollow Carbon Nanowires for Battery Applications. *Nano Lett.* **2012**, *12* (7), 3783–3787.
- (19) Chen, T.; Liu, Y.; Pan, L.; Lu, T.; Yao, Y.; Sun, Z.; Chua, D. H. C.; Chen, Q. Electrospun Carbon Nanofibers as Anode Materials for Sodium Ion Batteries with Excellent Cycle Performance. *J. Mater. Chem. A* **2014**, *2* (12), 4117.
- (20) Hong, K.; Qie, L.; Zeng, R.; Yi, Z.; Zhang, W.; Wang, D.; Yin, W.; Wu, C.; Fan, Q.; Zhang, W.; Huang, Y. Biomass Derived Hard Carbon Used as a High Performance Anode Material for Sodium Ion Batteries. *J. Mater. Chem. A* **2014**, *2* (32), 12733.
- (21) Chen, T.; Pan, L.; Lu, T.; Fu, C.; Chua, D. H. C.; Sun, Z. Fast Synthesis of Carbon Microspheres via a Microwave-Assisted Reaction for Sodium Ion Batteries. *J. Mater. Chem. A* **2014**, *2*, 1263.
- (22) Eletsii, A. V; Iskandarova, I. M.; Knizhnik, A. a; Krasikov, D. N. Graphene: Fabrication Methods and Thermophysical Properties. *Physics-USpekhi* **2011**, *54* (3), 227–258.
- (23) Hariharan, S.; Saravanan, K.; Ramar, V.; Palacín, M. R. A Rationally Designed Dual Role Anode Material for Lithium-Ion and Sodium-Ion Batteries: Case Study of Eco-

- Friendly Fe₃O₄. *Phys. Chem. Chem. Phys.* **2013**, *15* (8), 2945.
- (24) Jian, Z.; Zhao, B.; Liu, P.; Li, F.; Zheng, M.; Chen, M.; Shi, Y.; Zhou, H. Fe₂O₃ Nanocrystals Anchored onto Graphene Nanosheets as the Anode Material for Low-Cost Sodium-Ion Batteries. *Fire Rescue Mag.* **2014**, *50* (10), 1215–1217.
- (25) Li, H.; Xu, L.; Sitanimaluwa, H.; Wasalathilake, K.; Yan, C. *Coating Fe₂O₃ with Graphene Oxide for High-Performance Sodium-Ion Battery Anode*; 2016; Vol. 1.
- (26) Yang, J.; Zhou, T.; Zhu, R.; Chen, X.; Guo, Z.; Fan, J.; Liu, H. K.; Zhang, W. X. Highly Ordered Dual Porosity Mesoporous Cobalt Oxide for Sodium-Ion Batteries. *Adv. Mater. Interfaces* **2016**, *3* (3), 1–7.
- (27) Su, D.; Xie, X.; Munroe, P.; Dou, S.; Wang, G. Mesoporous Hexagonal Co₃O₄ for High Performance Lithium Ion Batteries. *Sci. Rep.* **2014**, *4*, 6519.
- (28) Xiao, X.; Liu, X.; Zhao, H.; Chen, D.; Liu, F.; Xiang, J.; Hu, Z.; Li, Y. Facile Shape Control of Co₃O₄ and the Effect of the Crystal Plane on Electrochemical Performance. *Adv. Mater.* **2012**, *24* (42), 5762–5766.
- (29) Liu, Y.; Cheng, Z.; Sun, H.; Arandiyan, H.; Li, J.; Ahmad, M. Mesoporous Co₃O₄ sheets/3D Graphene Networks Nanohybrids for High-Performance Sodium-Ion Battery Anode. *J. Power Sources* **2015**, *273*, 878–884.
- (30) Rahman, M. M.; Sultana, I.; Chen, Z. Ex Situ Electrochemical Sodiation/desodiation Observation of Co₃O₄ Anchored Carbon Nanotubes: A High Performance Sodium-Ion Battery Anode Produced by Pulsed Plasma in a Liquid. *Nanoscale* **2015**, *7* (30), 13088–13095.
- (31) Lu, Y. C.; Ma, C.; Alvarado, J.; Kidera, T.; Dimov, N.; Meng, Y. S.; Okada, S. Electrochemical Properties of Tin Oxide Anodes for Sodium-Ion Batteries. *J. Power Sources* **2015**, *284*, 287–295.
- (32) Su, D.; Xie, X.; Wang, G. Hierarchical Mesoporous SnO₂ Microspheres as High Capacity Anode Materials for Sodium-Ion Batteries. *Chem. - A Eur. J.* **2014**, *20* (11), 3192–3197.
- (33) Gu, M.; Kushima, A.; Shao, Y.; Zhang, J.-G.; Liu, J.; Browning, N. D.; Li, J.; Wang, C. Probing the Failure Mechanism of SnO₂ Nanowires for Sodium-Ion Batteries. *Nano Lett.* **2013**, *13* (11), 5203–5211.
- (34) Jung, S. C.; Jung, D. S.; Choi, J. W.; Han, Y.-K. Atom-Level Understanding of the Sodiation Process in Silicon Anode Material. *J. Phys. Chem. Lett.* **2014**, *5*, 1283–1288.

- (35) Lu, X.; Adkins, E. R.; He, Y.; Zhong, L.; Luo, L.; Mao, S. X.; Wang, C.-M.; Korgel, B. A. Germanium as a Sodium Ion Battery Material: In Situ TEM Reveals Fast Sodiation Kinetics with High Capacity. *Chem. Mater.* **2016**, *28* (4), 1236–1242.
- (36) Baggetto, L.; Keum, J. K.; Browning, J. F.; Veith, G. M. Germanium as Negative Electrode Material for Sodium-Ion Batteries. *Electrochem. commun.* **2013**, *34*, 41–44.
- (37) Wang, J. W.; Liu, X. H.; Mao, S. X.; Huang, J. Y. Microstructural Evolution of Tin Nanoparticles during In Situ Sodium Insertion and Extraction. *Nano Lett.* **2012**, *12* (11), 5897–5902.
- (38) Ellis, L. D.; Hatchard, T. D.; Obrovac, M. N. Reversible Insertion of Sodium in Tin. *J. Electrochem. Soc.* **2012**, *159* (11), A1801–A1805.
- (39) Chevrier, V.; Ceder, G. Challenges for Na-Ion Negative Electrodes. *J. Electrochem. Soc.* **2011**, *158* (9), A1011.
- (40) Jow, T. R. The Role of Conductive Polymers in Alkali-Metal Secondary Electrodes. *J. Electrochem. Soc.* **1987**, *134* (7), 1730.
- (41) Qian, J.; Chen, Y.; Wu, L.; Cao, Y.; Ai, X.; Yang, H. High Capacity Na-Storage and Superior Cyclability of Nanocomposite Sb/C Anode for Na-Ion Batteries. *Chem. Commun. (Camb.)* **2012**, *48* (56), 7070–7072.
- (42) Liu, X.; Gao, Y.; Jin, R.; Luo, H.; Peng, P.; Liu, Y. Scalable Synthesis of Si Nanostructures by Low-Temperature Magnesiothermic Reduction of Silica for Application in Lithium Ion Batteries. *Nano Energy* **2014**, *4*, 31–38.
- (43) Jung, D. S.; Ryou, M.-H.; Sung, Y. J.; Park, S. Bin; Choi, J. W. Recycling Rice Husks for High-Capacity Lithium Battery Anodes. *Proc. Natl. Acad. Sci. U. S. A.* **2013**, *110* (30), 12229–12234.
- (44) Liu, N.; Huo, K.; McDowell, M. T.; Zhao, J.; Cui, Y. Rice Husks as a Sustainable Source of Nanostructured Silicon for High Performance Li-Ion Battery Anodes. *Sci. Rep.* **2013**, *3* (c), 1919.
- (45) Komaba, S.; Matsuura, Y.; Ishikawa, T.; Yabuuchi, N.; Murata, W.; Kuze, S. *Redox Reaction of Sn-Polyacrylate Electrodes in Aprotic Na Cell*; 2012; Vol. 21.
- (46) Lim, C.-H.; Huang, T.-Y.; Shao, P.-S.; Chien, J.-H.; Weng, Y.-T.; Huang, H.-F.; Hwang, B. J.; Wu, N.-L. Experimental Study on Sodiation of Amorphous Silicon for Use as Sodium-Ion Battery Anode. *Electrochim. Acta* **2016**, *211*, 265–272.

- (47) Datta, M. K.; Epur, R.; Saha, P.; Kadakia, K.; Park, S. K.; Kumta, P. N. Tin and Graphite Based Nanocomposites: Potential Anode for Sodium Ion Batteries. *J. Power Sources* **2013**, *225*, 316–322.
- (48) Zhu, H.; Jia, Z.; Chen, Y.; Weadock, N.; Wan, J.; Vaaland, O.; Han, X.; Li, T.; Hu, L. Tin Anode for Sodium-Ion Batteries Using Natural Wood Fiber as a Mechanical Buffer and Electrolyte Reservoir. *Nano Lett.* **2013**, *13* (7), 3093–3100.
- (49) Ramireddy, T.; Sharma, N.; Xing, T.; Chen, Y.; Leforestier, J.; Glushenkov, A. M. Size and Composition Effects in Sb-Carbon Nanocomposites for Sodium-Ion Batteries. *ACS Appl. Mater. Interfaces* **2016**, *8* (44), 30152–30164.
- (50) Xiao, L.; Cao, Y.; Xiao, J.; Wang, W.; Kovarik, L.; Nie, Z.; Liu, J. High Capacity, Reversible Alloying Reactions in SnSb/C Nanocomposites for Na-Ion Battery Applications. *Chem. Commun. (Camb)*. **2012**, *48* (27), 3321–3323.
- (51) Lin, Y.-M.; Abel, P. R.; Gupta, A.; Goodenough, J. B.; Heller, A.; Mullins, C. B. Sn–Cu Nanocomposite Anodes for Rechargeable Sodium-Ion Batteries. *ACS Appl. Mater. Interfaces* **2013**, *5* (17), 8273–8277.
- (52) Baggetto, L.; Marszewski, M.; Górka, J.; Jaroniec, M.; Veith, G. M. AlSb Thin Films as Negative Electrodes for Li-Ion and Na-Ion Batteries. *J. Power Sources* **2013**, *243*, 699–705.
- (53) Farbod, B.; Cui, K.; Kalisvaart, W. P.; Kupsta, M.; Zahiri, B.; Kohandehghan, A.; Lotfabad, E. M.; Li, Z.; Lubner, E. J.; Mitlin, D. Anodes for Sodium Ion Batteries Based on Tin-Germanium-Antimony Alloys. *ACS Nano* **2014**, *8* (5), 4415–4429.
- (54) Yang, X.; Zhang, R.; Chen, N.; Meng, X.; Yang, P.; Wang, C.; Zhang, Y.; Wei, Y.; Chen, G.; Du, F. Assembly of SnSe Nanoparticles Confined in Graphene for Enhanced Sodium-Ion Storage Performance. *Chem. - A Eur. J.* **2016**, *22* (4), 1445–1451.
- (55) Li, W.-J.; Chou, S.-L.; Wang, J.-Z.; Liu, H.-K.; Dou, S.-X. Simply Mixed Commercial Red Phosphorus and Carbon Nanotube Composite with Exceptionally Reversible Sodium-Ion Storage. *Nano Lett.* **2013**, *13* (11), 5480–5484.
- (56) Sun, J.; Zheng, G.; Lee, H. W.; Liu, N.; Wang, H.; Yao, H.; Yang, W.; Cui, Y. Formation of Stable Phosphorus-Carbon Bond for Enhanced Performance in Black Phosphorus Nanoparticle-Graphite Composite Battery Anodes. *Nano Lett.* **2014**, *14* (8), 4573–4580.

- (57) Sun, J.; Lee, H.-W.; Pasta, M.; Yuan, H.; Zheng, G.; Sun, Y.; Li, Y.; Cui, Y. A Phosphorene–graphene Hybrid Material as a High-Capacity Anode for Sodium-Ion Batteries. *Nat. Nanotechnol.* **2015**, No. September.
- (58) Dahbi, M.; Yabuuchi, N.; Fukunishi, M.; Kubota, K.; Chihara, K.; Tokiwa, K.; Yu, X.-F.; Ushiyama, H.; Yamashita, K.; Son, J.-Y.; Cui, Y.-T.; Oji, H.; Komaba, S. Black Phosphorus as a High-Capacity, High-Capability Negative Electrode for Sodium-Ion Batteries: Investigation of the Electrode/ Electrolyte Interface.
- (59) Zhang, C.; Wang, X.; Liang, Q.; Liu, X.; Weng, Q.; Liu, J.; Yang, Y.; Dai, Z.; Ding, K.; Bando, Y.; Tang, J.; Golberg, D. Amorphous Phosphorus/Nitrogen-Doped Graphene Paper for Ultrastable Sodium-Ion Batteries.
- (60) Yang, Z.; Choi, D.; Kerisit, S.; Rosso, K. M.; Wang, D.; Zhang, J.; Graff, G.; Liu, J. Nanostructures and Lithium Electrochemical Reactivity of Lithium Titanites and Titanium Oxides: A Review. *J. Power Sources* **2009**, *192*, 588–598.
- (61) Zhu, G.-N.; Wang, Y.-G.; Xia, Y.-Y. Ti-Based Compounds as Anode Materials for Li-Ion Batteries. *Energy Environ. Sci.* **2012**, *5* (5), 6652.
- (62) Xiong, H.; Slater, M. D.; Balasubramanian, M.; Johnson, C. S.; Rajh, T. Amorphous TiO₂ Nanotube Anode for Rechargeable Sodium Ion Batteries. *J. Phys. Chem. Lett.* **2011**, 2560–2565.
- (63) Wu, L.; Bresser, D.; Buchholz, D.; Giffin, G.; Castro, C. R.; Ochel, A.; Passerini, S. Unfolding the Mechanism of Sodium Insertion in Anatase TiO₂ Nanoparticles. *Adv. Energy Mater.* **2014**, 1–11.
- (64) Tahir, M. N.; Oschmann, B.; Buchholz, D.; Dou, X.; Lieberwirth, I.; Panthöfer, M.; Tremel, W.; Zentel, R.; Passerini, S. Extraordinary Performance of Carbon-Coated Anatase TiO₂ as Sodium-Ion Anode. *Adv. Energy Mater.* **2015**, n/a-n/a.
- (65) Xu, J.; Ma, C.; Balasubramanian, M.; Meng, Y. S. Understanding Na₂Ti₃O₇ as an Ultra-Low Voltage Anode Material for a Na-Ion Battery. *Chem. Commun.* **2014**, *50* (83), 12564–12567.
- (66) Naguib, M.; Kurtoglu, M.; Presser, V.; Lu, J.; Niu, J.; Heon, M.; Hultman, L.; Gogotsi, Y.; Barsoum, M. W. Two-Dimensional Nanocrystals Produced by Exfoliation of Ti₃AlC₂. *Adv. Mater.* **2011**, *23* (37), 4248–4253.
- (67) Wang, X.; Kajiyama, S.; Iinuma, H.; Hosono, E.; Oro, S.; Moriguchi, I.; Okubo, M.;

- Yamada, A. Pseudocapacitance of MXene Nanosheets for High-Power Sodium-Ion Hybrid Capacitors. *Nat. Commun.* **2015**, *6*, 6544.
- (68) Kajiyama, S.; Szabova, L.; Sodeyama, K.; Iinuma, H.; Morita, R.; Gotoh, K.; Tateyama, Y.; Okubo, M.; Yamada, A. Sodium-Ion Intercalation Mechanism in MXene Nanosheets.
- (69) Wang, H.-W.; Naguib, M.; Page, K.; Wesolowski, D. J.; Gogotsi, Y. Resolving the Structure of Ti₃C₂T_x MXenes through Multilevel Structural Modeling of the Atomic Pair Distribution Function.

CHAPTER V: SIBs cathode materials review

1. Introduction

As anticipated in **Error! Reference source not found.**, the number of publications thoroughly exploring cathode and anode materials for sodium rechargeable batteries, has increased exponentially since 2010. A tremendous quantity of different classes including inorganic compounds, composites and pure elements has been investigated so far, nevertheless meeting the requirements of a reliable and stable active material, still represents a leap that hasn't been filled yet. In this chapter an in-depth literature review of the electrode material so far synthesized and characterized will be provided, and analysis of classes to which materials coming from the present research work, will be particularly stressed. Going through the materials, layered transition metal oxides will be described at first place whose study has recently regained enthusiasm. Additionally most recently proposed advancement, such as polyanionic and NASICON-type of compounds, will be discussed as they tried to enhance the cycle stability, environmental friendliness and reliability and energy densities. Switching from lithium to sodium intrinsically bare with itself the drawback represented by a lower standard reduction potential of Na/Na⁺ redox couple, this is the reason why efforts have to be put in extending reversible capacity in order to reach comparable energy densities. It can be calculated that, in order to overcome the ~0.5 V discrepancy between lithium and sodium based systems, a 12.5 % specific capacity excess should be kept in mind in designing an innovative active material. As previously stated, studies of sodium intercalation in inorganic layered material

started at the end of the 1980s, in conjunction with lithium ones. They were both referred to cathode materials, TiS_2 ¹ and $\text{P2-Na}_x\text{CoO}_2$ ^{2,3} for which sodium intercalation was confirmed and quantified, as well as anode sodium-lead alloys. Prototypes of full sodium-ion cells were also assembled demonstrating surprisingly high cyclability for more than 300 cycles at a operational potential slightly lower than 3.0 V. Precisely this latter feature, didn't particularly draw the attention if compared to high voltage LiCoO_2 /graphite systems. After the sodium renaissance started due to mounting sustainability concerns back in 2010, a plethora of materials have been proposed as cathode, including layered and tunnel-like transition metal oxides^{4,5}, transition metal sulfides and fluorides⁶, polyanionic compounds⁷⁻⁹, Prussian blue analogues¹⁰ as well as organic carboxylates and polymers¹¹. More productive, but mostly in terms of number of works published and not of substantial advancement generated, has been the research around the anode side. Hard carbon, alloys, elemental phosphorus are few of the materials taken into consideration and that will be analyzed in detail later. Starting from the cathode side and proceeding later with the anode, a fast screening of the already known materials will be provided, so that the an easier and more immediate comparison with the contribution given by this experimental work will be possible.

2. Layered transition metal oxide (TMO)

According to the classification Delmas et al. conceived based on i) coordination configuration that sodium ions assume once inserted in the layered structure and ii) layers stacking sequence, described in Chapter III different layered oxides have been here listed, providing the most relevant electrochemical and structural features as cathode material for sodium batteries.

2.1. P2-type TMOs

Na_xCoO_2 and Na_xMnO_2 stand as the most widely investigated P2-type layered material in sodium environment. Na_xCoO_2 can be prepared relatively easily in almost every layered configuration according to synthetic temperature and sodium precursor content¹² as illustrated in Figure V-1. P2 phase Na_xCoO_2 has a well defined stability window related to a sodium composition (x) included in the range $0.46 < x < 0.83$, while for higher content of Na ($0.83 < x < 1.00$) it tends to convert to O3- Na_xCoO_2 . P2- Na_xCoO_2 phase potential profile shows a substantially different trend if compared to lithium analogue one. While in the latter case a

single and stable plateau at moderately high potential (4.0 V) with low polarization is observed, the former compounds show a stepwise potential change, spread over a wider window of potential values. As a consequence of that, energy densities will be considerably lower. In sodium analogue the potential profile, exemplified in image a) in Figure V-2, originates from both single-phase, referred to solid solution like mechanism, and two-phase processes. In the second case a two-phase like behavior might manifest inside the same stability range of a P or O, namely the same phase, due to sodium sub-lattice pattern formation. Interestingly, together with phase transformation also a sensible variation in sodium diffusion is obtained. O3- Na_xCoO_2 outperform P2- Na_xCoO_2 at high sodium content, while the trend is reversed for lower sodium concentration in the lattice due to fast Na diffusion in a honeycomb-like sub-lattice. In general, for Na_xCoO_2 , diffusion coefficients are higher by an order of magnitude¹³ (approximately $0.5\text{--}1.5 \times 10^{-10} \text{ cm}^2\cdot\text{s}^{-1}$ vs. $1 \times 10^{-11} \text{ cm}^2\cdot\text{s}^{-1}$) than Li_xCoO_2 , and this will result also true for other insertion material. A plausible explanation to this effect might be related to the weaker nature of Na^+ as a Lewis acid compared to Li^+ that would allow a faster diffusion between layers. Speaking about electrochemical performances, P2- $\text{Na}_{0.74}\text{CoO}_2$ synthesized by a solid-state route, exhibits a reversible discharge capacity of $107 \text{ mAh}\cdot\text{g}^{-1}$ at 0.1 C over a potential range spanning from 2.0 to 3.8 V.

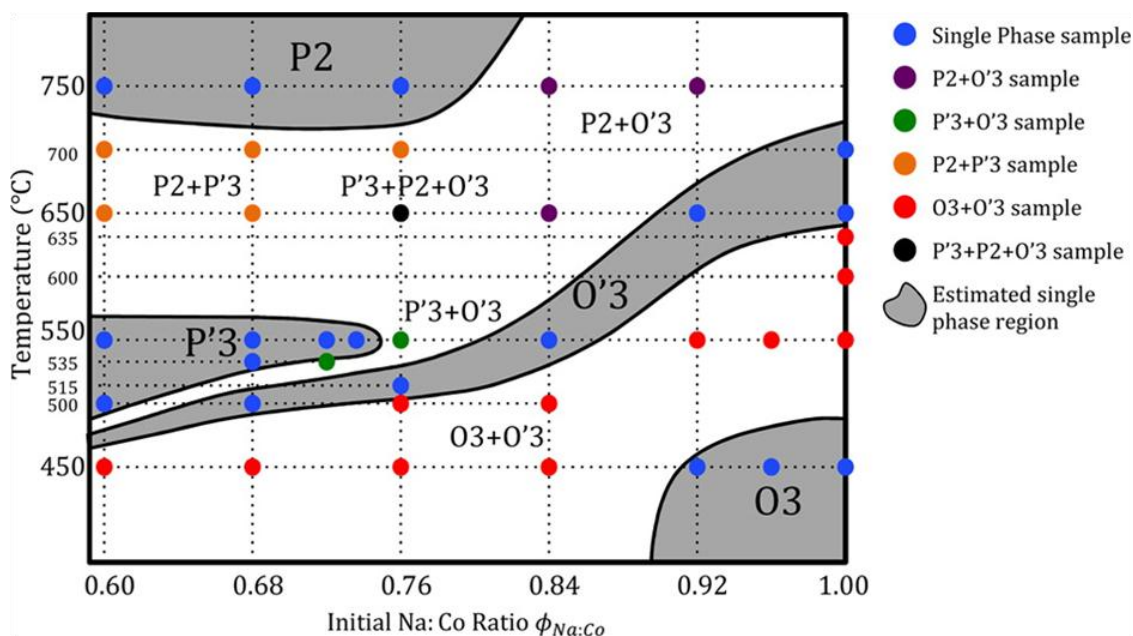


Figure V-1: temperature/composition phase diagram of layered CoO_2 compound in which single phase stability zones and equilibrium lines of different structures are indicated.

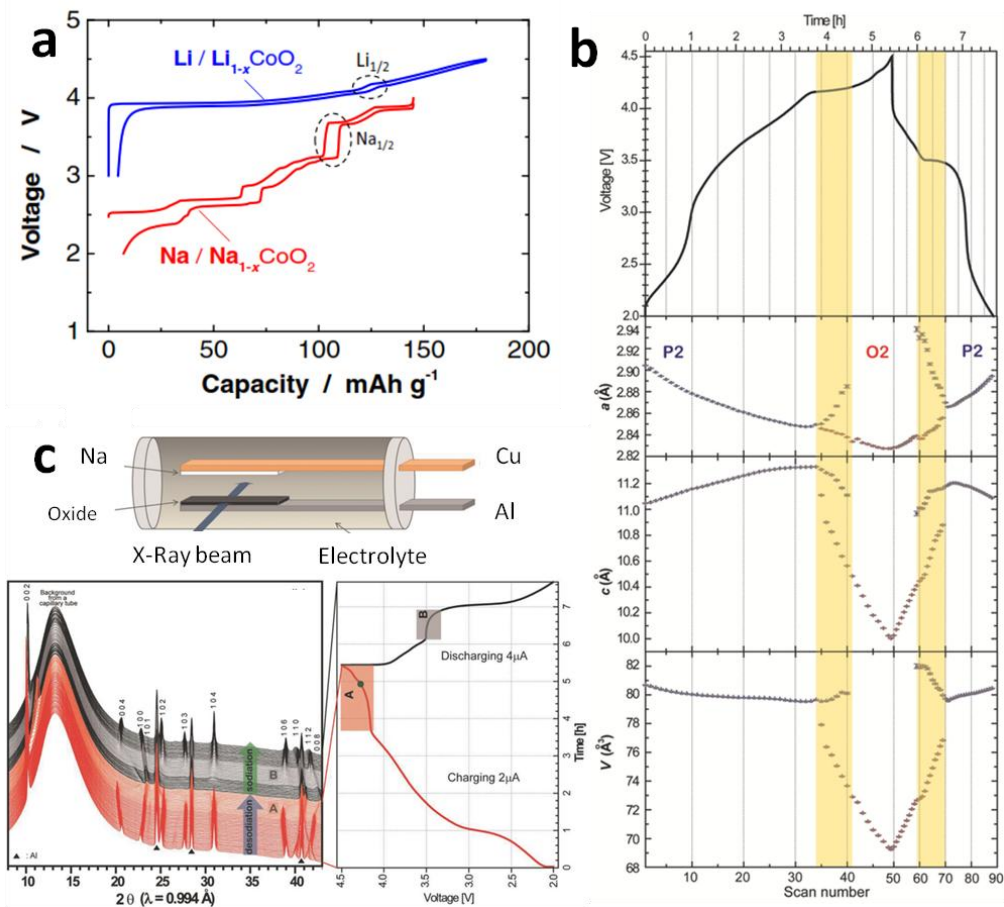


Figure V-2: a) intercalation/de-intercalation potential vs. capacity profile of layered CoO₂ with lithium (blue curve) and sodium (red curve); b) lattice parameters evolution of P2-Na_{0.7}Fe_{0.4}Mn_{0.4}Co_{0.2}O₂ electrode from *in situ* synchrotron analysis, potential profile of capillary cell is also reported at the top of the image; c) schematic illustration used in a capillary cell used in synchrotron analysis and *in situ* XRD patterns P2-Na_{0.7}Fe_{0.4}Mn_{0.4}Co_{0.2}O₂ evolution as the Na// P2-Na_{0.7}Fe_{0.4}Mn_{0.4}Co_{0.2}O₂ was cycled inside the capillary cell.

P2-Na_xMnO₂, despite the electrochemical activity comparable to those of cobalt analogue in the 0.45-0.85 composition range, showed low sodium diffusion and poor structural reversibility due to a strong Jahn-Teller^d effect of Mn³⁺¹⁴. In recent investigations, the cations substitution has been revealed an efficient method to enhance structural stability Na_xMnO₂. Ni/Mn, Fe/Mn and Co/Mn substitutions have been considered and some research groups

^d Spontaneous symmetry breaking and geometrical distortion of molecules and ions associated with certain electron configurations.

succeeded in suppressing the multiple phase transitions improving reversibility. For example, P2-Na_{0.67}Ni_{0.33}Mn_{0.67}O₂ has been claimed by Lu et al. to provide 170.7 mAh·g⁻¹ by the reversible extraction of 0.67 x of sodium. Further XRD analysis revealed how P2 phase is maintained until 0.33 stoichiometry is reached while a co-existence of P2, phase O2-type stacking faults and O2 phase Ni_{0.33}Mn_{0.67}O₂ was occupied below 0.33 x¹⁵. Apparently the only efficient way to increase reversibility excluding deleterious phase transitions, is to narrow the operative potential window. An important contribution to the understanding of phase transition mechanisms was given by Jung et al.¹⁶ by *in-situ* Synchrotron X-ray diffraction of the compound P2-Na_{0.7}[(Fe_{0.5}Mn_{0.5})_{1-x}Co_x]O₂ (x = 0, 0.05, 0.10, and 0.20). Lattice parameters has been observed varying according to multiple effects occurring during charging and discharging (image b) and c) in Figure V-2). During de-sodiation (charging), a general contraction on the *ab* plane (aligned TMO₂ slabs) is observed due to a decrease in transition metal atoms radii from oxidation. Along *c* direction instead an expansion is observed due to a mounting unbalanced electrostatic repulsion between oxygen atoms. Since no phase transition are so far involved, at least below 4.1 V vs. Na/Na⁺, the general behavior of the material is the one of a solid-solution, with a slight cell volume change (2.1 %) and a sloping operational potential. Above 4.1, a phase transition from P2 (*P6₃/mmc*) to a O2 (*P6₃mc*) structure occurs as clearly visible from the plateau region A and B in the profile potential and appearance of O2 diffraction peaks while P2 ones progressively fade (image c) in Figure V-2). The phase transition finds its explanation in the gliding of TMO₂ sheets, that modify the sodium coordination sites; this structural modification induces a severe volume contraction ~15 %, accompanied by mechanical stresses that progressively lead to a capacity loss with cycling. Reduction in lattice cell volume has to be specifically connected to shrinking of sheets spacing along *c* axis due to deep de-sodiation, process already observed for P2-Na_{2/3}[Ni_{1/3}Mn_{2/3}]O₂¹⁷(image b) in Figure V-2). Nevertheless, this mechanism shows an interesting reversibility even with a conspicuous hysteresis due to dramatic cell parameters change. Electrochemical performances account for a starting specific capacity of 170 mAh·g⁻¹ averagely equal for all the Co level of doping, that moderately decreases during the first 60 cycles reaching 100 mAh·g⁻¹.

2.2. O3-type TMOs

As an excess of sodium precursor is employed during layered oxide preparation O3 phase is more likely to be obtained over a wide range of synthesis temperatures. O3-TMOs (M = Mn, Cr, Fe and Ni) are thus intrinsically provided with a higher starting content of sodium and could potentially deliver stable capacities suitable for commercial rechargeable cells. O3-NaCrO₂ has been widely investigated and the most promising results line up on capacities between 113 and 120 mA·g⁻¹, stable for 50 cycles¹⁸ or more, depending on the application of a carbon coating¹⁹. The carbon coating in the latter and other cases has proven to be extremely beneficial, a part from to increase electrode rate capabilities, also in preventing the transition metal ions leaching from the structure during cycling, a drawback imputable for capacity fading. Komaba et al., working on O3-NaNiO₂ pure and Mn-doped compounds, highlighted how as in P3-TMOs, likewise in O3-TMOs the potential window amplitude has a crucial role in limiting deleterious phase transitions. By 0.5 Mn doping of the structure better performances can be obtained in terms of rate capabilities and stability, stable specific capacities between 105 and 125 mAh·g⁻¹ can be obtained over a large range of current densities (240-4.8 mA·g⁻¹) in the 2.2-3.8 V vs. Na/Na⁺ window. Capacities drastically improves if the de-sodiation is pushed further up to 4.5 V, inevitably involving additional phase transition that for O3-NaNi_{0.5}Mn_{0.5}O₂ amount to 4, O3→O'3→P3→P'3→P3'' ,just as much the steps appearing in the potential profile²⁰. Despite these multiple steps involved, the material ensures a good reversibility, symptom of the high tolerance to phase transition of a layered structure in which covalent bonds are not involved in vertical ordering. The equilibriums Ni²⁺/Ni³⁺/Ni⁴⁺ are responsible for the charge compensation inside the structure during de-sodiation while Mn ions behave as inactive species. A benefit of Ni-rich layered phases resides also in the great difference in the ionic radius between Na⁺ (1.02 Å) and Ni²⁺ (0.69 Å), which likely avoids ion exchange between Na⁺ and Ni²⁺ in the layers, extending stability and the high-capacity delivery. An outstanding contribution to this topic has been given by Hwang et al.²¹ which in 2015 proposed a O3 cathode constituted by spheres made of radially aligned columnar structures with a gradient composition transitioning from an inner part richer in Na[Ni_{0.75}Co_{0.02}Mn_{0.23}]O₂ to an outer one where Na[Ni_{0.58}Co_{0.06}Mn_{0.36}]O₂ was the major phase (Figure V-3). To control the Ni concentration a co-precipitation synthetic procedure using Ni solutions at progressively increasing Ni concentrations was employed. By SEM probe analysis the Ni concentration

reduction, from 80 to 58 % by weight has been verified to occur along all the 6 μm long columnar structures. In a sodium half-cell configuration this material delivered reversible specific capacity of $157 \text{ mAh}\cdot\text{g}^{-1}$ at $15 \text{ mA}\cdot\text{g}^{-1}$, while in a whole-cell set up, coupled with a hard carbon anode, it demonstrated a high capacity retention of 80 % after 300 cycle. The improved stability has been addressed to the higher resistance of a Ni poorer phase to electrolyte corrosion compared to a richer phase, which, by many others, has been demonstrated to be more electrochemically active towards sodium intercalation. Among O3 phases, even Li-doped compounds such as $\text{Na}_{0.95}\text{Li}_{0.15}(\text{Ni}_{0.15}\text{Mn}_{0.55}\text{Co}_{0.1})\text{O}_2$ ²², $\text{Na}_{0.78}\text{Li}_{0.18}\text{Ni}_{0.25}\text{Mn}_{0.583}\text{O}_2$ ²³ as well as quaternary phases $\text{Na}(\text{Mn}_{0.25}\text{Fe}_{0.25}\text{Co}_{0.25}\text{Ni}_{0.25})\text{O}_2$ ²⁴, have been recently prepared and suggested as high energy cathodes, delivering $\sim 200 \text{ mAh}\cdot\text{g}^{-1}$ and improved reversibility compared to $\text{NaNi}_{0.33}\text{Mn}_{0.33}\text{Co}_{0.33}\text{O}_2$.

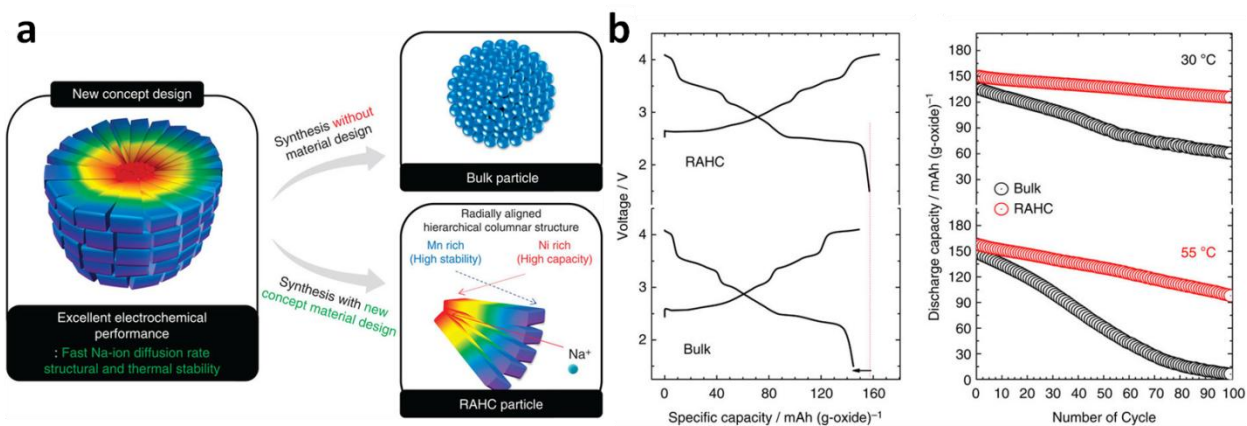


Figure V-3: a) material design of radially aligned spherical particles with a gradient composition and b) charge/discharge profile (left) and GCPL electrochemical characterization at different temperature (right) of radially aligned particle and a control bulk sample.

Concluding this brief overview of the layered TMO class, a note of merit has to be reserved to their chemical stability. Despite being highly promising for what concern their electrochemical behavior, they heavily suffer stability issues connected to moisture and CO_2 sensitiveness. As synthesized O3- $\text{NaNi}_{0.33}\text{Mn}_{0.33}\text{Co}_{0.33}\text{O}_2$ progressively convert into O1-phase to end up to P3 phase if aged in air for 300 days²⁵. Intercalation of water, instead, competes with Na insertion progressively excluding the latter and reducing its inserted amount below 0.33 per formula unit upon cycling as demonstrated for $\text{Na}_x \text{Ni}_{0.22}\text{Co}_{0.11}\text{Mn}_{0.66}\text{O}_2$. Also carbonated insertion, aided by water, has been discussed as a relevant factor that oxidizes Mn^{3+}

to Mn^{4+} and decreases reversibility and increases overpotential. Further improvements are thus required to make them not sensitive toward air for their mass production, effort recently put in developing a water-proof cathode material $\text{O}_3\text{-Na}_{0.9}[\text{Cu}_{0.22}\text{Fe}_{0.30}\text{Mn}_{0.48}] \text{O}_2$ are heading in the right direction²⁵.

3. Polyanionic compounds

3.1. Single-electron compounds

This class of compounds takes its name from the tetrahedral XO_4 and trigonal XO_3 groups that partially replace MO_6 octahedral metal clusters. A considerable quantity of transition metal phosphates, fluorophosphates, sulfates and pyrophosphates, just to cite a few, offers the opportunity to exploit their peculiar 3D open-framework structure created by edge or corner sharing polyhedrons, to host alkaline ions. Instead of vertically aligned slabs of covalently bonded atoms, as in layered transition metal oxides, straight or tangled channels with relatively low Na^+ diffusion energies permeate the structure. Due to the extensively higher rigidity of a covalent 3D network, polyanionic compounds show thermal stability and impressive resistance to oxidation without phase transitioning connected to sodium uptake. Added to this an overall higher operational voltage has been observed for polyanionic compounds either for lithium and sodium batteries.

Since the introduction of olivine LiFePO_4 compounds by Goodenough et al. in 1997 as a high energy cathode for lithium batteries²⁶, appeared clear that large PO_4^{3-} anion, thanks to its strong inductive effect and high electronegativity, has the power of sensibly increase the operational potential. Nevertheless NaFePO_4 , in its most thermodynamically stable maricite phase, does not show any activity due to the absence of a sufficiently wide pathway for sodium insertion. An electrochemically active triphylite-type phase obtained from alkaline cation exchange in olivine LiFePO_4 , delivered $125 \text{ mAh}\cdot\text{g}^{-1}$ with capacity retention of 88 % after 50 cycles²⁷. Interestingly, NaFePO_4 charge/discharge mechanism, occur with different potential profiles (see image b) in Figure V-4). If during discharge two plateaus are observed, during charge only one is present, indicating that sodiation and de-sodiation might occur through different electrochemical routes. The keystone has been demonstrated to be the intermediate phase $\text{Na}_{0.7}\text{FePO}_4$ and the difference in volumetric mismatch between sodium-free phase FePO_4 and $\text{Na}_{0.7}\text{FePO}_4$ (13.48 %) compared to $\text{Na}_{0.7}\text{FePO}_4$ and NaFePO_4 one (3.62 %). This means that

during charge, before FePO_4 starts to form a complete conversion of NaFePO_4 to $\text{Na}_{0.7}\text{FePO}_4$ must occur, thus the two-step process is clearly visible in potential curve even at high current rates. During discharge, instead, due to the low energetic barrier between sodium-containing phases, once the lattice mismatch between FePO_4 and $\text{Na}_{0.7}\text{FePO}_4$ is overcome, sodiation of FePO_4 and $\text{Na}_{0.7}\text{FePO}_4$ can happen concurrently and a one-step curve is achieved²⁸.

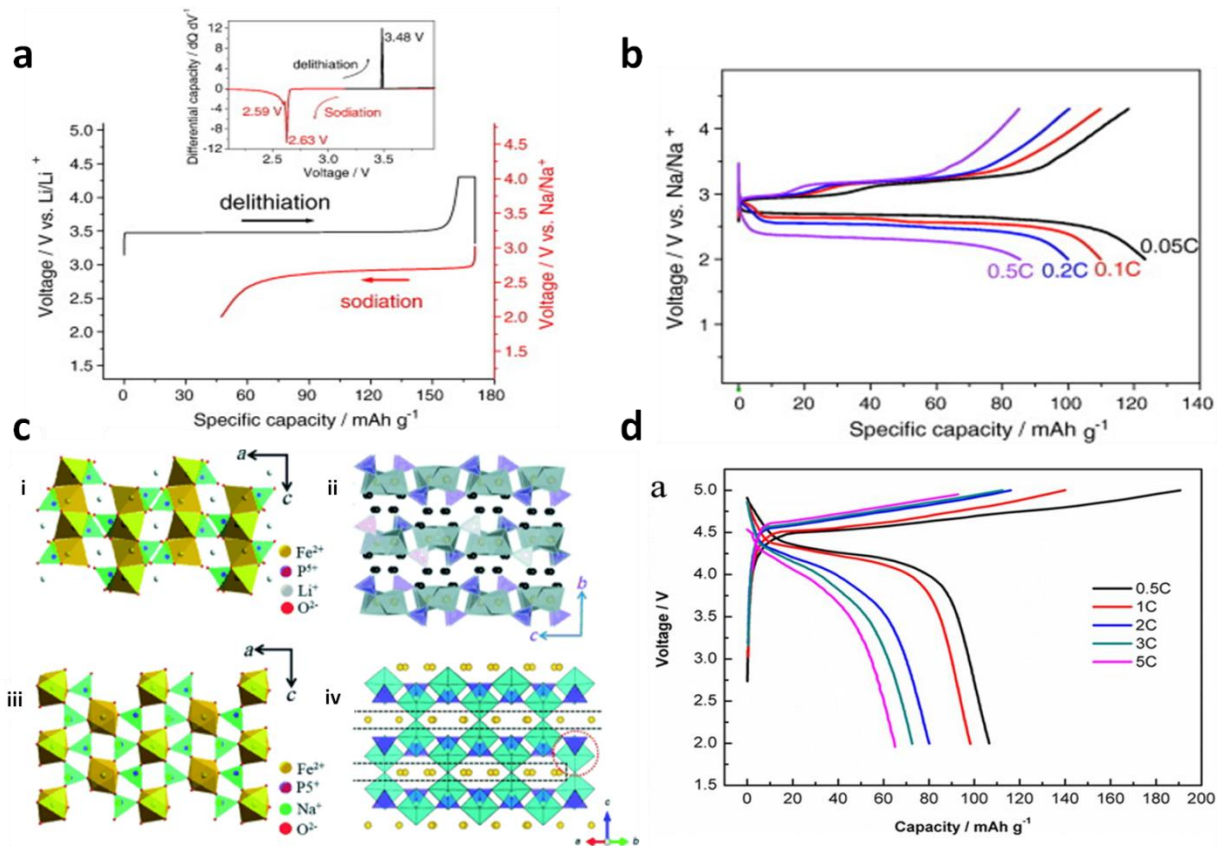


Figure V-4: a) mechanism of li-Na substitution in olivine LiFePO_4 structure, in order to maintain an electrochemically active phase to sodium insertion; b) electrochemical performances of NaFePO_4 at different charge/discharge rates, c(i) is related to olivine LiFePO_4 , c(ii) maricite NaFePO_4 in 101 plane, c(iii) refers to layered structure of $\text{Na}_2\text{FePO}_4\text{F}$ structured (FeO_6 octahedral shown in grey, PO_4 tetrahedral in purple, and sodium ion are depicted as black spheres), c(iv) is crystal structure of $\text{Na}_{1.5}\text{VPO}_{4.8}\text{F}_{0.7}$ with $\text{VO}_5\text{F}/\text{VO}_4\text{F}_2$ octahedral shown in cyan and yellow spheres representing the Na^+ ions, d) charge/discharge profile of layered $\text{Na}_2\text{CoPO}_4\text{F}$ structure.

An interesting and handy way to induce sensible lattice modification and create new sodium pathways in a phosphate structure is to insert another anion as a charge-balancing species. It has been done including fluorine atom in the new fluorophosphates class of material, recently investigated as cathode for both lithium and sodium-ion batteries. $\text{Na}_2\text{FePO}_4\text{F}$ ²⁹ and its

iso-structural $\text{Na}_2\text{CoPO}_4\text{F}$ ³⁰ have been recently proposed thanks to their interesting electrochemical properties as layered insertion materials in which intercalation mechanism proceeds with a solid-solution redox process rather than with a two-phase mechanism. The positive effect induced by F⁻ ion emerges from its pronounced electronegativity, which further enhance the inductive effect and thus the potential. Added to this, the higher ionicity of Na-F bond substantially modifies the coordination geometry of sodium as pseudo-octahedral. The exclusive layered structure of fluorine-enriched phosphates results in the uncommon coordination of transition metal ion (Fe, Co, or Mn) which for $\text{Na}_2\text{FePO}_4\text{F}$ consists in octahedrons whose vertex positions are occupied by four O and two F. The octahedrons are then arranged in face-sharing pairs ($\text{Fe}_2\text{O}_6\text{F}_3$). These units are corner-sharing connected (via fluorine atoms) to other pairs, forming chains along *a* direction. Corner-sharing PO_4^{3-} tetrahedra complete the stacking along *c* direction (image c) in Figure V-4). Further improvement were achieved by carbon-coating $\text{Na}_2\text{CoPO}_4\text{F}$ ³¹. Carbon coating inorganic particles is a procedure that, carried out by pyrolysis of a previously adsorbed organic molecule onto electrochemically active material surface, improves its electronic conduction and then the kinetic properties. In the latter case, $\text{Na}_2\text{CoPO}_4\text{F}/\text{C}$ nanoparticles showed interesting properties for what concern specific capacity of the first cycle, around $120 \text{ mAh}\cdot\text{g}^{-1}$, and a flat plateau at high potential, namely 4.5 V vs. Na/Na^+ (image d) in Figure V-4), although further effort should be put in extending its electrochemical stability.

NASICON(Na^+ superionic conductor)-type materials have been largely studied as solid electrolytes in high-temperature Na-S batteries. Since the exploratory work by Delmas et al.³², back in 1987, NASICON compounds with the general formula $\text{A}_x\text{M}_2(\text{XO}_4)_3$ (where A = Li, Na; M = V, Fe, Mn, Co and X = P,S,W) have been investigated to be applied as electrode material for both LIBs and NIBs. The most representative compound of the class, $\text{Na}_3\text{V}_2(\text{PO}_4)_3$, acquires a 3D framework of PO_4 tetrahedra and VO_6 octahedra. Electrochemical investigating of this composite showed two primary redox processes occurring at 3.4 and 1.6 V vs. Na/Na^+ highlighted by sharp peaks in cyclic voltammetry and corresponding to $\text{V}^{3+}/\text{V}^{4+}$ and $\text{V}^{2+}/\text{V}^{3+}$ redox couples. Galvanostatic cycling analysis (GCPL) revealed a reversible capacity of $90.9 \text{ mAh}\cdot\text{g}^{-1}$ after 10 cycles within the 2.7-3.8 V potential window, unfortunately the CE remains a major limit. Even though NASICON-type materials show an outstanding ionic conductivity, they are scarce electron conductors, for this reason electrochemical properties are severely

limited. Jiean et al. developed a ball-milling based method, followed by Ar-annealing, to deposit a thickness-tunable carbon coating, extremely beneficial for the material performances. Nano-structuring and carbon-coating have been many times demonstrated to be valid approaches to overcome poor cycle stability and rate capability. Following is reported a recent and particularly clever method employed to extend NASICON performances by means of electrospun carbon fiber embedding $\text{Na}_3\text{V}_2(\text{PO}_4)_3$ nanoparticles. The extremely simple preparation was made of two steps: i) electrospinning of an aqueous formulation containing both the carbon fiber precursor (PEO), and NASICON precursors (NaH_2PO_4 and NH_4VO_3) and ii) an annealing step in Ar atmosphere³³. The outcome has been a homogeneous dispersion of nanometric particles confined in the center axis of structurally stable carbon fibers and outstanding cycling performances at relatively high currents (2C) guaranteeing more than $70 \text{ mAh}\cdot\text{g}^{-1}$, provided at a stable potential of 3.4 V vs. Na/Na^+ . As for general phosphate compounds, also NASICON-type materials can be subjected to fluorination with some beneficial effects. An example is NASICON analogue $\text{Na}_3\text{V}_2(\text{PO}_4)_2\text{F}_3$, interesting for its high average voltage of 3.9 V and single-phase behavior with modest volume change (2 %). Other examples include $\text{Na}_2\text{FePO}_4\text{F}$ and $\text{Na}_{1.5}\text{VPO}_{4.8}\text{F}_{0.7}$ ³⁴. The latter revealed excellent cycling performances, with capacities retention of 95% and 84% after 100 and 500 cycles, respectively at 1C. Such a promising feature has been recognized to be related to small volume change, fast Na diffusion ($E_a \sim 0.35 \text{ eV}$) in *ab* plane and lack of ordered compositions within the redox window³⁵. Other NASICON-type materials includes $\text{Na}_3\text{Ti}_2(\text{PO}_4)_3$. Unlike previously cited NASICON material, and similarly to Ti based compounds, $\text{Na}_3\text{Ti}_2(\text{PO}_4)_3$ has been proposed as an high performing anode for SIBs, due to its low operational voltage plateaus ($< 1.0 \text{ V}$ vs Na/Na^+). The clear Faradaic process occurring at such low potential is attributed to $\text{Ti}^{3+}/\text{Ti}^{2+}$ redox couple, made available by the strong inductive effect of PO_4 ³⁶. Recently transition metal pyrophosphate arose as promising material proposed by Barpanda et al. $\text{Na}_2\text{FeP}_2\text{O}_7$ was the first of its kind, exhibiting a modest reversible capacity of $82 \text{ mAh}\cdot\text{g}^{-1}$ at C/20 in the potential window between 2.0 to 4.0 V vs. Na/Na^+ . In $\text{Na}_2\text{FeP}_2\text{O}_7$ lattice Fe^{2+} ions reside in two different sites and subsequently undergo oxidation to Fe^{3+} upon charge³⁷. Particularly, $\text{Na}_2\text{FeP}_2\text{O}_7$ supports quasi-3D sodium diffusion network with activation energy that slightly varies according to sites accessibility and transition metal substitution. Energy barriers are indeed lower for $\text{Na}_2\text{FeP}_2\text{O}_7$ ($< 0.49 \text{ eV}$) and higher for $\text{Na}_2\text{MnP}_2\text{O}_7$ (0.58 eV)³⁸. Other polymorphs and

analogues have been prepared, including β - $\text{Na}_2\text{MnP}_2\text{O}_7$ ³⁹ $\text{Na}_2\text{CoP}_2\text{O}_7$ ⁴⁰ but they all showed similar modest capacities ($\sim 80 \text{ mAh}\cdot\text{g}^{-1}$), poor cyclability, stability and rate capabilities. The unique structure of pyrophosphate, despite some of them show a layered structure⁴⁰, arises from large tunnels formed by alternate stacking of layers of FeO_6 octahedra and layers containing P_2O_7 units. Interestingly, together with a promising thermal stability up to $600 \text{ }^\circ\text{C}$, they show also a polymorphic transition happening at $560 \text{ }^\circ\text{C}$ with no oxygen evolution nor structural rupture, but with a phase change from a triclinic (P-1) to a monoclinic ($\text{P}2_1/\text{c}$) structure⁴¹. This stability by far exceeds that of layered oxides and is comparable to other polyanion compounds. Intrinsic stability of pyrophosphate building block is the responsible for its inertness and represents an added value to safety. More exotic polyanion compounds are those based on nitridophosphate group such as $\text{Na}_3\text{TiP}_3\text{O}_9\text{N}$ ⁴². $\text{Na}_3\text{TiP}_3\text{O}_9\text{N}$ was the first member of CUBICON family of materials that showed reversible Na^+ insertion at room temperature. Despite the sodium diffusivity inside CUBICON framework is considerably lower compared to lithium analogues, the ionic conductivity is good as well as thermal stability. Inside structure different sites and sodium paths are possible and substitution of Ti with other aliovalent transition metals with more than one redox pair achievable might extend the practical capacities, limited for $\text{Na}_3\text{TiP}_3\text{O}_9\text{N}$ to $80 \text{ mAh}\cdot\text{g}^{-1}$. As previously reported, $\text{P}2\text{-Na}_x[\text{Fe}_{0.5}\text{Mn}_{0.5}]\text{O}_2$ ⁴³ and $\text{O}3\text{-NaFeO}_2$ ⁴⁴ layered transition metal oxides suffer from low operating voltage, usually around 3.0 V . Yamada et al. recently reported an alluaudite-type structure cathode compound based on $(\text{SO}_4)^{2-}$ anion, $\text{Na}_4\text{Fe}_3(\text{SO}_4)_3$ ⁴⁵. The stable 3D structure made of Fe_2O_{10} dimers interconnected via $(\text{SO}_4)^{2-}$ groups, ensures relatively fast sodium diffusion happening at potential of 3.8 V vs Na/Na^+ , extraordinarily high for $\text{Fe}^{3+}/\text{Fe}^{2+}$ redox couple. Theoretic calculation suggested that a partial Co doping of the above mentioned compound could further raise the operational potential to 4.76 V , when a partial desodiation would occur. Full desodiation would have been predicted to happen at 5.76 V . Experimental detail are still lacking due to the difficulties in finding electrolyte solutions stable enough at such potential values⁴⁶.

3.2. Multi-electron compounds

Sidorenkite- $\text{Na}_3\text{MPO}_4\text{CO}_3$ (where $\text{M} = \text{Fe}^{2+}, \text{Co}^{2+}, \text{Ni}^{2+}, \text{V}^{2+}$ and Mn^{2+}) can undergo a two-electron redox reaction, along with the insertion of 2 Na^+ . $\text{Na}_3\text{MnPO}_4\text{CO}_3$ shows reversible Na^+ intercalation involving subsequent $\text{Mn}^{2+}/\text{Mn}^{3+}$ ($\sim 4.0 \text{ V}$) and $\text{Mn}^{3+}/\text{Mn}^{4+}$ ($\sim 3.4 \text{ V}$) redox reactions, providing good cyclability at relatively high average potential of 3.7 V and high

capacity ($\sim 125 \text{ mAh}\cdot\text{g}^{-1}$)⁴⁷. Due to the structural complexity of transition metal carbonophosphates a poor electron conductivity is expected and actually observed, for this reason nanostructuring of carbonophosphate particles and embedding in a conductive matrix (carbon black) has been recently proposed by simple ball milling method⁴⁸. The intimate connection thus achieved, guaranteed high capacity of $176.7 \text{ mAh}\cdot\text{g}^{-1}$ (92.5 % of the theoretical capacity derived from bi-electron transfer) even if with a 60 % by weight of carbon added to the solid mixture. Interesting capacities can be also extracted from $\text{Fe}^{3+}/\text{Fe}^{4+}$ and $\text{Fe}^{2+}/\text{Fe}^{3+}$ redox couples in $\text{Na}_3\text{FePO}_4\text{CO}_3$, with the highest redox process occurring at 4.5 V vs. Na/Na^+ , safely within the stability window of the most commonly used electrolyte solution in SIBs. Unfortunately the two redox plateaus are separated by a considerably high potential gap (~ 1.8 V) that enormously curbs the energy density of the material⁴⁹. During sodium extraction/insertion no change in lattice structure is observed⁵⁰, suggesting that the whole process is a single-phase one. To complete the brief report on multi-electron polyanion compounds, vanadium fluorophosphates are worth to be mentioned. Extraordinary electrochemical performances have been obtained from Na^+ -insertion reaction in $\text{Na}_{1.5}\text{VPO}_{4.8}\text{F}_{0.7}$. In the work by Kang et al., indeed, the multi-electron nature of vanadium reduction is discussed. Due to excess in specific capacity of pure $\text{Na}_{1.5}\text{VPO}_{4.8}\text{F}_{0.7}$ obtained during the first sodiation compared to theoretical capacity of a one-electron process ($\sim 134 \text{ mAh}\cdot\text{g}^{-1}$ vs $129.1 \text{ mAh}\cdot\text{g}^{-1}$), a multi-electron mechanism is hypothesized. This conclusion is backed up by theoretical calculation that expects 1.2 electrons per formula unit to be transferred during the sodiation/de-sodiation, for a theoretical specific capacity of $155.6 \text{ mAh}\cdot\text{g}^{-1}$ ⁵¹. From galvanostatic cycling, two distinct plateaus evolve at 3.61 and 4.02 V vs. Na/Na^+ . From $\text{Na}_{1.5}\text{VPO}_{4.8}\text{F}_{0.7}$ crystal structure refinement appears clear that corner-sharing PO_4 tetrahedral and $\text{VO}_5\text{F}/\text{VO}_4\text{F}_2$ octahedral units (where vanadium oxidation number is changing) construct the 3D pseudolayered open framework (Figure V-5). Vanadium aided by the inductive effect of fluoride, acts as a high potential redox center, conferring an extraordinarily

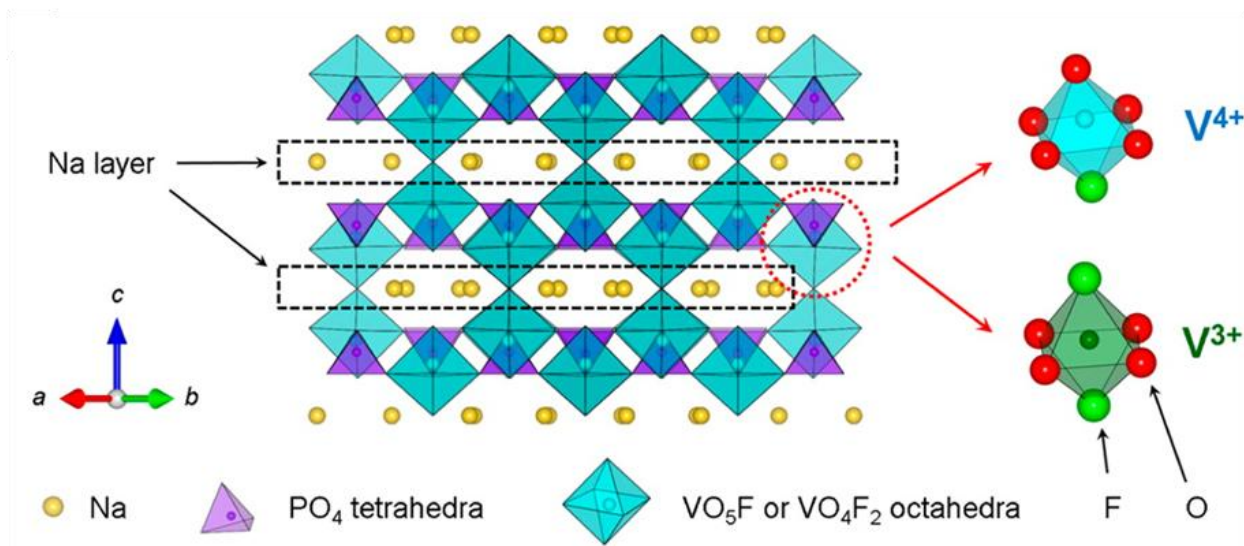


Figure V-5: Crystal structure of $\text{Na}_{1.5}\text{VPO}_{4.8}\text{F}_{0.7}$, with the two different environment built around V^{4+} and V^{3+} centers (i.e., VO_5F and VO_4F_2 octahedra respectively). Na, V, P, O and F are depicted as yellow, cyan, purple, red and green spheres, respectively.

positive value to the half cell operational voltage. As a consequence, thanks also to the after all modest specific capacity ($130 \text{ mAh}\cdot\text{g}^{-1}$ at 0.2 C), $\text{Na}_{1.5}\text{VPO}_{4.8}\text{F}_{0.7}$ is one of the positive SIBs material with the highest theoretical energy density as can be easily seen in image a) in Figure V-6). Added to this, among the investigated cathode material for LIBs and CIBs, reports also the lowest and almost negligible volume change during sodiation/de-sodiation (2.9 %) as can be spotted in the histogram in image c) in figure below. Kim and co-workers recently investigated the interaction between $\text{Na}_3\text{V}_2\text{O}_{2x}(\text{PO}_4)_2\text{F}_{3-2x}$ and carbon polymorphs (MWCNT, rGO and Super P), in order to overcome the intrinsic low electronic conduction. They found out that carbon nanotubes would generate a positive effect guaranteeing a stable capacity of $98 \text{ mAh}\cdot\text{g}^{-1}$, and interesting kinetic properties⁷.

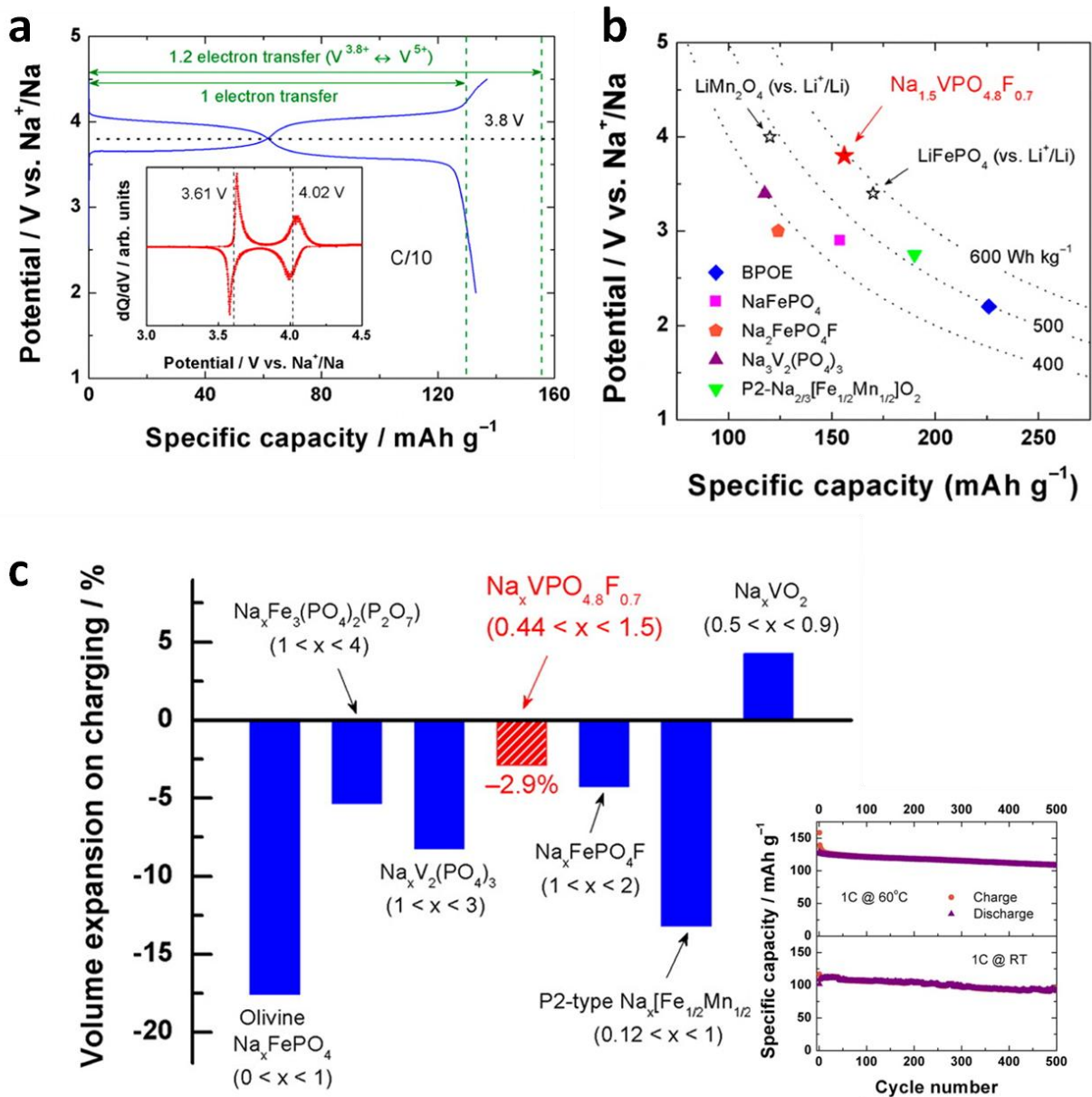


Figure V-6: a) charge/discharge profile of Na_{1.5}VPO_{4.8}F_{0.7} in the one-electron window, inset of the figure reports the differential capacity graph; b) potential vs. specific capacity plot of widely investigated cathode for LIBs among which Na_{1.5}VPO_{4.8}F_{0.7} is inserted as element of comparison, (BPOE = polyethylene oxide based battery); c) volume expansion for recently investigated cathodes for SIBs and correspondent stoichiometric sodium composition, in the bottom right corner cycling stability at room temperature and at 60 °C is reported.

4. Bibliography

- (1) Newmann, G. H.; Klemann, L. P. Ambient Temperature Cycling of an Na - TiS₂ Cell. *J. Electrochem. Soc.* **1980**, *127* (10), 2097–2099.
- (2) Berthelot, R.; Carlier, D.; Delmas, C. Electrochemical Investigation of the P2–Na_xCoO₂ Phase Diagram. *Nat. Mater.* **2011**, *10* (1), 74–80.
- (3) Braconnier, J.-J.; Delmas, C.; Fouassier, C.; Hagenmuller, P. Comportement Electrochimique Des Phases Na_xCoO₂. *Mater. Res. Bull.* **1980**, *15* (12), 1797–1804.
- (4) Ruffo, R.; Fathi, R.; Kim, D. K. J.; Jung, Y. H.; Mari, C. M.; Kim, D. K. J. Impedance Analysis of Na_{0.44}MnO₂ Positive Electrode for Reversible Sodium Batteries in Organic Electrolyte. *Electrochim. Acta* **2013**, *108*, 575–582.
- (5) D’Arienzo, M.; Ruffo, R.; Scotti, R.; Morazzoni, F.; Mari, C. M.; Polizzi, S. Layered Na(0.71)CoO(2): A Powerful Candidate for Viable and High Performance Na-Batteries. *Phys. Chem. Chem. Phys.* **2012**, *14* (17), 5945–5952.
- (6) Ryu, W.-H.; Jung, J.-W.; Park, K.; Kim, S.-J.; Kim, I.-D. Vine-like MoS₂ Anode Materials Self-Assembled from 1-D Nanofibers for High Capacity Sodium Rechargeable Batteries. *Nanoscale* **2014**, *6*, 10975–10981.
- (7) Kumar, P. R.; Jung, Y. H.; Kim, D. K. Influence of Carbon Polymorphism towards Improved Sodium Storage Properties of Na₃V₂O_{2x}(PO₄)₂F_{3-2x}. *J. Solid State Electrochem.* **2016**.
- (8) Ung, Y. H.; Lim, C. H.; Kim, D. K. Graphene-Supported Na₃V₂(PO₄)₃ as a High Rate Cathode Material for Sodium-Ion Batteries. *J. Mater. Chem. A* **2013**, *1* (37), 11350.
- (9) Jung, Y. H.; Lim, C. H.; Kim, J.-H.; Kim, D. K. Na₂FeP₂O₇ as a Positive Electrode Material for Rechargeable Aqueous Sodium-Ion Batteries. *RSC Adv.* **2014**, *4* (19), 9799.
- (10) Lee, H.-W.; Wang, R. Y.; Pasta, M.; Lee, S. W.; Liu, N.; Cui, Y. Manganese Hexacyanomanganate Open Framework as a High-Capacity Positive Electrode Material for Sodium-Ion Batteries. *Nat. Commun.* **2014**, *5* (5280).
- (11) Deng, W.; Liang, X.; Wu, X.; Qian, J.; Cao, Y.; Ai, X.; Feng, J.; Yang, H. A Low Cost, All-Organic Na-Ion Battery Based on Polymeric Cathode and Anode. *Sci. Rep.* **2015**, *3* (2671).
- (12) Lei, Y.; Li, X.; Liu, L.; Ceder, G. Synthesis and Stoichiometry of Different Layered Sodium Cobalt Oxides. *Chem. Mater.* **2014**, *26* (18), 5288–5296.

- (13) Shibata, T.; Fukuzumi, Y.; Kobayashi, W.; Moritomo, Y. Fast Discharge Process of Layered Cobalt Oxides due to High Na^+ Diffusion. *Sci. Rep.* **2015**, *5*:9006.
- (14) Delmas, C.; Mendiboure, A.; Hagenmuller, P. Electrochemical Intercalation and Deintercalation of Na_xMnO_2 Bronzes. *J. Solid State Chem.* **1985**, *57*, 323–331.
- (15) Lu, Z.; Dahn, J. R. In Situ X-Ray Diffraction Study of $\text{P}2 - \text{Na}_{2/3} [\text{Ni}_{1/3} / 3\text{Mn}_{2/3}] \text{O}_2$. *J. Electrochem. Soc.* **2001**, *148*, A1225.
- (16) Jung, Y. H.; Christiansen, A. S.; Johnsen, R. E.; Norby, P.; Kim, D. K. In Situ X-Ray Diffraction Studies on Structural Changes of a P2 Layered Material during Electrochemical Desodiation/Sodiation. *Adv. Funct. Mater.* **2015**, 3227–3237.
- (17) Lee, D. H.; Xua, J.; Meng, Y. S. An Advanced Cathode for Na-Ion Batteries with High Rate and Excellent Structural Stability. *Phys. Chem. Chem. Phys.* **2013**, *15* (9), 3304–3312.
- (18) Chen, C.-Y.; Matsumoto, K.; Nohira, T.; Hagiwara, R.; Fukunaga, A.; Sakai, S.; Nitta, K.; Inazawa, S. Electrochemical and Structural Investigation of NaCrO_2 as a Positive Electrode for Sodium Secondary Battery Using Inorganic Ionic Liquid NaFSA–KFSA. *J. Power Sources* **2013**, *237*, 52–57.
- (19) Yu, C.-Y.; Park, J.-S.; Jung, H.-G.; Chung, K.-Y.; Aurbach, D.; Sun, Y.-K.; Myung, S.-T. NaCrO_2 Cathode for High-Rate Sodium-Ion Batteries. *Energy Environ. Sci. Energy Environ. Sci* **2015**, *8*, 2019–2026.
- (20) Komaba, S.; Yabuuchi, N.; Nakayama, T.; Ogata, A.; Ishikawa, T.; Nakai, I. Study on the Reversible Electrode Reaction of $\text{Na}_{1-x}\text{Ni}_{0.5}\text{Mn}_{0.5}\text{O}_2$ for a Rechargeable Sodium-Ion Battery.
- (21) Hwang, J.-Y.; Oh, S.-M.; Myung, S.-T.; Chung, K. Y.; Belharouak, I.; Sun, Y.-K. Radially Aligned Hierarchical Columnar Structure as a Cathode Material for High Energy Density Sodium-Ion Batteries. *Nat. Commun.* **2015**, *6*, 6865.
- (22) Kataoka, R.; Mukai, T.; Yoshizawa, A.; Sakai, T. Development of High Capacity Cathode Material for Sodium Ion Batteries $\text{Na}_{0.95}\text{Li}_{0.15}(\text{Ni}_{0.15}\text{Mn}_{0.55}\text{Co}_{0.1})\text{O}_2$. *J. Electrochem. Soc.* **2013**, *160* (6), A933–A939.
- (23) Liu, H.; Xu, J.; Ma, C.; Meng, Y. S. A New O3-Type Layered Oxide Cathode with High Energy/power Density for Rechargeable Na Batteries. *Chem. Commun. Chem. Commun* **2015**, *51* (51), 4693–4696.

- (24) Li, X.; Wu, D.; Zhou, Y.-N.; Liu, L.; Yang, X.-Q.; Ceder, G. *O3-Type Na(Mn_{0.25}Fe_{0.25}Co_{0.25}Ni_{0.25})O₂: A Quaternary Layered Cathode Compound for Rechargeable Na Ion Batteries*; 2014; Vol. 49.
- (25) Sathiya, M.; Hemalatha, K.; Ramesha, K.; Tarascon, J.-M.; Prakash, A. S. Synthesis, Structure, and Electrochemical Properties of the Layered Sodium Insertion Cathode Material: NaNi^{1/3}Mn^{1/3}Co^{1/3}O₂. *Chem. Mater.* **2012**, *24* (10), 1846–1853.
- (26) Padhi, A. K.; Nanjundaswamy, K. S.; Goodenough, J. B. Phospho-Olivines as Positive-Electrode Materials for Rechargeable Lithium Batteries. *J. Electrochem. Soc.* **1997**, *144* (4), 1188.
- (27) Casas-Cabanas, M.; Roddatis, V. V.; Saurel, D.; Kubiak, P.; Carretero-González, J.; Palomares, V.; Serras, P.; Rojo, T. Crystal Chemistry of Na Insertion/deinsertion in FePO₄–NaFePO₄. *J. Mater. Chem.* **2012**, *22* (34), 17421.
- (28) Oh, S.-M.; Myung, S.-T.; Hassoun, J.; Scrosati, B.; Sun, Y.-K. Reversible NaFePO₄ Electrode for Sodium Secondary Batteries. *Electrochem. commun.* **2012**, *22*, 149–152.
- (29) Kawabe, Y.; Yabuuchi, N.; Kajiyama, M.; Fukuhara, N.; Inamasu, T.; Okuyama, R.; Nakai, I.; Komaba, S. *Synthesis and Electrode Performance of Carbon Coated Na₂FePO₄F for Rechargeable Na Batteries*; 2011; Vol. 13.
- (30) Ellis, B. L.; Makahnouk, W. R. M.; Rowan-Weetaluktuk, W. N.; Ryan, D. H.; Nazar, L. F. Crystal Structure and Electrochemical Properties of A₂MPO₄F Fluorophosphates (A = Na, Li; M = Fe, Mn, Co, Ni) †. *Chem. Mater.* **2010**, *22* (3), 1059–1070.
- (31) Zou, H.; Li, S.; Wu, X.; Mcdonald, M. J.; Yang, Y. Spray-Drying Synthesis of Pure Na₂CoPO₄F as Cathode Material for Sodium Ion Batteries. *ECS Electrochem. Lett.* **2015**, *4* (6), 53–55.
- (32) Delmas, C.; Nadiri, A.; Soubeyroux, J. L. The Nasicon-Type Titanium Phosphates A₂Ti₂(PO₄)₃ (A=Li, Na) as Electrode Materials. *Solid State Ionics* **1988**, *28*, 419–423.
- (33) Liu, J.; Tang, K.; Song, K.; Van Aken, P. A.; Yu, Y.; Maier, J. Electrospun Na₃V₂(PO₄)₃/C Nanofibers as Stable Cathode Materials for Sodium-Ion Batteries.
- (34) Kundu, D.; Telaie, E.; Duffort, V.; Nazar, L. F. The Emerging Chemistry of Sodium Ion Batteries for Electrochemical Energy Storage. *Angew. Rev.* **2015**, *54*, 3431–3448.
- (35) Park, Y.-U.; Seo, D.-H.; Kwon, H.-S.; Kim, B.; Kim, J.; Kim, H.; Kim, I.; Yoo, H.-I.; Kang, K. A New High-Energy Cathode for a Na-Ion Battery with Ultrahigh Stability. *J.*

- Am. Chem. Soc.* **2013**, *135* (37), 13870–13878.
- (36) Wang, D.; Liu, Q.; Chen, C.; Li, M.; Meng, X.; Bie, X.; Wei, Y.; Huang, Y.; Du, F.; Wang, C.; Chen, G. NASICON-Structured $\text{NaTi}_2(\text{PO}_4)_3$ @C Nanocomposite as the Low Operation-Voltage Anode Material for High-Performance Sodium-Ion Batteries.
- (37) Barpanda, P.; Ye, T.; Nishimura, S.; Chung, S.-C.; Yamada, Y.; Okubo, M.; Zhou, H.; Yamada, A. Sodium Iron Pyrophosphate: A Novel 3.0V Iron-Based Cathode for Sodium-Ion Batteries. *Electrochem. commun.* **2012**, *24*, 116–119.
- (38) Clark, J. M.; Barpanda, P.; Yamada, A.; Islam, M. S. Sodium-Ion Battery Cathodes $\text{Na}_2\text{FeP}_2\text{O}_7$ and $\text{Na}_2\text{MnP}_2\text{O}_7$: Diffusion Behaviour for High Rate Performance. *J. Mater. Chem. A* **2014**, *2* (30), 11807.
- (39) Barpanda, P.; Ye, T.; Avdeev, M.; Chung, S.; Yamada, A. A New Polymorph of $\text{Na}_2\text{MnP}_2\text{O}_7$ as a 3.6 V Cathode Material for Sodium-Ion Batteries. *J. Mater. Chem. A* **2013**, *1* (13), 4194.
- (40) Barpanda, P.; Lu, J.; Ye, T.; Kajiyama, M.; Chung, S.-C.; Yabuuchi, N.; Komaba, S.; Yamada, A. A Layer-Structured $\text{Na}_2\text{CoP}_2\text{O}_7$ Pyrophosphate Cathode for Sodium-Ion Batteries. *RSC Adv.* **2013**, *3* (12), 3857.
- (41) Chung, S.; Yamada, Y.; Yamada, A. $\text{Na}_2\text{FeP}_2\text{O}_7$: A Safe Cathode for Rechargeable Sodium-Ion Batteries. *Chem. Mater.* **2013**.
- (42) Liu, J.; Chang, D.; Whitfield, P.; Janssen, Y.; Yu, X.; Zhou, Y.; Bai, J.; Ko, J.; Nam, K.-W.; Wu, L.; Zhu, Y.; Feygenson, M.; Amatucci, G.; Van der Ven, A.; Yang, X.-Q.; Khalifah, P. Ionic Conduction in Cubic $\text{Na}_3\text{TiP}_3\text{O}_9\text{N}$, a Secondary Na-Ion Battery Cathode with Extremely Low Volume Change. *Chem. Mater.* **2014**, *26* (10), 3295–3305.
- (43) Yabuuchi, N.; Kajiyama, M.; Iwatate, J.; Nishikawa, H.; Hitomi, S.; Okuyama, R.; Usui, R.; Yamada, Y.; Komaba, S. P2-Type $\text{Na}_x[\text{Fe}_{1/2}\text{Mn}_{1/2}]\text{O}_2$ Made from Earth-Abundant Elements for Rechargeable Na Batteries. *Nat. Mater.* **2012**, *11* (6), 512–517.
- (44) Zhao, J.; Xu, J.; Lee, D. H.; Dimov, N.; Meng, Y. S.; Okada, S. Electrochemical and Thermal Properties of P2-Type $\text{Na}_{2/3}\text{Fe}_{1/3}\text{Mn}_{2/3}\text{O}_2$ for Na-Ion Batteries-Type $\text{Na}_{2/3}\text{Fe}_{1/3}\text{Mn}_{2/3}\text{O}_2$ Electrochemical Properties X-Ray Absorption Spectroscopy Thermal Stability. *J. Power Sources* **2014**, *264*, 235–239.
- (45) Barpanda, P.; Oyama, G.; Nishimura, S.; Chung, S.-C.; Yamada, A. A 3.8-V Earth-Abundant Sodium Battery Electrode. *Nat. Commun.* **2014**, *5*, 4358.

- (46) Dwibedi, D.; Gond, R.; Dayamani, A.; Araujo, R. B.; Chakraborty, S.; Ahuja, R.; Barpanda, P. Na_{2.32}Co_{1.84}(SO₄)₃ as a New Member of the Alluaudite Family of High-Voltage Sodium Battery Cathodes. *Dalt. Trans.* **2017**, 2, 510.
- (47) Chen, H.; Hao, Q.; Zivkovic, O.; Hautier, G.; Du, L.-S.; Tang, Y.; Hu, Y.-Y.; Ma, X.; Grey, C. P.; Ceder, G. Sidorenkite (Na₃MnPO₄CO₃): A New Intercalation Cathode Material for Na-Ion Batteries.
- (48) Wang, C.; Sawicki, M.; Emani, S.; Liu, C.; Shaw, L. L. Na₃MnCO₃PO₄ – A High Capacity, Multi-Electron Transfer Redox Cathode Material for Sodium Ion Batteries
Keywords: Na₃MnCO₃PO₄ Carbonophosphates Na-Ion Batteries Electronic Conductivity. *Electrochim. Acta* **2015**, 161, 322–328.
- (49) Chen, H.; Hautier, G.; Jain, A.; Moore, C.; Kang, B.; Doe, R.; Wu, L.; Zhu, Y.; Tang, Y.; Ceder, G. Carbonophosphates: A New Family of Cathode Materials for Li-Ion Batteries Identified Computationally. *Chem. Mater.* **2012**, 24 (11), 2009–2016.
- (50) Huang, W.; Zhou, J.; Li, B.; Ma, J.; Tao, S.; Xia, D.; Chu, W.; Wu, Z. Detailed Investigation of Na_{2.24}FePO₄CO₃ as a Cathode Material for Na-Ion Batteries. *Sci. Rep.* **2014**, 4, 4188.
- (51) Park, Y.-U.; Seo, D.-H.; Kwon, H.-S.; Kim, B.; Kim, J.; Kim, H.; Kim, I.; Yoo, H.-I.; Kang, K. A New High-Energy Cathode for a Na-Ion Battery with Ultrahigh Stability. *J. Am. Chem. Soc.* **2013**, 135, 13870–13878.

CHAPTER VI: Co_3O_4 negative electrode material for SIBs: investigation of conversion reaction mechanism and morphology-performances correlation

1. Introduction

Transition metal oxides have recently aroused a renewed and increasing interest as conversion anode materials for sodium ion batteries. Being their electrochemical performances strongly dependent on morphological aspects as described in Chapter IV, has been here proposed a straightforward approach to modulate morphological characteristics of a transition metal oxide (Co_3O_4) using a low cost synthetic route. The as obtained optimized morphology allows the realization of high practical specific capacities higher than $500 \text{ mAh}\cdot\text{g}^{-1}$ after 50 cycles, and represents a valid candidate for further optimization. This outstanding result is uniquely ascribable to peculiar morphological characteristics of the investigated conversion material, since no conductive matrix substrate has been employed in the synthesis. In this section is also addressed the material chemical pre-treatment as a possible solution to large irreversible capacity experimented in the first cycle. As a matter of fact, the importance of the electrode pre-sodiation treatment for conversion materials, has been pointed out as well: it has been indeed demonstrated that it sensibly decreases the irreversible capacity correlated to the first cycle and improves cycle ability.

2. Background

In order to recall the technologic landscape in which oxide-based conversion materials as anode in SIBs find their place, a brief review of the most investigated anode materials for sodium-ion rechargeable batteries, is here proposed. For a more exhaustive analysis of the categories of materials here only sketched, the reader is invited to refer to Chapter III.

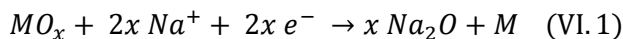
Lithium-ion battery (LIB) technology has ended to cover, in almost 25 years, the 95 % of the whole battery market thanks to its versatility, high round trip efficiency and adequate energy density. Its market permeability relates to portable electrical goods (mobile phones, laptops, cameras, working tools)¹, where a high energy density is desirable over a high power

density, as well as to the automotive field. The recent positive momentum for LIBs technology applied to cars propulsion (Hybrid electric vehicles HEV, Plug-in hybrid electric vehicle PHEV, and Electric vehicles EV) is expected to lead in a few years to a dramatic increase in LIBs technology exploitation. This aspect, together with political issues related to inhomogeneity distribution of raw materials for LIB manufacturing, concurred to arise a growing concern in relation to the future sustainability of this technology²⁻⁴. The Sodium-ion battery (SIB) system seems to be a valid and more sustainable alternative to Lithium economy, according to the easier procurement of raw materials and the rather similar chemistry between Li and Na^{5,6}. SIBs would be a better choice, especially for large scale application, such as stationary storage connected to renewable power sources, in which costs are critical⁷. Developing efficient SIBs worthwhile to be employed in on-grid storage and other fields may lower the exploitation load over LIBs technology, reducing the strategic interest for the raw materials. Many efforts have already been made in the design and characterization of both anode and cathode materials for Na-ion batteries so far⁸⁹. For what concern cathode side of SIBs, promising results have been achieved in relation to the stability and charge retention of electroactive intercalation materials as widely described in the review by Masquelier *et al.*¹⁰.

In this extensive dissertation the authors go through several promising polyanionic ((PO₄)²⁻, (SiO₄)⁴⁻ and (SO₄)²⁻) based compounds proposed in recent years as cathode materials in LIBs, in the place of fully investigated transition metal oxides (Li_{1-x}MO₂ with M = Co, Ni, Fe, Mn). The performances of the latter in a Na environment are also collected. As a result, polyanion frameworks are capable of an efficiently sodium cations intercalation, with a high structure retention through cycling. The advantages in their utilization resides also in the polyanion inductive effect that boosts the cathode operating voltage, higher stability, large variety of obtainable structure and atoms arrangements and the lower costs of manufacturing. Anode materials, conversely, still represent a challenging topic needy to be investigated. Many solutions have been proposed to overcome the intrinsic limits of negative electrode materials, namely the low practical specific charge and the fast degradation of electrode characteristics. Other delicate features that have to be taken into consideration are the operating voltage, that must be suitable for the utilization of the investigated compound as an anode inside the cell and the problematic irreversible capacity related to the first cycle. For these reasons several classes of materials have been taken into account^{6,11}. Transposition of graphitic anodes already

employed in LIBs to sodium environment has been considered at first glance: nevertheless, since intercalation of the larger sodium ion into graphite sheets structure induces exfoliation, nano-structured hard-carbons have been investigated instead¹²⁻¹⁴. The performances are controversial and are affected by high irreversible capacity during the first charge/discharge loop and sloping charge/discharge profiles. Sodium alloying with 14th and 15th group elements (Sb^{15,16}, Sn¹⁷, Ge and In¹⁸) has been also exploited to obtain anode materials for SIBs: the high theoretical capacity of sodium rich phase Na-Sn alloy (847 mAh·g⁻¹ for Na₁₅Sn₄) led to the study of the performances in sodium half-cell of a SnSb particles dispersion over a carbonaceous matrix. Xiao *et al.* obtained a reversible alloying of Na and a stable capacity of ~400 mAh·g⁻¹¹⁹.

Transition metal oxides (MO_x with M=Fe²⁰, Co²¹, Cu²²), with electrochemical active transition metal ions, have drawn the attention as possible low cost and easy-to-manufacture SIB conversion anode materials. Their reactivity, electrochemical performances, and effects of morphology and structural properties on lithium storage, have been widely analyzed. On the contrary, same type of studies related to reactivity with Na, remain poorly explored. The study of Na reactivity with spinel Co₃O₄ nanoparticles has been recently reported by few groups, and a first understanding of the possible undergoing conversion mechanism has been hypothesised. The general reaction proposed for the sodium reactivity with spinel type oxides and other conversion materials is here recalled¹¹:



Notable aspects of the reaction above reported are its reversibility and the theoretical capacity of oxides (> 600 mAh·g⁻¹), considerably higher if compared to carbonaceous materials or intercalation materials for which capacity is limited by the number of available sites for Na⁺ insertion⁶(~300 mAh·g⁻¹). Spinel Co₃O₄, thanks to its high theoretical capacity (~890 mAh·g⁻¹), has aroused, since the early stages of LIB technology development, a great interest as a high capacity conversion anode material^{21,23,24}. Along with the advantage of having a high theoretical capacity comes also the challenge represented by the large particle volume variation during sodiation which leads rapidly to a considerable fade in material properties. In a recent work by Sun *et al.* a Co₃O₄ porous particles/graphene compound has been investigated as active anode material in a sodium ion battery²⁵. The hybrid compound ensured a good capacity (~500

mAh·g⁻¹) and good cycle stability at the current density of 25 mAh·g⁻¹. Owing to the volume variation connected to conversion mechanism, morphology of active material particles acquires a primary importance. Crystal shape, exposed facets, hierarchical structures and porosity of particles are essential features to be taken into consideration when it comes to minimize the deleterious effect of excessive volume change induced stresses. Effect of different morphology of Co₃O₄ particles over the electrochemical performances has been highlighted in the case of lithium batteries, and the better performances of polycrystalline hierarchical structure compared to single nano-crystals has been confirmed²⁶. Another negative aspect related to conversion materials is the irreversible capacity involved in the first charge/discharge loop. It determines a significant drop in the residual capacity available for the following cycles. By many, this behaviour has been addressed to the SEI formation which involves a non-negligible amount of active species.

In the present work, three different morphologies of spinel Co₃O₄ have been prepared. These have been synthesized using facile and easily scalable synthetic routes and they have been deeply investigated under the electrochemical point of view as anode materials in metallic sodium half-cells; conclusions related to the morphology influence have thus been made. The problem related to the first cycle irreversible capacity has also been tackled. In particular, the effect of a chemical pre-sodiation of the Co₃O₄ electrode has been taken into consideration.

3. Experimental

3.1. Material synthesis

Hydrothermal synthesis technique is known to be a versatile synthetic route that allows to obtain a large variety of different morphologies by changing operating conditions, namely temperature, volume (fill factor), hydrothermal step time, precursor and capping agents concentration and pH^{24,26}. In studying spinel Co₃O₄ morphology effects over the electrochemical behaviour, several structures have been prepared and tested. In this work, the preparation and characterization of just the three most significant ones, according to their electrochemical performances, are reported. The three samples are here listed with their codes: NR7, NR16 and NR21. All the chemicals were of analytical grade and were used as received. The cobalt precursor, Co(NO₃)₂·6 H₂O (ACS reagent, ≥98 %, Sigma-Aldrich®) has been dissolved in deionized water together with CO(NH₂)₂ (ACS reagent, Sigma-Aldrich®), used as

a mineralizing agent, and the solution has been transferred to a 100 mL Teflon lined stainless steel autoclave. The autoclave has been heated starting from room temperature using a heating rate of $4^{\circ}\cdot\text{min}^{-1}$, and after the dwelling at the set-point temperature (according to the synthetic route) it has been let to cool down naturally to room temperature again. The operational parameters for the three samples mentioned above are reported in the Table VI-1. After the hydrothermal step the intermediate was collected by centrifugation from the autoclave, washed several times with deionized water and ethanol and finally dried in an oven at 60°C , overnight. The obtained product underwent calcination in air at 400°C for 12 hours.

Table VI-1: hydrothermal step parameters employed for the Co intermediated synthesis.

Sample	Co(NO ₃) ₂ ·6 H ₂ O (mol L ⁻¹)	CO(NH ₂) ₂ (mol L ⁻¹)	Autoclave fill factor (%)	Hydrothermal step
NR7	0.023	0.12	70	160 °C, 12 hours
NR16	0.022	0.11	85	100 °C, 12 hours
NR21	0.12	-	85	180°C, 5 hours

3.2. Samples characterization

Samples morphology was evaluated using a SEM (HITACHI, S-4800) and TEM (FEI, Tecnai G² F30 S-Twin) micrographs, while the crystal phases of the samples were checked via X-ray powder diffraction using a Rigaku diffractometer (D/Max-2500, 0.154 nm Cu K- α radiation). The diffraction patterns were collected in the 2θ window between 15° and 70° , at $3^{\circ}\cdot\text{min}^{-1}$ scan rate. In order to monitor the active material phase changes over cycles, X-ray diffraction has been performed on cycled electrodes. XRD measurements on electrodes have been performed using a Rigaku MiniFlex 600 diffractometer (0.154 nm Cu K- α radiation). For this analysis the diffraction patterns were collected in the 2θ window between 20° and 80° , at $3^{\circ}\cdot\text{min}^{-1}$ scan rate. AAS (Atomic Absorption Spectroscopy) elemental analysis (microCUBE, Elementar) was employed to estimate the amount of sodium included in the pre-sodiated sample in relation to the electrode exposure time to metallic sodium.

3.3. Electrochemical measurements

Electrodes for electrochemical measurements were assembled by mixing the as prepared active material (nanostructured Co₃O₄) with carbon matrix (Super P, MM Carbon) and

polyacrylic acid (average $M_v \sim 450000$, Sigma-Aldrich®) as the binder, with the weight ratio of 75:17:8. As dispersing solvent, 1-methyl-2-pyrrolidinone (ACS reagent, 99 %, Aldrich®) was employed. Polyacrylic acid has been chosen as the binder according to the recent findings concerning the binder-active material coupling²⁷. Polyacrylic acid better accommodates volume change-related mechanical stresses of oxide-based materials than PVDF, a well-known binder employed in lithium-ion batteries electrode formulation where the active material is typically an intercalation material. The obtained slurry was film casted onto a copper foil and the deposition was then let dry to the complete evaporation of the solvent, in a vacuum oven at 80 °C. The film was thus calendered and 10 mm diameter disks were punched out to be used as positive electrodes in half-cells. Load of active material on each electrode was always included between 0.5 and 1 mg cm⁻². All the electrochemical tests were performed in a three electrodes Swagelok type half-cells, assembled in an argon-filled glove box (Mbraun). The electrolyte employed was a Propylene carbonate ($\geq 99.9\%$, Merck) 1 M NaClO₄ (ACS reagent, $\geq 98\%$, Sigma-Aldrich®) solution with 2 % wt fluoroethylene carbonate 99%, (Aldrich®) addition. The electrolyte solution was immobilized onto a glass fiber disk used as the separator. Sodium metal (99.9 %, trace metal basis, Sigma-Aldrich®) disks were employed as counter electrode as well as reference electrode.

3.4. Electrode sodiation

For what concern the chemical pre-sodiation of the electrodes, a metallic sodium disk (99.9 %, trace metal basis, Sigma-Aldrich®) was placed in direct contact with the cobalt oxide containing electrode, previously wetted with the electrolyte, and held in place for an interval of time. After this step, the electrode was assembled in the electrochemical cell as already described, and subjected to electrochemical characterization.

4. Result and discussion

In Figure VI-1, XRD patterns of the as-prepared samples are reported. Phase purity is confirmed and diffraction peaks have been addressed to the cubic phase of Co₃O₄ spinel, identified by the space group *Fd-3m* (ICDD card No. 00-043-1003).

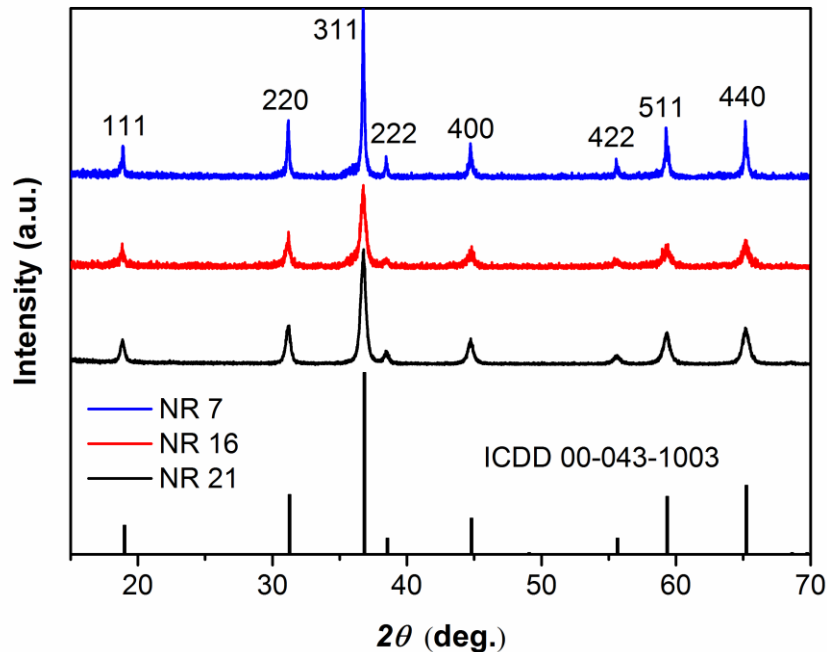


Figure VI-1: XRD pattern of Co_3O_4 samples.

The morphological comparison among the three proposed samples is presented in Figure VI-2, where SEM and TEM micrographs are displayed. Differences in the morphology are substantial and are mainly related to the way primary nanometric sized crystallites, whose presence is appreciable in TEM images (image d), e and f) in Figure VI-2), assemble in secondary structures. In the case of NR7, large slabs (several square micrometers wide and hundreds of nanometers thick) were obtained. Further magnification of slab edges reveals the highly porous nature of the secondary structure. Among the platelets, nanometric octahedral crystals can be also spotted. Needles like secondary structures were obtained in the case of NR16, as can be noted in image b) and e) in Figure VI-2. Each needle is hundreds of nanometers long and between 20 and 50 nanometers wide, and is composed by coagulated globular crystallites forming rows. NR21 particles (image c) and f)), eventually, assumed a flake-like morphology, characterized by high porosity.

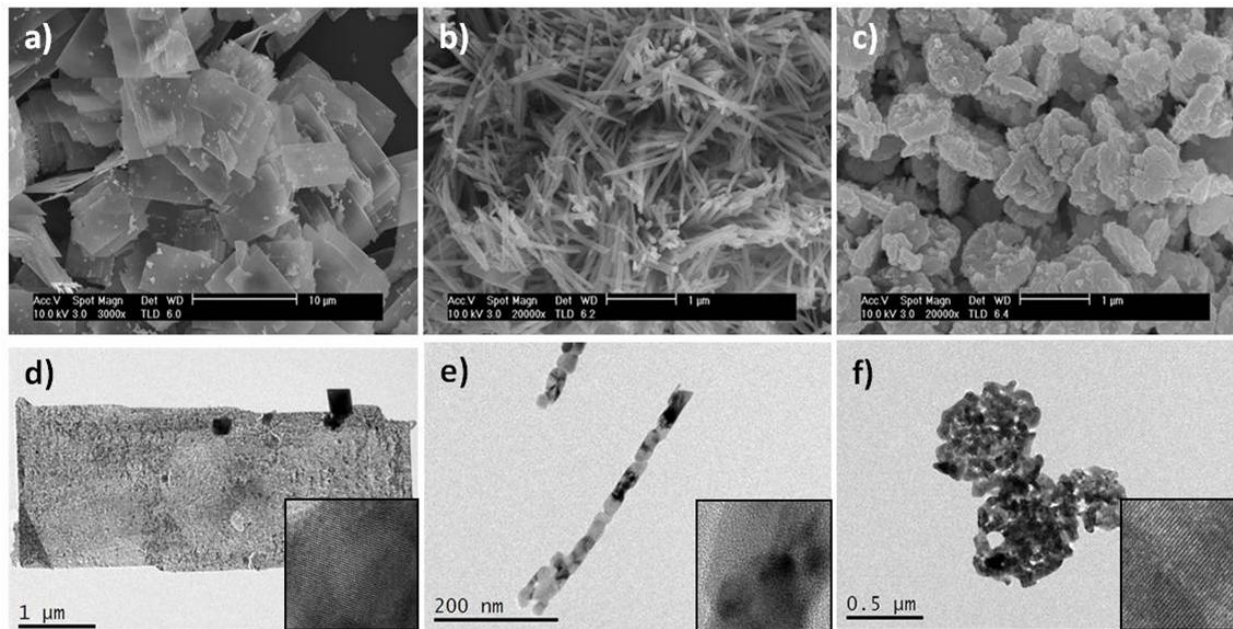
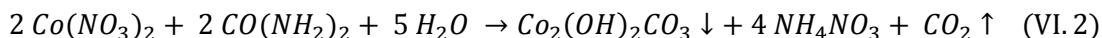


Figure VI-2: SEM and TEM micrographs of (a,d) NR7, (b,e) NR16 and (c,f) NR21; insets of images d9, e9, f9 show magnification of Co₃O₄ crystallites in which lattice fringes are visible.

Pores diameter can be assessed from TEM micrographs in the case of NR7 and NR 21, while NR16 doesn't always show an appreciable 3D porosity owing the poor 3D domain of needles-like structure. In both cases (NR7 and NR21) pores dimensionality falls in the mesopore regime, with the pores width never exceeding 50 nm (images a) and c) in Figure VI-3). In CO_S case, pores appear to be slightly smaller if compared to CO_F pores. Pores dimensions have been evaluated statistically by taking measurement directly on TEM images, as illustrated in Figure VI-3. The difference in pores dimensionality can be ascribed to urea utilization during synthesis. It can be noted how the use of urea as the mineralizing agent drives the formation of smaller pores (CO_S and CO_N). This positive aspect can be related to the slow hydrolysis urea undergoes in a hydrothermal environment compared to other Bronsted bases, such as NaOH²⁸. The slow hydrolysis leads to low grades of super saturation during precipitation of cobalt compounds primary particles, and this translates in a better packing of them forming a secondary structure with finer porosity. Temperature, instead, has clearly a direct effect onto the formation of complex structure extended in the 3D domain. The cooling down of the autoclave, performed always at the same rate, drives the growth of secondary structure accordingly to the starting temperature: the higher the temperature, the more extended the secondary structure. This well explains the low dimensionality of CO_N, whose synthesis has

been performed at 100 °C. The mesopores domain has been described as being a favourable feature in conversion materials for sodium storage, according to the facilitation in mass diffusion/transport and exposing a high active surface area²⁵. For all the samples, primary round-shaped particles, appear to be highly crystalline, as suggested by the lattice fringes clearly visible in image d), e) and f) insets on Figure VI-3. For hydrothermal synthesis in which urea has been employed as mineralizing agent (NR7 and NR16), the following mechanism was proposed²⁹:



The $\text{Co}_2(\text{OH})_2\text{CO}_3$ primary crystallites formation and agglomeration occur inside the autoclave under vigorous CO_2 degassing, with a consequent increment in the internal pressure of the system. In condition of low temperature treatment (100 °C for NR16), the further agglomeration of crystallites is prevented and the low dimensionality of final species is thus promoted. At higher temperature (160 °C for NR7), platelets like structures are instead obtained²⁶. Added to this, pH conditions forthcoming the neutrality do not favour any particular crystalline shape formation or, in other words, growth of any particular crystalline facet is promoted²⁴. For this reason round shaped primary particle, which do not show a net prevalence of a crystal facet over the others, are obtained and no octahedral crystallites were spotted in the NR21 sample.

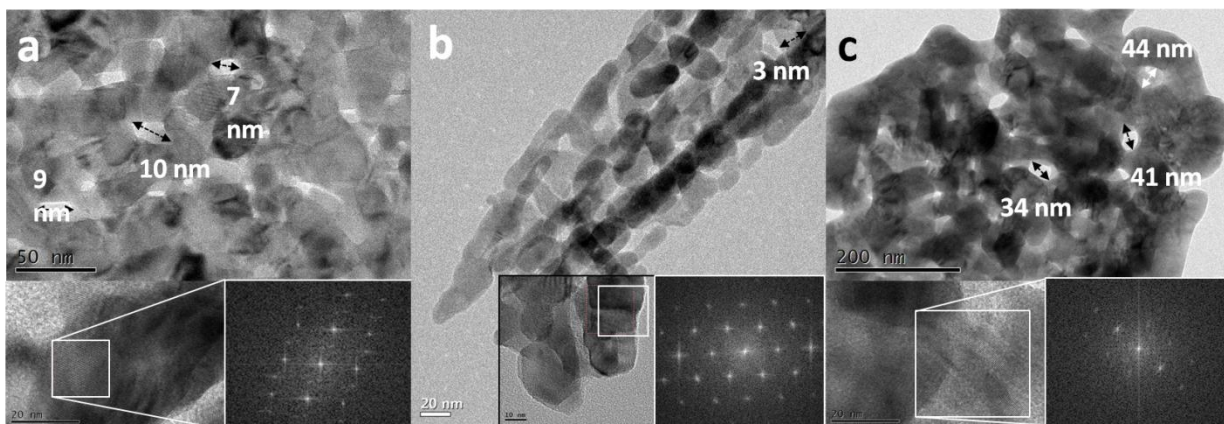


Figure VI-3: High magnification TEM images of a) NR7, b) NR16 and c) NR21 samples. Each composition includes a lower magnification image in which some pores are quantified in width; magnifications are different in order to appreciate the fine porous structure of each sample. In the lower left corner of the composition is reported a HRTEM image in which the area from which electron diffraction pattern has been obtained is highlighted; the correspondent SAEDs FFT are reported on the lower right corners.

Primary direct consequences of morphology discrepancies can be observed in galvanostatic cycling trends (image a) in Figure VI-4). The test has been taken at the rate of 1 C (850 mA·g⁻¹), at 25° C. It can be noted that while NR7 and NR 21 show a gradual and constant decrease in specific capacity, NR 16 shows a higher capacity and a milder decrease in capacity retention over cycles. After 50 cycles, NR 16 can still provide 360 mAh·g⁻¹ against 220 and 167 mAh·g⁻¹ for NR 7 and NR 21 respectively. In order to highlight the occurring processes, charge/discharge profiles for NR 16 has been reported in image b) in Figure VI-4. The curves are reported in the potential window ranging from 0.01 to 3.00 V vs. Na/Na⁺, and the capacities are normalized over the mass of the active material alone, namely Co₃O₄ (with 890 mAh·g⁻¹ theoretic specific capacity). According to many works reported in literature, a high irreversible capacity is registered during the first sodiation/de-sodiation (black curve in image b) inFigure VI-4)^{25,30,31}.

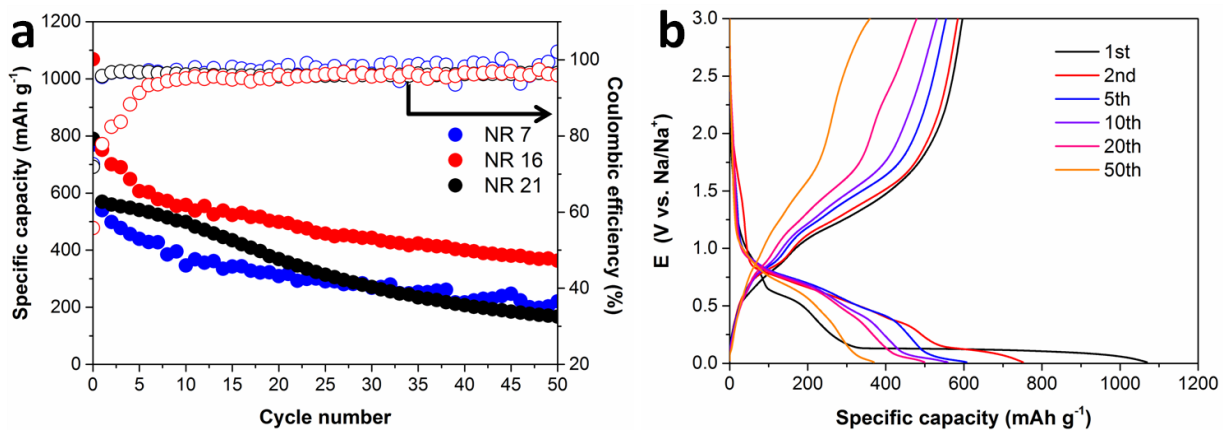


Figure VI-4: a) Electrochemical characterization of Co₃O₄ powders using galvanostatic cycling with potential limitation (GCPL); b) discharge/charge profiles are reported for NR16 sample, all the electrodes have been discharged/charged at 0.1 C (89 mA·g⁻¹).

Quantitatively, close to the 30 % of initial sodiation capacity is not recovered during the following cycle sodiation step. For what concern the capacity extracted during the first discharge (sodiation), NR 16 sets the highest value among the materials tested (1068 mAh·g⁻¹), while NR 7 and NR 21 lead to considerably lower values (770 and 789 mAh·g⁻¹ respectively). The coulombic efficiencies for the different materials for the first cycle are 70.3 %, 70.2 % and 71.1 % for NR 16, NR 7 and NR 21 respectively. Moreover, By looking at the 1st charge profile (downward black curve in image b) Figure VI-4), three different processes can be recognised: a

first small faint step can be located at 0.8 V vs. Na/Na⁺, followed by a more significant one at 0.57 V.

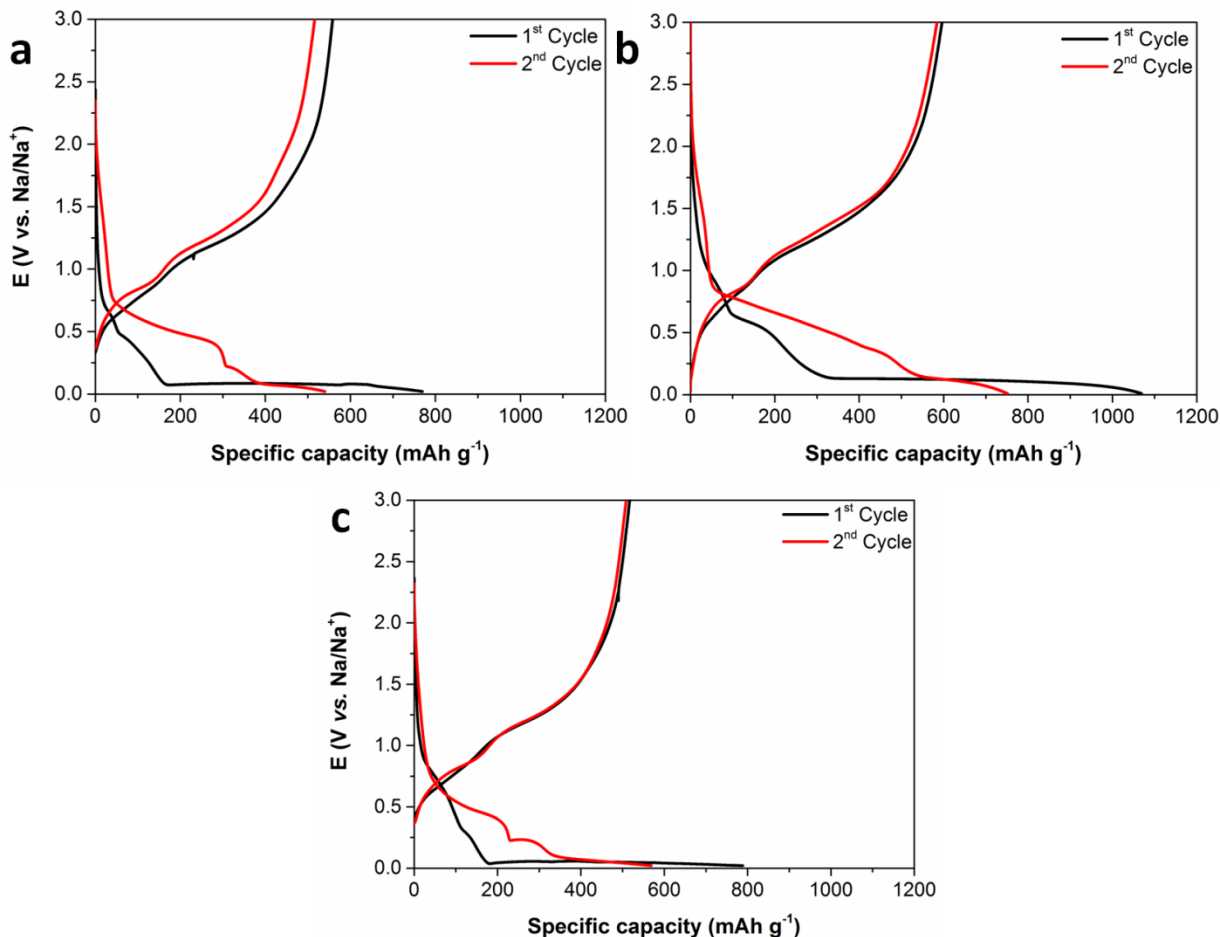


Figure VI-5: sodiation/de-sodiation profiles related to first and second cycle for a) NR7, b) NR16 and c) NR21 respectively.

The main capacity is connected to the long flat plateau centred at 0.12 V. The highest loss in capacity retention, if 1st and 2nd cycle sodiation steps are compared (Figure VI-5), is related to the flat plateau occurring at low potential, for all the three materials. This plateau reduces by 72% during the second sodiation, in the case of NR 16, in favour of the enhancement of a higher potential plateau that assumes the shape of a leaning line centred around 0.6 V (downward red curve), few millivolts above the 0.57 V step that becomes hardly recognisable. The case of NR 7 and NR 21 are slightly different, being all the steps shifted at lower potentials and the corresponding plateaus flatter. For what concern the overpotential between the charge and discharge processes, no appreciable differences were spotted among the

materials investigated. The low potential irreversible plateau has not been addressed to sodium interaction with carbon matrix for mainly two reasons: firstly, the capacity extracted from the flat step at 0.2 V is not consistent with the relative amount of Carbon Black included in the electrode formulation (17 %). Secondly, as Komaba *et al.* showed, sodium interaction with hard carbon type conductive matrixes happens close to 0.0 V and in a wide range of potential values from 3 down to 0.5 V vs Na/Na⁺ with sloping trends, depending on graphitization level and porosity of the carbon³² (see also Chapter IV). The possibility of an electrolyte decomposition process forming the SEI layer is also unlikable. It usually occurs over a wider potential window owing the large number of different forming species²¹. The first small plateau at 0.8 V coincides with the formation of the SEI layer³³ while the other processes, including the low potential irreversible step, were attributed to the Co₃O₄ reduction to metallic cobalt (Co)³³⁻³⁵. The latter process happens in two steps (see discussion hereafter) explaining the two different plateaus spotted in the first sodiation²⁵. In the following cycles, as demonstrated by *ex-situ* HRTEM analysis conducted by others³⁴, metallic Co can't be clearly identified as the product of sodiation of the electrode, while Na₂O crystals distinctly appear. In order to shed light onto the process occurring during the very first cycles, *ex-situ* XRD measurements have been performed as well. In Figure VI-6 are reported the diffractograms taken on pristine and cycled electrodes. While in the pristine electrode Co₃O₄ diffraction peaks can be easily indexed, the same peaks are not recovered after a full sodiation/de-sodiation cycle; peaks other than those addressable to spinel Co₃O₄ appear instead. Those signals have been attributed to CoO (ICDD card No. 00-078-0431), this would be in contrast with results reported by others that tend to support the complete restoration of Co₃O₄ after the first discharge/charge cycle³³. The formation of a species other than spinel Co₃O₄ might be also explicative of the considerable difference between the first and second sodiation profile while the desodiation profile fashion is preserved. Even if not visible in the XRD diffractogram of the cycled electrode, sodium has been detected using energy dispersive X-ray analysis (image b) and c) in Figure VI-6) since from the first cycle. Its presence well supports the thesis of the conversion to CoO phase instead of fully oxidised Co₃O₄ and agrees with some works present in literature^{33,35,36}.

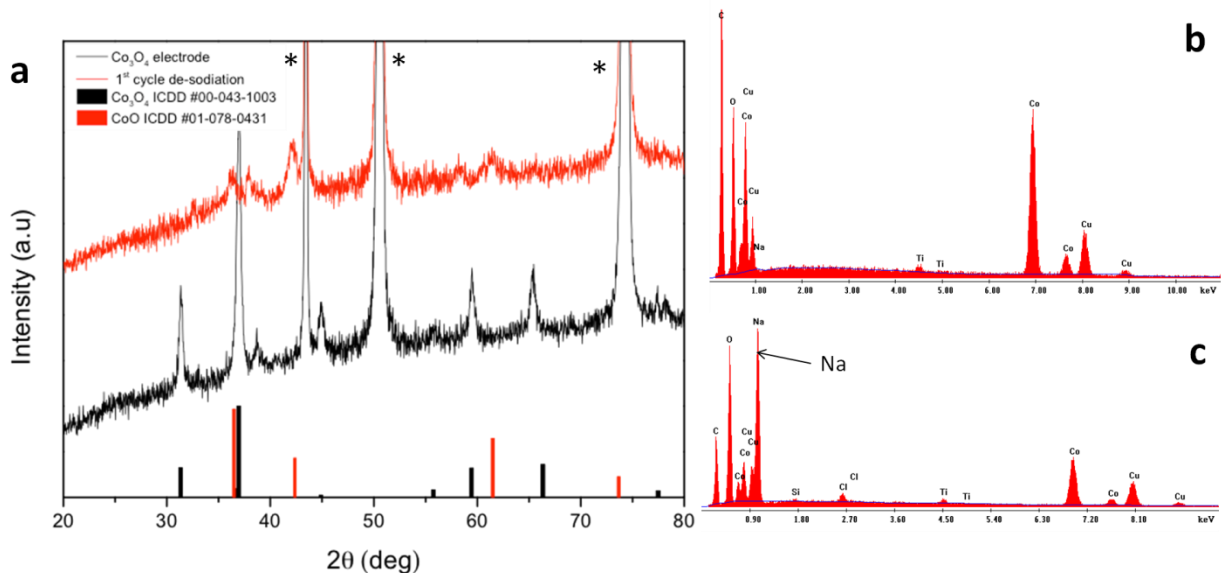


Figure VI-6: a) XRD diffractograms of pristine NR16 electrode (black) and cycled one (red); with asterisks are indicated diffraction peaks coming from copper current collector; b) EDX taken on pristine electrode and c) on cycled one after the 4th de-sodiation step.

The needle-like structures are hardly maintained after sodiation/desodiation cycles and encounter a complete pulverization during the following cycles, as can be clearly spotted by the ex-situ SEM micrograph reported in Figure VI-7. This process common to many conversion-like processes, gains here a positive hint thanks to the low dimensionality of the original structure (needles), distinguishable in image a) in Figure VI-7, that drives the pulverization of the active material towards a less dense-packed and somewhat cloudy bulk material (image b) and c) in Figure VI-7).

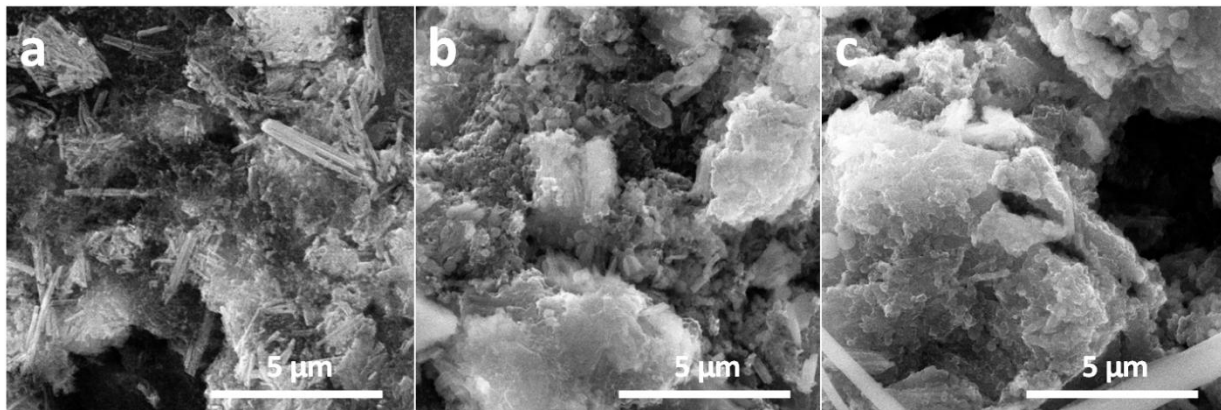
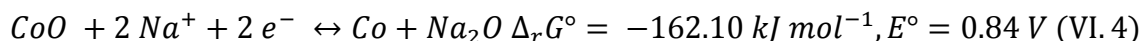


Figure VI-7: SEM micrographs of CO_N electrode at different times during GCPL tests; a) refers to the pristine electrode as prepared after blade casting of the active material on the current collector; b) and c) The other two pictures were taken disassembling the coin cells after 1st and 4th cycles respectively (following the desodiation step of Co_3O_4 electrodes) inside the argon-filled glove box and washing the working electrode with pure acetonitrile in order to remove SEI layer as much as possible.

After these considerations, two different conversion reactions can be then proposed, taking in account formation of CoO during the first irreversible reduction and the following reversible reaction involving CoO :



An analogous mechanism has been recently proposed for Co_3O_4 lithiation, and together with the SEI formation, would account for the capacity loss afflicting the first cycle³⁵. Theoretically speaking, electrochemical de-sodiation of the electrode, giving CoO as the stable oxidised material, instead of Co_3O_4 , would be accountable for a reduction in reversible capacity from $890 \text{ mAh}\cdot\text{g}^{-1}$, to $668 \text{ mAh}\cdot\text{g}^{-1}$ (-25 %). Considering the total capacity loss related to the first cycle, the residual capacity loss, not ascribable to CoO conversion mechanism, would be comprised between 3.8 % and 4.7 % of the initial capacity, depending on the Co_3O_4 initial morphology. Indeed the residual capacity loss would be directly correlated to the SEI layer formation whose entity is strongly bonded to the total surface area of the active material.

The rate test of the promising NR16 has been conducted and the results are reported in Figure VI-8. Capacity extracted progressively decrease with the rising in the charge/discharge current as expected. Nevertheless at 5 C ($4470 \text{ mA}\cdot\text{g}^{-1}$) a surprisingly high capacity of $160 \text{ mAh}\cdot\text{g}^{-1}$ is obtained. When the current is set back to 0.1 C ($90 \text{ mA}\cdot\text{g}^{-1}$) a reversible capacity of

415 $\text{mAh}\cdot\text{g}^{-1}$ can still be achieved. The value at 5C sets, as far as we know from the literature, a new mile stone in the high rate performance for nanostructured cobalt oxide devoid of a conductive substrate employed in sodium ion batteries. In recent works discrete capacities have been obtained using high current drains (with $3200 \text{ mA}\cdot\text{g}^{-1}$ as maximum³¹) from composite materials in which a conductive matrix, namely carbon nanotubes or reduced graphene sheets, took upon themselves an effective electron conductivity inside the bulk of the material. Since in this case no conductive substrate has been employed, a part from the carbon black for electrode formulation, all the spotted favourable features must be addressed to the active material itself. In particular, high rate capabilities can be related to i) the thickness of the needles and the nanometric sized particles that offer a short path to sodium diffusion and electron motion, and ii) higher degree of freedom of nanometric particles arranged in a 1D fashion in bearing the volume variations during sodiation and de-sodiation processes. As comparison, in the recent work by Ahmad *et al.*²⁵, $83 \text{ mAh}\cdot\text{g}^{-1}$ were obtained at $500 \text{ mA}\cdot\text{g}^{-1}$ using cobalt oxide nanoplatelets grafted onto reduced graphene oxide sheets. The increase in scan rates, does not change sensibly the charge/discharge profiles appearance, as can be clearly seen in image b) in Figure VI-8. Nonetheless, stepping from 5 C back to 0.1 C determines the appearance of a slight hump in the desodiation curve around 2.0 V, whose origin is not clear. As observed in multiple other oxide-based materials, the hysteresis between charge and discharge curves increases slightly as the charge/discharge current goes up.

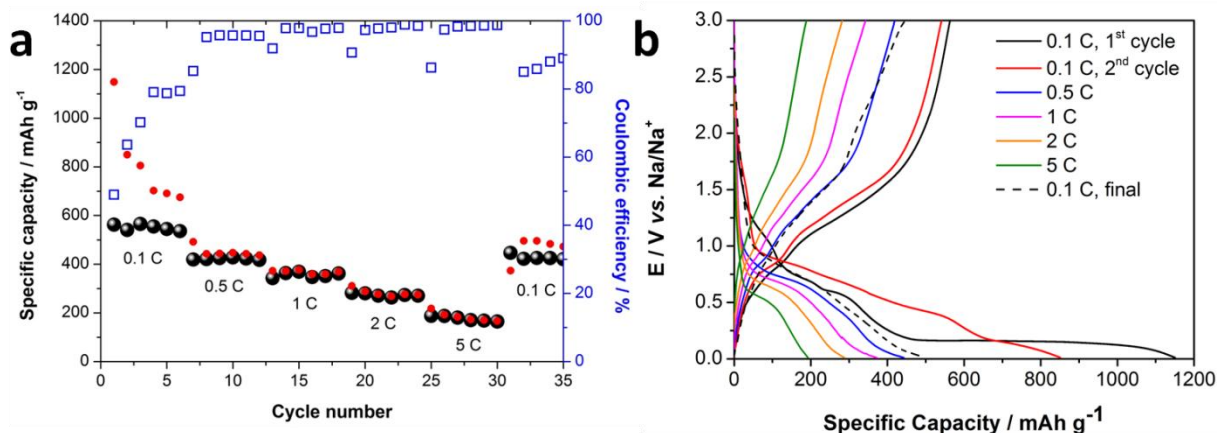


Figure VI-8: a) Rate test on CO_N . For each current density, six cycles have been performed, progressively going from 0.1C ($89 \text{ mA}\cdot\text{g}^{-1}$), 0.5C ($445 \text{ mA}\cdot\text{g}^{-1}$), 1C ($890 \text{ mA}\cdot\text{g}^{-1}$), 2C ($1780 \text{ mA}\cdot\text{g}^{-1}$) and as high as 5C ($4450 \text{ mA}\cdot\text{g}^{-1}$); b) charge/discharge profiles obtained derived from rate test performed on CO_N sample, last cycle performed at low rate (0.1 C) is reported with the black dashed line.

As previously quoted in the present work, the irreversible capacity affecting the first cycle is a major concern for a possible application of the technology. The irreversible process accountable for the capacity loss, being either SEI formation or an irreversible conversion reaction step as hypothesized by Du *et al.*³⁵, represents a massive sodium consumption inside the cell, and it's not an acceptable compromise assumed the high theoretical capacity of the active material. This observation led, as a possible solution, to a chemical pre-sodiation of the electrode in order to pre-condition the active material supplying the sodium that would otherwise come from the cathode once assembled the cell. Similar treatments have been used in preparing materials for other types of anodes³⁷, but employing it with a conversion compound might be surpassingly useful in order to direct the conversion reaction to a well-defined and thermodynamically driven product. The sodium uptake has been assessed with an elemental analysis (AAS) in order to highlight the dependence with the sodiation times (Table VI-2). Since the sodium amount detected was the same for the 60 and 90 minutes sodiation, respectively, the first condition was considered the required amount of time to obtain the saturation of the electrode. In Figure VI-9, 1st and 2nd cycle profiles of pre-sodiated and pristine NR16 electrode are reported. The severe reduction in the irreversible capacity is clearly visible, furthermore a sensibly different charge/discharge profile is also achieved. The long lasting plateau at 0.12 V is indeed completely suppressed in favour of a shorter process occurring at higher potential (0.31 V) that has its correspondent recognisable event above 1 V, in the upward discharge curve. Owing the similarities between charge/discharge profile of pre-sodiated electrodes and second cycle profile of electrochemically sodiated/desodiated ones, a parallelism between the mechanism highlighted via *ex-situ* XRD characterization and the chemical sodiation products can be sketched. CoO, rather than Co₃O₄, can be recognized as the electrochemically stable species in a chemically reducing environment, and might be also addressed as the most oxidized state of cobalt recovered after the desodiation of chemically treated electrodes. The thermodynamic of chemical sodiation of cobalt oxide is associated with a highly spontaneous process characterized by the $\Delta_r G^\circ$ value of $-710.30 \text{ kJ} \cdot \text{mol}^{-1}$. This has a direct correlation with the considerable lattice energy ($\Delta_{\text{lattice}} H^\circ$) of the corresponding product of the conversion reaction (Na₂O): $1239 \text{ kJ} \cdot \text{mol}^{-1}$, the highest among sodium chalcogenides, halides and hydrides¹¹. Owing these considerations, the conversion reaction expected during the electrodes pre-treatment is the complete conversion of Co₃O₄ to metallic cobalt. We can thus

conclude that the pre-conditioning of electrodes positively direct following sodiation/desodiation processes by ensuring a complete reduction of Co_3O_4 to metal Co. Persistency of Co_3O_4 in the electrode through cycling has to be then considered as a deleterious agent for a correct and stable operation, and a chemical sodiation of the electrode provides a complete and effective conversion of the totality of Co_3O_4 to metal Co. The electrochemical sodiation, on the contrary, still represents a controversial and somewhat inefficient approach that involves a heterogeneous process (partial reduction of Co_3O_4 to metal Co, SEI formation and other decomposition products) far to be extensively understood. Nevertheless standard electrochemical studies on different morphologies of the Co_3O_4 precursor, have stressed the importance of high aspect ratio and low dimensionality primary particles agglomerates in indexing a more efficient conversion reaction and in sensibly affecting the overall performances of the sodium half cell.

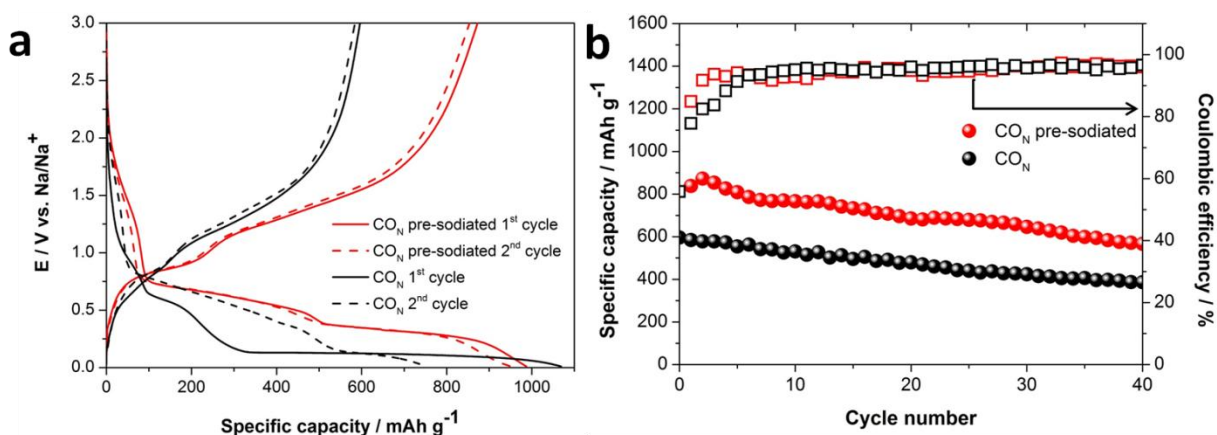


Figure VI-9: a) Sodiation/desodiation profiles of pre-treated (red) and pristine (black) CO_N electrode, solid and dashed lines refer to first and second cycle respectively; b) cycling stability and coulombic efficiency of the two electrodes, namely CO_N pristine (black) and CO_N pre-sodiated (red). Tests taken at 0.1 C (89 $\text{mA}\cdot\text{g}^{-1}$).

Table VI-2: Sodium uptake evaluated using AAS correlated to sodiation times.

Sodiation time / min	x in $\text{Na}_x\text{Co}_3\text{O}_4$
30	0.94
60	1.50
90	1.50

The beneficial effect of the pre-sodiation can be spotted also throughout all the cycling in image b) in Figure VI-9. Interestingly the low starting OCV of the pre-treated electrode (~ 0.4 V vs Na/Na⁺) suggests a heavily sodiated state of the active material, for this reason the galvanostatic cyclation started with a charging step (de-sodiation). Differently, NR21 could not be chemically sodiated completely. After coin cell assembling an open circuit potential of 1.5 V has been measured denoting only a partial sodium uptake. Thus a further positive current step has been employed in this case in order to reach the complete sodiation of the electrode (Figure VI-10). A general higher specific capacity is obtained, presumably thanks to the smaller amount of active material compromised during the electrochemical sodiation involved in the first cycle. Starting capacity value for the sodiated electrode, $987 \text{ mAh}\cdot\text{g}^{-1}$, is above the theoretical value previously discussed ($668 \text{ mAh}\cdot\text{g}^{-1}$) and this might be due to SEI layer formation as well as to parasitic processes occurring during first cycles. However, the large irreversible capacity above the theoretical value is sensibly reduced. Another aspect worth to be noted is that the inevitable capacity fading through cycling does not follow an exponential decay in the very first cycles, as occurs for a common Co₃O₄ electrode. The capacity loss sticks more to a linear decay starting from a capacity value, considering the irreversible processes taking place in the first cycles, only 100 mAh g^{-1} above the theoretical value. After 50 cycle, the reversible capacity, $508 \text{ mAh}\cdot\text{g}^{-1}$, still lies above the value of the pristine NR16 electrode, $348 \text{ mAh}\cdot\text{g}^{-1}$.

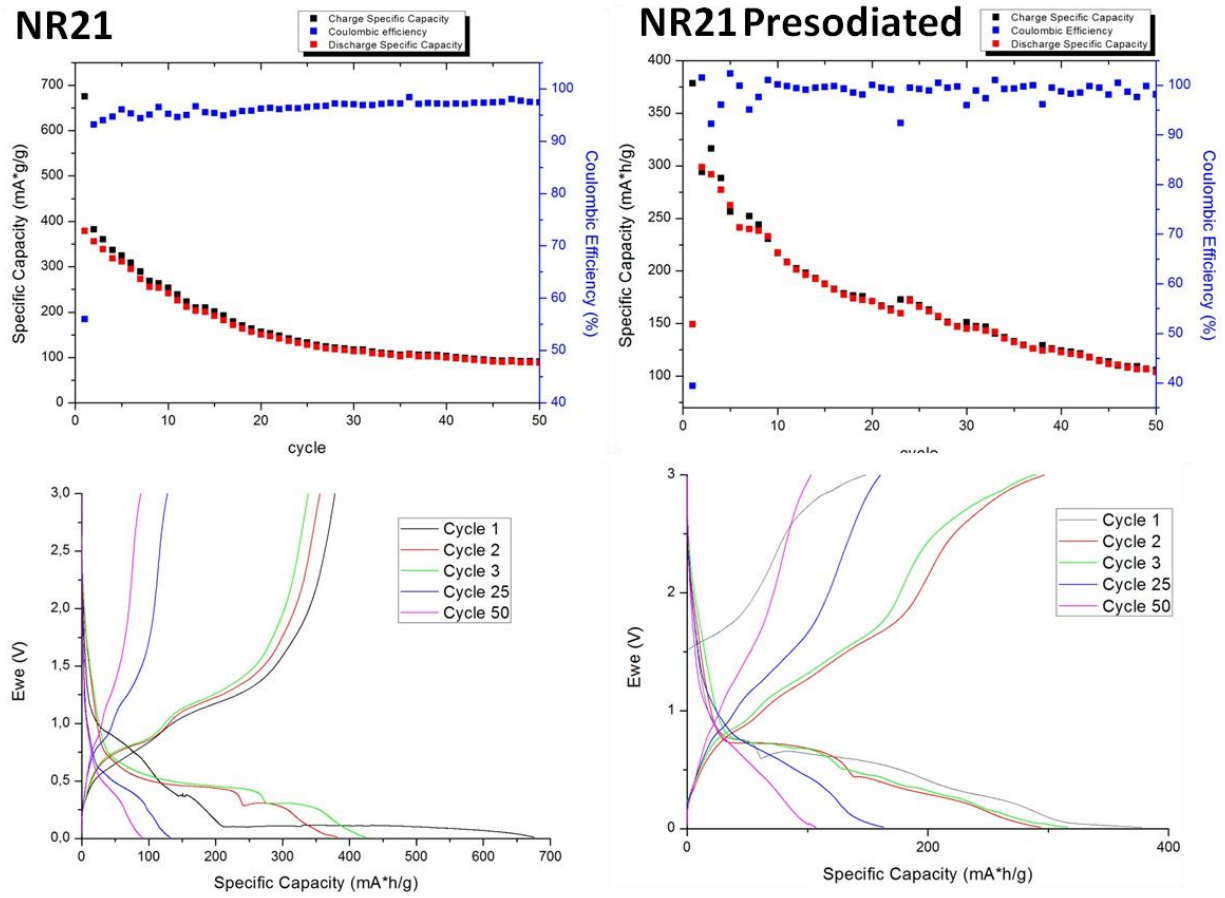


Figure VI-10: GCPL tests on pristine (left) and pre-sodiated (right) Co_3O_4 flakes (NR21).

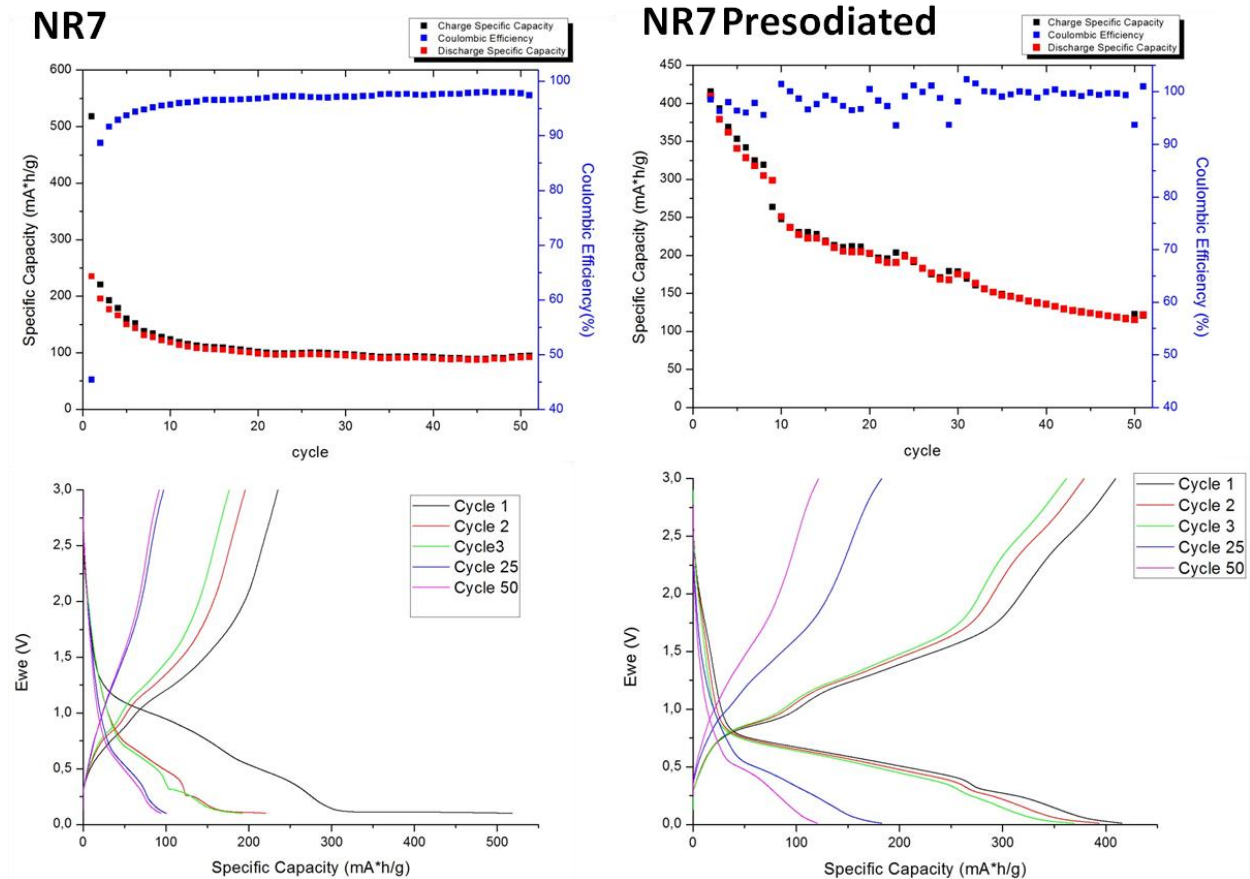


Figure VI-11: GCPL tests on pristine (left) and pre-sodiated (right) Co_3O_4 slabs (NR7).

As can be observed from Figure VI-11 and Figure VI-10, NR7 and NR21 subjected to the same pre-sodiation treatment, didn't show the same behavior as NR16. Despite NR7 showed a higher immediate capacity and a reduction of the initial irreversible process, it ended up, after 50 cycles, matching pristine electrodes capacity. Furthermore pre-treated NR21 electrode gives lower capacities and worse cycling capability compared to pristine one. These results prove that CO_N needle-like structure carries out also a positive influence during the chemical sodiation, while more three-dimensional structures (slabs and flakes) are clearly not suitable for a chemical sodiation pre-treatment.

5. Conclusions

In the present work, a cost effective and easy to reproduce synthetic path has been proposed to easily modulate the morphological characteristics of a spinel- Co_3O_4 hierarchical structure. The modulation of the synthetic parameters allowed to obtain primary nanometric

sized crystalline particles aggregation in different hierarchical structures. During the preparation route, no conductive substrate was employed in order to effectively isolate the behaviour of Co_3O_4 morphologies alone. Three morphologies have been extensively characterized under the electrochemical point of view. For the first time, at the best of our knowledge, a needle like structure was obtained for Co_3O_4 employed as anode material in sodium ion batteries. A high porosity and high aspect ratio of agglomerates seem to facilitate the electrochemical processes involving the active material. The most promising among the structure investigated, NR16, assured discrete performances in galvanostatic tests and considerable reversible capacities were also obtained high operational currents up to 5C. Finally, the beneficial effect of a pre-sodiation treatment directly on the electrodes was also highlighted, and should be kept as a viable alternative to the electrochemical performance optimization of conversion materials for sodium ion batteries. This research aim is to encourage further studies around conversion materials for sodium batteries, since they might really play a relevant role in the design of future low cost battery technologies. The presented results and experiments still display room for additional improvement (capacity stability, general reliability of the material and irreversible capacity reduction) but positively tackle some of the challenges anode materials for SIBs still hold nowadays.

6. Bibliography

- (1) Goodenough, J. B.; Park, K. *The Li-Ion Rechargeable Battery : A Perspective*. 2013.
- (2) Tarascon, J. M.; Armand, M. *Issues and Challenges Facing Rechargeable Lithium Batteries*. *Nature* 2001, 414 (November), 359–367.
- (3) Armand, M.; Tarascon, J.-M. *Building Better Batteries*. *Nature* 2008, 451 (February), 652–657.
- (4) Tarascon, J.-M. *Is Lithium the New Gold?* *Nat. Chem.* 2010, 2 (6), 510.
- (5) Dahbi, M.; Yabuuchi, N.; Kubota, K.; Tokiwa, K.; Komaba, S. *Negative Electrodes for Na-Ion Batteries*. *Phys. Chem. Chem. Phys.* 2014.
- (6) Kim, Y.; Ha, K.-H.; Oh, S. M.; Lee, K. T. *High-Capacity Anode Materials for Sodium-Ion Batteries*. *Chemistry* 2014, 20 (38), 11980–11992.
- (7) Slater, M. D.; Kim, D.; Lee, E.; Johnson, C. S. *Sodium-Ion Batteries*. *Adv. Funct. Mater.* 2013, 23 (8), 947–958.
- (8) Chevrier, V.; Ceder, G. *Challenges for Na-Ion Negative Electrodes*. *J. Electrochem. Soc.* 2011, 158 (9), A1011.
- (9) Ung, Y. H.; Lim, C. H.; Kim, D. K. *Graphene-Supported Na₃V₂(PO₄)₃ as a High Rate Cathode Material for Sodium-Ion Batteries*. *J. Mater. Chem. A* 2013, 1 (37), 11350.
- (10) Masquelier, C.; Croguennec, L. *Polyanionic (Phosphates, Silicates, Sulfates) Frameworks as Electrode Materials for Rechargeable Li (or Na) Batteries*. *Chem. Rev.* 2013, 113 (8), 6552–6591.
- (11) Klein, F.; Jache, B.; Bhide, A.; Adelhelm, P. *Conversion Reactions for Sodium-Ion Batteries*. *Phys. Chem. Chem. Phys.* 2013, 15 (38), 15876–15887.
- (12) Xia, X.; Dahn, J. R. *Study of the Reactivity of Na/Hard Carbon with Different Solvents and Electrolytes*. *J. Electrochem. Soc.* 2012, 159 (5), A515.
- (13) White, R. J.; Tauer, K.; Antonietti, M.; Titirici, M.-M. *Functional Hollow Carbon Nanospheres by Latex Templating*. *J. Am. Chem. Soc.* 2010, 132 (49), 17360–17363.
- (14) Chen, T.; Liu, Y.; Pan, L.; Lu, T.; Yao, Y.; Sun, Z.; Chua, D. H. C.; Chen, Q. *Electrospun Carbon Nanofibers as Anode Materials for Sodium Ion Batteries with Excellent Cycle Performance*. *J. Mater. Chem. A* 2014, 2 (12), 4117.

(15) Qian, J.; Chen, Y.; Wu, L.; Cao, Y.; Ai, X.; Yang, H. High Capacity Na-Storage and Superior Cyclability of Nanocomposite Sb/C Anode for Na-Ion Batteries. *Chem. Commun. (Camb)*. 2012, 48 (56), 7070–7072.

(16) He, M.; Kravchyk, K. V.; Walter, M.; Kovalenko, M. V. Monodisperse Antimony Nanocrystals for High-Rate Li-Ion and Na-Ion Battery Anodes: Nano versus Bulk. *Nano Lett.* 2014, 14 (3), 1255–1262.

(17) Wang, Y.; Su, D.; Wang, C.; Wang, G. SnO₂@MWCNT Nanocomposite as a High Capacity Anode Material for Sodium-Ion Batteries. *Electrochem. commun.* 2013, 29, 8–11.

(18) Farbod, B.; Cui, K.; Kalisvaart, W. P.; Kupsta, M.; Zahiri, B.; Kohandehghan, A.; Lotfabad, E. M.; Li, Z.; Lubner, E. J.; Mitlin, D. Anodes for Sodium Ion Batteries Based on Tin-Germanium-Antimony Alloys. *ACS Nano* 2014, 8 (5), 4415–4429.

(19) Xiao, L.; Cao, Y.; Xiao, J.; Wang, W.; Kovarik, L.; Nie, Z.; Liu, J. High Capacity, Reversible Alloying Reactions in SnSb/C Nanocomposites for Na-Ion Battery Applications. *Chem. Commun. (Camb)*. 2012, 48 (27), 3321–3323.

(20) Kumar, P. R.; Jung, Y. H.; Bharathi, K. K.; Lim, C. H.; Kim, D. K. High Capacity and Low Cost Spinel Fe₃O₄ for the Na-Ion Battery Negative Electrode Materials. *Electrochim. Acta* 2014, 146, 503–510.

(21) Su, D.; Xie, X.; Munroe, P.; Dou, S.; Wang, G. Mesoporous Hexagonal Co₃O₄ for High Performance Lithium Ion Batteries. *Sci. Rep.* 2014, 4, 6519.

(22) Yuan, S.; Huang, X. L.; Ma, D. L.; Wang, H. G.; Meng, F. Z.; Zhang, X. B. Engraving Copper Foil to Give Large-Scale Binder-Free Porous CuO Arrays for a High-Performance Sodium-Ion Battery Anode. *Adv. Mater.* 2014, 26 (14), 2273–2279.

(23) Guo, J.; Chen, L.; Zhang, X.; Chen, H. Porous Co₃O₄ Nanorods as Anode for Lithium-Ion Battery with Excellent Electrochemical Performance. *J. Solid State Chem.* 2014, 213, 193–197.

(24) Xiao, X.; Liu, X.; Zhao, H.; Chen, D.; Liu, F.; Xiang, J.; Hu, Z.; Li, Y. Facile Shape Control of Co₃O₄ and the Effect of the Crystal Plane on Electrochemical Performance. *Adv. Mater.* 2012, 24 (42), 5762–5766.

(25) Liu, Y.; Cheng, Z.; Sun, H.; Arandiyani, H.; Li, J.; Ahmad, M. Mesoporous Co₃O₄ sheets/3D Graphene Networks Nanohybrids for High-Performance Sodium-Ion Battery Anode. *J. Power Sources* 2015, 273, 878–884.

(26) Chen, J. S.; Zhu, T.; Hu, Q. H.; Gao, J.; Su, F.; Qiao, S. Z.; Lou, X. W. Shape-Controlled Synthesis of Cobalt-Based Nanocubes, Nanodiscs, and Nanoflowers and Their Comparative Lithium-Storage Properties. *ACS Appl. Mater. Interfaces* 2010, 2 (12), 3628–3635.

(27) Ming, J.; Ming, H.; Kwak, W.-J.; Shin, C.; Zheng, J.; Sun, Y.-K. The Binder Effect on an Oxide-Based Anode in Lithium and Sodium-Ion Battery Applications: The Fastest Way to Ultrahigh Performance. *Chem. Commun. (Camb)*. 2014, 50 (87), 13307–13310.

(28) Rao, M. M.; Reddy, B. R.; Jayalakshmi, M.; Jaya, V. S.; Sridhar, B. Hydrothermal Synthesis of Mg-Al Hydrotalcites by Urea Hydrolysis. *Mater. Res. Bull.* 2005, 40 (2), 347–359.

(29) Cui, L.; Li, J.; Zhang, X. G. Preparation and Properties of Co₃O₄ Nanorods as Supercapacitor Material. *J. Appl. Electrochem.* 2009.

(30) Deng, Q.; Wang, L.; Li, J. Electrochemical Characterization of Co₃O₄/MCNTs Composite Anode Materials for Sodium-Ion Batteries. *J. Mater. Sci.* 2015, 50 (11), 4142–4148.

(31) Jian, Z.; Liu, P.; Li, F.; Chen, M.; Zhou, H. Monodispersed Hierarchical Co₃O₄ Spheres Intertwined with Carbon Nanotubes for Use as Anode Materials in Sodium-Ion Batteries. *J. Mater. Chem. A* 2014, 2 (34), 13805.

(32) Komaba, S.; Murata, W.; Ishikawa, T.; Yabuuchi, N.; Ozeki, T.; Nakayama, T.; Ogata, A.; Gotoh, K.; Fujiwara, K. Electrochemical Na Insertion and Solid Electrolyte Interphase for Hard-Carbon Electrodes and Application to Na-Ion Batteries. *Adv. Funct. Mater.* 2011, 21 (20), 3859–3867.

(33) Rahman, M. M.; Glushenkov, A. M.; Ramireddy, T.; Chen, Y. Electrochemical Investigation of Sodium Reactivity with Nanostructured Co₃O₄ for Sodium-Ion Batteries. *Chem. Commun. (Camb)*. 2014, 50 (39), 5057–5060.

(34) Rahman, M.; Sultana, I.; Chen, Z.; Srikanth, M.; Li, L. H.; Dai, X. J.; Chen, Y. A High Performance Sodium-Ion Battery Anode Produced by Pulsed Plasma in a Liquid. 2015, 13088–13095.

(35) Su, Q.; Zhang, J.; Wu, Y.; Du, G. Revealing the Electrochemical Conversion Mechanism of Porous Co₃O₄ Nanoplates in Lithium Ion Battery by in Situ Transmission Electron Microscopy. *Nano Energy* 2014, 9, 264–272.

(36) Yang, J.; Zhou, T.; Zhu, R.; Chen, X.; Guo, Z.; Fan, J.; Liu, H. K.; Zhang, W. X. Highly Ordered Dual Porosity Mesoporous Cobalt Oxide for Sodium-Ion Batteries. *Adv. Mater. Interfaces* 2016, 3 (3), 1–7.

(37) Hassoun, J.; Bonaccorso, F.; Agostini, M.; Angelucci, M.; Betti, M. G.; Cingolani, R.; Gemmi, M.; Mariani, C.; Panero, S.; Pellegrini, V.; Scrosati, B.; Betti, G.; Cingolani, R.; Gemmi, M.; Mariani, C.; Panero, S.; Pellegrini, V.; Scrosati, B. An Advanced Lithium-Ion Battery Based on a Graphene Anode and a Lithium Iron Phosphate Cathode. *Nano Lett.* 2014, 14, 1–17.

CHAPTER VII: The Na₂FeP₂O₇-carbon nanotubes composite as high rate cathode material

1. Introduction

Among the viable positive electrode materials recently proposed for Na-ion secondary batteries, Na₂FeP₂O₇ was investigated thanks to its facile preparation, the use of highly abundant and low cost raw materials, and the highest thermal stability among all others cathode materials. In the present chapter the electrochemical features of the Na₂FeP₂O₇ are improved by synthesizing a Na₂FeP₂O₇-carbon nanotubes composite with prominent high-rate performances. The material shows a reversible specific capacity of 86 mAh·g⁻¹ for 140 cycles at 1C and 68 mAh·g⁻¹ at 10C. An in depth investigation about the Na⁺ diffusion rates inside the material was conducted by electrochemical impedance spectroscopy (details in the text).

2. Background

High energy density (120-150 Wh·dm⁻³)¹, the lightweight, the remarkable round-trip efficiency, and high power^{2,3} are predominant characteristics that have made LIBs the best choice for a wide range of applications: from electric cars (Electric vehicle and hybrid electric vehicle) to high-end portable electronics (smart phones, laptops and entertainment electronics). The most advanced lithium ion batteries can also rely on impressively fast kinetics materials, whose fast insertion chemistries can substantially curtail recharge time⁴. Quick kinetics will be thus the mandatory requirements for future batteries especially directed to automotive and stationary storage market. If for the former utilization fast charge/discharge behavior translate into faster charges and sudden current drain during acceleration, in the latter, it means a fast response to swift energy transients if batteries are coupled to renewable energy sources like photovoltaic modules or wind turbines. In investigating SIBs chemistries, as valuable alternative to lithium ones, it should be kept in mind that advantages might derive also from faster kinetics or peculiar sodium reactivity not observed in the case of lithium, and not only from the concern for a future sustainability. The most relevant technological obstacle that has to be overcome in sodium-ion technology is the chemical-physical limit coming from the higher

hindrance of the sodium cation that implies poor stability of conversion compounds and sluggish diffusion in host structures⁵. For this reason a new series of tailored anode and cathode materials with improved rate capabilities has been proposed^{5,6}. Amongst the most promising, worthy to be mentioned are the layered P2- and O3-structured TMOs such as Na_xCoO₂⁷, Na_xVO₂⁸, Na_x(Fe_{1/2}Mn_{1/2})O₂⁹ and Na(Mn_{1/3}Co_{1/3}Ni_{1/3})O₂¹⁰ capable of storing between 100 and 200 mAh·g⁻¹ but with mediocre rate capabilities. Capacity are in fact more than halved if C-rate as high as 4C are used¹¹. Also when highly ordered O3- and P2-NaCoO₂ thin films are synthesized via pulsed laser deposition (PLD) technique, serious limitation to electrochemical performances at high drain currents happen¹². A series of polyanionic compounds has been widely investigated as well. Some of the most recent works about these compounds describe the promising performances of Na₃V₂(PO₄)₃¹³ and Na₄M₃(PO₄)₂(P₂O₇) with M=Fe, Co^{14,15}. They show an operational potential ranging from 2.5 to 4.5 V vs. Na/Na⁺, and capacities between 80 and 100 mAh g⁻¹, but poor rate capabilities. In order to keep the manufacturing cost as low as possible, the attention has been addressed to low cost Na-Fe-P-O systems. In particular pyrophosphates have been taken into account considering their thermal stability and the relative facile process of preparation. Pyrophosphate compounds (M_xP₂O₇) originate from the heat treatment of phosphates under reducing condition (H₂/Ar mixture), so that oxygen is thermodynamically prompted to abandon the phosphate lattice, creating oxygen-poor units: P₂O₇ or (PO_{4-x})₂¹⁶. Furthermore, the lithium analog compound, Li₂FeP₂O₇, demonstrated itself to be thermally stable up to 1400 °C, much more than phosphates that undergo decomposition at 700 °C¹⁶. High performance pyrophosphates (Na₂FeP₂O₇) preparation routes already investigated, include highly energetic ceramic methods^{17,18} and solid state synthesis¹⁹. These methods, beside to the advantage of the crystalline phase fine control, have the drawback of the highly energetic steps involved in precursors processing, such as high temperature heat treatments and ball-milling. A low cost, soft-chemistry synthetic approach to a high performance Na₂FeP₂O₇ cathode, still is missing. For what concern electronic conductivity of pyrophosphate, other than iron pyrophosphate, many studies have been carried out, and specifically for transition metal pyrophosphate, a mild mixed ionic-electronic conductivity has been proposed²⁰. This not-so-high electronic conductivity has been attributed also to Na₂FeP₂O₇ and has been tackled using different approaches such as down-sizing the particles dimension,

carbon-coating the $\text{Na}_2\text{FeP}_2\text{O}_7$ particles²¹, or, ultimately, increasing the carbonaceous (carbon black) conductive matrix in the electrode formulation.

In light of these considerations, a $\text{Na}_2\text{FeP}_2\text{O}_7$ /MWCNT composite has been prepared using an aqueous synthesis followed by a mild thermal treatment, and has been evaluated as a promising material for low-cost and kinetically-performing cathode material for Na-ion batteries. In order to overcome the intrinsic low conductive nature of the material, a new perspective has been employed for this material: a multiple walled carbon nanotubes network has been used as growing substrate for the material. Low percentages of multiple walled nanotubes have been chosen instead of pricier materials (single walled nanotubes or graphene) to keep the overall preparation process economically affordable. A facile and easy-to-reproduce synthetic path has been employed, and an exhaustive electrochemical characterization of the composite has been carried out in order to provide evidences of the benignity of $\text{Na}_2\text{FeP}_2\text{O}_7$ /MWCNT as a viable and trustworthy cathode material for sodium ion batteries based on an organic electrolyte solution. Added to this, electrochemical impedance spectroscopy has been used in calculating, for the first time, the sodium diffusion coefficient inside $\text{Na}_2\text{FeP}_2\text{O}_7$ phase, providing further proofs of the benignity of the material and giving experimental justification to theoretic considerations made elsewhere²².

3. Experimental

3.1. Material synthesis

In order to present an organic and thorough work, two different batches have been prepared: a pure $\text{Na}_2\text{FeP}_2\text{O}_7$ compound batch has been addressed as a reference material, while a $\text{Na}_2\text{FeP}_2\text{O}_7$ /MWCNT composite with a nominal 10 % concentration in weight of MWCNTs (6-9 nm X 5 μm , >95 %, Sigma Aldrich®) was considered the main term of comparison. The synthetic route, in both cases, was kept the same. For the preparation of pristine $\text{Na}_2\text{FeP}_2\text{O}_7$, $\text{Fe}(\text{NO}_3)_3 \cdot 9\text{H}_2\text{O}$ (ACS reagent, ≥ 98 %, Sigma Aldrich®) was firstly dissolved in 100 mL deionized water under vigorous magnetic stirring (400 RPM). $\text{H}_2\text{C}_2\text{O}_4 \cdot 2\text{H}_2\text{O}$ (ACS reagent, ≥ 99 %, Sigma Aldrich®) was added, obtaining a weary turn of the solution color from a robust orange to a faint yellow. Subsequently, $\text{NH}_4\text{H}_2\text{PO}_4$ (ACS reagent, ≥ 99.0 %, Fluka) was added, and after that, Na_2CO_3 (ACS reagent, ≥ 99.5 %, Alfa Aesar®) was dissolved as the sodium precursor. The temperature of the stirred solution was then set to 80 °C, and the solvent was

evaporated completely (6-10 hours) until a dense yellow paste was obtained by coprecipitation of mixed Na and Fe cations phosphate. All the precursors were used as obtained without further purification. The product was recovered and dried at 100 °C inside an oven overnight. For the synthesis of the other composite, the process was the same apart from the slow dropping of a water-based suspension of carbon nanotubes (MWCNT) just before raising solution temperature. The amount of carbon nanotubes added in the composites synthesis was calculated in order to achieve the desired final nominal concentration of 10 % by weight. For clarity, the composite will be referred as NFPy/MWCNT, while the sample with no nanotubes, as NFPy. A heat treatment was disposed for all the batches by putting the powders into an alumina crucible and housing it inside a quartz sealed tube. The tube, equipped with gas inlet/outlet, was connected to 5 % H₂/Ar (Sapio®) gas mixture line and was then placed into a tubular oven (Carbolite). The temperature program was constituted by a ramp through which the sample was heated at 5 °C·min⁻¹ to 600 °C, dwelling for 10 hours. During the whole heat treatment a steady 70 cc·min⁻¹ flow of the H₂/Ar mixture was provided. The as obtained materials were subjected to different chemical-physical characterizations.

3.2. Sample characterization

Morphological characterizations of as-prepared materials were analyzed by both SEM (HITACHI, S-4800) and TEM (FEI, Tecnai G² F30 S-Twin). Elemental analysis was performed using a FLASH 2000 series (Thermo Scientific) in order to assess the amount of carbon included in the Na₂FeP₂O₇/MWCNT composite and to evaluate the entity of other impurities. High resolution X-ray powder diffraction pattern was collected from a Rigaku diffractometer (D/Max-2500). Diffraction patterns were acquired in the 2θ window between 5° and 70°, at 4°·min⁻¹ scan rate.

3.3. Electrochemical characterization

The GCPL was employed to evaluate the electrochemical behavior of the materials. Electrodes were prepared by casting a dense slurry composed by the active material (NFPy or NFPy/MWCNT), a carbonaceous matrix (Carbon Black) and the binder (PVDF, Solvay® 6020) suspended in the minimum amount of 1-methyl-2-pyrrolidinone, onto an aluminum foil (30 μm thick). The proportion among the components of the slurry was 75:17:8 by weight, respectively. After the casting, the wet film was let to cure in an oven at 80 °C under vacuum. 9 mm and 16

mm diameter disks were punched out from the dried film, and three-electrodes Swagelok-type cells and two-electrodes CR2032 coin cell type cells were assembled in an Ar-filled glove box (Mbraun) using a sodium disk as reference and counter electrodes. The two different cell configurations were employed in order to perform different tests, depending on the more suitable set up (two or three electrodes) for the experiment itself: for instance, GCPLs were performed assembling two-electrodes coin cells while EIS measurements required a three electrodes set up. The material load deposited on each electrode was calculated to be around $1 \text{ mg}\cdot\text{cm}^{-2}$ and the final thickness of the deposition was determined as $20 \text{ }\mu\text{m}$. On every electrode the precise amount of the active material ($\text{Na}_2\text{FeP}_2\text{O}_7$) has been esteemed by mean of a 1/100 mg resolution laboratory scale (MettlerToledo). During each cell assembly, a glass fiber disk soaked in the electrolyte solution was employed as the separator between positive and negative electrode. The electrolyte solution employed was obtained by dissolving NaClO_4 (ACS reagent, $\geq 98\%$, Sigma-Aldrich®) in PC ($\geq 99.9\%$, Merck) to obtain a 1 M solution, and adding 2 % by weight of FEC (99%, Aldrich®). Together with single C rate Galvanostatic Cycling under Potential Limitation (GCPL) tests, experiment at progressively increasing C rates was also performed. GITT and Potentio-Electrochemical impedance spectroscopy (PEIS) tests were performed on the three electrodes configuration Swagelok cell, at different temperatures, using a thermostatic chamber (ACS test chamber). For the impedance measurements, a bias voltage of 10 mV was applied and each was scanned between 200 kHz and 0.05 Hz. For all the electrochemical tests a VSP-300 BioLogic galvanostat/potentiostat was employed.

4. Result and discussion

4.1. Chemical-physical characterization

SEM micrographs of the as synthesized materials are reported in Figure VII-1. It can be seen how micrometric sized particles were obtained from the synthetic route described above. The main difference between the two samples resides in the average dimension of the particles, which was considerably lower in the case of NFPy/MWCNT. For what concerns NFPy, large globular agglomerates larger than $5 \text{ }\mu\text{m}$ with a relative rough surface can be observed. On the other hand, Carbon nanotubes partially embedded in smaller and rougher NFPy/MWCNT particles can be easily spotted in image d) in Figure VII-1. From both SEM and TEM pictures, the distribution of nanotubes can be assessed as homogeneous inside the sample. Despite the

crystalline nature of the samples highlighted by the XRD diffraction patterns showed below, electrons diffraction lattice fringes can be hardly seen in high magnification TEM images c) and f) in the same figure, due to the high 3D domain of the particles. Starting from what can be seen in NFPy/MWCNT SEM micrographs, a nucleation and a growth of sodium iron pyrophosphate precursor particles around nanotubes flakes can be hypothesized. In order to precisely evaluate the accurate amount of nanotubes inside NFPy/MWCNT sample, an elemental analysis was performed and the results reported in Table 1. The real amount of carbon sensed inside NFPy/MWCNT sample was evaluated to be 7.15 % by weight. In first approximation it has been all addressed to nanotubes content, and it will be taken into consideration in the future calculation involving the real amount of the electrochemical active material, namely the sodium iron pyrophosphate alone.

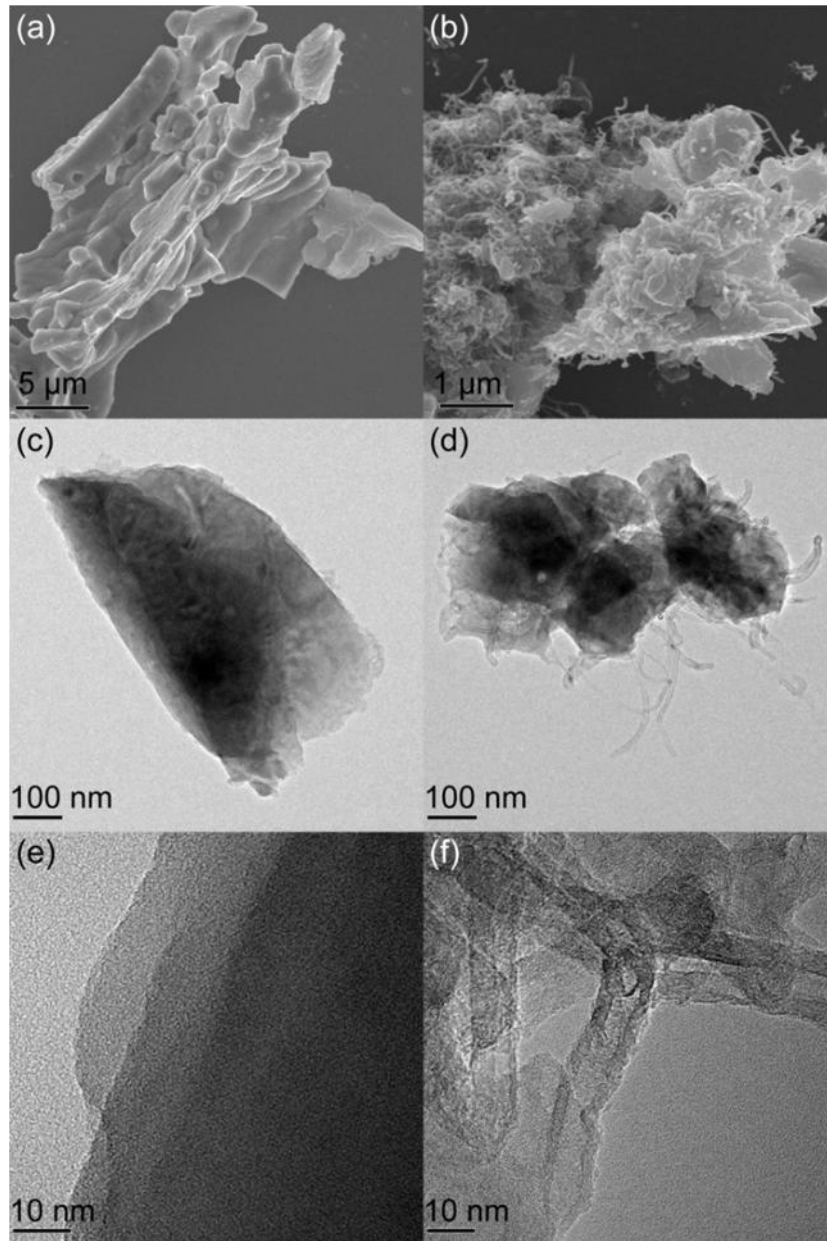


Figure VII-1: SEM micrographs of as synthesized a) NFPy and b) NFPy/MWCNT. TEM images at increasing magnification of b), c) NFPy and e), f) NFPy/MWCNT composite.

Table VII-1: elemental analysis of NFPy and NFPy/MWCNT.

	NFPy	NFPy/MWCNT
Nitrogen	0.09185 ± 0.0001	0.05199 ± 0.0002
Carbon	0.16496 ± 0.0017	7.14635 ± 0.0374
Hydrogen	0.07936 ± 0.0001	0.09824 ± 0.0001
Sulfur	0.06681 ± 0.0013	0.04024 ± 0.0001

In this concentration, MWCNT can be considered not to heavily influence the overall production costs of the material, owing also the relative lower value of multiple carbon nanotubes compared to single walled carbon nanotubes or graphene, utilized as conductive matrixes as well. Carbon content in NFPy is below 0.2 % and can be addressed to carbon residues coming from precursors employed during the synthesis, such as oxalic acid and sodium carbonate. The distribution of constitutive elements of the compounds has been evidenced by EDS elemental mapping reported in Figure VII-2. No preferential segregation of elements is observed, symptom of the coprecipitation synthetic process benignity.

From the diffraction patterns reported in Figure VII-3, the highly crystalline nature of the two samples can be noticed. In the same picture, the reference peaks calculated from the Rietveld refinement reported elsewhere²³ are shown, so that the correspondence between the diffraction signals of the obtained compounds and reference data can be appreciated. On this basis the crystal structure was evaluated to have a triclinic unit cell, in a configuration ascribable to the *P-1* space group (No. 2). In this arrangement, a continuous frame made of FeO₆- FeO₆ and PO₄-PO₄ corner and edge-sharing units¹⁶ creates an infinite 3-D network, in whose channels the Na cations can easily diffuse. This crystalline structure is iso-structural with other pyrophosphate already investigated in literature, such as Na₂CoP₂O₇²⁴.

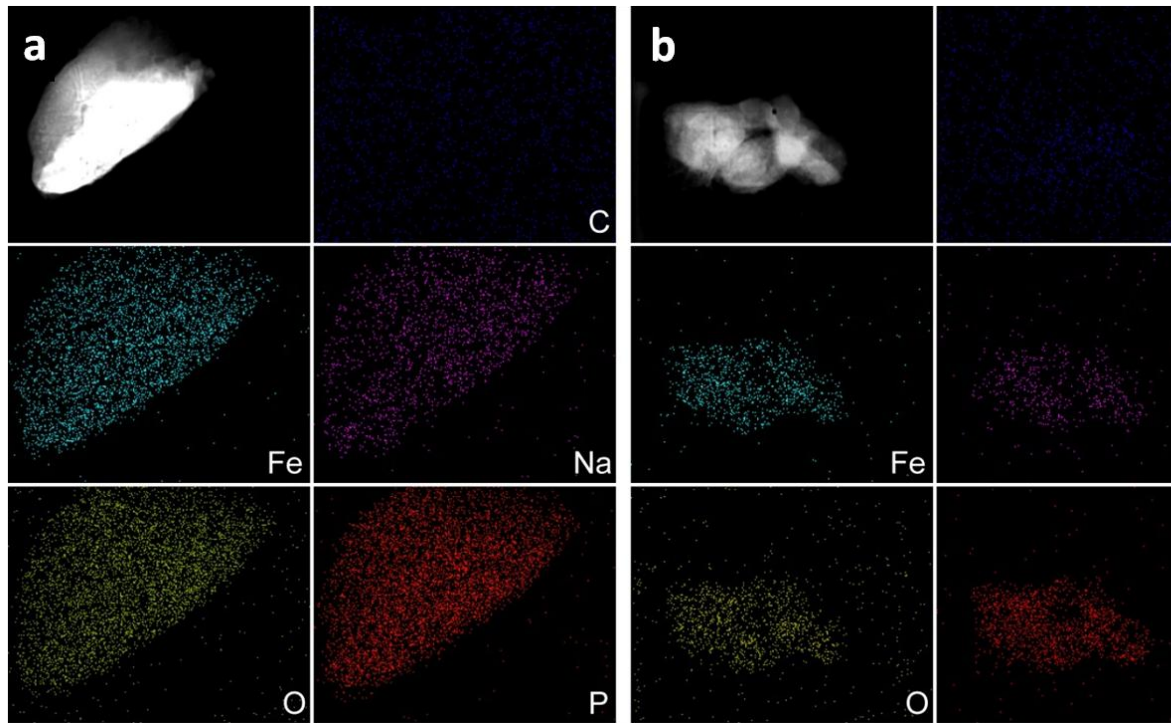


Figure VII-2: STEM images and EDS elemental mapping of (a) as-synthesized NFPy and (b) NFPy/MWCNT particles.

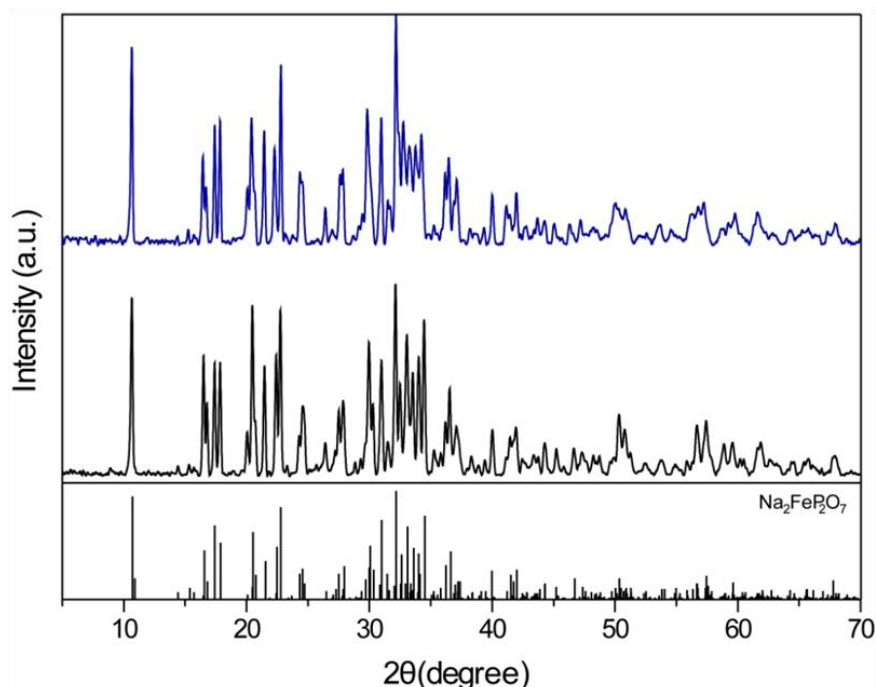


Figure VII-3: Diffraction pattern of NFPy (black line) and NFPy/MWCNT composite (blue line)

4.2. General electrochemical characterization

A conspicuous number of different electrochemical tests were performed in order to draw attention to limits and qualities of the prepared materials. In image a) of Figure VII-4, the intrinsic limit of NFPy alone is highlighted. While NFPy/MWCNT is being charged and discharged for more than 60 cycles, without recording nearly any substantial loss in capacity, the capacity extracted from NFPy electrode is considerably lower and it fades fastly during the first 20 cycles, reaching 23 mAh·g⁻¹ at the 50th cycle. On the contrary, NFPy/MWCNT composite ensures a capacity close to 85 mAh·g⁻¹ for more than 60 cycles, equal to 87.6 % of the theoretical specific capacity for the material (97 mAh·g⁻¹). This value is comparable with data reported in literature registered at the same current (1 C) in the same experimental condition²⁵, nevertheless a Coulombic efficiency of 99.8 % ± 0.25, averaged over 60 cycles, has never been reported in literature for this material. It might be interesting to compare also the performance of the NFPy/MWCNT composite material when formulated as electrode with or without the carbon black additive (image b) Figure VII-4). In this latter case the electrode deliver a stable capacity of 68 mAh·g⁻¹ at 1C. It is clear that the MWCNTs presence is essential to stabilize the properties over cycling while only the interaction between MWCNTs and carbon black particles creates an efficient electronically conductive network able to exploit the active

material full capacity at high rate. Charge/discharge profiles of the NFPy/MWCNT are shown in image c) in Figure VII-4. At the end of the very first charging process (black upward curve), a capacity above $86 \text{ mAh}\cdot\text{g}^{-1}$ is reached (1C), which means that the starting condition of $\text{Na}_{2-x}\text{Fe}^{\text{II}}_{1-x}\text{Fe}^{\text{III}}_x\text{P}_2\text{O}_7$, is addressable to an almost completely sodiated ($x = 0$) material. The voltage profile of the same curve shows a first plateau around 2.5 V and a longer second one at 3.0 V. Two slight humps are also noticeable around 3.1 and 3.2 V vs. Na/Na^+ , and their possible nature will be discussed later on.

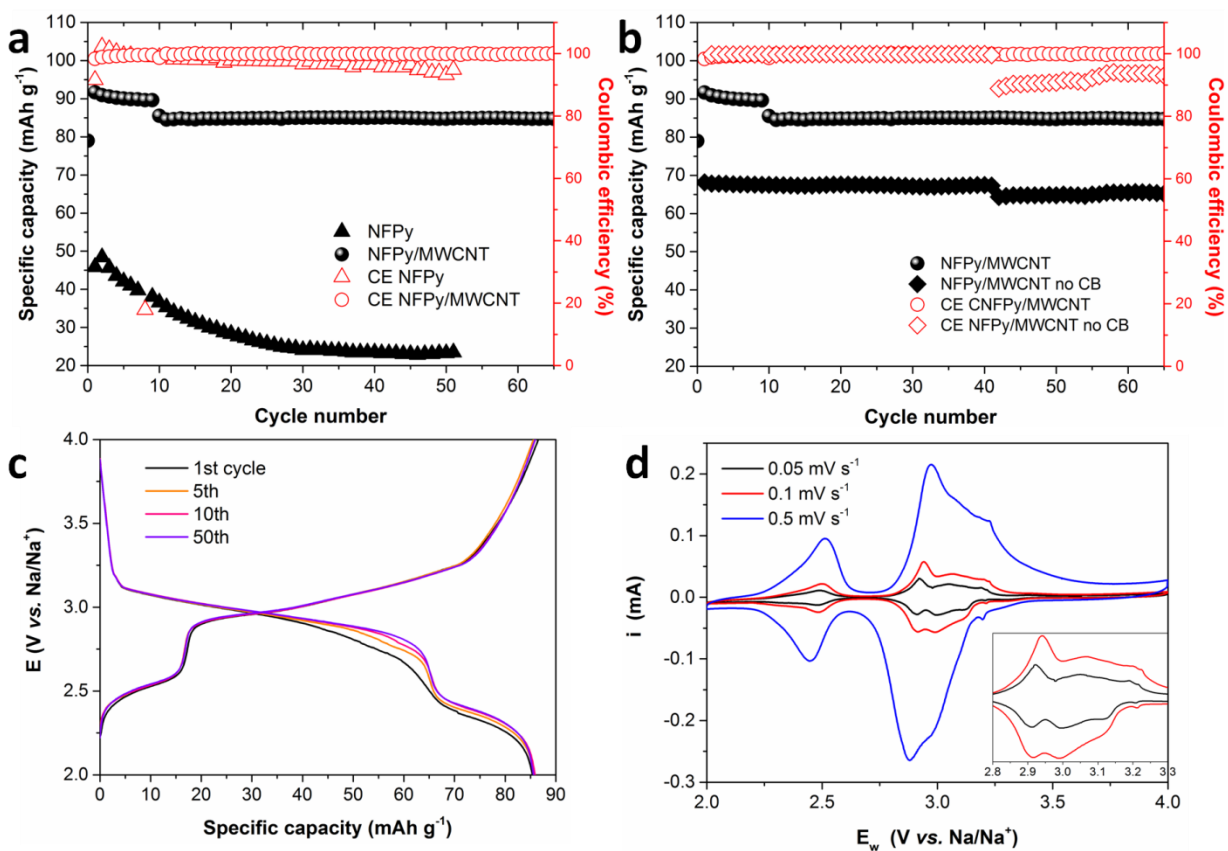


Figure VII-4: Capacity retention tests for a) NFPy and NFPy/MWCNT at 1 C (the first 10 cycles for NFPy/MWCNT composite have been recorded at C/10 the rest at 1 C); b) NFPy/MWCNT electrodes fabricated with and without carbon black; c) charge and discharge profiles of NFPy/MWCNT composite recorded cycling the electrode at 2 C ($97 \text{ mA}\cdot\text{g}^{-1}$); d) cyclic voltammograms of NFPy/MWCNT electrode obtained at different scan rates, insets of figure contains the magnification of middle section of lower scan rates curves.

A substantial difference between discharge voltage profile (downward curves) of first cycles (up to the 10th) and the following decades can be noticed. It is related to the additional step at 2.9 V that progressively disappear through cycles. Since it doesn't have its counterpart in

the charge profile, this was addressed to an irreversible structural change towards the most stable iron pyrophosphate phase. The 5th cycles of cyclic voltammograms obtained at different scan rates are reported as well in Figure VII-4 image d). At around 2.5 and 3.0 V, can be recognized the peaks correlated to the two main plateaus obtained in the galvanostatic cycling. Worthy to be noted is the extremely low polarization, even at high scan rate, compared to CVs reported in literature for the same material²³. To be more precise, the peaks centered at around 3.2 V create a set of three different signals (at 2.92, 3.04 and 3.18 V) accounting for a series of different mechanisms occurring during the main intercalation process, embodied by the plateau at 3.0 V in the GCPL. A small peak at 3.21 V can be noted as well, especially at low scan rate (inset of image d) of Figure VII-4). According to DFT calculation reported elsewhere²¹, the peak at 2.52 V (anodic curve at a scan rate of 0.5 mV·s⁻¹) refers to the more thermodynamically and kinetically accessible Na to be extracted from pyrophosphate lattice. Signals at higher potentials, instead, all refer to Na extraction mechanisms occurring at comparable activation energies, and differentiating from one another depending on the slight differences in de-intercalation/intercalation pathways. 1D and/or 2D paths are involved in this phase, as reported in simulated structures²².

Rate tests of the most promising material, namely NFPy/MWCNT, are reported in Figure VII-5. Even at high current rates (10 C), more than 60 mAh·g⁻¹ of discharge capacity was achieved. Capacity value extracted at 10 C (70 mAh g⁻¹) is comparable with the one reported in the work by Chen et al.²⁶, in which a more stable and reliable ionic liquid based electrolyte has been employed. This aspect is highly welcomed considering that, even not using an optimized and costly electrolyte solution, the material shows high stability and valuable kinetic properties, with more than 50 mAh g⁻¹ capacity at 20 C. Added to this, using a PC-NaClO₄ solution, no temperature increase is needed to bring the IL to a suitable level of viscosity in order not to slow down the diffusion processes inside the cell²⁵. This is a value considerably higher than those reported in literature referring to test conducted in the same conditions²⁷. Added to this promising performance, the cells assembled and tested at increasing C-rates do not show appreciable losses in capacity if brought back to low rates (images a),b) and c) in Figure VII-5). An efficient and fast process kinetics coupled to a general stability of the material and of the SEI layer can be assumed, as also proved by the charge/discharge profiles (Figure VII-5, image d)). On the other part, the electrode fabricated without the carbon

black additive shows stable capacity, as already pointed out but slower kinetic properties at current higher than 2C (image a) in the same figure). The electrical network created by the interconnection between CB particles and MWCNT is essential to exploit the material properties at high rate.

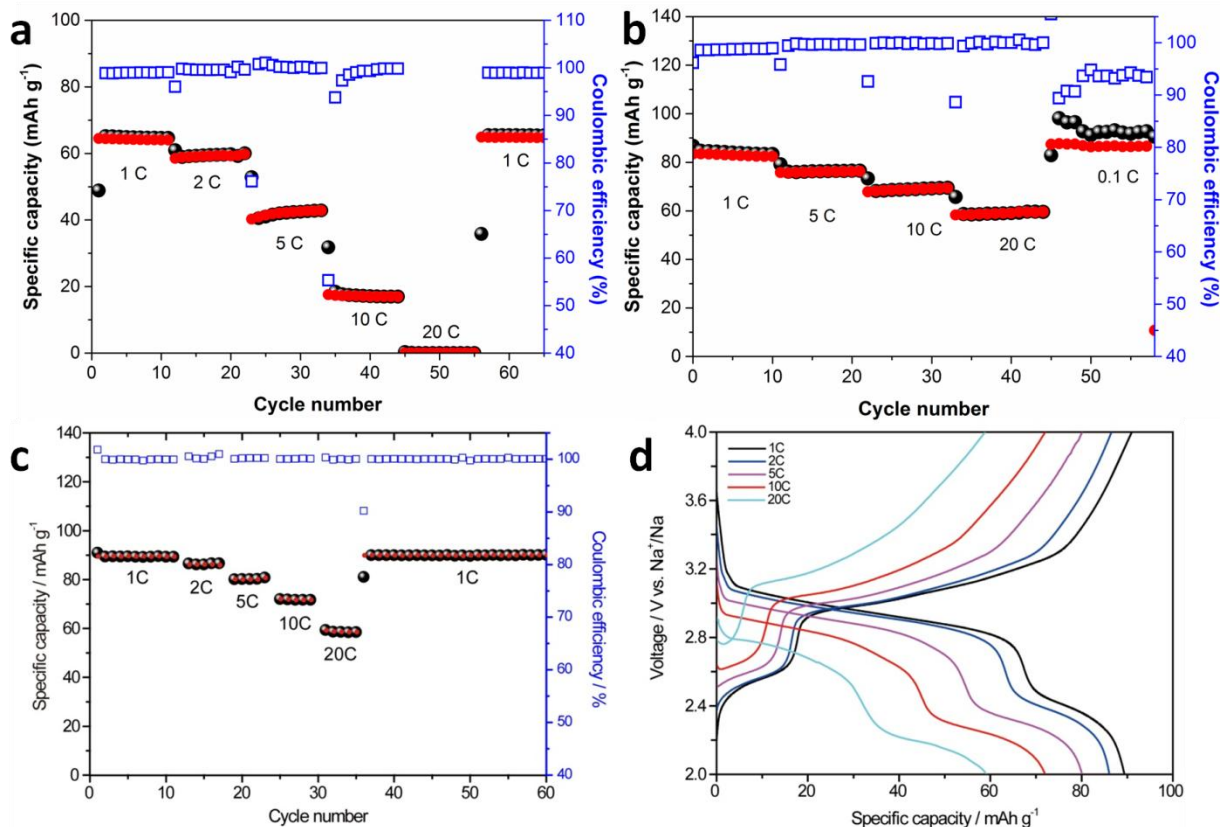


Figure VII-5: Rate capability tests: a) NFPy/MWCNT electrode fabricated without carbon black; b) NFPy/MWCNT electrode fabricated with carbon black; c) rate test of a second coin cell of NFPy/MWCNT electrode prepared with carbon black addition; d) charge discharge profiles of NFPy/MWCNT electrode fabricated with carbon black.

4.3. EIS measurements

To deepen the understanding of the electrochemical behavior of the two materials investigated, a plenty of EIS tests have been conducted. The cell set up employed during the analysis was a three electrode Swagelok-like cell assembly. For the whole duration of the EIS tests, the cells were kept in a climatic chamber with the possibility of a fine temperature and humidity conditions control (± 0.1 °C and ± 0.1 % of relative humidity). The same thermostatic chamber was also useful to perform EIS analysis at different temperatures, which was conducted in order to assess the entity of thermally activated processes. All the tests were

conducted after a 5-charge/discharge cycles of each cell, ending up at an SOC of 0.5 (~3.0 V vs. Na/Na⁺). In Figure VII-6, EIS spectra for both NFPy/MWCNT and NFPy electrodes obtained at 25 °C are reported. Solid and dashed black lines superimposed to experimental data refer to the equivalent circuit fitting. Due to the substantial difference between the two signals, two different equivalent circuits have been taken into consideration. In the case of NFPy/MWCNT, where different RCs contribution can be easily deconvoluted, circuit 1 (inset of Figure VII-6) was considered. It was built up starting from a common Randles-like circuit, and adding a further R_{int}C_{int} parallel in series between the resistance accounting for the solution IR drop (R_s) and the R_{ct}C_{dl} with the Warburg element (W). In this way the separation between the particles interfacial resistance, capacitance (correlated to Na⁺ desolvation and extended double layer capacitance), charge transfer process and double layer capacitance was obtained. This kind of equivalent circuit was already taken into account to model several types of battery chemistries^{28,29}. In the NFPy case, a simple Randles circuit was employed (circuit 2 in the inset Figure VII-6) due to the complexity of deconvolution of processes having similar time domains. In each circuit, every capacitor has been substituted by a Constant Phase Element (CPE) to overcome the deviation from a ideal capacitance behavior. A pure Warburg element has been considered in both circuits in order to model the solid phase semi-infinite Na⁺ diffusion in the intercalating material. It should be noted that extending the analysis frequencies to very low frequency values (0.5 mHz), a deviation from a pure Warburg signal is commonly obtained (image a) in Figure VII-7)³⁰. In this case, a Modified Restricted Diffusion element would have been more suitable to model the Na⁺ diffusion inside the active material in series with a physical blockage to a further diffusion due to the presence of the aluminum current collector, in which Na alloying is not possible. Nevertheless, we felt legitimate to exclude this low frequencies region, since the main interest was to discuss Na diffusive properties in the active material by Warburg Z_D impedance values analysis.

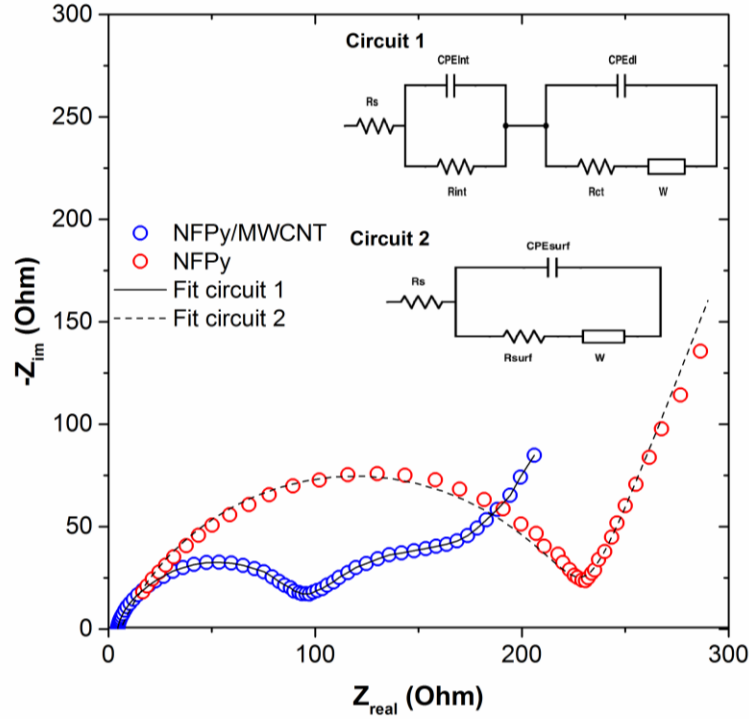


Figure VII-6: EIS tests set composed by (a) Nyquist plot of NFPy/MWCNT and NFPy electrodes. In black lines are reported the equivalent circuits fitting curves and in the inset are reported schematically the related equivalent circuits.

Experimental data obtained from the fitting are reported in Table VII-2. In order to make a first comparison between the materials possible, NFPy/MWCNT R_{int} and R_{ct} values were summed and compared to the surface resistance value (R_{surf}) obtained from NFPy electrode impedance analysis. From these values, the beneficial effect of the addition of carbon nanotubes can be noted. The lower resistance (177 Ω) for NFPy/MWCNT sample can be attributed to a more efficient electric connection of particle-particle and particle-conductive matrix rather than to a more effective charge transfer process, considering the similar nature of the active materials. The sodium diffusion coefficient (D_{Na}) in the solid solution, was calculated from the Warburg impedance values (Z_D) reported in the table according to the following equations^{29,31,32}:

$$Z_D = V_m \frac{\left(\frac{dE}{dx}\right)}{n F D_{Na}^{1/2} A} \quad (\text{VII. 1})$$

from which, rearranging, we obtain

$$D_{Na} = \left[\left(\frac{V_m}{n F Z_D A} \right) \left(\frac{dE}{dx} \right) \right]^2 \quad (\text{VII. 2})$$

Table VII-2: results of impedance spectroscopy analysis.

	NFPy/MWCNT	NFPy
R_s / Ω	5.495	4.52
R_{int} / Ω	92	-
R_{ct} / Ω	85	-
R_{surf} / Ω	177	224
Z_D	31.77	110.6

V_m is the molar volume of the species Na₂FeP₂O₇, calculated from the SXRD Rietveld refinement data reported in literature for the same crystalline phase¹⁶, n is the number of electrons exchanged for Na atom, F is the Faraday constant, A is the electrode material active area, and (dE/dx) is the slope of the equilibrium potential versus composition. This latter value was obtained from a Galvanostatic Intermittent Titration technique (GITT) conducted on the same electrode using 5 mAh g⁻¹ impulses at 0.5 C, and a resting period of 30 minutes after each impulse. The value of D_{Na} obtained at 25 °C was 8.45 X 10⁻¹³ cm² s⁻¹. It is one order of magnitude higher than diffusion coefficient values of Na in oxides, such as Na_{0.44}MnO₂²⁹ and two order of magnitude higher than Li ion diffusion inside iron pyrophosphate measured at the same SOC, as reported in a recent work by Deng et al.³³ in which Li₂FeP₂O₇ was synthesized in a monoclinic structure (space group: P21/C) providing a 2D diffusion network for Li⁺ diffusion. Doing the same calculation for pristine NFPy, a Na diffusion coefficient of 2.79 X 10⁻¹³ cm²·s⁻¹ was obtained. This slight discrepancy with the previous value might be attributed to morphological differences of the particles induced by nanotubes-driven growing process. These somewhat high diffusion coefficients, reported for sodium iron pyrophosphate here for the first time as far as we know, are consistent with the structural and diffusive properties of sodium iron pyrophosphate theoretically discussed elsewhere. In the work by Barpanda et al.²², it is pointed out how the FeO₆ octahedra and PO₄ tetrahedra are interconnected in a staggered fashion, creating large 3D pathways in which alkali ions (Na⁺) can easily diffuse despite their dimension, with modest activation energies (0.49 eV for Na⁺ in Na₂FeP₂O₇). These values are

generally higher than the corresponding values in other intercalating materials such as LiFePO_4 and NaFePO_4 in which alkali atoms diffusion follow a stricter 1D path³⁴.

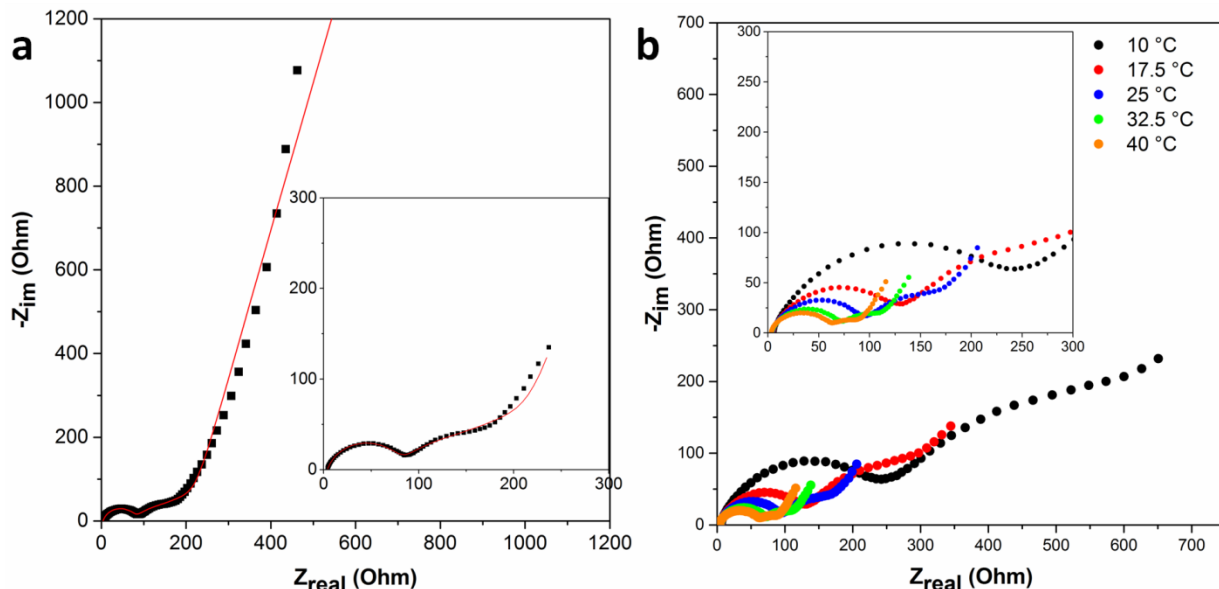


Figure VII-7: a) Nyquist plot of NFPy/MWCNT EIS analysis, having the frequencies window extended to 0.5 mHz, in order to highlight the deviation from the pure warburg behavior at mid-low frequencies; b) EIS spectra conducted at different temperature (SOC 0.5); inset refers to mid-high frequency range.

In Figure VII-7 image b), NFPy/MWCNT EIS spectra collected at different temperature are reported. For each temperature step, after increasing the temperature (using a liner program with a slope of $0.5 \text{ }^\circ\text{C min}^{-1}$), the system was allowed equilibrating for 1 h before registering the impedance. OCV was monitored during this resting period. The temperature window investigated ranged from $10 \text{ }^\circ\text{C}$ to $40 \text{ }^\circ\text{C}$ with $7.5 \text{ }^\circ\text{C}$ steps. As can be appreciated from the Nyquist plot, EIS signals show substantial differences. Table VII-3 displays the values for R_s , R_{int} and R_{ct} extrapolated at different temperatures. As can be easily noted, all the resistance values decrease as the temperature rises in a fashion that leads R_{int} and R_{ct} to be comparable at $25 \text{ }^\circ\text{C}$. In image a) in Figure VII-8, it can be spotted the Arrhenius dependence between resistance values and temperature, suggesting the thermally activated nature of interfacial sodium diffusion and charge transfer mechanism. The values of i_0 , exchange current for the charge transfer process, were calculated from R_{ct} , considering the approximation of the Butler-Volmer relation for small overpotentials:

$$i_0 = \frac{RT}{R_{\text{ct}} n F} \quad (\text{VII. 3})$$

From the $\ln(i_0)$ vs. $100/T$ plot slope, the activation energy E_a for the charge transfer process has been calculated. i_0 values range from 36 to 583 $\mu\text{A}\cdot\text{cm}^{-2}$ at 10 °C and 40 °C respectively and the related value of E_a was 0.68 eV. Comparing the latter value and the activation energy related to interface processes mechanism (0.39 eV), it can be concluded that the charge transfer process constitutes the kinetically limiting step of the whole cathode electrochemical mechanism. The relatively low value of the charge transfer activation energy suggests that there are no significant obstacles to the surface electrochemical mechanism, accordingly to the mixed ionic-electronic conductive nature of the compound proposed by Hafidi *et al.*²⁰.

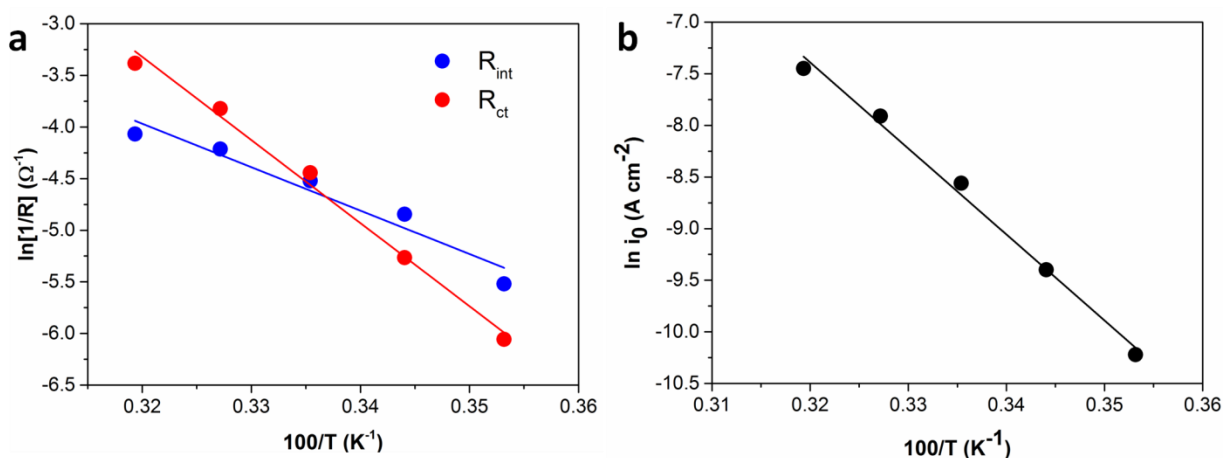


Figure VII-8: Arrhenius plot for a) resistance values related to interface resistance and charge transfer resistance, and b) exchange current i_0 .

Table VII-3: Temperature dependence of electrode resistances

	Temperatures / K				
	283.15	290.65	298.15	305.65	313.15
R_s / Ω	6.35	5.26	4.52	3.95	3.65
R_{int} / Ω	249.7	127	92	67.55	58.5
R_{ct} / Ω	426.8	193.7	85.02	45.74	29.45

5. Conclusions

A facile, easily scalable and effective co-precipitation synthetic route, instead of highly energetic synthetic strategies as reported in literature¹⁶⁻¹⁸, is proposed as a viable preparation process for a Na₂FeP₂O₇/MWCNT composite and the further exhaustive electrochemical

characterization has been conducted to legitimate the material mentioned above as a valid cathode material for aprotic sodium ion secondary batteries. Based on the rate tests, the surprisingly high performance of the material is highlighted. Thanks to the reliability of the compound even at high charge/discharge rates, it could also fulfill demanding application such as heavy duty secondary batteries employed in the automotive field or stationary energy storage (SES). Behind this notable feature, the composite shows an excellent stability and high capacity retention through cycles. Apart from the mere performance aspect, with this contribute we also tried to answer to the open question about the mechanism and energies involved in sodium diffusion through material-electrolyte interface and inside the material lattice. We derived values for the diffusion coefficients and activation energies from experimental evidences. To conclude, $\text{Na}_2\text{FeP}_2\text{O}_7/\text{MWCNT}$ composite constitutes an extremely encouraging candidate appropriate to applications in which a high fidelity is needed. The low manufacturing costs, lastly, make this material preferable to the technologies based on Lithium, for the on grid energetic storage application.

6. Bibliography

- (1) Hassoun, J.; Bonaccorso, F.; Agostini, M.; Angelucci, M.; Betti, M. G.; Cingolani, R.; Gemmi, M.; Mariani, C.; Panero, S.; Pellegrini, V.; Scrosati, B. An Advanced Lithium-Ion Battery Based on a Graphene Anode and a Lithium Iron Phosphate Cathode. *Nano Lett.* **2014**, *14*, 1–17.
- (2) Armand, M.; Tarascon, J.-M. Building Better Batteries. *Nature* **2008**, *451* (February), 652–657.
- (3) Goodenough, J. B.; Kim, Y. Challenges for Rechargeable Li Batteries. *Chem. Mater.* **2010**, *22*, 587–603.
- (4) Wang, C.; Xu, T.; Ge, S.; Zhang, G.; Yang, X.; Ji, Y. A Fast Rechargeable Lithium-Ion Battery at Subfreezing Temperatures. *J. Electrochem. Soc.* **2016**, *163* (9), A1944–A1950.
- (5) Wang, L. P.; Yu, L.; Wang, X.; Srinivasan, M.; Xu, Z. J. Recent Developments of Electrode Materials for Sodium Ion Batteries. *J. Mater. Chem. A* **2015**.
- (6) Kundu, D.; Telaie, E.; Duffort, V.; Nazar, L. F. The Emerging Chemistry of Sodium Ion Batteries for Electrochemical Energy Storage. *Angew. Rev.* **2015**, *54*, 3431–3448.
- (7) Berthelot, R.; Carlier, D.; Delmas, C. Electrochemical Investigation of the P₂-Na_xCoO₂ Phase Diagram. *Nat. Mater.* **2011**, *10* (1), 74–80.
- (8) Didier, C.; Guignard, M.; Denage, C.; Szajwaj, O.; Ito, S.; Saadoune, I.; Darriet, J.; Delmas, C. Electrochemical Na-Deintercalation from NaVO₂. *Electrochem. Solid-State Lett.* **2011**, *14* (5), A75.
- (9) Yabuuchi, N.; Kajiyama, M.; Iwatate, J.; Nishikawa, H.; Hitomi, S.; Okuyama, R.; Usui, R.; Yamada, Y.; Komaba, S. P₂-Type Na_x[Fe_{1/2}Mn_{1/2}]O₂ Made from Earth-Abundant Elements for Rechargeable Na Batteries. *Nat. Mater.* **2012**, *11* (6), 512–517.
- (10) Sathiyaraj, M.; Hemalatha, K.; Ramesha, K.; Tarascon, J.-M.; Prakash, a. S. Synthesis, Structure, and Electrochemical Properties of the Layered Sodium Insertion Cathode Material: NaNi_{1/3}Mn_{1/3}Co_{1/3}O₂. *Chem. Mater.* **2012**, *24*, 1846–1853.
- (11) Fang, C.; Huang, Y.; Zhang, W.; Han, J.; Deng, Z.; Cao, Y.; Yang, H. Routes to High Energy Cathodes of Sodium-Ion Batteries. *Adv. Energy Mater.* **2016**, *6* (5).
- (12) Shibata, T.; Fukuzumi, Y.; Kobayashi, W.; Moritomo, Y. Fast Discharge Process of Layered Cobalt Oxides due to High Na⁺ Diffusion. *Sci. Rep.* **2015**, *5*:9006.
- (13) Ung, Y. H.; Lim, C. H.; Kim, D. K. Graphene-Supported Na₃V₂(PO₄)₃ as a High Rate

- Cathode Material for Sodium-Ion Batteries. *J. Mater. Chem. A* **2013**, *1* (37), 11350.
- (14) Kim, H.; Park, I.; Seo, D. H.; Lee, S.; Kim, S. W.; Kwon, W. J.; Park, Y. U.; Kim, C. S.; Jeon, S.; Kang, K. New Iron-Based Mixed-Polyanion Cathodes for Lithium and Sodium Rechargeable Batteries: Combined First Principles Calculations and Experimental Study. *J. Am. Chem. Soc.* **2012**, *134* (25), 10369–10372.
- (15) Nose, M.; Nakayama, H.; Nobuhara, K.; Yamaguchi, H.; Nakanishi, S.; Iba, H. Na₄Co₃(PO₄)₂P₂O₇: A Novel Storage Material for Sodium-Ion Batteries. *J. Power Sources* **2013**, *234*, 175–179.
- (16) Chung, S.; Yamada, Y.; Yamada, A. Na₂FeP₂O₇: A Safe Cathode for Rechargeable Sodium-Ion Batteries. *Chem. Mater.* **2013**.
- (17) Honma, T.; Togashi, T.; Ito, N.; Komatsu, T. Fabrication of Na₂FeP₂O₇ Glass-Ceramics for Sodium Ion Battery. *J. Ceram. Soc. Japan* **2012**, *120* (1404), 344–346.
- (18) Honma, T.; Ito, N.; Togashi, T.; Sato, A.; Komatsu, T. Triclinic Na_{2-x}Fe_{1+x}/2P₂O₇/C Glass-Ceramics with High Current Density Performance for Sodium Ion Battery. *J. Power Sources* **2013**, *227*, 31–34.
- (19) Chen, C.-Y.; Matsumoto, K.; Nohira, T.; Hagiwara, R. Full Utilization of Superior Charge-Discharge Characteristics of Na_{1.56}Fe_{1.22}P₂O₇ Positive Electrode by Using Ionic Liquid Electrolyte. *J. Electrochem. Soc.* **2014**, *162* (1), A176–A180.
- (20) Hafidi, E.; El Omari, M.; El Omari, M.; Bentayeb, a.; Bennazha, J.; El Maadi, a.; Chehbouni, M. Conductivity Studies of Some Diphosphates with the General Formula Al₂B₂IIP₂O₇ by Impedance Spectroscopy. *Arab. J. Chem.* **2011**, 253–263.
- (21) Kim, H.; Shakoor, R. a.; Park, C.; Lim, S. Y.; Kim, J. S.; Jo, Y. N.; Cho, W.; Miyasaka, K.; Kahraman, R.; Jung, Y.; Choi, J. W. Na₂FeP₂O₇ as a Promising Iron-Based Pyrophosphate Cathode for Sodium Rechargeable Batteries: A Combined Experimental and Theoretical Study. *Adv. Funct. Mater.* **2013**, *23* (9), 1147–1155.
- (22) Clark, J. M.; Barpanda, P.; Yamada, A.; Islam, M. S. Sodium-Ion Battery Cathodes Na₂FeP₂O₇ and Na₂MnP₂O₇: Diffusion Behaviour for High Rate Performance. *J. Mater. Chem. A* **2014**, *2* (30), 11807.
- (23) Jung, Y. H.; Lim, C. H.; Kim, J.-H.; Kim, D. K. Na₂FeP₂O₇ as a Positive Electrode Material for Rechargeable Aqueous Sodium-Ion Batteries. *RSC Adv.* **2014**, *4* (19), 9799.
- (24) Barpanda, P.; Lu, J.; Ye, T.; Kajiyama, M.; Chung, S.-C.; Yabuuchi, N.; Komaba, S.;

- Yamada, A. A Layer-Structured Na₂CoP₂O₇ Pyrophosphate Cathode for Sodium-Ion Batteries. *RSC Adv.* **2013**, 3 (12), 3857.
- (25) Chen, C.-Y.; Matsumoto, K.; Nohira, T.; Ding, C.; Yamamoto, T.; Hagiwara, R. Charge-discharge Behavior of a Na₂FeP₂O₇ Positive Electrode in an Ionic Liquid Electrolyte between 253 and 363K. *Electrochim. Acta* **2014**, 133, 583–588.
- (26) Chen, C. Y.; Matsumoto, K.; Nohira, T.; Hagiwara, R.; Oriyasa, Y.; Uchimoto, Y. Pyrophosphate Na₂FeP₂O₇ as a Low-Cost and High-Performance Positive Electrode Material for Sodium Secondary Batteries Utilizing an Inorganic Ionic Liquid. *J. Power Sources* **2014**, 246, 783–787.
- (27) Barpanda, P.; Ye, T.; Nishimura, S.; Chung, S.-C.; Yamada, Y.; Okubo, M.; Zhou, H.; Yamada, A. Sodium Iron Pyrophosphate: A Novel 3.0V Iron-Based Cathode for Sodium-Ion Batteries. *Electrochem. commun.* **2012**, 24, 116–119.
- (28) Barsoukov, E.; Macdonald, J. R. *Impedance Spectroscopy: Theory, Experiment and Application.*; 2005.
- (29) Ruffo, R.; Fathi, R.; Kim, D. K. J.; Jung, Y. H.; Mari, C. M.; Kim, D. K. J. Impedance Analysis of Na_{0.44}MnO₂ Positive Electrode for Reversible Sodium Batteries in Organic Electrolyte. *Electrochim. Acta* **2013**, 108, 575–582.
- (30) Ho, C. Application of A-C Techniques to the Study of Lithium Diffusion in Tungsten Trioxide Thin Films. *J. Electrochem. Soc.* **1980**, 127 (2), 343.
- (31) Shaju, K. M.; Subba Rao, G. V.; Chowdari, B. V. R. EIS and GITT Studies on Oxide Cathodes, O₂-Li_{(2/3)+x}(Co_{0.15}Mn_{0.85})O₂ (X = 0 and 1/3). *Electrochim. Acta* **2003**.
- (32) Weppner, W. Determination of the Kinetic Parameters of Mixed-Conducting Electrodes and Application to the System Li₃Sb. *J. Electrochem. Soc.* **1977**, 124 (10), 1569.
- (33) Tan, L.; Zhang, S.; Deng, C. Fast Lithium Intercalation Chemistry of the Hierarchically Porous Li₂FeP₂O₇/C Composite Prepared by an Iron-Reduction Method. *J. Power Sources* **2015**, 275, 6–13.
- (34) Tripathi, R.; Wood, S. M.; Islam, M. S.; Nazar, L. F. Na-Ion Mobility in Layered Na₂FePO₄F and Olivine Na Fe,Mn PO₄. *Energy Environ. Sci.* **2013**, 6 (8), 2257–2264.

CHAPTER VIII: Morphology/properties correlation in nano-structured TiO₂ as negative electrode in SIBs

1. Introduction

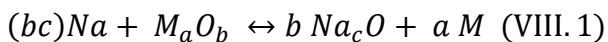
Rechargeable sodium-ion batteries are becoming a viable alternative to lithium-based technology in energy storage strategies, due to the wide abundance of sodium raw material. In the last decade, this has generated a booming of research interest in such systems. Notwithstanding the large number of research papers concerning sodium-ion battery electrodes, the development of a low cost, good performing anode material remains the largest obstacle to overcome. Although the well-known anatase, one of the allotropic forms of natural TiO₂, was recently proposed for such applications, the material generally suffers from reduced cyclability and limited power, due to kinetic drawbacks and to its poor charge transport properties. A systematic approach in the morphological tuning of the anatase nanocrystals is thus needed, in order to optimize its structural features towards the electrochemical properties and to promote the material interaction with the conductive network and the electrolyte. Aiming to face with these issues we have been able to obtain a fine tuning of the nanoparticle morphology and to expose the most favorable nanocrystal facets to the electrolyte and to the conductive wrapping agent (graphene), thus overcoming the intrinsic limits of anatase transport properties. The result is a TiO₂-based composite electrode able to deliver an outstandingly stability over cycles (150 mAh g⁻¹ for more than 600 cycles in the 1.5-0.1 V potential range) never achieved with such a low content of carbonaceous substrate (5%). Moreover, it has been demonstrated for the first time than these outstanding performances are not simply related to the overall surface area of the different morphologies, but has to be directly related to the peculiar surface characteristics of the crystals.

2. Background

Efficient energy storage will be an essential asset in a society increasingly starved of energy. If the economically and industrially developed countries stick to current policies, the world's energy needs will be 50 % higher in 2030 than today, with a suggested annual growth

rate of 1.6 %. Despite the pivotal role of developed countries in paving the way towards a more energetically sustainable and less fossil fuel dependent future, two third of the energy demand steady increase will derive from currently developing countries. Leading parties of the latter argue that, in a free market landscape, it is rather unfair intervening with strict international policies regarding emissions curbing and fossil fuels exploitation restraint, since this would represent a violation of the legitimate right to growth, experienced by developed countries in the past centuries. The transition towards a more sustainable development, passes necessarily through a more efficient handling of energy production and exploitation, whichever the energy source might be. The energy storage, in particular, is of primary importance in many fields, such as the effective integration of renewable energy sources (RES) and power quality and reliability¹. Among the energy storage technologies today available, such as pumping hydro, mechanical (flywheels), electrical, chemical and electrochemical², secondary batteries represent the more versatile and efficient choice. Lithium ion batteries (LIB), in particular, embodied for more than two decades the role of the most performing electric storage facility, thanks to their high round trip efficiency, prominent energy density and notable power density³⁻⁵. The massive diffusion of lithium-ion battery technology in the last 20 years contributed to the arising of concerns connected to the future availability of battery-grade lithium compounds, especially considering energy intensive applications of the technology, such as the electric vehicles market and on grid storage facilities^{6,7}. The picture gets grimmer if all the other applications that require a considerable amount of lithium are considered, indeed battery manufacturing accounts for 30 % only of the world lithium production (measured as LCE, namely unit of lithium carbonate equivalent), other applications include glass, lubricant, and metallurgy industry⁸. Lastly, is the implementation of lithium energy storage technology actually heading for a curtailment of CO₂ emissions? The steadily increase of the utilization of LIB forecasted for the next decades casts a shadow on the actual environmental friendliness of all the phases of battery manufacturing. Life cycle assessments (taking into account battery production, materials processing and recycling) have revealed that 400 kWh are needed to make 1 kWh Li-ion battery, with an associated CO₂ emission of about 75 kg, equivalent to burning 35 l of gasoline^{7,9}. Owing to these considerations, other battery chemistries have begun to be investigated in the recent times. SIBs have recently known a renaissance and a renovated interest thanks to the rather similar chemistry to LIB and, above all, thanks to the unique

abundance of raw materials^{10,11}. Studies have revealed how switching to SIB technology would reduce production costs especially connected to materials manufacturing¹². Materials for the SIB positive electrode have been extensively investigated¹³: easy-to-manufacture and environmentally friendly compounds with promising features in terms of energy density and cyclability have been proposed. Layered oxides of naturally abundant transition metals^{14,15}, similar to those employed in LIBs, showed interesting electrochemical properties in intercalating Na⁺: for instance, gravimetric capacities well above 150 mAh g⁻¹ have been measured for P2-Na_{2/3}[Fe_{1/2}Mn_{1/2}]O₂¹⁶. Following the success of phospho-olivines, introduced by J. B. Goodenough as Co-free positive material for lithium batteries¹⁷, a large number of polyanion compounds have been suggested as promising materials for SIB, exploiting the benign effect of [PO₄]³⁻ on working potential tailoring. Fluorophosphate (Na₂MnPO₄F¹⁸) and pyrophosphate¹⁹⁻²² have been extensively studied as well. Despite all these admirable efforts in designing a robust positive cathode, the most demanding challenge is represented by the negative electrode. Many exhaustive reviews have been published providing an in-depth description of the anode materials proposed along the years^{12,23-25}. In recalling the fundamental prerequisites for SIB anode materials can be included the i) high capacity and low operational potential, ii) chemical stability and high Coulombic efficiency, iii) natural abundance of precursors and scalable synthetic routes. Concerning on the accessibility of synthetic routes and scalability of processes, transition metal oxides represent a valid choice. Fe₃O₄^{26,27} and Co₃O₄^{28,29} have been reported as valuable anode material compounds for SIBs thanks to their easy preparation and high theoretical capacity (~890 mAh·g⁻¹). The courageous proposition of this kind of materials signs a complete paradigm shift in the chemistry involved in alkaline metal based batteries. The classic rocking chair intercalation mechanism (core process in the graphite-lithium metal oxide battery) is abandoned in favor of compounds that interact with sodium via the conversion reaction²⁴:



where M_aO_b is a general transition metal oxide. The reported reaction relies just on an ideal behavior, while the actual mechanism might include products other than Na₂O (thermodynamically stable in most cases) and the bare metal M. For instance, Su *et al.*³⁰ claimed that CoO is involved in the reversible de-lithiation of a Co₃O₄ anode rather than Co₃O₄ itself, which has been demonstrated to undergo an irreversible transformation during the first

lithiation cycle. A well agreed-upon flaw of this class of materials, as previously stated, is the intrinsic poor cyclability, due to excessive volume change experienced during conversion reactions. The relevant stresses values the active material particles are exposed to, lead to sudden fracturing of particles and rupturing of the SEI layer, driving the whole system towards a gradual deterioration of capacity retention. A transition metal oxide that seems to answer to this technological challenge is TiO₂. TiO₂ polymorphs have been extensively investigated as potential anode materials for SIBs thanks to their exceptional stability, non-toxicity, natural abundance and low cost. Despite being chemically active towards Li intercalation, anatase-TiO₂ doesn't intercalate efficiently Na ions. Even though anatase polymorphs present the least dense packing of TiO₆ octahedra, Na⁺ ion dimensions appear to be a limiting factor for reversible insertion in the lattice. Nevertheless, anatase-TiO₂, has been demonstrated to give a decent capacity of 180 mAh·g⁻¹ at 0.2 C, and a considerable stability over cycles³¹. Recent studies by Passerini on commercial anatase powders unveiled different mechanisms contributing to the total capacity of TiO₂ in SIB³². In particular, after a pseudo-capacitance behavior, accounting for 4 % of the total capacity extracted during the first cycle (360 mAh·g⁻¹), a considerable amount of charge is stored via what it has been demonstrated to be, an insertion process of Na⁺ in TiO₂ lattice which occurs at intermediate potentials (1.0-0.3 V vs Na/Na⁺). Below 0.3 V, a significative and progressive deterioration of the crystallinity of the material, not recovered in the following cycles, takes place. Despite the multiplicity of anatase structures and morphologies analyzed so far, data relative to capacities and, most of all, stability of the compound through cycling are still scattered and controversial³³⁻³⁶.

3. Experimental

3.1. Synthesis

In this work we tried to shed light onto the general mechanism underneath the interaction between sodium ions and different TiO₂ morphologies, giving particular attention to how different exposed crystal facet ratios might influence and guide the intercalation and conversion mechanisms. Inspired by the exploratory work by Dihn *et al.*³⁷ and following outstanding contributes to materials synthesis^{38,39}, we've been able to selectively obtain anatase-TiO₂ nanocrystals with four peculiar surface characteristics by solvothermal route employing tetrabutyl orthotitanate (TB) as TiO₂ precursor and in presence of capping agents

(oleic acid and oleylamine). In a common synthetic procedure, an homogeneous mixture of oleic acid (≥ 93 %, Sigma Aldrich), oleylamine (≥ 98 %, Sigma Aldrich), tetrabutyl orthotitanate(IV) (≥ 97 %, Fluka) in different proportion (see image a) on the right side in Figure VIII-1), together with 20 mL of absolute ethanol (ACS reagent, Sigma Aldrich), has been placed in a Teflon-lined stainless steel autoclave. Before the autoclave sealing, 70 mL of a mixture made of ethanol and deionized water in proportion 38:1 by weight has been rapidly added to the Teflon beaker. The reaction mixture underwent a solvothermal step for 18 hours at 180 or 140 °C (140 °C in the case of the nanobars morphology, under vigorous stirring. The yellowish solid precipitate was then recovered by centrifugation and thoroughly washed several times with ethanol and dried in vacuum overnight. In order to remove as more accurately as possible the capping agents from TiO₂ crystals, a cleaning step procedure was employed. A suspension made of 200 mg of TiO₂ powder and 10 mL of dry hexane (anhydrous, 95 %, Sigma Aldrich), was added to a solution of 150 mg of nityrosil tetrafluoroborate (95 %, Aldrich) in acetonitrile (anhydrous, 99.8 %, Sigma Aldrich). The biphasic mixture was subjected to 10 minutes sonication/10 minutes rest cycles repeatedly, until a visible bleaching of the solid. The product was recovered by centrifugation and washed with DMF (dimethylformamide, 99 %, Sigma Aldrich) first, and then with anhydrous toluene (≥ 99 %, Sigma Alrich) for three to five times, until a clear supernatant was obtained. Lastly the powder was left drying overnight at 60 °C in vacuum. The graphene oxide (GO) employed for the crystals wrapping, was prepared using a modified exfoliation Hummer's method described elsewhere⁴⁰, starting from graphite flakes. In order to produce a positive electrostatic interaction between TiO₂ crystals and grapheme oxide oxidized groups, anatase nanoparticle surfaces were previously functionalized using (3-aminopropyl)triethoxysilane, APTES (≥ 98 %, Sigma Aldrich). Functionalization step was performed refluxing for 24 hours a suspension of TiO₂ powder (150 mg) in an APTES 15 mM (0.375 wt %) dry toluene solution. The product was centrifuged, recovered and washed thoroughly with dry toluene several times. Functionalized TiO₂ nanocrystals (50 mg) were eventually suspended in deionized water and a sonicated water dispersion of GO (50 mL of a 0.05 mg mL⁻¹ suspension) was added drop wise under vigorous stirring in order to achieve the desired GO load (5 % by weight) in the final composite. After 3 hours of ulterior mild stirring at room temperature, the final composite was easily recovered by centrifugation, washed with absolute ethanol end, after a complete drying in a vacuum oven at 80 °C, subjected to a heat

treatment in N₂ flux at 400 °C for 2 h in order to obtain a partial reduction of GO to rGO (reduced graphene oxide). The GO wrapping procedure was analogous for the three TiO₂ synthesis performed, and, for convenience, the rGO lettering will be omitted in the following discussion. Samples coding used in this chapter, namely RE, R, NB and SP have to be thus considered, unless indicated otherwise, as referred to TiO₂ nanocrystals grafted onto reduced graphene oxide sheets. An accurate morphological and electrochemical characterization has been subsequently performed to clarify the sodium uptake mechanisms occurring in a Na-ion half cell battery using the nanostructured composite as active anode material.

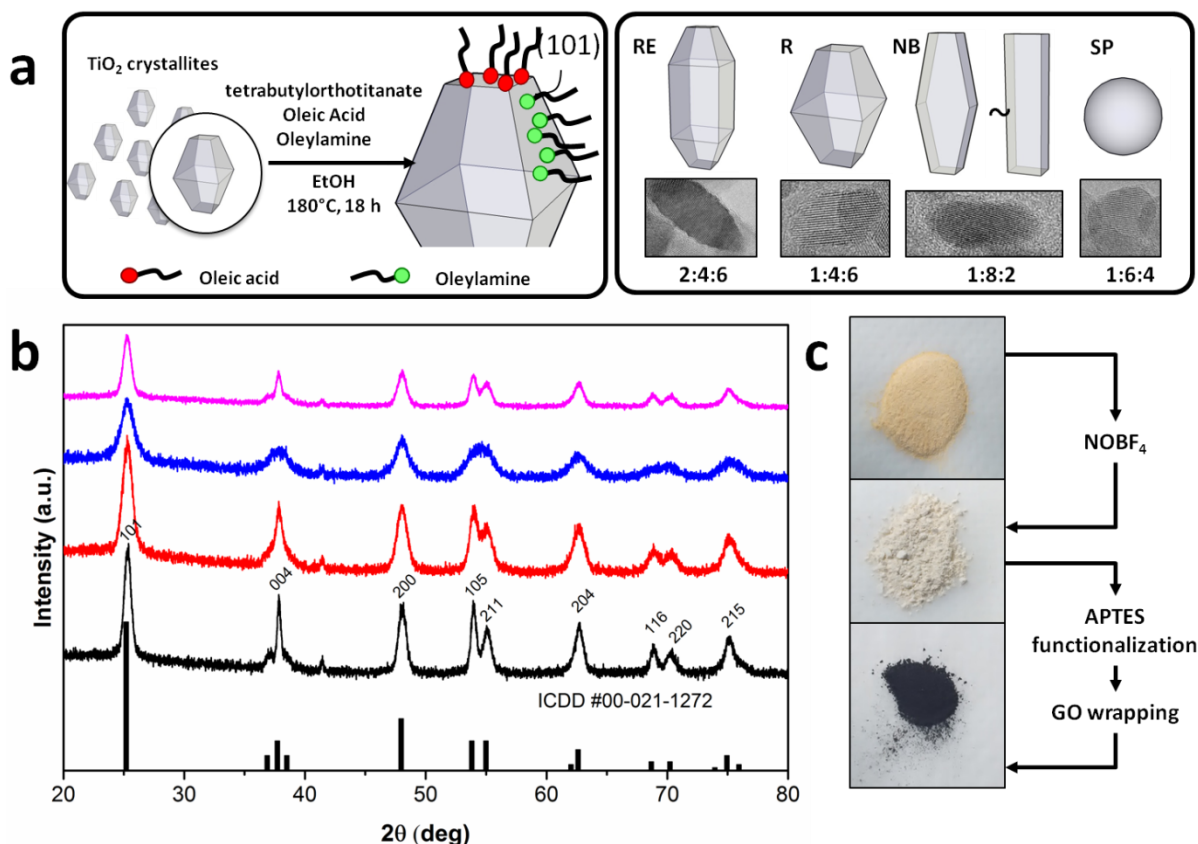


Figure VIII-1: a) left part, schematic representation of the shape-controlled growth mechanism and synthesis condition of TiO₂ crystallites thanks to the selective capping effect of oleic acid (OA) and oleylamine (OM); a) right part, 3D-sketching of the investigated morphologies with the corresponding TEM magnification on single particles and the relative amount of the three reactants employed in the synthetic routes; b) X-ray diffractograms of anatase-TiO₂ nanocrystals (RE black, R red, NB blue and SP purple lines) and PDF card 00-021-1272 peaks of tetragonal anatase (vertical black lines); c) overall appearance of TiO₂ powders during processing.

3.2. Sample characterization

The as synthesized TiO₂ powders were subjected to XRD analysis using an Expert-PRO diffractometer (PANalytical), employing Cu-K α radiation at 1.54 Å. Samples were scanned in the 2 θ window ranging from 20° to 80° using a 2theta-omega configuration, setting the step size to 0.01°. All the X-ray diffraction analysis taken directly onto electrodes, were carried out using a MiniFlex 600 diffractometer (Rigaku), spanning the 20°-80° 2 θ window at 3° min⁻¹. The radiation utilized was, even in this case, the Cu-K α radiation (1.54 Å). The morphological features of TiO₂ samples were identified by High Resolution Transmission Electron Microscopy (TEM-HRTEM), by using a Jeol 3010 apparatus operating at 300 kV with a high-resolution pole piece (0.17 nm point-to-point resolution) and equipped with a Gatan slow-scan 794 CCD camera. Samples were prepared by placing 5 μ L drop of a dilute toluene dispersion of the nanocrystals on a holey carbon film supported on a 3 mm copper grid. Further characterizations were thermal gravimetric analysis and infrared spectroscopy analysis. In the former case TGA-DSC tests were performed in the 30-900 °C window at a heating rate of 10 °C min⁻¹, fluxing N₂ inside the furnace chamber at 20 mL min⁻¹. The instrument employed was a TGA/DSC1 STAR^e System (MettlerToledo).

3.3. Electrochemical characterization

Electrodes were prepared by blade-casting a thick slurry made by suspending the active material a carbonaceous additive (Carbon Black, Timcal) and a polymeric binder (PVDF, Solvay[®] 6020) in the minimum amount 1-Methyl,2-Pyrrolidone (anhydrous, 99.5 %, Sigma-Aldrich), onto a Cu current collector foil. The relative ratio among the solid slurry components was 80:17:8. The deposition was let dry at 80°C in vacuum overnight and 16 mm diameter discs were punched out after roll pressing the casting. 2032 type Coin cells were assembled in order to carry out the electrochemical tests of the prepared materials. Inside an argon-filled glove box (MBraun), with a level of oxygen lower than 1 ppm, the electrode carrying the active material was piled together with a glass fiber separator wetted with the electrolyte solution and a sodium metal disc. The electrolyte used was a propylencarbonate (\geq 99 %, Merck) 1 M NaClO₄ (ACS reagent, \geq 98 %, Sigma Aldrich) solution additivated by 2 wt% of fluoroethylene carbonate (99 %, Aldrich). All the chemicals employed for electrochemical testing were used as purchased without further purification. Electrochemical tests, namely Galvanostatic Cycling with a Potential Limitation (GCPL) and Cyclic Voltammetry (CV), were carried out using a

VMP3 potentiostat/galvanostat (BioLogic). The cell set-up employed in this phase, used a two electrodes approach, with the TiO₂ deposition as the working electrode, and the sodium metal disk both as the counter and reference electrode.

4. Result and discussion

4.1. Chemical-physical characterization

The TEM images of the three pristine powders (without GO) after the decapping process, are reported in Figure VIII-2: all the structures appear highly uniform in shape and in particles dimensions. According to the reaction mechanism sketched in image a) in Figure VIII-1, selective adsorption of oleic acid (OA) occurs onto high energy crystalline facets (001), while oleylamine (OM) molecules are adsorbed preferentially onto lower energy facets (101)^{38,39}. Owing to these considerations, the modulation of TB:OA:OM ratio allows the crystal growth along specific directions. Moreover, the concentration of titanium precursor plays a key role in determining the final morphology. In detail, for OA:OM ratio = 4:6, an increase of Ti concentration leads to the particle elongation along the [001] direction, resulting in an elongated rhombohedral morphology (RE). Keeping constant the relative amount of OA and OM but sensibly decreasing the TiO₂ precursor, small rhombic crystals (R), outstandingly homogeneous in shape and dimensions, have been obtained. On the other hand, a large excess of oleic acid, sensibly limits the particles growth, due to the strong adsorption of the carboxylic acid also onto crystalline facets other than (001)³⁸, and produces slightly smaller crystals that resemble parallelepipeds (i.e. nanobars, NB) in shape. Lastly a relative ratio of 6:4 leads to spherical particles (SP) with apparently no preferential evolution and growth of primary crystallites towards any direction. After the successful removal of the capping agents, no significant agglomeration, nor a preferential orientation of particles driven by high energy face to face interactions can be spotted in TEM images.

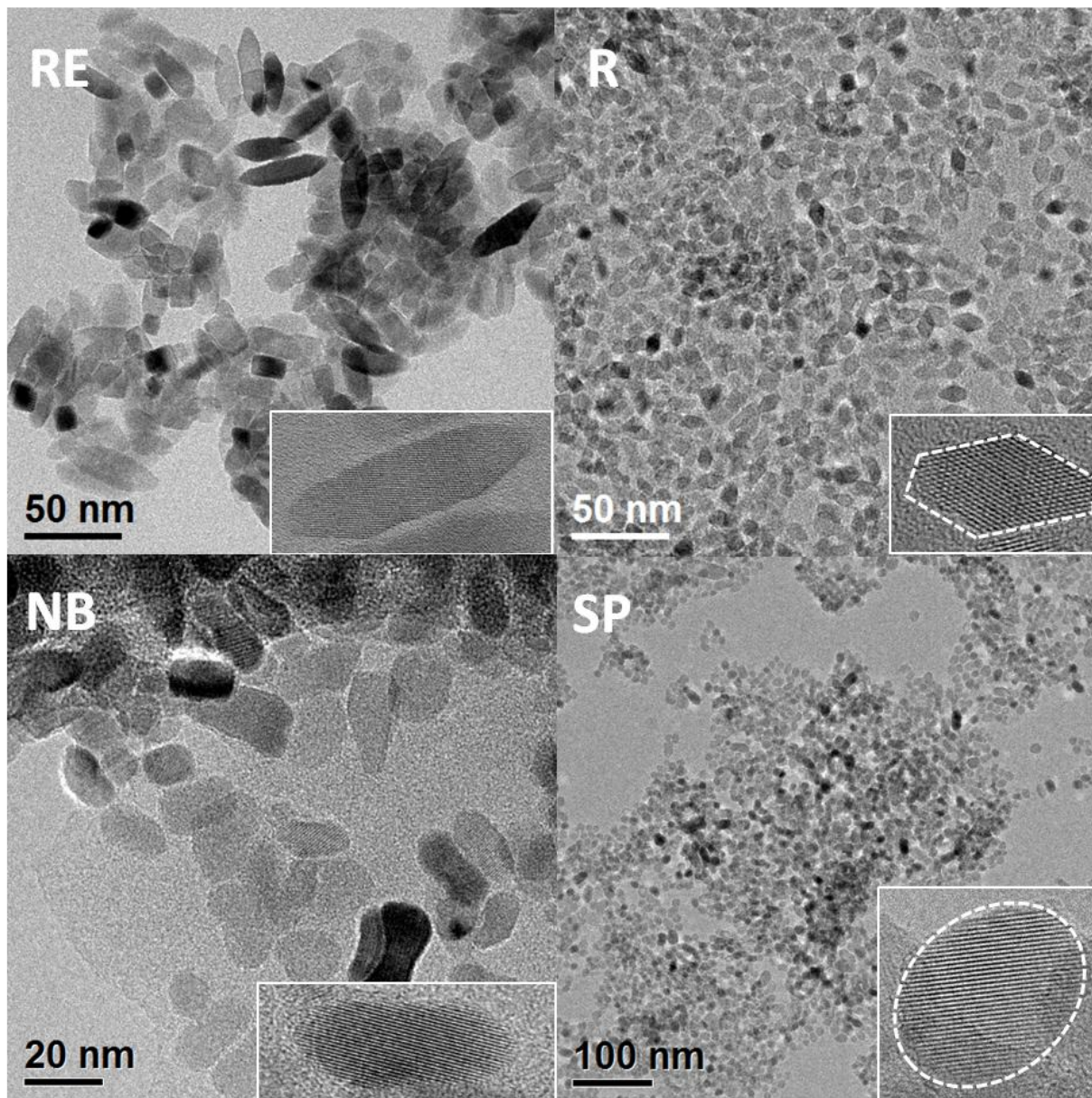


Figure VIII-2: TEM images of the as synthesized TiO_2 nano-crystals morphologies immediately after the de-capping process. In each image is reported an inset with a single magnified particle.

XRD diffractograms reported in image b) in Figure VIII-1 clearly support the high crystallinity of the samples as well as the absence of interfering impurities, while from the diffraction peaks width a quantitative insight on crystal dimensions, using Scherrer's relation, can be achieved. In agreement with the TEM images, the largest particles belong to RE sample, due to the strong elongation along [001] and the high amount of TB precursor employed in the synthesis. Switching to rhombic (R) and consequently to nanobars (NB) and spherical (SP) morphologies, a progressive reduction in particles dimension occurs, as can be seen also from

the broadening of the X-ray diffraction peaks. TGA analysis of pristine TiO₂ were carried out (Figure VIII-3) before and after the cleaning treatment to measure the residual amount of organic species still adsorbed onto TiO₂ surfaces. The NB sample showed the highest weight loss (-17.7 % before cleaning and -5.97 % after cleaning), probably due to either the large excess of oleic acid used in the synthesis to the resulting decomposition of residual organic capping agents, which is less effectively removed from NB crystals surfaces even after a remarkable oxidative treatment. Conversely, RE R and SP, strongly benefit from the cleaning procedure, since only weight losses of 0.32 % and 1.19 % respectively, are observed. Water content, adsorbed on crystal surfaces and causing the samples weight loss below 200 °C, is limited to few percentage points (< 5 %) for all the morphologies.

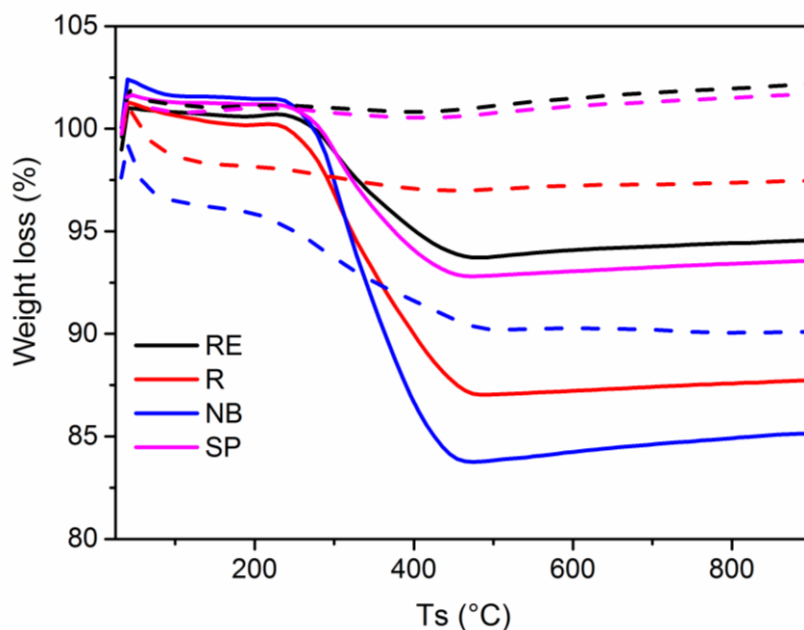


Figure VIII-3: TGA analysis of the as prepared TiO₂ samples from the solvothermal step (solid lines), and after the cleaning procedure using nytrosil tetrafluoroborate (dashed lines). Black lines refer to RE, while red and blue lines refer to R and NB samples respectively.

4.2. Crystal dimensions and facets extension determination

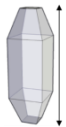
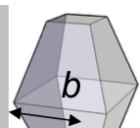
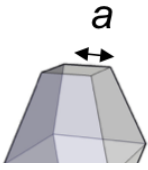
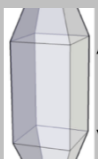
Exploiting Scherrer's relation, lengths along specific crystalline directions can be calculated (Table VIII-1), nonetheless due to cumulative effects contributing to XRD peak broadening, such as instrumental factors, dimensions directly measured from TEM images have been taken in consideration for further calculations. The crystal dimensions directly measured from TEM images according to criteria listed in Table VIII-2 have been thus summarized in

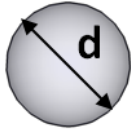
Table VIII-3. SP for which the dimension along a preferential lattice direction could not be evaluated due to round shape, an average value is provided.

Table VIII-1: Crystals dimension calculated from Scherrer's equation along three different direction: [101], [004] and [200]. Together with particles lengths and widths, 2theta angles and full width at half maximum of corresponding peaks are reported.

	[101]			[004]			[200]		
	deg.	FWHM	$L_{[101]}$ (nm)	deg.	FWHM	$L_{[004]}$ (nm)	deg.	FWHM	$L_{[200]}$ (nm)
RE	5.31	0.715	1.89	7.86	0.39	2.57	8.06	0.809	1.23
R	5.29	1.151	7.39	7.85	0.81	0.84	8.03	1.055	.61
NB	5.27	2.116	4.02	7.78	1.42	6.19	8.03	1.341	6.77
SP	5.23	0.777	0.95	7.79	0.50	7.58	8.05	0.844	0.77

Table VIII-2: Measured dimensions of TiO₂ crystals. These values has utilized used to calculate the relative percentage exposure of crystalline facets using the equations reported elsewhere.

	RE		R		NB		SP	
	Mean (nm)	Std.dev. (nm)	Mean (nm)	Std.dev. (nm)	Mean (nm)	Std.dev. (nm)	Mean (nm)	Std.dev. (nm)
	1.2	4.59	8.44	2.02	1.34	1.74	-	-
	3.61	1.19	0.38	1.07	-	-	-	-
	4.79	0.73	3.68	0.46	10.79	1.09	-	-
Middle section 	3.17	3.37	-	-	-	-	-	-



- - - - - 2.50 2.50

Table VIII-3: Crystals dimension measured manually from TEM images along two crystalline direction corresponding to length and width of each geometry.

	[004]	[200]	Average size
	L _{TEM} (nm)	L _{TEM} (nm)	L _{TEM} (nm)
RE	41.2	13.6	-
R	18.4	10.4	-
NB	21.3	10.8	-
SP	-	-	12.5

RE particles shows the highest anisotropy with a length (measured along [001] direction) extending up to 40 nm and a width accounting for 13 nm. Conversely R and NB show comparable dimensions, measuring circa 20 nm in length and 10 nm in width. In Figure VIII-4 an exhaustive example of direct particle measurement is provided for some of the morphologies investigated. As will appear clear soon, SP could not have been included in the percentage of crystalline facets exposure evaluation since it does not display a well defined geometry. The round shaped SP particles, whose surface construction is achieved by an averaged contribution of multiple crystalline facets will be, starting from this moment, treated as a reference species comparable to benchmark TiO₂-anatase nanopowder already investigated in literature.

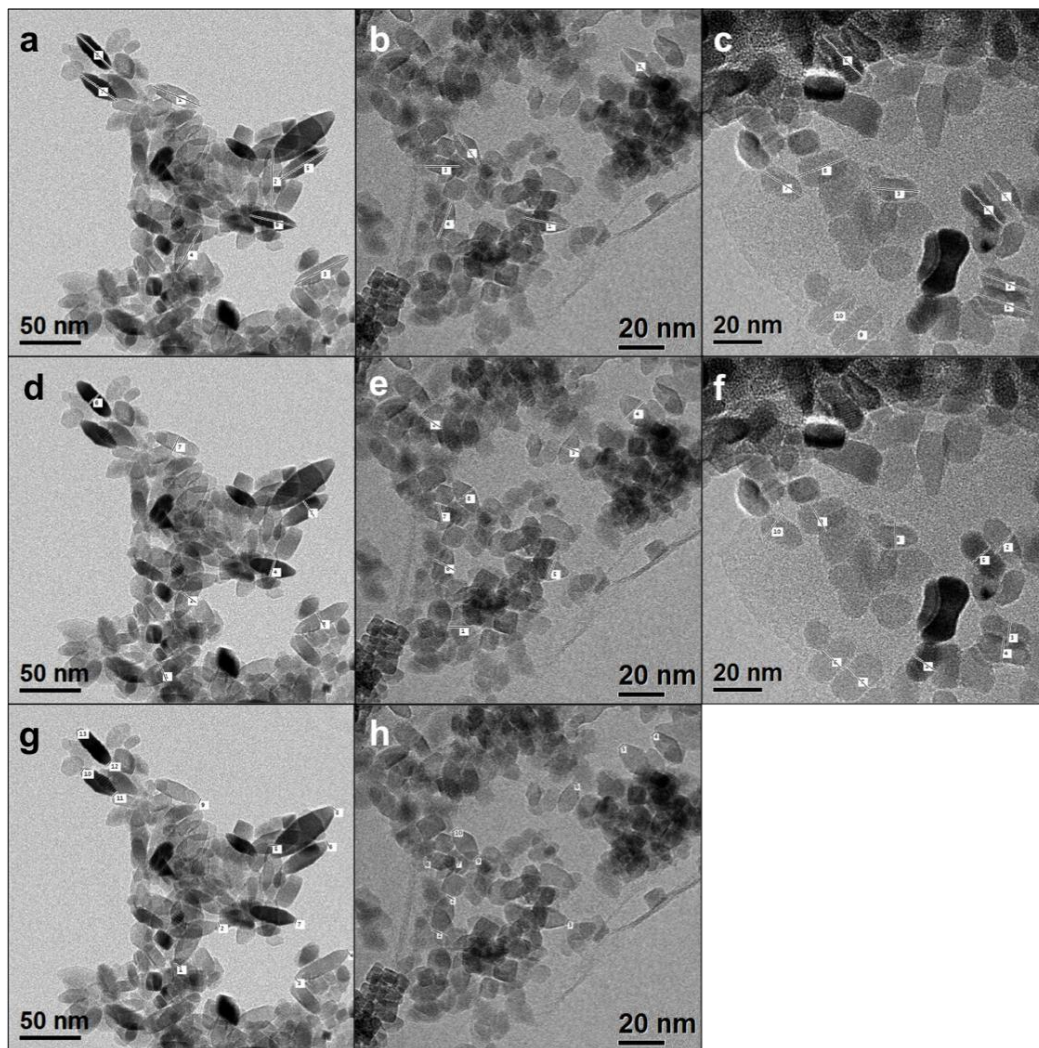


Figure VIII-4: Graphic example of the particle size evaluation from TEM pictures for (a) total length along [001] direction, (d) width and (g) (001) face edges length of RE particles; (b) length, (e) major edge and (h) minor edge of R sample particles and (c) length and (f) width of NB particles

The actual exposure of the hypothesized crystalline facets for RE, R and NB samples, has been confirmed from HRTEM images (images a) to f) in Figure VIII-5). The RE crystals revealed the (101) and (002) exposed facets. The distance referred to {200} planes can be measured along the direction perpendicular to the middle rectangular section of RE particles ($d_{200}=0.37$ nm). This is a proof that, unlike R crystals, RE exhibit also (200) and (010) facets exposed. In the case of NB particles, only (101) and (011) facets, and the corresponding planes spacing (0.35 and 0.34 nm respectively), can be clearly distinguished. In NB, (101) facets are believed to be less prominent relatively to (001), if compared to R and RE case. Angles between detectable crystalline planes have been also measured, since their amplitude is a

further confirmation of the presence of specific lattice planes. The angle spanning between the supposed {001} and {101} planes shows an amplitude of 68.9°, close to the theoretical one (68.3°). The evaluation of the percentage exposure of crystalline facets, essential to elucidate the correlation between electrochemical performances and crystals characteristics, has been done using relatively simple geometric equations conveniently modified to fit different crystal shapes and collected below. SP sample, although included as a reference in further discussion concerning the electrochemical characterization, has been left behind in crystalline facets exposure determination.

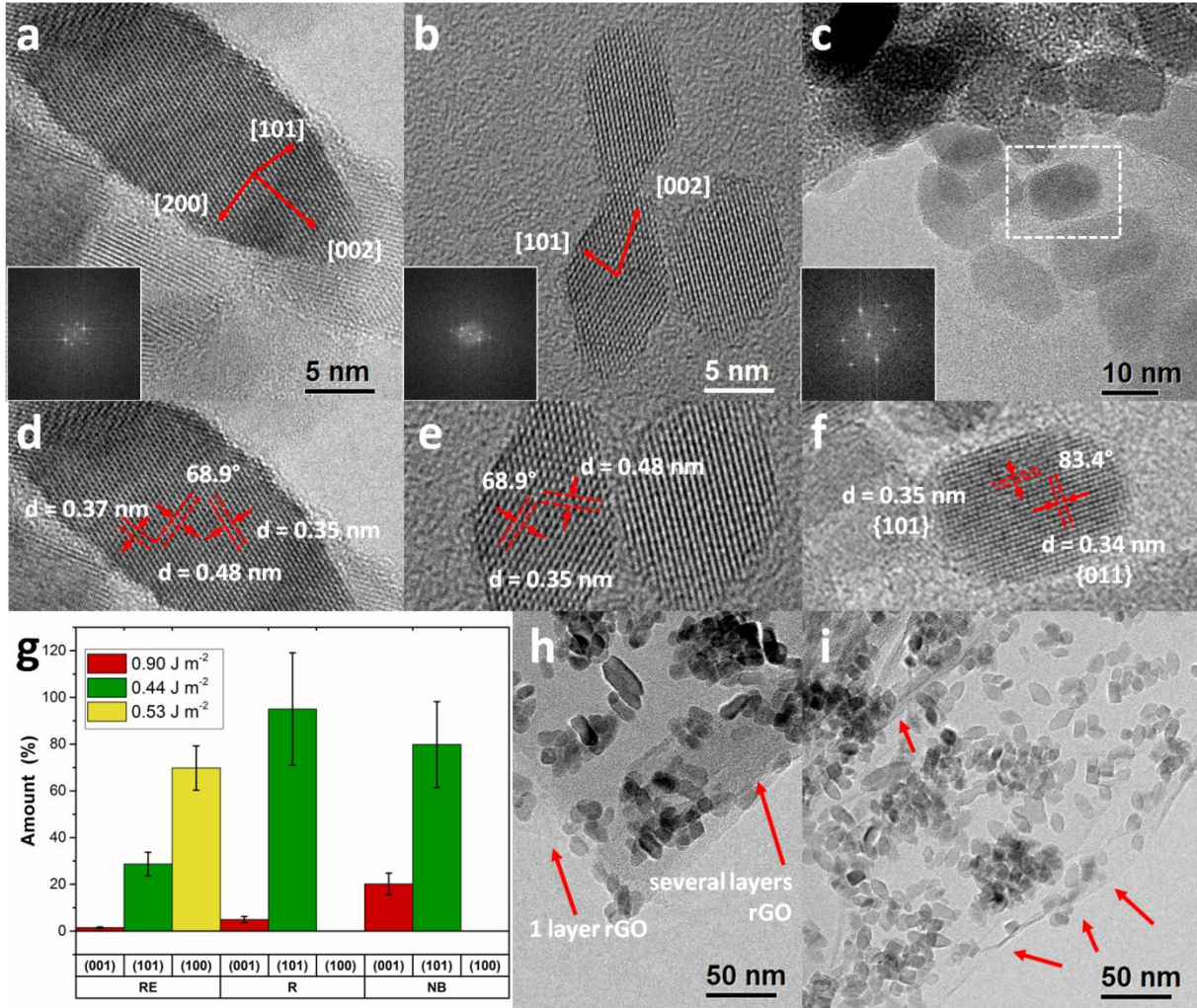


Figure VIII-5: HRTEM images of (a,d) RE, (b,e) R and (c,f) NB. From lattice fringes in magnified images (d-f), through images processing, the characteristic lattice plane spacings and angles have been identified (red dashed lines and arrows) and numeric values are reported on the images using white lettering and numbering; (g) histogram collecting the percentage of crystal facets exposure for each morphology, the color code represents the energy density of each crystalline face; (h,i) TEM images of TiO₂ nanocrystals grafted on reduced graphene oxide, red arrows pointing at the graphene oxide sheets.

For RE, equations used to calculate (001) and (100) exposure, are:

$$\begin{aligned}
 \%RE_{S\{001\}}_{exp} &= \frac{S\{001\}}{(S\{101\} + S\{001\} + S\{100\})} \\
 &= \frac{2a^2}{[2a^2 + 8(b + a)(b - a) \tan(68.9^\circ) + 4mb]} \times 100 \quad (\text{VIII. 2})
 \end{aligned}$$

$$\begin{aligned} \%RE_{S\{100\}exp} &= \frac{S\{100\}}{S\{101\} + S\{001\} + S\{100\}} \\ &= \frac{4mb}{[2a^2 + 8(b+a)(b-a)\tan(68.9^\circ) + 4mb]} \times 100 \quad (\text{VIII. 3}) \end{aligned}$$

where 68.9 ° is the angle between {001} and {101} planes and a , b and m are the dimensions derived from crystal models (see Table VIII-2). For R and NB, where just (001) and (101) have been considered relevant for this dissertation, the useful equations have been:

$$\%R_{S\{001\}exp} = \frac{S\{001\}}{S\{101\} + S\{001\}} = \frac{2a^2}{[2a^2 + 8(b+a)(b-a)\tan(68.9^\circ)]} \times 100 \quad (\text{VIII. 4})$$

$$\%NB_{S\{001\}exp} = \frac{S\{001\}}{S\{101\} + S\{001\}} = \frac{2w^2}{[4lw + 2w^2]} \times 100 \quad (\text{VIII. 5})$$

where l and w are the length, namely the extension of (101) facets, and the width (sides of (001) facets) of NB crystals if they were depicted as simple parallelepipeds. The relative percentage of crystal facets surfaces has been summarized in image g) in Figure VIII-5 in which also the energetic content of each surface is intuitively sketched thanks to the color palette, assigning the green color to the less energetic one, namely {101} with 0.44 J·m⁻² surface energy density, and red color to {001} facets with the highest value of surface energy density (0.90 J·m⁻²) according to literature³⁹. Worth noticing is how the relative ratio between {101} and {001} exposure is kept constant (about 19:1) for RE and R. This can be connected to the relative amount of OA and OM used, that was the same for the two morphologies, and that directed {001} and {101} growth in similar fashion. This ratio decreases significantly (4:1) in the case of NB, in which the contribute of {001} to total surface of the particles is higher. Growth along [001] direction has been indeed hindered due to the relevant absorption of oleic acid on {001}, driving crystal development along other crystalline directions. To confirm the successful graphene oxide wrapping of anatase particles, TEM images have been taken after the wrapping procedure (image h) and i) in Figure VIII-5). Graphene sheets, probably made of the stacking of multiple single graphene layers, can be easily spotted, and are highlighted in the pictures with red arrows pointing at their edges. As it can be furthermore noted, TiO₂ crystals have preserved their morphologies despite the thermal treatment, without undergoing significant agglomeration, Ostwald ripening process or oriented attachment by specific surfaces as suggested in

literature⁴¹, and appearing securely grafted onto the graphene oxide sheets. Presumably, has been the effective hooking itself deriving from APTES functionalization that kept the particles away from large agglomeration phenomena to occur.

4.3. Surface and pore distribution analysis (BET and BJH)

Nitrogen physisorption experiments have been performed on the pristine TiO₂ after the removal of capping agents. Surface area quantifications will be useful later on in this dissertation in order to shed light onto surface extension-electrochemical properties correlation and the actual influence of crystalline exposed facets on this relation. All four samples appear mesoporous with an IV type Brunauer isotherm curve (Figure VIII-6). After the monolayer completion in the lower half of relative pressure values ($<0.40 p/p^\circ$), multilayer adsorption starts and a horizontal plateau, clearly visible for NB sample, appears at higher relative pressures. This is a clear symptom of an occurring capillary condensation inside porosity. Curve adsorption/desorption hysteresis communicates the confinement effect on condensation/evaporation mechanism in meso-porosity presumably related to particles agglomerates. The pressure at which the hysteresis loop closes corresponds again to the situation of an adsorbed multilayer film in equilibrium with a vapor in the core of the pore and the bulk gas phase. In Figure VIII-6, together with each adsorption/desorption BET isotherm, is plotted $x/V(1-x)$ (here called $1/[Q(p^\circ/p-1)]$) against a sufficiently narrow window of relative pressure values (typically referred to the monolayer adsorption and thus <0.4). $x/V(1-x)$ derives from BET equation itself (see correspondent appendix paragraph in Chapter X). From the obtained linear relation and in particular from slopes (b) and intercepts (i) it has been possible to obtain the monolayer volume and consequently the associated specific surface area (SSA_{BET}). Finally, the pore size distribution has been evaluated as well, using a BJH method. All the mentioned data are collected in Table VIII-4, where, using the percentage of exposed {001} and {101} facets, the relative SSA_{BET} has been also calculated.

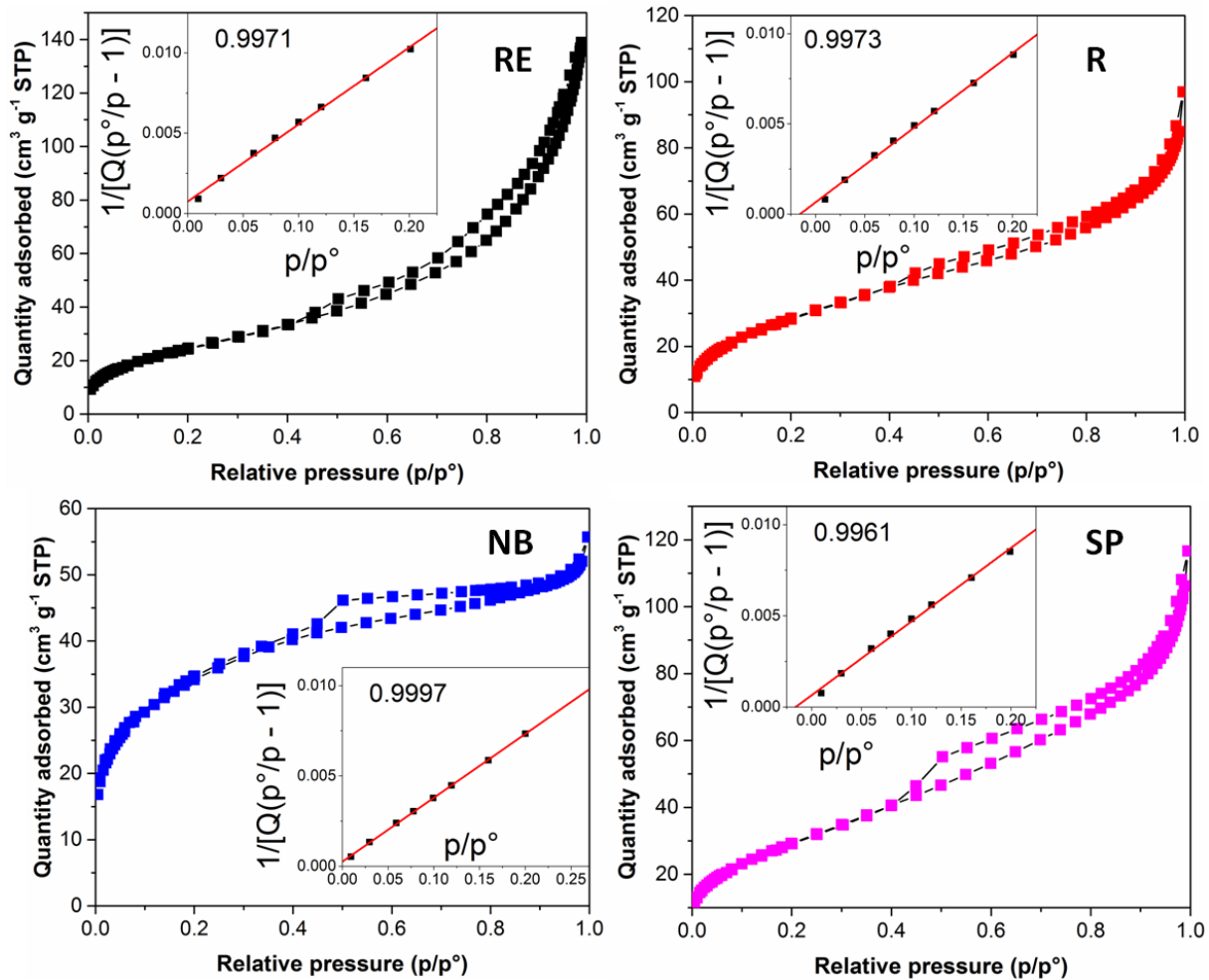


Figure VIII-6: Adsorption isotherms for RE, R, NB and SP samples; each image includes the graphs plotting the linear relation between relative pressure below 0.4 and adsorbed monolayer volume. From the intercept the value of the surface area (SSA_{BET}) has been calculated.

Table VIII-4: Characteristic parameters for Re,R,NB and SP morphologies, SSA_{BET} associated to each exposed facets for RE, R and NB samples.

sample	Slope (b)	Intercept (i)	Q_m (cm ³ ·g ⁻¹)	SSA_{BET} (m ² ·g ⁻¹)	Pore volume (cm ³ ·g ⁻¹)
R	0.04136	0.000647	23.81	103.6	0.1597
RE	0.06409	0.000366	15.51	67.5	0.1854
SP	0.04038	0.000644	24.37	106.1	0.1877
NB	0.03535	0.000253	28.09	122.3	0.06519

sample	{001} (%)	{101} (%)	{100} (%)	SSA _{BET} {001} (m ² ·g ⁻¹)	SSA _{BET} {101} (m ² ·g ⁻¹)	SSA _{BET} {100} (m ² ·g ⁻¹)
R	4.96	95.04	-	5.14	98.51	-
RE	2.33	33.67	64.00	1.57	22.74	43.22
NB	20.18	79.82	-	24.67	97.59	-

4.4. Electrochemical characterization results

Galvanostatic tests, for the three materials investigated, are reported in Figure VIII-7. The sequence of the currents used (C-rate), has been chosen accordingly to the positive effect experimented using a growing trend versus a decreasing one. In the former case, the typical activation time required to achieve a stable capacity at lower currents, is reduced as can be seen from cycles performed at 1C (500 mA·g⁻¹).

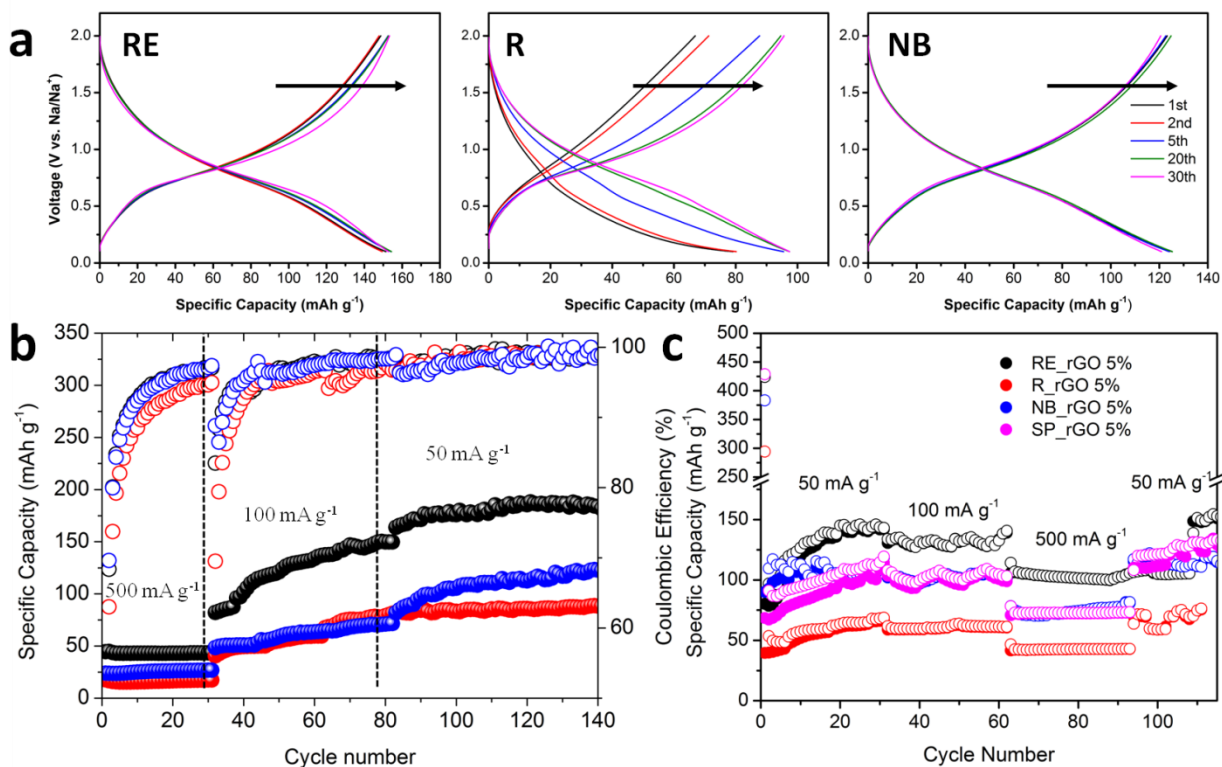


Figure VIII-7: a) charge/discharge profiles for RE,R and NB, taken cycling the half cell at 50 mA·g⁻¹; first cycles (whose capacity can be presumed from rate tests) have been voluntarily omitted in order to better appreciate the curve profile evolution through cycling; b) GCPL result for RE (black line), R (red line) and NB (blue line) rGO wrapped samples at progressively increasing currents; c) rate test performed on all the four samples, including SP rGO wrapped one (purple line).

Interestingly, all of the morphologies investigated electrochemically show increasing or steady capacities. RE sample appeared to be the one that allowed reaching the highest capacity values at all the three C-rates investigated. Indeed, a remarkable steady capacity of 180 mAh·g⁻¹ is achieved at 0.1 C (50 mA·g⁻¹) after 70 cycles, for NB and R this value is limited to 123 and 88 mAh·g⁻¹ respectively. If the rate test reported in image c) in Figure VIII-7 is considered, in which also the SP sample has been included, an interesting aspect emerges: none of the four morphologies shows a gradual decline towards lower capacities, as reported in recent works investigating this material^{36,42}, this behavior represents a puzzling aspect about oxide-based anode materials for SIBs. Moreover, with the increase in the cycling current to 0.2 C (100 mA·g⁻¹), an almost negligible reduction in capacity is obtained. A considerable drop in capacity is instead registered for currents as high as 1C (500 mA·g⁻¹): around 100 mAh·g⁻¹ can be extracted from rhombic elongated crystals (RE), and even a lower amount, 72 and 77 mAh·g⁻¹, from SP and NB morphologies respectively. R samples shows poor performances either in terms of capacity at low current rates either in capacity retention during a rate test with only 42 mAh·g⁻¹ provided at 1 C. It can be argued that the not so impressive rate capabilities of the prepared materials might be a severe limit, but we believe that a noteworthy improvement is possible by optimizing the graphene oxide wrapping procedure of TiO₂ nanoparticles. As illustrated by TEM images (Figure VIII-8), the condition under which the graphene oxide wrapping is obtained, namely the not optimal fragmentation of TiO₂ agglomerates when TiO₂ is suspended in water, leads to TiO₂ conglomerates wrapping to be achieved, instead of single particles grafting on graphene sheets.

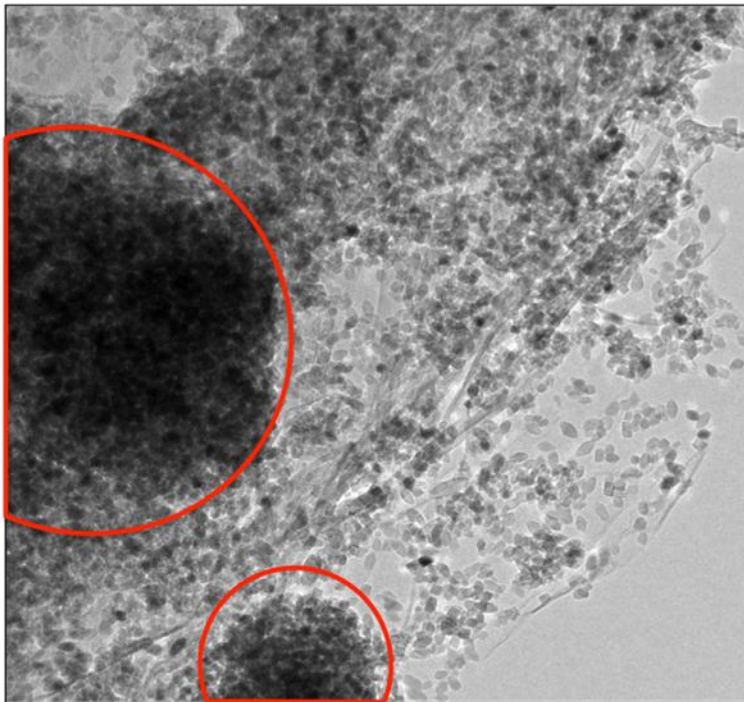


Figure VIII-8: reduced graphene oxide wrapped TiO₂ R sample: particles agglomerates are evidenced in the TEM image; red arrows point at graphene oxide sheets.

The core of these isolated pomegranate-like structures is less available for electrochemical processes, and the insulating nature of anatase-TiO₂ makes this effect even worse at higher current rates. Nevertheless the stability of the material over cycles is remarkable, and as can be seen from the cycles performed at 1 C (500 mA·g⁻¹) in Figure 2e, capacity of 105 mAh·g⁻¹ can still be obtained. To better elucidate the motivation beyond the mild concentration of rGO employed, compared to other works in which higher content (10 wt%) is utilized⁴³, a comparison between the electrochemical properties of RE, R and NB nanocrystals with and without the reduced graphene oxide wrapping, has been provided (below).

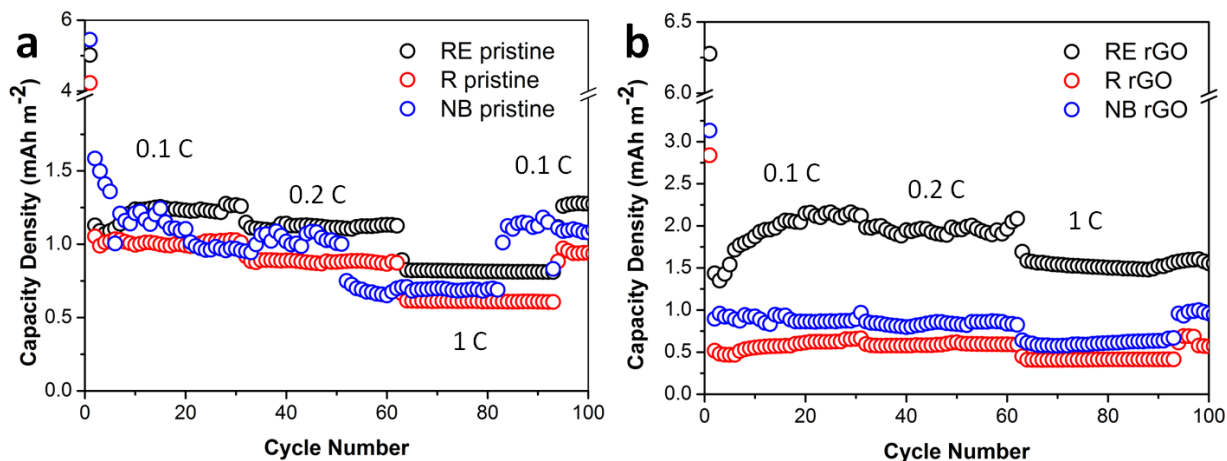


Figure VIII-9: a) GCPL tests taken at different C-rate (0.1, 0.2 and 1 C), of pristine RE, R and NB samples, with the specific capacity normalized over the specific surface area (from BET analysis, 67.53 and 103.64 m²·g⁻¹ and 122.27 for RE, R and NB respectively); b) GCPL tests, conducted at 1, 0.2 and 0.1 C, of reduced graphene oxide RE, R and NB composites, with specific capacity normalized over the specific surface area of the sample

The results have been reported in terms of specific capacities normalized over the specific BET area of the samples, (see Table VIII-4), obtaining a parameter expressed in mAh·m⁻² of active material, plotted against the cycles number. This allowed to highlight that, the pure surface contact with the surroundings, namely the specific surface area of the sample, heavily affects the electrochemical performances without the beneficial effect of an electronically connecting substrate capable of overcoming the conductive limits of TiO₂ nanocrystals. Presumably the major reactivity deriving from crystalline facets with high surface energies {001} plays a role in driving sodium uptake. As a matter of facts in capacity density graphs of pristine TiO₂, NB sample, provided with the higher percentage of high energy surfaces, shows comparable performances to RE and R (image a) in Figure VIII-9) despite its high surface area. Nevertheless the higher energetic profile of NB is also accountable, as reported in literature⁴³, for a selective interaction with GO, this leads to the blockage of {001} facets and to the consequent severe limitation in capacity density. The case of RE morphology, instead, stresses the importance of having intermediate energy density facets available. It can be indeed assumed that low percentage of {001} of RE guides TiO₂-GO interactions as well, but instead of witnessing a deterioration of electrochemical performances, a considerable amount of capacity density is gained, together with an improvement in performances at higher currents of

the material (image b) in the same figure). It is then believed that 5 % by weight graphene wrapping embodies a sensible tradeoff, behaving as an efficient electron conductive substrate without heavily interfering with surface properties of the material. Coulombic efficiencies give an important insight into the reversibility of electrochemical processes. They hover around 99% for rGO wrapped RE, R and NB as well, which is a symptom of the electrochemical processes reversibility as well as the stability of the formed SEI layer. An outstanding average Coulombic efficiency value of 99.55 % is achieved over more than 500 cycle in the case of RE (Figure VIII-10). An overall stability of the morphological and structural properties of the active material is thus suggested.

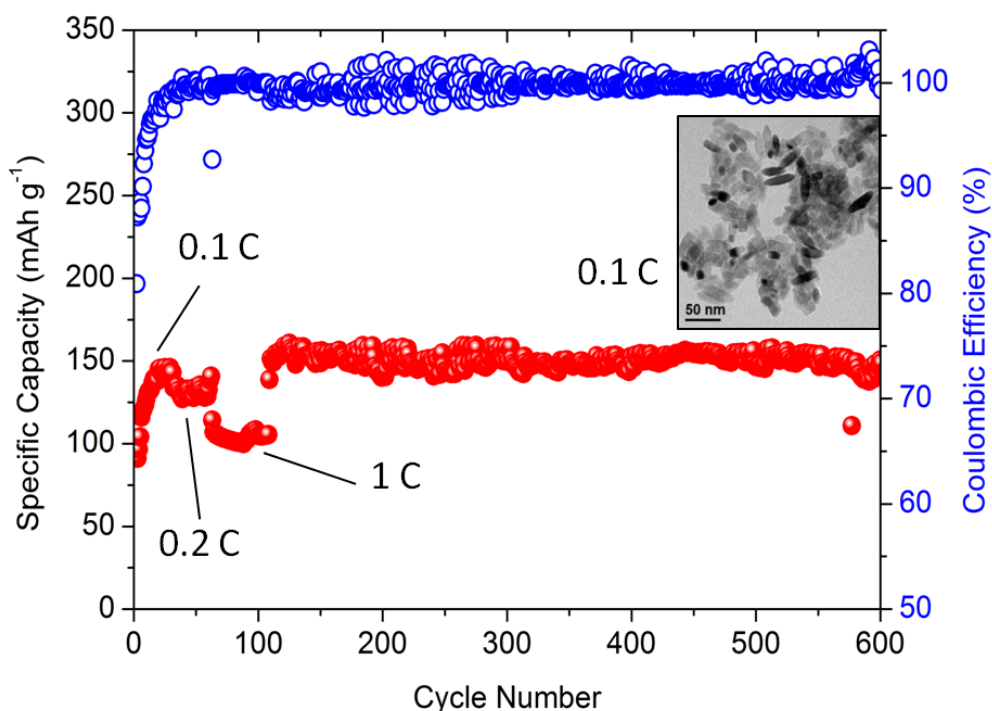


Figure VIII-10: Stability test performed on RE electrode alone, over 600 cycles. In all the electrochemical tests Cut-off potentials of 0.1 and 2.0 V vs. Na/Na⁺ were used during the sodiation and de-sodiation step respectively.

Lower values of the Coulombic efficiencies are often indicative of a recursive SEI formation mechanism, occurring during each sodiation step; this is ascribed to severe volume changes of material particles that produces the detachment and fracturing of the present SEI layer. Potential profiles, as illustrated in image a) in Figure VIII-7, resemble those of extremely reversible processes. Operative potentials, similar for RE, R and NB, are as low as 0.83 V vs. Na/Na⁺, and represent an interesting starting point for the implementation of these materials as

low cost anodes for SIBs. This value is sensibly lower than that referred to Li intercalation in lithium titanates⁴⁴ (~1.8 V vs. Li/Li⁺), aspect that makes TiO₂ anodes in SIBs notably more interesting for practical applications.

5. Investigation of energy storage mechanism in TiO₂

Contrary to what is reported in literature about the particle size and electrochemical behavior of anatase TiO₂, we observed that a higher size, and particularly a higher aspect ratio, is beneficial to the electrochemical performance of the material. This is here attributed to the different morphological features of the nanoparticles. In the works of Passerini⁴⁵ and Mulder *et al.*⁴⁶, averagely spherical particles, with no predominance in crystalline facets exposure and thus that can be assimilated to the above investigated spherical morphology (SP), were taken into consideration. Considering these systems, what might be a peculiar effect of Na interaction with crystalline surface is dampened, and the only significant factor heavily limiting the electrochemical behavior, as capacity and rate capabilities, is the better electronic conduction achieved with smaller TiO₂ particles, in the nanometric range, compared to larger ones. A direct confirm of the retained anatase phase and size properties during the galvanostatic cycling, was given by *ex-situ* XRD analysis taken on a cycled RE electrode (image b) in Figure VIII-11). After 10 cycles at 0.1 C, not only the anatase phase is preserved, without the appearance of any notable impurity, but also the dimensions computable from peaks full widths at half maximum are comparable with those of the pristine material. For completeness, also the X-ray diffractograms for each pristine electrode have been reported in image a) in the same figure.

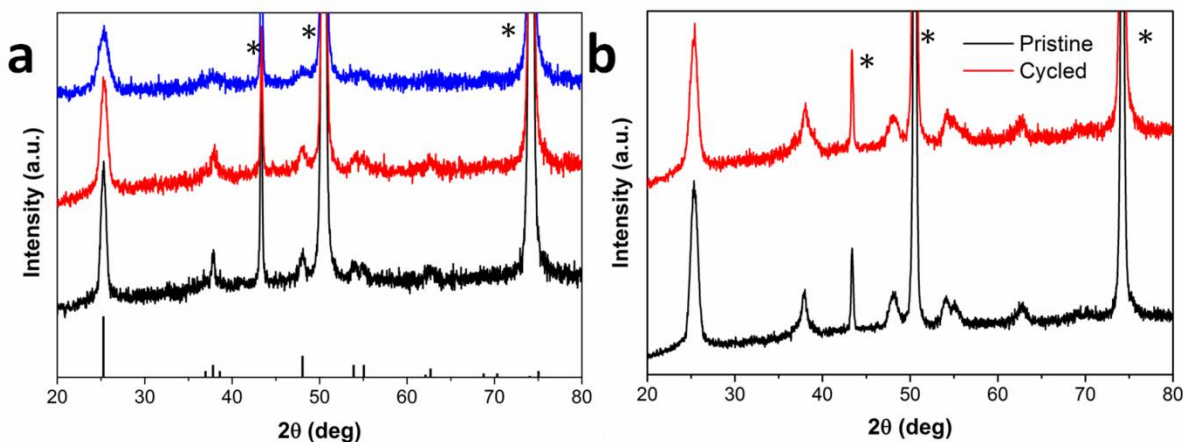


Figure VIII-11: a) XRD diffractograms of the RE, R and NB electrodes (black, red and blue line respectively), asterisks mark the peaks coming from Cu current collector; b) XRD diffractograms taken on a fresh RE electrode (black line) and on a cycled one (red line), after the 10th cycle of a GCPL analysis, where the last current step was a de-sodiation one; asterisks refer to diffraction peaks of the Cu current collector.

The electrochemical reaction mechanism of sodium ions with anatase TiO₂ has been the subject of several investigations. Different mechanisms, depending on the charge state, the particle size and shape have been proposed and validated. Indeed, submicrometric particles have shown a state of charge dependent behavior with three different regimes: i) a pseudocapacitive region at high potential (short capacity), ii) the structural intercalation in the particle bulk (up to 0.7 Na per unit formula) and iii) a further conversion reaction at low potential³². However, it has been also demonstrated that using much smaller particles or nanostructures the share of the pseudocapacitive domain is extended and the pseudocapacitive charge becomes dominant³³, indeed, intercalation pseudocapacitance has been already found to be the prevalent capacitance harvesting mechanism in a 10 wt% graphene-TiO₂ compound, due to the Na⁺ fast intercalation in gaps formed between TiO₂ surfaces and partially bonded graphene sheets⁴³. To elucidate the nature of the capacity extracted from our TiO₂ nanocrystals, cyclic voltammetry tests were performed on pure RE-TiO₂ electrodes, without graphene oxide wrapping (image a) to c) in Figure VIII-12). We found out that also for naked TiO₂ nanocrystals an intercalation pseudocapacitance behavior can be highlighted: from the $\log(i)$ - $\log(v)$ plot (image d) in figure below), currents values collected from CV peaks at different scan rates (0.5, 1, 2, 5, 20 mV·s⁻¹) correlate linearly to the scan rates for values lower or equal than 2 mV·s⁻¹ (Figure 4d), while slightly deviate from the linear relation above this value.

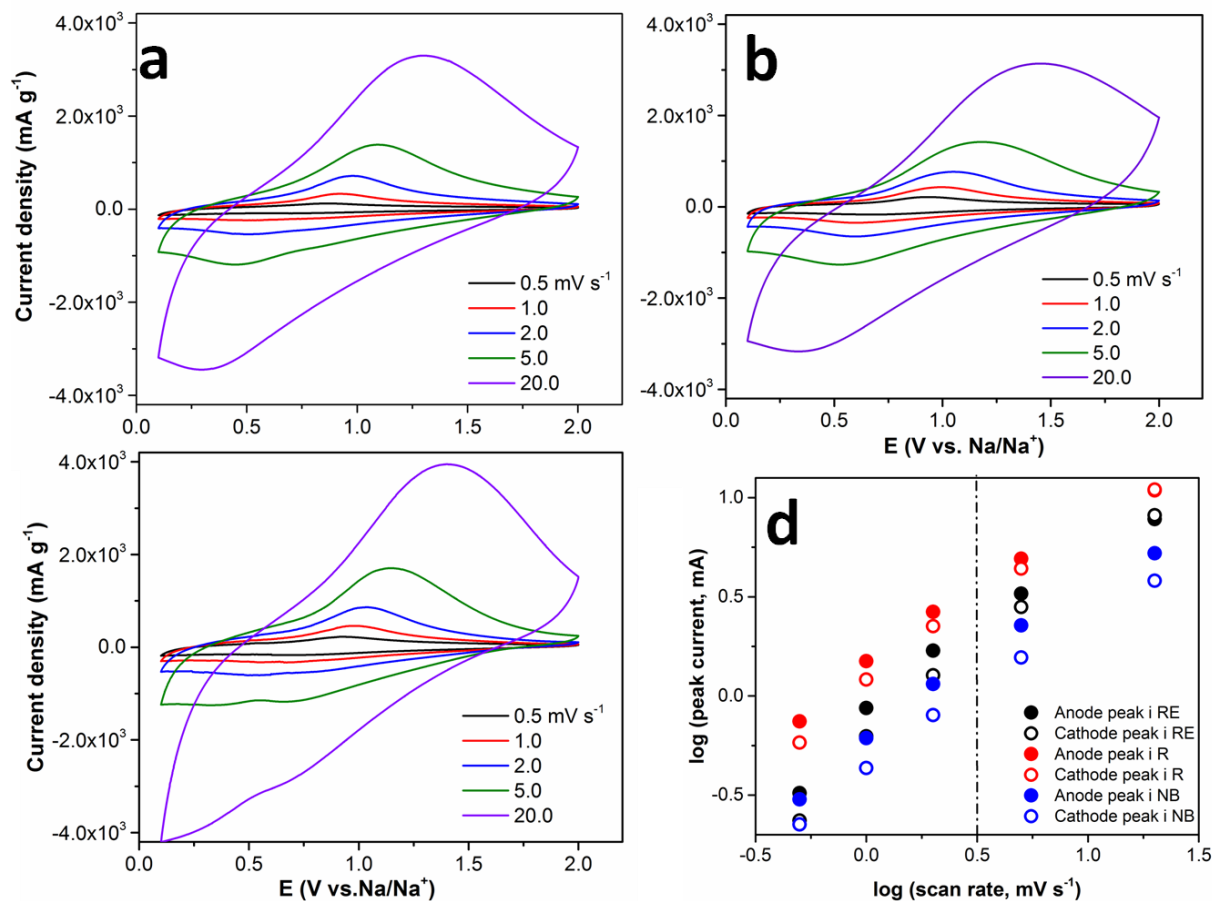


Figure VIII-12: a) RE, (b) R and c) NB Cyclic voltammetry curves of pure samples (no rGO wrapping) registered at different scan rates; d) log(*i*)-log(*v*) plot for the investigated morphologies where the vertical dashed line separates the linear regime (*b*-value = 1) from the non-linear one (*b*-value < 1) of log(*i*).

This hints for a progressive shift from a capacitive behavior towards a diffusion-controlled electrochemical process, with an increase in the scan rate. Mathematically this coincides with a change in *b*-value, calculated from the slope of log(*i*)-log(*v*) curve, from 1 to 0.8, in the following equation:

$$i = av^b \quad (\text{VIII. 6})$$

where *v* is the scan rate used in the measurement. For this reason, since the peak currents don't scale with *v*^{1/2}, capacity must originate from a capacitive-like mechanism. This feature together with the slight shifts in peak potentials at low scan rates, supports the hypothesis of a bulk intercalation capacitance as it has been highlighted for other oxides such as Nb₂O₅⁴⁷. It can be also argued that a percentage of the observed capacity might be also related to a pure double-layer capacitive mechanism. Typically, the amount of capacity coming from this type of non-

Faradaic process in non-aqueous electrolyte lies between 10 and 50 $\mu\text{F}\cdot\text{cm}^{-2}$ while pseudo-capacitive behaviors, including intercalation pseudo-capacitance, underpin values by 10 to 1000 times higher⁴⁸. From cyclic voltammetry curve integration of a non-Faradaic portion of potential sweep and application of well-known equations reported in literature⁴⁹, an esteem of the capacity density can be made for RE. The calculated value is 26 $\mu\text{F}\cdot\text{cm}^{-2}$ which agrees with the esteemed values for pure double-layer capacitive behavior. Concerning the occurring Faradaic processes, they accurately resemble the intercalation pseudo-capacitive voltammetric signals already highlighted for Li in TiO_2 polymorphs^{50,51}, namely broad peaks with slight drifts at high scan rates, and with peak currents proportional to scan rate.

6. Conclusion

In summary, four different nanostructured TiO_2 morphologies have been successfully synthesized using a solvothermal method implying surfactants as capping agents to direct TiO_2 crystal growth. Rhombic elongated (RE), rhombic (R) nanobars (NB) and spheres-like (SP) particles clearly show noticeable differences in crystal facets type exposition, as well as a substantial different behavior for what concern the interaction with sodium ions inside a Na-ion half cell. Including 5 % reduced graphene oxide wrapping, the electrochemical affect of facets exposure has been selectively evaluated excluding the limiting factors deriving from total surface area and particle size. After a deep electrochemical investigation, it can be concluded that an over-coordinated state of Ti atoms on the crystal surface (high energy density (101) facet of NB and R moieties) strongly inhibits the sodium uptake, while a goldilocks condition seems to occur for crystalline facets with intermediate energy densities, like (100) in RE. These experimental results are also backed up by recent theoretical studies performed on conveniently cleaved TiO_2 anatase crystals. Yang stressed the importance of energy state of the crystal surface in promoting sodium attachment, being surfaces themselves the gateways for sodium atom from the electrolyte into the lattice³¹. The attachment energies are identified by the equation reported below.

$$E_{at} = -\frac{E_{\text{Na-hkl}} - E_{\text{hkl}} - E_{\text{Na}}}{n} \quad (\text{VIII. 7})$$

Here E_{hkl} and $E_{\text{Na-hkl}}$ are total energies of the crystalline surfaces before and after sodium atoms attachment onto a specific {hkl} surface. E_{Na} is the energy of sodium atoms and n is the number of sodium atoms linked to the surface per unit area. E_{at} values have been calculated for

(100), (001) and (101) to be 1.51, 0.33 and 0.50 eV respectively^{52,53}. As can be noted, this trend is in contrast with the one expressed by TiO₂ surface energies alone (image g) in Figure VIII-5), from which the (001) facet appeared to have the higher reactivity. The reason why this order is twisted must be sought in the n parameter, specific for each facet and dependent on available sites for sodium attachment. This parameter is higher for the (001) facet, due to a higher concentration of oxygen octahedrons on it, and thus the resulting E_{at} per sodium atom per unit area ends up to be the lower among those considered. The surpassingly favored energetic interaction with (100) facets must be furthermore attributed to a better accommodation of Na atoms on the monoatomic step on the facet, whilst the (001) planar surface forces sodium atoms to pack with a higher density and thus conveying lateral un-favorable interactions. For what concern Na uptake mechanism, the change from a linear to a polynomial dependence between peak currents and scan rate, in a double logarithmic plot, clearly evidences an intercalation pseudocapacitance contribution to the total material capacity, at least for what concern moderate current densities. The reduced graphene oxide-TiO₂ composite, allows to obtain outstandingly stable capacities ($\sim 150 \text{ mAh}\cdot\text{g}^{-1}$ for more than 600 cycles) never achieved so far with such a low content of carbonaceous substrate (5 wt %). It has been also proven that these notable performances are not related to the overall surface area of the different morphologies but has to be directly connected to the peculiar surface characteristics of the crystals. Further efforts have to be directed in overcoming the puzzling irreversible capacity connected to the first cycle, particularly evident if low current are used. Owing this, it is important that in the future design of oxide-based and TiO₂-based anode materials for SIBs a special consideration is addressed to the crystalline characteristics of the particles and to theoretical studies concerning the Na interaction with different energetic content surfaces.

7. Bibliography

- (1) “Electrical Energy Storage Technology Options.” *Electr. Power Res. Inst.* **2010**, Report 102.
- (2) Dunn, B.; Kamath, H.; Tarascon, J.-M. Electrical Energy Storage for the Grid: A Battery of Choices. *Science (80-.)*. **2011**, 334 (6058), 928–935.
- (3) Bruce, P. G.; Scrosati, B.; Tarascon, J.-M. Nanomaterials for Rechargeable Lithium Batteries. *Angew. Chemie Int. Ed.* **2008**, 47, 2930–2946.
- (4) Goodenough, J. B. Electrochemical Energy Storage in a Sustainable Modern Society. *Energy Environ. Sci.* **2014**, 7 (1), 14–18.
- (5) Ellis, B. L.; Lee, K. T.; Nazar, L. F. Positive Electrode Materials for Li-Ion and Li-Batteries. *Chem. Mater.* **2010**, 22, 691–714.
- (6) Tarascon, J.-M. Is Lithium the New Gold? *Nat. Chem.* **2010**, 2 (6), 510.
- (7) Larcher, D.; Tarascon, J.-M. Towards Greener and More Sustainable Batteries for Electrical Energy Storage. *Nat. Chem.* **2014**, 7 (1), 19–29.
- (8) The lithium market www.signumbox.com/lithium-reports/.
- (9) Division, E. S. A Review of Battery Life-Cycle Analysis : State of Knowledge and Critical Needs. *Transp. Res.* **2010**, 45.
- (10) Wang, L. P.; Yu, L.; Wang, X.; Srinivasan, M.; Xu, Z. J. Recent Developments of Electrode Materials for Sodium Ion Batteries. *J. Mater. Chem. A* **2015**.
- (11) Kubota, K.; Komaba, S. Review—Practical Issues and Future Perspective for Na-Ion Batteries. *J. Electrochem. Soc.* **2015**, 162 (14), A2538–A2550.
- (12) Kim, Y.; Ha, K.-H.; Oh, S. M.; Lee, K. T. High-Capacity Anode Materials for Sodium-Ion Batteries. *Chemistry* **2014**, 20 (38), 11980–11992.
- (13) Longoni, G.; Wang, J. E.; Jung, Y. H.; Kim, D. K.; Mari, C. M.; Ruffo, R. The Na₂FeP₂O₇-Carbon Nanotubes Composite as High Rate Cathode Material for Sodium Ion Batteries. *J. Power Sources* **2016**, 302, 61–69.
- (14) Ruffo, R.; Fathi, R.; Kim, D. K. J.; Jung, Y. H.; Mari, C. M.; Kim, D. K. J. Impedance Analysis of Na_{0.44}MnO₂ Positive Electrode for Reversible Sodium Batteries in Organic Electrolyte. *Electrochim. Acta* **2013**, 108, 575–582.
- (15) D’Arienzo, M.; Ruffo, R.; Scotti, R.; Morazzoni, F.; Mari, C. M.; Polizzi, S. Layered Na(0.71)CoO(2): A Powerful Candidate for Viable and High Performance Na-Batteries.

- Phys. Chem. Chem. Phys.* **2012**, *14* (17), 5945–5952.
- (16) Yabuuchi, N.; Kajiyama, M.; Iwatate, J.; Nishikawa, H.; Hitomi, S.; Okuyama, R.; Usui, R.; Yamada, Y.; Komaba, S. P2-Type Na_x[Fe_{1/2}Mn_{1/2}]O₂ Made from Earth-Abundant Elements for Rechargeable Na Batteries. *Nat. Mater.* **2012**, *11* (6), 512–517.
- (17) Padhi, A. K.; Nanjundaswamy, K. S.; Goodenough, J. B. Phospho- olivines as Positive- Electrode Materials for Rechargeable Lithium Batteries. *J. Electrochem. Soc.* **1997**, *144* (4), 1188–1194.
- (18) Recham, N.; Chotard, J.-N.; Dupont, L.; Djellab, K.; Armand, M.; Tarascon, J.-M. Ionothermal Synthesis of Sodium-Based Fluorophosphate Cathode Materials. *J. Electrochem. Soc.* **2009**, *156* (12), A993–A999.
- (19) Kundu, D.; Tripathi, R.; Popov, G.; Makahnouk, W. R. M.; Nazar, L. F. Synthesis, Structure, and Na-Ion Migration in Na₄NiP₂O₇F₂: A Prospective High Voltage Positive Electrode Material for the Na-Ion Battery. **2015**, *4906* (5), 5349.
- (20) Chen, C. Y.; Matsumoto, K.; Nohira, T.; Hagiwara, R.; Orikasa, Y.; Uchimoto, Y. Pyrophosphate Na₂FeP₂O₇ as a Low-Cost and High-Performance Positive Electrode Material for Sodium Secondary Batteries Utilizing an Inorganic Ionic Liquid. *J. Power Sources* **2014**, *246*, 783–787.
- (21) Chen, C.-Y.; Matsumoto, K.; Nohira, T.; Ding, C.; Yamamoto, T.; Hagiwara, R. Charge-discharge Behavior of a Na₂FeP₂O₇ Positive Electrode in an Ionic Liquid Electrolyte between 253 and 363K. *Electrochim. Acta* **2014**, *133*, 583–588.
- (22) Chung, S.; Yamada, Y.; Yamada, A. Na₂FeP₂O₇: A Safe Cathode for Rechargeable Sodium-Ion Batteries. *Chem. Mater.* **2013**.
- (23) Dahbi, M.; Yabuuchi, N.; Kubota, K.; Tokiwa, K.; Komaba, S. Negative Electrodes for Na-Ion Batteries. *Phys. Chem. Chem. Phys.* **2014**.
- (24) Klein, F.; Jache, B.; Bhide, A.; Adelhelm, P. Conversion Reactions for Sodium-Ion Batteries. *Phys. Chem. Chem. Phys.* **2013**, *15* (38), 15876–15887.
- (25) Chevrier, V.; Ceder, G. Challenges for Na-Ion Negative Electrodes. *J. Electrochem. Soc.* **2011**, *158* (9), A1011.
- (26) Zhang, S.; Li, W.; Tan, B.; Chou, S.; Li, Z.; Dou, S. One-Pot Synthesis of Ultra-Small Magnetite Nanoparticles on the Surface of Reduced Graphene Oxide Nanosheets as Anodes for Sodium-Ion Batteries. *J. Mater. Chem. A* **2015**, *3* (9), 4793–4798.

- (27) Kumar, P. R.; Jung, Y. H.; Bharathi, K. K.; Lim, C. H.; Kim, D. K. High Capacity and Low Cost Spinel Fe₃O₄ for the Na-Ion Battery Negative Electrode Materials. *Electrochim. Acta* **2014**, *146*, 503–510.
- (28) Wang, D.; Yu, Y.; He, H.; Wang, J.; Zhou, W.; Abruna, H. D. Template-Free Synthesis of Hollow-Structured Co₃O₄ Nanoparticles as High-Performance Anodes for Lithium-Ion Batteries. *ACS Nano* **2015**, No. 2, 1775–1781.
- (29) Liu, Y.; Cheng, Z.; Sun, H.; Arandiyani, H.; Li, J.; Ahmad, M. Mesoporous Co₃O₄ sheets/3D Graphene Networks Nanohybrids for High-Performance Sodium-Ion Battery Anode. *J. Power Sources* **2015**, *273*, 878–884.
- (30) Su, Q.; Zhang, J.; Wu, Y.; Du, G. Revealing the Electrochemical Conversion Mechanism of Porous Co₃O₄ Nanoplates in Lithium Ion Battery by in Situ Transmission Electron Microscopy. *Nano Energy* **2014**, *9*, 264–272.
- (31) Yang, X.; Wang, C.; Yang, Y.; Zhang, Y.; Jia, X.; Chen, J.; Ji, X. Anatase TiO₂ Nanocubes for Fast and Durable Sodium Ion Battery Anodes. *J. Mater. Chem. A* **2015**, *3*, 8800–8807.
- (32) Wu, L.; Bresser, D.; Buchholz, D.; Giffin, G.; Castro, C. R.; Ochel, A.; Passerini, S. Unfolding the Mechanism of Sodium Insertion in Anatase TiO₂ Nanoparticles. *Adv. Energy Mater.* **2014**, 1–11.
- (33) Xiong, H.; Slater, M. D.; Balasubramanian, M.; Johnson, C. S.; Rajh, T. Amorphous TiO₂ Nanotube Anode for Rechargeable Sodium Ion Batteries. *J. Phys. Chem. Lett.* **2011**, 2560–2565.
- (34) Xu, Y.; Memarzadeh Lotfabad, E.; Wang, H.; Farbod, B.; Xu, Z.; Kohandehghan, A.; Mitlin, D. Nanocrystalline Anatase TiO₂: A New Anode Material for Rechargeable Sodium Ion Batteries. *Chem. Commun. (Camb)*. **2013**, *49* (79), 8973–8975.
- (35) Wu, L.; Buchholz, D.; Bresser, D.; Gomes Chagas, L.; Passerini, S. Anatase TiO₂ Nanoparticles for High Power Sodium-Ion Anodes. *J. Power Sources* **2014**, *251*, 379–385.
- (36) Kim, K.-T.; Ali, G.; Chung, K. Y.; Yoon, C. S.; Yashiro, H.; Sun, Y.-K.; Lu, J.; Amine, K.; Myung, S.-T. Anatase Titania Nanorods as an Intercalation Anode Material for Rechargeable Sodium Batteries. *Nano Lett.* **2014**, *14* (2), 416–422.
- (37) Dinh, C.-T.; Nguyen, T.-D.; Kleitz, F.; Do, T.-O. Shape-Controlled Synthesis of Highly

- Crystalline Titania Nanocrystals. *ACS Nano* **2009**, 3 (11), 3737–3743.
- (38) D'Arienzo, M.; Carbajo, J.; Bahamonde, A.; Crippa, M.; Polizzi, S.; Scotti, R.; Wahba, L.; Morazzoni, F. Photogenerated Defects in Shape-Controlled TiO₂ Anatase Nanocrystals: A Probe to Evaluate the Role of Crystal Facets in Photocatalytic Processes. *J. Am. Chem. Soc.* **2011**, 133 (44), 17652–17661.
- (39) Liu, G.; Yang, H. G.; Pan, J.; Yang, Y. Q.; Lu, G. Q. M.; Cheng, H. M. Titanium Dioxide Crystals with Tailored Facets. *Chem. Rev.* **2014**, 114 (19), 9559–9612.
- (40) Eletsii, A. V.; Iskandarova, I. M.; Knizhnik, A. a.; Krasikov, D. N. Graphene: Fabrication Methods and Thermophysical Properties. *Physics-Uspekhi* **2011**, 54 (3), 227–258.
- (41) Raju, M.; Van Duin, A. C. T.; Fichthorn, K. A. Mechanisms of Oriented Attachment of TiO₂ Nanocrystals in Vacuum and Humid Environments: Reactive Molecular Dynamics. *Nano Lett.* **2014**, 14 (4), 1836–1842.
- (42) Ge, Y.; Jiang, H.; Zhu, J.; Lu, Y.; Chen, C.; Hu, Y.; Qiu, Y.; Zhang, X. High Cyclability of Carbon-Coated TiO₂ Nanoparticles as Anode for Sodium-Ion Batteries. *Electrochim. Acta* **2015**, 157, 142–148.
- (43) Perfonrranc, I.; Area, P.; Leaders, Q.; Teams, T. C.; Improvement, C.; Dmt, D. T. S.; Sepg, D.; Chen, C.; Wen, Y.; Hu, X.; Ji, X.; Yan, M.; Mai, L.; Hu, P.; Shan, B.; Huang, Y. Na(+) Intercalation Pseudocapacitance in Graphene-Coupled Titanium Oxide Enabling Ultra-Fast Sodium Storage and Long-Term Cycling. *Nat. Commun.* **2015**, 6, 6929.
- (44) Li, N.; Zhou, G.; Fang, R.; Cheng, H.; Li, F.; Cheng, H. TiO₂/graphene Sandwich Paper as an Anisotropic Electrode for High Rate Lithium Ion Batteries. *Nanoscale* **2013**, 5 (17), 3–6.
- (45) Tahir, M. N.; Oschmann, B.; Buchholz, D.; Dou, X.; Lieberwirth, I.; Panthöfer, M.; Tremel, W.; Zentel, R.; Passerini, S. Extraordinary Performance of Carbon-Coated Anatase TiO₂ as Sodium-Ion Anode. *Adv. Energy Mater.* **2015**, n/a-n/a.
- (46) Wagemaker, M.; Borghols, W. J. H.; Mulder, F. M. Large Impact of Particle Size on Insertion Reactions . A Case for Anatase Li T_xO₂. *J. Am. Chem. Soc.* **2007**, 129 (March), 4323–4327.
- (47) Augustyn, V.; Come, J.; Lowe, M. a; Kim, J. W.; Taberna, P.-L.; Tolbert, S. H.; Abruña,

- H. D.; Simon, P.; Dunn, B. High-Rate Electrochemical Energy Storage through Li⁺ Intercalation Pseudocapacitance. *Nat. Mater.* **2013**, *12* (6), 518–522.
- (48) Conway, B. E. E.; Birss, V.; Wojtowicz, J. The Role and Utilization of Pseudocapacitance for Energy Storage by Supercapacitors. *J. Power Sources* **1997**, *66* (1–2), 1–14.
- (49) Chen, W.; Fan, Z.; Gu, L.; Bao, X.; Wang, C. Enhanced Capacitance of Manganese Oxide via Confinement inside Carbon Nanotubes. *Chem. Commun.* **2010**, *46* (22), 3905.
- (50) Wang, J.; Polleux, J.; Lim, J.; Dunn, B. Pseudocapacitive Contributions to Electrochemical Energy Storage in TiO₂ (Anatase) Nanoparticles. **2007**, *2*, 14925–14931.
- (51) Dylla, A. G.; Henkelman, G.; Stevenson, K. J. Lithium Insertion in Nanostructured TiO₂ (B) Architectures. **2013**, *46* (5).
- (52) Neugebauer, J.; Scheffler, M. Adsorbate-Substrate and Adsorbate-Adsorbate Interactions of Na and K Adlayers on Al(111). *Phys. Rev. B* **1992**, *46* (24), 16067–16080.
- (53) Clark, S. J.; Segall, M. D.; Pickard, C. J.; Hasnip, P. J.; Probert, M. I. J.; Refson, K.; Payne, M. C. First Principles Methods Using CASTEP. *Zeitschrift für Krist.* **2005**, *220* (5-6–2005), 567–570.

CHAPTER IX: Conclusions and Outlook

In this doctoral work an extensive and in-depth analysis of functional inorganic materials for rechargeable sodium-ion batteries has been carried out. The entire project focused on facile synthetic routes perpetration and the investigation of occurring fundamental mechanisms accountable for energy storage and reversible sodium uptake. The preliminary results obtained on a conversion-type nano-structured anode material (Co_3O_4) stressed the importance of the physical characteristics, namely porosity, hierarchical structures and crystallinity on reversibility of conversion reaction. *Ex situ* investigation allowed to better sketch the ongoing processes. We successfully proved that conversion mechanisms occurring during the very first electrochemical sodiation and de-sodiation are sensibly different if compared to those connected to following cycles, and that a pure conversion reaction yielding back to Co_3O_4 after discharging is not to be taken for granted. On the contrary an incomplete re-oxidation giving CoO instead of spinel Co_3O_4 has been observed having a major role upon cycling. Chemical sodiation electrode pre-treatment has been applied to TMO and beneficial effects have been observed especially in terms of first cycle irreversible capacity, heavily reduced in this case. In investigating the transition metal oxide, voluntarily no carbonaceous matrix substrate has been included in the electrode formulation. Doing so any kind of electrochemical effect biasing pure activity of cobalt oxide has been excluded. Nevertheless interesting specific capacities, with reasonably high Coulombic efficiencies, have been observed. To the attainment of high performing materials employing low-cost and safe synthetic routes has been dedicated the majority of the experimental dissertation. A sodium-iron pyrophosphate/ multiplewalled carbon nano-tubes composite, obtained via simple coprecipitation route, arose throughout the investigated compounds as an outstandingly stable cathode material manifesting impressive kinetic performances. Synthetic procedure revealed itself as highly beneficial to the establishment of an extended conductive network partially embedded in pyrophosphate particles bulk. Thank to this unique set-up achieved through a procedure that is suitable for a low-cost industrial scale-up, high-rate sodium atom diffusion through pyrophosphate crystalline open structure could be fully exploited.

After a thorough screening of low-cost non-toxic anode materials, nano-structured anatase TiO_2 has been targeted as an illustrative candidate to operate systematic studies related

to interaction with sodium on. Exploiting acquired expertise in nano-crystals shaping strategies using solo-thermal methods, peculiar crystalline facets exposure have been modulated on crystallite surface. In defining electrochemical performances of the as-synthesized samples, a strong correlation between energy storage based onto a pseudo-capacitive mechanism and specific surface energies of crystalline facets has been observed. This finding agrees experimentally with theoretical studies present in literature which confers to intermediate surface energy facets the highest capacity of reversibly interacting with sodium atoms. Added to these more fundamental mechanistic studies, are here recalled the interesting electrochemical performances in terms of stability, Coulombic efficiencies and reversible capacities. Rhombohedral elongated nano-particles/reduced graphene oxide composite can be cycled for hundreds cycles providing a stable capacity of $150 \text{ mAh}\cdot\text{g}^{-1}$ affected by a negligible fade.

Systematic studies related to peculiar surfaces-alkaline cations interaction should be perpetrated and encouraged, being the surface crystalline facets gates for sodium (or lithium) uptake and further bulk diffusion (for insertion materials). Surface energetic landscape acquires thus a primary role in defining the electrochemical performances of morphologically homogeneous nano-particles.

CHAPTER X: Appendix

1. GITT (Galvanostatic Intermittent Titration Technique)

Canonic electrochemical techniques such as Cyclic Voltammetry (CV), Galvanostatic Cycling with Potential Limitation (GCPL) and other potentiodynamic methods, are widely used in this work. Their detailed description is far behind the purposed of this chapter and the reader is encouraged to find elsewhere their analysis¹. Galvanostatic Intermittent Titration Technique (GITT) is instead peculiar of battery materials analysis and in particular suited for precise physical characteristics determination. This will be thus described here in detail. GITT is known to be a reliable electroanalytical technique employed to determine physical properties, such as diffusion coefficients (D), connected to solid state redox processes and in particular variation in phase composition (x). GITT is based on a chronoamperometric electroanalytical method which relies on the application of subsequent current impulses (I_0) of duration τ , of the same magnitude, followed by open circuit voltage periods with relatively short duration. This technique applies to intercalation compounds hosting alkaline metals (Na^+ and Li^+ for example). Every current pulse, depending on the direction of the current itself, bring a modification in hosting material composition accounting for $x \pm \Delta x$. Following a Nernstian behavior the potential has to change accordingly, switching from the starting value E_0 to a new equilibrium value E_S . The resulting voltage profile of a single current pulse is reported in Figure X-1 with a schematic labeling of significant parameters. On the application of a constant current, the cell potential increase instantaneously from its equilibrium value E_0 tending to reach a new dynamic equilibrium value that as the IR drop, deriving from electrolyte solution resistivity, superimposed. After the impulse, during the resting period, the potential sets to a new equilibrium E_S , condition dictated by the stoichiometry variation. The change in associated steady state voltage $\Delta E_S (= E_S - E_0)$ is thus determined. This procedure is then repeated until the composition interval of interest (x) is covered. Worth noting is that diffusion coefficients are here determined electrochemically, and for this technique to be consistent, the approximation of a pure insertion mechanism has to be done. This technique loses its significance if other types of proces, being conversion or alloying reactions for example, in which a pure diffusion of alkaline cations inside a crystalline lattice cannot be hypothesized, occur. For a composition

interval in which the process taking place is believed to be purely diffusive, ΔE_S will tend to be equal for subsequent current pulses. Diffusion value is ultimately obtained by applying the Fick's second law of diffusion and after a series of assumptions for sufficiently small current so that ΔE_S is small too, can be written²:

$$D_{Na^+} = \frac{4}{\pi} \left(\frac{m_B V_m}{M_B A} \right)^2 \left(\frac{\Delta E_S}{\tau (dE_t/d\sqrt{\tau})} \right)^2, \quad \tau \ll \frac{L^2}{D_{Na^+}} \quad (X.1)$$

where V_m is the molar volume of the compound, M_B and m_B are its molecular weight and mass, respectively, A is the total contact area between the electrolyte and the electrode and L the thickness of the electrode.

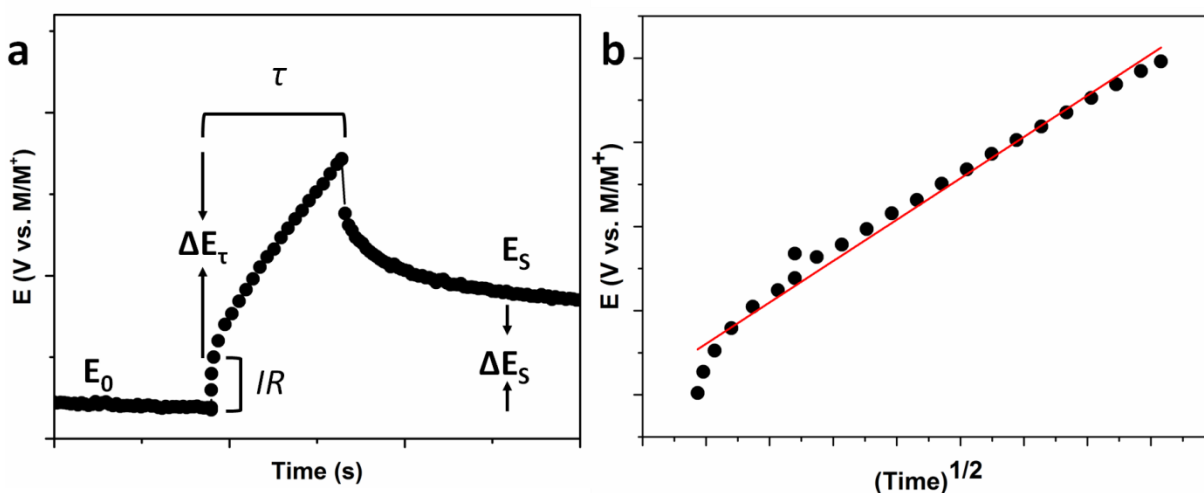


Figure X-1: a) Applied current pulse vs voltage profile for a single titration during a charging step with schematic representation of different parameters; b) variation of cell voltage for the above titration plotted against $\tau^{1/2}$ to show the linear fit.

The variation of cell voltage during the time period τ on application of I_0 at time t_0 is plotted against $\tau^{1/2}$ in image b) in Figure X-1. As can be clearly seen E vs. $\tau^{1/2}$ is shows a straight line behavior over the entire time period end hence previous equation can be further simplified in:

$$D_{Na^+} = \frac{4}{\pi} \left(\frac{m_B V_m}{M_B A} \right)^2 \left(\frac{\Delta E_S}{\Delta E_t} \right)^2 \quad (X.2)$$

The value of D_{Na^+} can be obtained by substituting in equation X.2 simply the slope of straight line. As a double check, the diffusion coefficient values in solids can be also calculated in some circumstances, using impedance analysis (as reported elsewhere in this chapter).

Nevertheless even in that case the differential $\Delta E/\Delta x$, which appear in the corresponding equation as well, can be estimated from the titration curve.

2. BET (Brunauer-Emmet-Teller Surface Area Analysis)

The Brunauer, Emmett and Teller (BET) technique is the most common method for determining the specific surface area and porosity of powder and porous materials. Specific surface area is expressed in $\text{m}^2 \text{g}^{-1}$, and is the result of measuring surface roughness as well as quantity and size distribution of open pores. This analysis is required for a number of very different applications, principally where the materials surface is the key active part, for as in catalysis, sensors, and electrode materials. The BET theory extends the Langmuir theory of monolayer molecular gas adsorption to multilayer gas adsorption.

Adsorption is defined as the adhesion of atoms or molecules of gas to a surface. The adsorbed amount of gas depends on the temperature, on the gas pressure, on the strength of interaction between the gas and solid and on the sample morphology in terms of both surface extension and exposed facets. In BET surface area analysis, nitrogen is usually used as adsorbate because of easy availability in high purity and its strong interaction with most solids. As the interaction between gaseous and solid phases is usually weak (physisorption, with energies of the range between 10-100 mV), the surface is cooled using liquid N_2 to obtain detectable amounts of adsorption; therefore known amounts of nitrogen gas are then released stepwise into the sample cell. Relative pressure less than atmospheric pressure is achieved by creating conditions of partial vacuum and after the saturation pressure, no more adsorption occurs regardless of any further increase in pressure. After the adsorption layers are formed, the sample is removed from the nitrogen atmosphere and heated to cause the adsorbed nitrogen to be released from the material and quantified. The data collected is displayed in the form of a BET isotherm, which plots the amount of gas adsorbed as a function of the relative pressure.

The BET theory assumes that where the surface is covered with only one layer of adsorbate, an equilibrium exists between that layer and the vapour; where two layers are adsorbed, the upper layer is in equilibrium with the vapour, and so forth. Since the equilibrium is dynamic, the actual location of the surface sites covered by one, two or more layers may vary but the number of molecules in each layer will remain constant³. The BET equation X.3, is the

most commonly used method to determine the number of molecules required to form a monolayer and specific surface area.

$$\frac{x}{V(1-x)} = \frac{1}{V_m C} + \frac{x(C-1)}{V_m C} \quad (\text{X.3})$$

Where V is the volume of the adsorbed molecules, x is the relative pressure P/P_0 , V_m is the monolayer volume and C is the BET constant, that is related to the energy of adsorption in the first adsorbed layer and consequently this value is an indication of the magnitude of the adsorbent/adsorbate interactions. In general the higher the value of C , the higher the interaction. Five types of adsorption isotherms, whose profiles can be appreciated in Figure X-2, can be distinguished depending on the physicochemical conditions of the interactions:

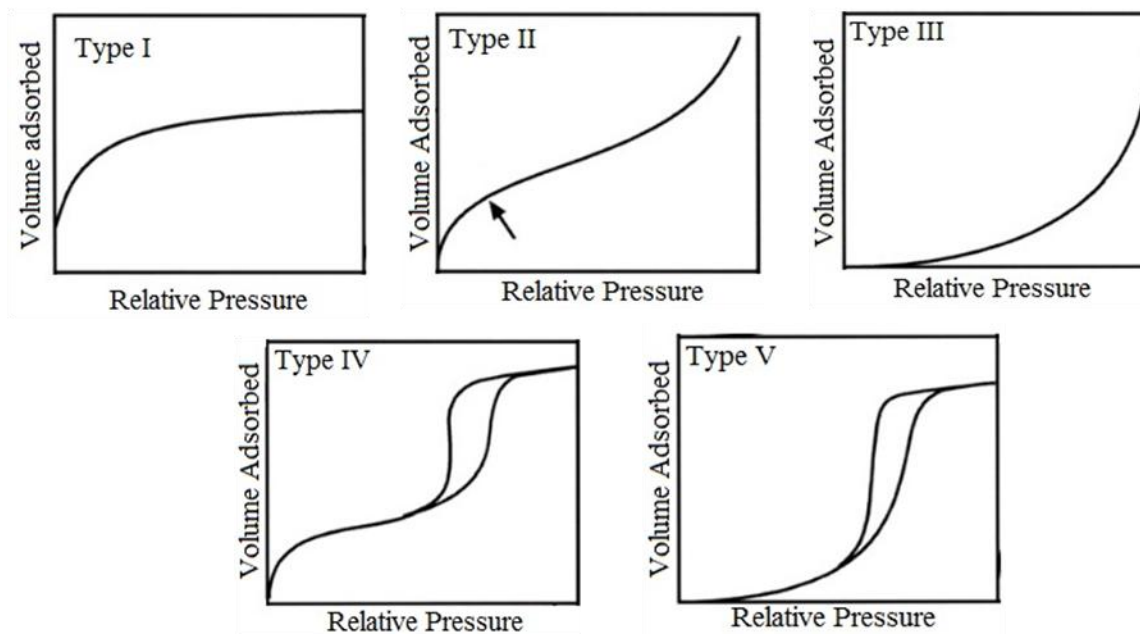


Figure X-2: adsorption isotherms, see text for further description.

Type I isotherm shows a rapid rise which approaches a maximum value asymptotically as the vapour pressure increases, indicating the completion of monolayer adsorption (pseudo-Langmuir isotherm). Due to the negligible forces of attraction of the adsorbed molecules, multilayered molecule adsorption is not possible. A type I isotherm is obtained when $P/P_0 < 1$ and $C > 1$ in the BET equation. The characterization of microporous materials, with pore diameters less than 2 nm, gives this type of isotherm.

Type II isotherm refers to reversible and unrestricted multilayer physical adsorption in nonporous or macroporous solids, displaying a point of inflexion or knee which is attributed to the formation of monolayer. After the monolayer adsorption, further increase in partial pressure

result in extensive adsorption and followed by multilayer coverage. A type II isotherm is obtained when $C > 1$ in BET equation.

Type III isotherm is characterized by the convexity towards the partial pressure axis, starting at the origin. It occurs in situations where interactions between the adsorbate and adsorbent is relatively weak compared to the adsorbate-adsorbate interaction. Therefore it is necessary to have significant partial pressure of adsorbate before the adsorption process commences. This type of isotherm is obtained when $C < 1$ and shows the multilayer formation.

Type IV isotherm is characterized by an initial inflection that indicates the monolayer formation (analogous to type II isotherm) followed by a formation of multilayers. The most characteristic part of the type IV isotherm is the hysteresis loop, which is associated with the occurrence of pore condensation. Gases condense in the tiny capillary pores of the solids at pressure below the saturation pressure of the gas. The adsorption ceases, once all the pores are completely filled. This isotherm is typical for mesoporous materials with pore diameters between 2-50 nm.

Type V isotherm is characterized by an initial pathway similar to that of Type III, indicating relatively weak attractive interactions between the adsorbent and the adsorbate. Instead at higher pressure it is similar to type IV isotherm, indeed shows pore condensation and hysteresis.

The range of pressure in which experimental results agree with the BET isotherm is: $0.05 \leq P/P_0 \leq 0.30$; for pressures lower than those of the range, the BET equation under-estimates the actual adsorption, for higher pressure it over-estimates it. In data analysis, the plot of $x/V(1-x)$ versus x should give a straight line over a certain $x=(P/P_0)$ range. The data are considered acceptable if the correlation coefficient, R , of the linear regression is not less than 0.9975; that is, R^2 is not less than 0.995. By determining the slope and the intercept of the resulting linear plot, V_m (i.e. the amount of adsorbed gas when a monolayer is formed) can be determined.

Slope:

$$m = \frac{C - 1}{V_m C} \quad (\text{X.4})$$

Intercept:

$$b = \frac{1}{V_m C} \quad (\text{X.5})$$

Volume of monolayer:

$$V_m = \frac{1}{m + b} \quad (\text{X. 6})$$

The specific surface area (SSA) can thus be derived as:

$$SSA = \frac{V_m N_{Av} a_m}{v_m m_s} \quad (\text{X. 7})$$

where N_{Av} is the Avogadro's number ($6.022 \times 10^{23} \text{ mol}^{-1}$), a_m is the effective cross-section area of one adsorbed molecule (0.162 nm^2 for the N_2 molecule), v_m is the molar volume of one adsorbed molecule (22.414 mL of volume occupied by 1 mol of adsorbate gas at standard condition), and m_s is the mass of substrate/adsorbent.

Before the specific surface area (SSA) of the sample can be determined, it is important to remove gases and vapours chemically adsorbed onto the surface after manufacture and during treatment, handling and storage. If the outgassing is not achieved, the measured SSA values can be lower and may drift because an indeterminate area of the surface is being covered with molecules of the previously adsorbed gases or vapours. The outgassing conditions, defined by the temperature, pressure, and time, are critical for obtaining reproducible and accurate specific surface area measurements. Outgassing of many substances can be achieved by applying a vacuum or by purging the sample in a flowing stream of an inert, dry gas. In either case, elevated temperatures are sometimes applied to increase the rate at which the contaminants (preadsorbed molecules) leave the surface and remove chemisorbed species. Nonetheless, this has to be conducted without affecting the nature of the surface and the integrity of the sample, i.e., melting, dehydration, sintering, and decomposition.

The use of nitrogen adsorption for pore size analysis dates from the late 1940s. It is based on the application of the Kelvin equation, with a correction for the multilayer thickness on the pore walls. One of the first computational procedures was proposed by Shull but the method devised by Barrett, Joyner and Halenda (BJH) in 1951 remains the most popular way of deriving the pore size distribution from an appropriate nitrogen isotherm. According to the classical approach, a corrected form of the Kelvin equation can be used to evaluate the pore width from the pore filling pressure. It is necessarily assumed that the pores are rigid and all of the same shape (cylinders or parallel-sided slits) and that the meniscus curvature is dependent on the dimensions of the pores.

This method is based on the assumption that the initial relative pressure is close to unity and all pores are filled with the liquid⁴:

$$V_{P_n} = \left(\frac{r_{p_n}}{r_{K_n} + \Delta t_n} \right)^2 \left(\Delta V_n - \Delta t_n \sum_{j=1}^{n-1} c_j A_{p_j} \right) \quad (\text{X. 8})$$

where V_{P_n} is the pore volume, ΔV_n is the observed volume of gas (N_2) desorbed, Δt_n is the change in thickness of physically adsorbed layer of nitrogen, A_{p_j} is the area of each pore from which the physically adsorbed gas is desorbed, $c_j = \frac{\bar{r}_p - t_{\bar{r}}}{\bar{r}_p}$ in which \bar{r}_p is the capillary average radius and $t_{\bar{r}}$ is the thickness of physically adsorbed layer at the corresponding value of P/P_0 , $r_{K_n} = \frac{-4.14}{\log(P/P_0)}$ is the inner capillary radius calculated from Kelvin equation when nitrogen is

used as adsorbate and $r_{p_n} = r_k + t$ is the pore radius in which $t = 3.54 \left[\frac{-5}{\ln(P/P_0)} \right]^{1/3}$. The instrument used for this analysis was TriStar®II 3020 (Micromeritics Instrument Corporation system), Fig.2.10. The specific surface area (SSA, BET method), pore volume (desorption cumulative pore volume, DCPV), and pore size distribution (BJH method) were measured after evacuation at 200°C for 6 hours under nitrogen.

3. PEIS (Potentiondynamic Electrochemical Impedance Spectroscopy)

The electrochemical impedance spectroscopy is an alternated voltage-based technique in which a sinusoidal potential stimulus, with a progressively increasing period and thus associated frequency, is applied to an electrochemical system and the correspondent current response is registered.

$$X(t) = \int_{-\infty}^{+\infty} G(t - t')f(t')dt' \quad (\text{X. 9})$$

This equation describes the response, the function G , of the system to the sinusoidal stimulus assuming the points generating the response itself do not become stimulus sources. Applying the Fourier transform⁵ to the integral the following rearranged equation in the frequency domain can be obtained:

$$G(\omega) = \frac{X(\omega)}{f(\omega)} \quad (\text{X.10})$$

This means that in the frequency domain a monochromatic stimulus $f(\omega)$ multiplied by the response function $G(\omega)$ leads to a response $X(\omega)$. Owing this, by knowing stimulus function and response function the transfer function can be found. The latter describes the characteristics of the system and by its study an accurate determination of system properties can be achieved. Typically in an electrochemical system the potential stimulus is $V = V_m e^{i\omega t}$ and the correspondent response current can be thus expressed as $I = I_m e^{i\omega t'}$. The equation X.10 can give:

$$G(\omega) = \frac{I_m e^{i\omega t'}}{V_m e^{i\omega t}} = \frac{I_m}{V_m} e^{i\omega(t'-t)} = Y_m e^{i\psi} \quad (\text{X.11})$$

where Y_m is the modulus of a new complex quantity called admittance and ψ is the phase shift or offset between the original stimulus and the response. Being Y a complex quantity, it can be de-convoluted as follows:

$$Y = Y_m e^{i\psi} = Y' + iY'' \quad (\text{X.12})$$

being $Y' = Y_m \cos\psi$ and $Y'' = Y_m \sin\psi$. It can be further defined the impedance Z as the scalar quantity equivalent to the inverse of admittance Y . Admittance, impedance the dielectric function (not described here) and other quantities are some of the possible response functions of a system following a stimulus. Since each one of these relations embodies the characteristics of the system itself, by studying them, and how they evolve with frequency can unveil physical properties of the system that can be then quantified provided a proper equivalent circuit⁶.

3.1. Response functions of simple circuits

Systems analyzed in this work well fit with equivalent circuits built on resistors and capacitors only for which correspondent characteristic equations, expressed with impedance, are reported below. For a resistive element, made of a metallic conductor or a generic electronic conductor, the impedance response is $Z = Z' = R = \frac{V_0}{I_0}$. By applying an alternating sinusoidal potential to a resistor, an output current is obtained (in phase with the stimulus), whose values proportional, by the value R , to the entity of the generating stimulus, does not depend on the frequency value. Response function of a circuit solely composed by a capacitor with capacitance C , instead is $Z = Z'' = \frac{1}{\omega C}$. This equation describe the interface between an

electronic, considered purely blocking, and a ionic conductor (non-leaking double-layer capacitance). In this landscape the whole process will be ruled by charge/discharge processes only. In reality the physical system is also describe through a resistive element simulating the charge transfer at the interface. This element heavily affects the current entity available for the charge/discharge processes.

3.2. Response of a parallel RC circuit

In such a circuit the whole impedance response would be generated by the linear combination of discrete contributes derived from resistor and capacitor separately. By substituting the previously mentioned characteristic equations, it can be obtained:

$$Z = R + \frac{1}{i\omega C} \quad (\text{X. 13})$$

Rearranging and then multiplying numerator and denominator by $(1 - i\omega RC)$ can be obtained:

$$Z = \frac{R}{(1 + \omega^2 C^2 R^2)} - i\omega \frac{CR^2}{(1 + \omega^2 C^2 R^2)} \quad (\text{X. 14})$$

The first term is the real component Z' whilst the second is the imaginary part Z'' . Both the components appear in the often reported Nyquist plot. When the R and C components are short-circuited with the condensed charged, the velocity toward which the condenser is discharged depend on the circuit time constant $\tau = RC$. By substituting the time constant inside equation X.14, and reporting the two components separately, it can be obtained:

$$Z' = \frac{R}{[1 + (\omega\tau)^2]} \quad \text{and} \quad Z'' = \frac{R\omega\tau}{[1 + (\omega\tau)^2]} \quad (\text{X. 15})$$

From the real part, ω can be explicitated and substituted in the expression of Z'' obtaining:

$$Z'' = \frac{(CR)^2}{(1 + \omega^2 C^2 R^2)} \quad (\text{X. 16})$$

Or in other terms:

$$Z'' = \sqrt{(R - Z')}Z' \quad (\text{X. 17})$$

Equation X.17 is represented by a semicircle in the complex plane with the center of coordinates $(R/2; 0)$ and radius $R/2$, depicted in Figure X-3.

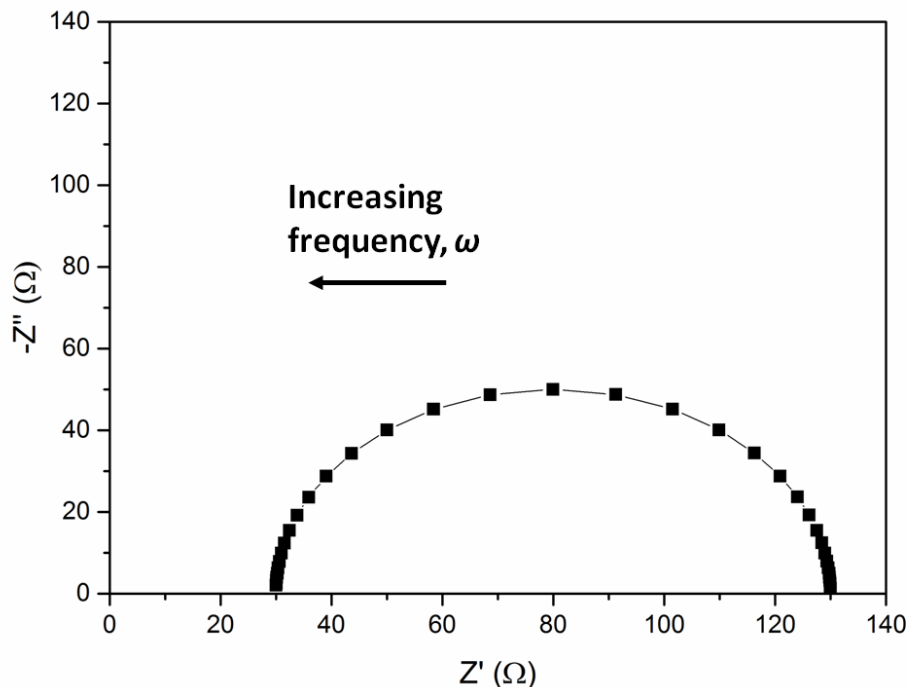


Figure X-3: Nyquist plot of a parallel RC circuit, with in series another resistive contribution (probably expressed by the electrolyte resistivity).

Often more than a single RC parallel has to be involved in order to meet the best fit of the response signal. A sequence of semicircles describes the presence of multiple mechanisms that can be reduced to the physical RC equivalent. This is the case in which both interface charge-transfer and double-layer mechanisms are being addressed, in an occurring electrode reaction, and they take place with sufficiently different time constants. Semicircles can partially overlap if time constants tend to be comparable. Capacitance values of equivalent capacitive elements have also a role in generating coalescence between semicircles.

3.3. Warburg impedance element

Sometimes pure resistors and capacitors are simply not sufficient in physically describing an electrochemical system. Elements such as Warburg element (W) and Constant Phase Elements (CPEs) have to be often introduced in order to account for deviation from an ideal behavior. CPE element, often named Q , lack of a pure physical meaning, but is introduced when in-homogeneities in electrode composition, reactivity and surface roughness are present. Its impedance contribute is:

$$Z = Y_0 (i\omega)^n \quad (\text{X.18})$$

Y_0 and n are CPE characteristic parameters, and for particular values of Y_0 and n , CPE can be connected to normal circuitual elements R and C . For $n = 0, 1, 1/2$, and -1 CPE identifies with a resistance, a capacitor a Warburg element or an inductance respectively. The Warburg element accounts for a diffusion-limited process occurring at the electrode. This contribute emerges at low frequencies when stationary conditions are approached and a potentiostatic electrolysis is instituted. Warburg element is a distributed element whose impedance is:

$$Z_W = Z_D \omega^{1/2} = \sigma \omega^{-1/2} - i \sigma \omega^{-1/2} \quad (\text{X.19})$$

In Warburg impedance imaginary and real components depends on diffusion coefficients (in particular they decrease as the diffusion coefficient progressively increase) and are identical, so that in Nyquist plot Warburg element is represented as a straight line with slope = 1. As can be noted in equation X.19 Warburg impedance depends on diffusion coefficients σ , and thus important information related to species diffusion in solid phase can be derived from its impedance value Z_W . following the relation below:

$$Z_D = V_m (dE/dx) / (zFD^{1/2}A) \quad (\text{X.20})$$

where Z_D is the pre-exponential factor of the Warburg impedance, V_m is the molar volume, F the Faraday constant, D the diffusion coefficient of the species, A the electrode area and (dE/dx) is the slope of equilibrium electrode potential vs. composition that can be modulated from a GITT experiment⁷.

4. XRPD

X-Ray Powder Diffraction is a non-destructive technique for qualitative analysis of crystalline materials in form of powder and it allows to identify unknown substances by comparing experimental diffraction data against a database of known phases. X-Rays, were discovered by Wilhelm Conrad Röntgen in 1895, are formed by electromagnetic radiation of very short wavelength (λ), ranging from 0.01 to 10 nm, and very high energy and they are used for their penetrating power in radiography, radiology, radiotherapy, and scientific research. The X-rays are produced using a sealed high-vacuum tube (image a) Figure X-4). Here, a focus beam of electrons generated by a voltage of 30-60 kV, is emitted by the cathode (usually an electrically heated tungsten filament), and it impinges on an anode made by a highly pure metal (usually Mo, or Cu, less often Ag, Fe, Cr, etc.). Thus, a small area (0.4X8 mm, 0.4X12 mm for “fine focus tubes” and 1X10 mm for “normal focus”) sustains a power input of up to 3kW, and

it is cooled by water. At the anode surface, X-rays are then produced by two separate mechanisms. In the former, the deceleration of the electrons by the field of the metal ions converts some of their energy into radiation. Since this gives a continuous energy spectrum, the radiation produced is called “white” radiation. The shortest wavelength that can be produced is simply related to the applied voltage:

$$\lambda_{min} = \frac{hc}{eU} \quad (\text{X. 21})$$

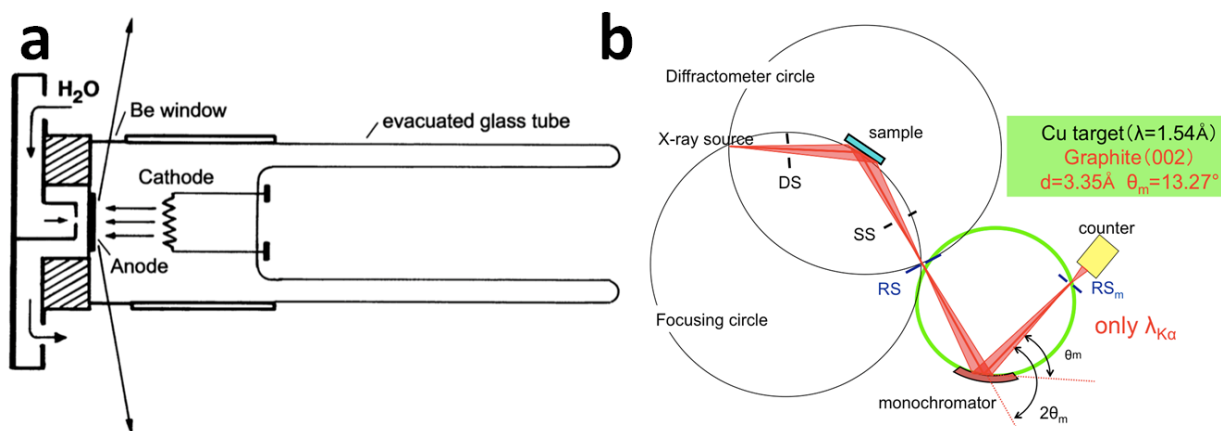


Figure X-4: a) Picture of a vacuum tube for X-Rays production; b) set-up of a diffractometer in the Bragg-Brentano configuration.

where h is Planck's constant, c is the velocity of light, e is the electronic charge and U is the applied voltage. If U is in kV, λ_{min} in \AA is thus approximately $12.4/U$.

In addition to this white radiation, the “characteristic radiation” is produced which is much more important for the study of crystal structure. This radiation arises as a result of many electrons being expelled from atoms the target material is made of, in particular from the K -shell (principal quantum number $n=1$). When an electron from a higher level (usually the L -shell, $n=2$) falls back into the vacancy left by kicked electron in the K -shell, an X-ray photon with a well-defined wavelength is emitted. This wavelength corresponding to the energy difference between the two levels. When Cu is used as target two particular radiations are emitted: $K\alpha$ and $K\beta$, the former is obtained when an electron falls back from the L -shell to the K -shell, while the latter when an electron falls back from the M -shell to the K -shell.

X-rays are generally filtered to a single wavelength (made monochromatic) and collimated to a single direction before they are allowed to strike the crystal. The filtering not only simplifies the data analysis, but also removes radiation that degrades the crystal without contributing useful information. The best method, to obtain a radiation of high intensity, is to use a single-crystal monochromator, image b) in Figure X-4. This consists of a thin, single-crystal flake usually of graphite, quartz, germanium or lithium fluoride, with an area of a few cm^2 , oriented toward the beam so that only the desired $K\alpha$ line meets the condition for constructive interference. The scattered radiation thus becomes the “primary beam” for the actual diffraction experiment. Using bent quartz or germanium monochromators, it is even possible to separate the $K\alpha_1$ and $K\alpha_2$ wavelengths. For most single crystal work, this is not necessary, and in order to get the highest possible intensity, graphite monochromators are used which do not split the $K\alpha_1/K\alpha_2$ doublet.

Diffraction occurs when light is scattered by a periodic array with long-range order, producing constructive interference at specific angles. This phenomena follows the Bragg’s law, the constructive interference from X-rays scattered by parallel planes of atoms produces a diffraction peak at the θ angle which can be obtained by:

$$n\lambda = 2d_{hkl}\sin\theta \quad (\text{X.22})$$

where d_{hkl} is the distance between parallel planes with identical triplets of Miller indices (hkl), θ is the incident angle, n is any integer, and λ is the wavelength of the beam. In most diffractometers, the X-ray wavelength λ is fixed and consequently a family of planes produces a diffraction peak only at a specific angle. Additionally, the plane normal [hkl] (is the direction perpendicular to the plane of atoms) must be parallel to the diffraction vector \bar{s} (the vector that bisects the angle between the incident and diffracted beam).

Powders Diffraction occurs when Bragg’s law is satisfied. The ideal powder sample contains tens of thousands of randomly oriented crystallites and every diffraction peak is the product of X-rays scattering from an equal number of crystallites but, only a small fraction of the crystallites in the specimen contribute to the measured diffraction pattern, thus irradiating a larger volume of material and spinning the sample ensure that a statistically relevant number of grains will contribute to the diffraction pattern. The latter is collected as 2θ versus absolute intensity, this way are shown different peak positions and intensities that are correlated to a

family of atomic planes $\{hkl\}$; whereby by measuring peak positions it is possible to identify the unit cell lattice parameters of the phases present in the sample.

Added to this, crystallites smaller than $\approx 120\text{nm}$ create broadening of diffraction peaks and this can be used to quantify the average crystallite size of nanoparticles using the Scherrer's equation:

$$L = \frac{K * \lambda}{\beta * \cos\theta} \quad (\text{X. 23})$$

where L is the crystallite size, K is Scherrer's constant (with a value close to unity), λ is the X-ray wavelength, β is the full width at the half maximum (FWHM) in radians (*rad*), and θ is the Bragg angle.

5. Bibliography

- (1) Bard, A. J.; Faulkner, L. R.; Swain, E.; Robey, C. *Fundamentals and Applications*.
- (2) Shaju, K. M.; Subba Rao, G. V.; Chowdari, B. V. R. EIS and GITT Studies on Oxide Cathodes, $O_2\text{-Li}_{(2/3)+x}(\text{Co}_{0.15}\text{Mn}_{0.85})\text{O}_2$ ($X = 0$ and $1/3$). *Electrochim. Acta* **2003**.
- (3) Lowell, S.; Shields, J. E.; Thomas, M. A. *Characterization of Porous Solids and Powders: Surface Area, Pore Size and Density*; 2004.
- (4) Barrett, E. P.; Joyner, L. G.; Halenda, P. P. The Determination of Pore Volume and Area Distributions in Porous Substances. I. Computations from Nitrogen Isotherms. *J. Am. Chem. Soc.* **1951**, 73 (1), 373–380.
- (5) Olver, P. J. *Applied Mathematics*; 2003; Vol. 0.
- (6) Barsoukov, E.; Macdonald, J. R. *Impedance Spectroscopy: Theory, Experiment and Application.*; 2005.
- (7) Ruffo, R.; Fathi, R.; Kim, D. K. J.; Jung, Y. H.; Mari, C. M.; Kim, D. K. J. Impedance Analysis of $\text{Na}_{0.44}\text{MnO}_2$ Positive Electrode for Reversible Sodium Batteries in Organic Electrolyte. *Electrochim. Acta* **2013**, 108, 575–582.